

**Okinawa Institute of Science and Technology
Graduate University**

**Thesis submitted for the degree
Doctor of Philosophy**

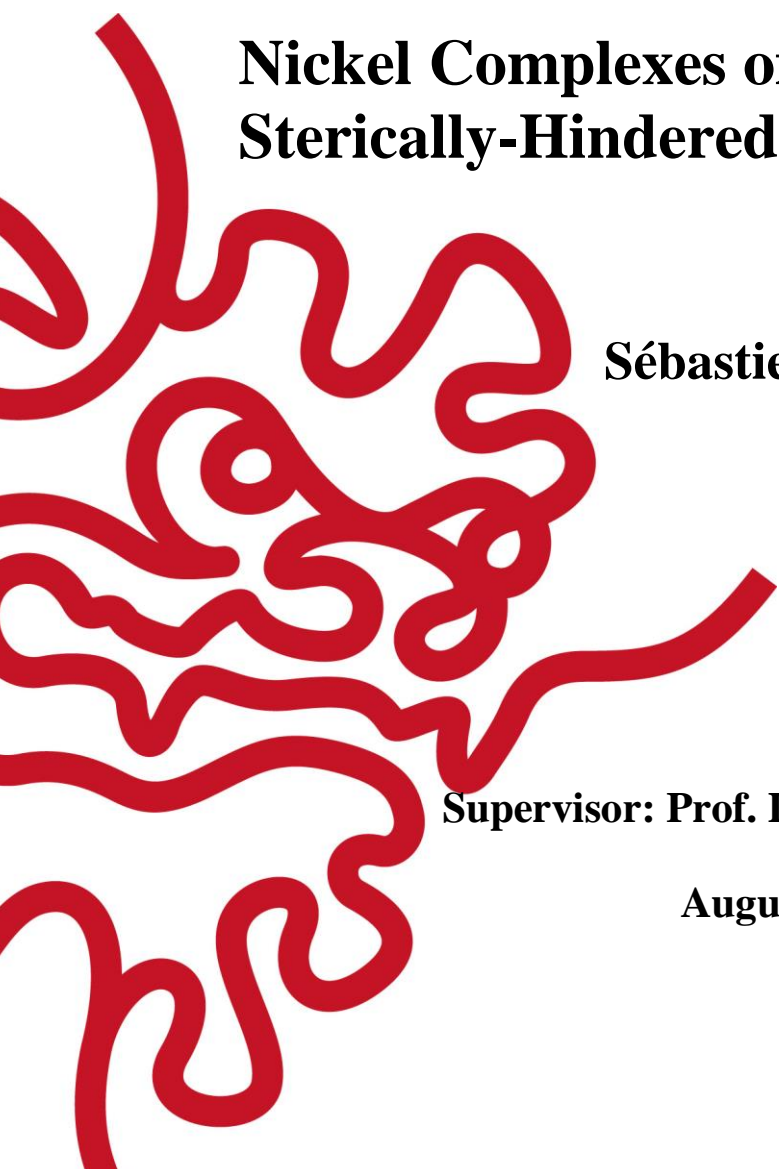
**Nickel Complexes of New Electron-Rich,
Sterically-Hindered PNP Pincer Ligands**

by

Sébastien Lapointe

Supervisor: Prof. Dr. Julia R. Khusnutdinova

August 2020



Declaration of Original and Sole Authorship

I, Sébastien Lapointe, declare that this thesis entitled *Nickel Complexes of New Electron-Rich, Sterically-Hindered PNP Pincer Ligands* and the data presented in it are original and my own work.

I confirm that:

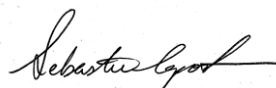
- This work was done solely while a candidate for the research degree at the Okinawa Institute of Science and Technology Graduate University, Japan.
- No part of this work has previously been submitted for a degree at this or any other university.
- References to the work of others have been clearly attributed. Quotations from the work of others have been clearly indicated, and attributed to them.
- In cases where others have contributed to part of this work, such contribution has been clearly acknowledged and distinguished from my own work.
- None of this work has been previously published elsewhere, with the exception of the following:

Lapointe S., Khaskin E., Fayzullin R. R., Khusnutdinova J. R. Stable Nickel(I) Complexes with Electron-Rich, Sterically-Hindered, Innocent PNP Pincer Ligands. *Organometallics* **2019**, 38, 1581-1594.

Lapointe S., Khaskin E. Fayzullin R. R., Khusnutdinova J. R. Nickel(II) Complexes with Electron-Rich, Sterically-Hindered PNP pincer ligands Enable Uncommon Modes of Ligand Dearomatization. *Organometallics* **2019**, 38, 4433-4447

- Authorization for the reuse of the work that includes co-author's contribution has been signed and attached to this document.

Signature:



Date: 17/08/2020

Thesis Abstract

This thesis describes the synthesis, characterization and reactivity studies of nickel complexes of a new family of electron-rich, bulky PNP pincer ligands (PNP = 2,6- $\{R_2PC(CH_3)_2\}_2$ -pyridine). The first chapter introduces the literature review of pincer complexes with a focus on nickel complexes and their applications. The second chapter introduces a new family of pyridine-based PNP pincer ligands that are based on the classic PNP framework, explores how the modified ligand influences the behavior of nickel complexes, and describes examples of mostly metal-based reactivity. This chapter mainly focuses on how this new family of PNP ligands can remain unreactive under specific reductive conditions, which allows the stabilization of complexes having unusual oxidation state of the metal center. The third chapter explores how it is possible to induce new types of ligand-based reactivity on the PNP pincer framework by blocking classical modes of metal-ligand cooperation, and how changes in the electronics and steric properties of the complex can lead to switching from metal-based reactivity to ligand-based reactivity.

Pour ma famille, mes amis et celui qui partage mon cœur.

To my family, my friends and the one who shares my heart

Acknowledgments

I would like to thank all those who stuck with me through those often difficult 5 years of research and had to endure my stupid questions, my loud laughter and stupid puns. You have made my day to day life here in Okinawa an enjoyable and memorable time.

First, thank you **Julia** for your supervision, your insights and for still believing in me even if I often asked stupid questions or gave you way too big of a workload because I couldn't write anything concisely (or simply repeating simple mistakes!). You helped to shape me into the scientist I am today, and I will always be grateful. Thank you **Pradnya** for being a supportive friend and colleague, and for listening to my problems. I'll always appreciate your messages and your bright smile. Thank you, **Ayumu**, for the many discussions we had during lunchtime and your enthusiasm to do many things outside of work with the group. I also wish you and **Miki** a long and prosper life full of love. Thank you, **Orestes**, for making me laugh, for being like a somewhat naughty older brother sometimes (both because of dirty jokes and because you didn't censor yourself, which I appreciate) and teaching me the proper ways to handle things in the lab. Thank you, **Abir**, for being awesome and sharing love of food like I do, and for discussions throughout your time here. I hope we can continue being awesome friends and colleague in the future. Thank you, **Abhishek**, for being an amazing colleague and an older brother to me; always smiling and having such a big and compassionate heart. Also, a big thanks to both you and **Jyoti** (and your lovely kid) for always receiving me with the tastiest of meals and for allowing me to tag along on many of our rides through Okinawa. A big thank you to **James G.** and **James O.** for lighting up my time here in Okinawa during your short three months internship, and a big sorry for having to endure me and my somewhat unclear teaching! I hope I did not make you lose too much interest in research! Thank you, **Robert**, for being a good friend and an amazing crystallographer. Even if we sometimes disagree on how to deal

with structures, you always push yourself towards perfection in finalizing structures for publication, and that made me push myself towards being more careful of how I deal with many things in my research. Thank you, **Wahidur** and **Moumita**, for letting me in your life for more than a year, and letting me enjoy some of the best curry, biryani and other Indian food that I've ever had up until now. Thank you, **Shubham**, for your help, but it's more of a sorry from myself for always being on your back and correcting you! I wish you a bright future and I hope you can find something that you like to do (even if it is being a tomato farmer!). Thank you, **Hòàn**, for all the sweets and the discussions we had, and I hope you can also find something that will make you happy, because you have a lot of potential. You can always talk to me whenever you want. Thank you, **Govindarajan**, **Yu-tao**, **Dilip**, **Tomas** and **Eugene**, for our discussions and the time we spent outside the lab, as well as the occasional help during synthesis, although I regret not talking to some of you more! I hope I don't cause you too much trouble **Dilip** in your current project! Also, thank you, **Olga**, for your constant dirty jokes and showing me weird pictures all the time, you were always brightening up my days, so that's something! Et oui, je ne t'ai pas oublié, **Vincent**! Même si tu m'as souvent niaisé sur mon accent, j'ai quand même beaucoup apprécié être ton voisin pendant un trop court moment! Ne change jamais, mon Parisien préféré! Finally, thanks to all the amazing interns that lightened up my days: **Aleksandr**, **Alexei**, **Boom**, **Andrey**, **Tanner**, **Sandra**, **Luca**, **Luke**, **Manuel**, **Alèria**, **Saiyyyna**, and **Tatianna**. You were all awesome and I wish you a bright future, make it whatever you want it to be!

And of course, all this would not be possible without the tons of friends I have made here on this tiny, but extremely friendly and rich in amazing people, island. I was able to experience the kindness and the best people of the world here. Thank you, **Sahar**, especially for always being there and brightening my days when I felt down. An enormous thank you to all the *Video Game and Board Game club members* and those who often played with me during those un-

forgettable gaming nights, you made it MUCH easier to get through this difficult journey (special mention to *René, Jessee, Florian, Anna, Ankur, Moe, Otis, Milena* and *Kim* for your awesomeness!).

Et pour finir, je veux remercier ceux et celles qui me tiennent le plus à cœur. Ceux et celles qui m'ont encouragé depuis ma jeunesse, qui m'ont soutenu durant les moments difficiles, et qui m'ont aidé à surmonter mes difficultés d'apprentissage. C'est en grande partie grâce à vous que je me suis rendu jusqu'ici et que je vais me rendre encore plus loin. Merci à mes parents (*Nathalie* et *Marc*) et à ma sœur (*Carolanne*) de m'avoir supporté jusqu'ici et merci d'avoir toujours été là pour moi.

Et surtout, merci à toi *Éric*, qui n'as pas arrêté de croire en moi ces dernières 8 années, dont la plupart ont été passés à distance. Tu m'as donné plus de courage et de volonté à continuer que tu ne peux l'imaginer.

And to whomever I couldn't include here or that I didn't specifically mention your name, you played an important role in my life in this little island. I will always remember our time fondly. Please always stay in touch with me through Facebook or e-mail and keep me updated. I am always happy to hear from you.

The doughnut creed:

As you ramble on through life, brother

whatever be your goal

keep your eye upon the doughnut

and not upon the hole.

Table of Contents

Declaration of Original and Sole Authorship	ii
Thesis Abstract	iii
Acknowledgments	v
Table of Contents	ix
Table of Figures	xi
List of Tables	xv
Table of Schemes	xvi
Abbreviations	xix
1 Chapter 1 Introduction to Pincer Chemistry	1
1.1 General introduction and challenges in organometallic chemistry and catalysis	2
1.2 Pincer Complexes of Late-Transition Metals: Synthesis and Applications	5
1.3 Ligand Centered Reactivity in Pincer Complexes	37
Thesis Outline	49
Declaration of Contribution from Co-authors	51
2 Chapter 2: Stabilization of Reactive Nickel(I) Species	52
2.1 Development of New Me ₄ PNP Pincer Ligands and Their Nickel(II) and Nickel(I) Complexes	53
2.2 Results and Discussion	66
2.3 Conclusion of Chapter 2	89
2.4 Experimental Section	90
	ix

Table of Contents

3	Chapter 3: Changing Metal-Centered Reactivity to Ligand-Centered Reactivity by Modifying Electronics and Sterics at the Nickel Center	111
3.1	Introduction to Nickel Hydride and Methyl Pincer Complexes	112
3.2	Results and Discussion	118
3.3	Conclusion of Chapter 3	152
3.4	Experimental Section	153
	Conclusions and Future Outlooks	172
4	Appendix of Chapter 2	xviii
5	Appendix of Chapter 3	xix
	Complete Reference List	xx

Table of Figures

Figure 1.1 Artistic representation of how the term “pincer” was used to represent a tridentate class of ligands based on its usefulness and its ability to bind a metal center similar to how a pincer pinches an object	4
Figure 1.2 Representation of the dual Lewis base (σ -donor) and acid (π -acceptor) character of phosphines.....	12
Figure 1.3 Calculated π -acceptor character for P- and N- based ligands, relative to CO. Determined by NBO analysis (Reprinted with permissions from <i>Organometallics</i> 2007, 26, 2637-2645). ⁷⁹	13
Figure 1.4 Artistic representation of the concept of Tolman’s cone angle, and some representative cone angles ⁸⁰	15
Figure 1.5 Visual representation of σ -donation and π -backbonding orbitals involved in pyridine interaction with transition metal centers.	15
Figure 1.6 The occluded area in blue is used to determine the ligand solid angle of Pd(BINAP) complex. This area is the result of the intricate overlap of many shadow cones (circles) of each individual atom. The yellow part is the area where the ligand is not covering, which is accessible for reactants or other ligands. Reproduced with permission from: Bilbrey J.A., Kazez A.H., Locklin J., and Allen W.D., <i>J. Chem. Theory Comput.</i> 2013, 9, 5734-5744.....	17
Figure 1.7 Effect of the nature of backbone substituent of POCOP cationic nickel pincer complexes 1.12-1.21 on their IR stretching frequencies of CN bond and on their Ni ^{II/III} oxidation potentials. ²⁴	19
Figure 1.8 Examples of unusual <i>fac</i> geometries for Ru and Ir PSiP pincer complexes 1.29-1.31. ⁹⁰	22
Figure 1.9 Example of Ru-N bond elongation when increasing pincer from 5-membered ring to 6-membered ring. ^{91, 92}	22
Figure 1.10 Selected scope of the direct alkylation of terminal alkynes catalyzed by 1.44. ^{110, 111}	26
Figure 1.11 Selected examples for the transfer hydrogenation of ketones catalyzed by 1.45. ¹¹²	27
Figure 1.12 Examples of redox active ligands in the literature. ^{148, 149, 150}	47
Figure 2.1 Classical PNP and Me ₄ PNP ligand systems.	53
Figure 2.2 All structurally characterized Ni ^I pincer and pincer-like complexes to date. ^{170, 173, 176-181}	57
Figure 2.3 Selected examples of Ni ^I pincer complexes 2.6-2.7 and 2.10-2.11, and their crystal structures to emphasize their geometry around the metal center. ^{173, 176, 177}	63
Figure 2.4 Examples of the <i>d</i> -orbital splitting diagram for nickel complexes in different geometries. Pincer complexes of nickel in +1 oxidation states are usually found in T-shaped geometries or in between square-planar and tetrahedral as a seesaw geometry. The seesaw diagram is based on a reported Ni ^{II} -methyl complex with a close to ideal seesaw geometry. ¹⁸⁸	63
Figure 2.5 Stacked ¹ H NMR spectra of 2.36 and 2.38 to show broadening of signals of ^t Bu groups from hindered rotation.....	68
Figure 2.6 Variable temperature NMR of 2.38 from 25 °C to -60 °C in CD ₂ Cl ₂	69
Figure 2.7 ORTEP diagrams for the cationic parts of complexes 2.32-2.35 with the thermal ellipsoids set at 50% probability level. Hydrogen atoms, counterions and solvent molecules are omitted for clarity.	70

Table of Figures

Figure 2.8 ORTEP diagrams for the cationic parts of complexes 2.36-2.39 with the thermal ellipsoids set at 50% probability level. Hydrogen atoms, counterions and solvent molecules are omitted for clarity. Only the main disordered component of 2.38 is shown.....	70
Figure 2.9 Full cyclic voltammogram of ligands L2.3 (black line) and L2.4 (red line). See caption of Figure 2.10 for experimental details.	72
Figure 2.10 (left) Full cyclic voltammogram of 2.37. (right) Cyclic voltammogram of complexes 2.36–2.39. Experimental conditions for both figures: 1 mM solution of complexes 2.36-2.39 in 0.1 M ⁿ Bu ₄ NPF ₆ /MeCN solution at 23 °C (scan rate 0.1 V s ⁻¹ ; 1.0 mm GC disk working electrode; the arrow indicates the initial scan direction). Left figure: Red trace is a CV recorded in a shorter range to estimate reversibility of Ni ^{II/I} wave; the curve was translated upwards in the vertical direction for clarity.....	72
Figure 2.11 Charge – time dependence during coulometry experiment performed using bulk electroreduction of 2.36 in anhydrous acetonitrile with a fixed potential of -1.5 V.	74
Figure 2.12 Experimental (black line) and simulated (red line) EPR spectra of Ni ^I complexes (top left) isolated complex 2.40 in solid black line, and the product of electroreduction of 2.36 in dashed blue line; (top right) isolated complex 2.41; (bottom left) isolated complex 2.42; (bottom right) isolated complex 2.43. See Table 2.4 for simulated and experimental parameters.....	76
Figure 2.13 Comparison of experimental spectra and EPR spectra simulated in EasySpin using g tensor and A values calculated in ORCA.....	78
Figure 2.14 ORTEP diagrams of complexes 2.40-2.43 with the thermal ellipsoids set at 50% probability level. Hydrogen atoms, solvent molecules and a minor disordered component for 2.41 are omitted for clarity.	81
Figure 2.15 Mulliken atomic spin density plots of 2.40-2.43 (DFT-optimized geometries, B3LYP, lanl2dz/6-311++G**). (a) Ni 88.8%, Br 1.2%, P 1.7%, N 3.4%; (b) Ni 87.9%, Cl 1.2%, P 2.4%, N 3.4%; (c) Ni 86.8%, Br 4.1%, P 0.9%, N 1.8%; (d) Ni 85.2%, Cl 3.8%, P 1.8%, N 1.4%.....	82
Figure 2.16 The SOMO representation of 2.40-2.43 (DFT-optimized geometries, B3LYP, lanl2dz (Ni, Br, Cl)/6-311++G**).	82
Figure 2.17 Selected ligand solid angle representations (gray area) of the optimized structure of 2.40 (a-c). Corresponding space filling model representation of the optimized structure of 2.40 (d-f). Nickel atom, green, phosphorous atoms, light orange, bromide atom, light brown. Atoms highlighted in red are the methyl groups on the ligand arms; the isopropyl C-H hydrogen is highlighted in magenta. Zero energy radii were used for computation.	86
Figure 2.18 Selected ligand solid angle representations (gray area) of the optimized structure of 2.42 (a-c). Corresponding space filling model representation of the optimized structure of 2.42 (d-f). Nickel atom, green, phosphorous atoms, light orange, bromide atom, light brown.	87
Figure 3.1 Examples of pincer nickel hydride complexes in the literature. ^{27, 59, 216-219}	112
Figure 3.2 Examples of pincer nickel methyl complexes in the literature. ^{177, 223-226}	116
Figure 3.3 ¹ H NMR spectrum of complex 3.27 with the characteristic hydride signal (400 MHz, CD ₃ CN).	120
Figure 3.4 ¹ H NMR spectrum of complex 3.33 with the characteristic methyl signal (600 MHz, CD ₃ CN) *Traces of C ₆ H ₆	121
Figure 3.5 ORTEP diagrams of complexes 3.26-3.32 with the thermal ellipsoids set at 50% probability level. Most hydrogen atoms except for those on the nickel center, a minor disorder component for 3.30, and counterions are omitted for clarity.....	122
Figure 3.6 (left) DFT-optimized structures of 3.25 without the counterion in the “up-up” and (middle) “up-down” conformations. (right) ORTEP diagram of complex 3.25 with disordered component in dashed lines. Ellipsoids	

are shown at 50% probability. Hydrogen atoms and the counterion has been omitted for clarity. The major disordered component is shown in the ellipsoid representation, while the minor disordered component is shown in the dashed wireframe representation. DFT-optimized geometries done in vacuo at B3LYP level of theory with 6-311G** basis set with LANL2DZ ECP approximations for Ni and Br atoms. 123

Figure 3.7 ORTEP diagrams of complexes 3.34-3.35 with the thermal ellipsoids set at 50% probability level. Hydrogen atoms except for those on the heterocycle are not shown. Complex 3.34 has two complexes in the asymmetric unit, only the first component is shown. Only the main component of the disorder is shown for complex 3.35. 125

Figure 3.8 (top) Description of equatorial and axial description of methyl groups compared to the P-N-P-Me plane. (bottom) ORTEP diagram of complex **3.37** in two different orientations. The major isomer has the dearomatized pyridine ring shown in hard black lines, while the minor isomer has the dearomatized pyridine ring shown in dashed bonds. Ellipsoids are drawn at 50% probability. Hydrogens, except those on the dearomatized pyridine rings were omitted. 127

Figure 3.9 Cyclic voltammograms of Ni methyl and hydride complexes in the cathodic region: a) complexes 3.7 (1 mM; red line) and 3.33 (0.5 mM, dashed black line); b) complexes 3.26 (1 mM; red line) and 3.29 (1 mM; dashed black line). Experimental conditions: 0.1 M $n\text{Bu}_4\text{NPF}_6/\text{MeCN}$ solution at 23 °C, scan rate 0.1 V s⁻¹, 1.0 mm GC disk working electrode; the arrow indicates initial scan direction. 129

Figure 3.10 ORTEP diagram of complex 3.38 with the thermal ellipsoids set at 50% probability level. Hydrogen atoms except for those on the heterocycle are not shown. Selected interatomic distances (Å) and angles (deg.): Ni1–N1 1.9028(17), Ni1–C24 1.954(2), Ni1–P1 2.1510(6), Ni1–P2 2.1585(6), N1–C1 1.405(3), N1–C5 1.408(3), C1–C2 1.343(3), C2–C3 1.509(3), C3–C4 1.505(3), C4–C5 1.341(3), C3–C3ⁱ 1.570(4), ∠P1–Ni1–P2 171.19(2), ∠N1–Ni1–C24 177.29(9). Equivalent atoms are labeled with the superscript *i* (–*x*, 1–*y*, 1–*z*). 131

Figure 3.11 Experimental (black line) and simulated (red line) EPR spectra after UV irradiation of a) 3.30 after UV irradiation for 1 h at 298 K in the presence of excess DMPO in acetone-*d*₆, b) 3.30 in the presence 1 equivalent of $n\text{Bu}_4\text{NBr}$ after UV irradiation for 1 h at 95 K in frozen acetone-*d*₆. Parameters for simulation: a) $g = 2.007$, $A_N = 14.25$ G, $A_H = 21.10$ G. b) $g_x = 2.328$, $g_y = 2.307$, $g_z = 1.998$ ($g_{\text{iso}} = 2.211$). 133

Figure 3.12 EPR spectra obtained at 93K in frozen acetone-*d*₆ from UV irradiation of a solution of 3.30 for 3.5 hours at rt. Possible metalloradical and ligand-based radical species are shown above. 134

Figure 3.13 EPR spectra obtained at 298K in acetone-*d*₆ from UV irradiation of a solution of 3.30 for 1 hour with an excess of DMPO. 136

Figure 3.14 Stacked ¹H NMR spectra of the reaction of 3.27 with CO up to 3 hours at 60 °C (500 MHz, acetone-*d*₆). 137

Figure 3.15 Stacked ³¹P{¹H} NMR spectra of the reaction of 3.27 with CO up to 3 hours at 60 °C (202 MHz, acetone-*d*₆). 137

Figure 3.16 Stacked ¹H NMR spectra of the reaction of 3.27 with O₂ up to 24 hours (400 MHz, CD₃CN). 138

Figure 3.17 Stacked ³¹P{¹H} NMR spectra of the reaction of 3.27 with O₂ up to 24 hours (162 MHz, CD₃CN). 139

Figure 3.18 Experimental (black line) and simulated (red line) EPR spectra of the complex formed from the reaction of 3.26 with O₂ in frozen acetone at 84K. Parameters for simulation: $g_{\text{perp}} = 2.003$, $g_{\text{para}} = 2.088$ 140

Figure 3.19 Stacked ¹H NMR spectra of the reaction of 3.29 with O₂ up to 24 hours (400 MHz, CD₃CN). 141

Figure 3.20 Stacked ³¹P{¹H} NMR spectra of the reaction of 3.29 with O₂ up to 24 hours (162 MHz, CD₃CN). 141

Figure 3.21 Stacked ¹H NMR spectra of the reaction of 3.32 with O₂ up to 22 hours at rt (400 MHz, acetone-*d*₆). 142

Table of Figures

Figure 3.22 Stacked $^{31}\text{P}\{^1\text{H}\}$ NMR spectra of the reaction of 3.32 with O_2 up to 22 hours at rt (162 MHz, acetone- d_6).....	142
Figure 3.23 DFT-optimized structures of cationic $\text{Ni}^{\text{II}}\text{-Me}$ $[\text{iPrNiMe}]^+$ and $[\text{tBuNiMe}]^+$; of cationic $\text{Ni}^{\text{II}}\text{-Br}$ $[\text{iPrNiBr}]^+$ and $[\text{tBuNiBr}]^+$, and their one-electron-reduced products, the neutral species $[\text{iPrNiMe}]^\bullet$ and $[\text{tBuNiMe}]^\bullet$. DFT optimized geometry. B3LYP, 6-311++G**/lanl2dz(Ni, Br).....	143
Figure 3.24 Spin density plots for complexes $[\text{iPrNiMe}]^\bullet$ and $[\text{tBuNiMe}]^\bullet$. DFT optimized geometry, B3LYP, 6-311++G**/lanl2dz(Ni), isovalue = 0.0007. See Figures 3.20 and 3.21 for the atomic contribution to the spin densities.	145
Figure 3.25 (left) Charge density (Truhlar's CM5 model) and (right) spin density (Mulliken) with the hydrogen summed for $[\text{iPrNiMe}]^+$ and $[\text{iPrNiMe}]^\bullet$	145
Figure 3.26 (left) Charge density (Truhlar's CM5 model) and (right) spin density (Mulliken) with the hydrogen summed for $[\text{tBuNiMe}]^+$ and $[\text{tBuNiMe}]^\bullet$	145
Figure 3.27 Molecular orbital diagram and HOMO-1, HOMO, SOMO, and LUMO representation of $[\text{iPrNiMe}]^+$ and $[\text{iPrNiMe}]^\bullet$. DFT optimized geometries, B3LYP, 6-311++G**/lanl2dz(Ni), alpha orbital representations, isovalue = 0.04.	146
Figure 3.28 Molecular orbital diagram and HOMO, SOMO and LUMO representation of $[\text{tBuNiMe}]^+$ and $[\text{tBuNiMe}]^\bullet$. DFT optimized geometries, B3LYP, 6-311++G**/lanl2dz(Ni), alpha orbital representations, isovalue = 0.04.	146
Figure 3.29 Molecular orbital diagram and of $[\text{iPrNiBr}]^+$ and iPrNiBrdearo . DFT optimized geometries, B3LYP, 6-311++G**/lanl2dz(Ni), alpha orbital representations, isovalue = 0.04.	148
Figure 3.30 Molecular orbital diagram of $[\text{tBuNiBr}]^+$ and tBuNiBrdearo . DFT optimized geometries, B3LYP, 6-311++G**/lanl2dz(Ni), alpha orbital representations, isovalue = 0.04.	148
Figure 3.31 Geometries before and after optimization for $[\text{iPrNiMe}]\text{CO-up}$, $[\text{iPrNiMe}]\text{CO-down}$, and $[\text{iPrNiMe}]\text{CO-bipy}$. DFT optimized geometry. B3LYP, 6-311G**/lanl2dz(Ni), THF solvent continuum.....	150
Figure 3.32 Geometries before and after optimization for $[\text{tBuNiMe}]\text{CO-up}$, $[\text{tBuNiMe}]\text{CO-down}$, and $[\text{tBuNiMe}]\text{CO-bipy}$. DFT optimized geometry. B3LYP, 6-311G**/lanl2dz(Ni), THF solvent continuum	150
Figure 3.33 Energy diagram for the optimized structures $[\text{iPrNiMe}]\text{CO-up}$, $[\text{iPrNiMe}]\text{CO-down}$, $[\text{iPrNiMe}]\text{CO-bipy}$. DFT optimized geometry. B3LYP, 6-311G**/lanl2dz(Ni), THF solvent continuum.....	151
Figure 3.34 Energy diagram for the optimized structures $[\text{tBuNiMe}]\text{CO-up}$, $[\text{tBuNiMe}]\text{CO-down}$, $[\text{NiMe}]\text{CO-bipy}$. DFT optimized geometry. B3LYP, 6-311G**/lanl2dz(Ni), THF solvent continuum.....	152

List of Tables

Table 1.1 CO stretching frequencies (ν_{CO}) values for $[\text{Ni}(\text{CO})_3\text{L}]$. ^a	14
Table 1.2. Hydrogen transfer reaction of cyclohexanone catalyzed by different Ru^{II} PCP pincer complexes 1.24-1.28 with varying degree of electronic properties on the phosphine moieties. ^{89 a}	20
Table 1.3 Selected examples of ketones, aldehydes, and imine hydrogenations using catalyst 1.69. ¹³⁴	35
Table 1.4 Hydroboration of sterically hindered alkenes catalyzed by 1.70. ¹³⁵	36
Table 1.5. Selected examples of dehydrogenative coupling of diols and amines catalyzed by 1.71. ¹³⁶	37
Table 2.1 Bond distances [\AA] and angles [deg] for complexes 2.32–2.39. The atom numbering corresponds to that of Figures 2.7-2.8.	71
Table 2.2 Redox potentials for L2.3 and L2.4.	72
Table 2.3 Electrochemical properties of complexes 2.36–2.39 (V vs. Fc)	73
Table 2.4 Selected EPR parameters ^a and effective magnetic moment μ_{eff} in solution for Ni^{I} complexes 2.40-2.43.	76
Table 2.5 Comparison between rhombic and axial signal simulation and RMSD values compared to the experimental spectrum for complex 2.40.	78
Table 2.6 ORCA-calculated EPR parameters for complexes 2.40-2.43.	79
Table 2.7 Selected bond distances [\AA] and angles [deg] for complexes 2.40-2.43.	80
Table 2.8 LCAO-MO analysis of the SOMO using Chemissian (highest contributions are shown). ²⁰⁰	83
Table 2.9 Natural population analysis for Ni center for complexes 2.40-2.41	83
Table 2.10 Natural population analysis for Ni center for complexes 2.42-2.43	84
Table 2.11 Exact ligand solid angle parameters from the DFT-optimized geometry Ni^{I} complexes with and without the halogen ^a	86
Table 2.12 Exact ligand solid angle parameters from the X-ray coordinates for Ni^{I} complexes with and without the halogen ^a	88
Table 3.1 Bond distances [\AA] and angles [deg] for complexes 2.36, 2.38, and 3.1–3.10 according to XRD data. ^a	121
Table 3.2 Bond distances [\AA] and angles [deg] for complexes 3.34–3.37 according to XRD data. ^a	125
Table 3.3 Electrochemical properties of complexes 3.26, 3.29, 3.30 and 3.33. ^a	129
Table 3.4 Selected partial atomic charges with summed hydrogens (Truhlar's Charge model 5) ^a for optimized complexes	149

Table of Schemes

Scheme 1.1 First PCP and NCN pincer complexes by Shaw and van Koten.....	5
Scheme 1.2 General types of pincer ligands	6
Scheme 1.3 Examples of pincer complexes in the literature ⁶⁰⁻⁶⁴	6
Scheme 1.4 Example of a synthesis of a POCOP ligand. ⁶⁵	7
Scheme 1.5 Example of the synthesis of an aromatic PNP ligand. ⁶⁶	7
Scheme 1.6 Example of the synthesis of an NCN ligand. ⁶⁷	8
Scheme 1.7 Example of the synthesis of an aliphatic PNP ligand. ⁶⁸	8
Scheme 1.8 Examples of synthesis of an unsymmetrical SCN pincer ligand. ⁶⁹	9
Scheme 1.9 Preparation of a cationic PONOP nickel chloride complex without bond activation on the ligand. ⁵³	9
Scheme 1.10 General scheme of C-Z bond activation with NCN pincer ligands. ⁷⁰	10
Scheme 1.11 Synthesis of substituted POCOP Nickel(II) bromide complexes via C-H activation. ⁶⁵	10
Scheme 1.12 Examples of one-pot synthetic procedures for the preparation of PCP, PNP and POCOP Nickel complexes. ^{22,72}	11
Scheme 1.13 Relative metalation rates for a wide range of aliphatic and aromatic POCOP and PNP pincer ligands. ⁸⁸	19
Scheme 1.14 Proposed mechanism for the direct amination of alcohols with ammonia catalyzed by 1.34. ⁹³	23
Scheme 1.15 Effect of the size of phosphine substituents on the oxidation state of the iridium center. ⁹⁴	24
Scheme 1.16 Electronic and steric effects of substituents on the pincer arms of 1.43 on the polymerization of ethylene. ⁹⁵	25
Scheme 1.17 Activation of small molecules at the nickel center of 1.46 after chloride atom abstraction. ¹¹³	28
Scheme 1.18 Reactions of 1.52, 1.53 and 1.56 towards CO ₂ , CO and O ₂ and their decomposition products. ^{31, 32}	29
Scheme 1.19 Normal and abnormal insertion of CO ₂ into Ni-H bond of 1.60. ¹¹⁴	30
Scheme 1.20 Examples of manganese pincer catalyzed reactions involving an alcohol. ¹²⁴⁻¹²⁷	31
Scheme 1.21 Selected example of the hydrogenation of ketones with KO ^t Bu catalyzed by 1.66 ^{98, 129}	32
Scheme 1.22 Selected examples of <i>E</i> -selective semihydrogenation of Alkynes catalyzed by 1.67. ^{98, 128}	32
Scheme 1.23 Examples of the dehydrogenation of formic acid to CO ₂ and H ₂ catalyzed by 1.67. ¹³⁰	33
Scheme 1.24 Iron pincer-like complex 1.75 for C-H azidation ¹³¹	33
Scheme 1.25 General scheme for the formation of a dearomatized lutidine-based PNP pincer ligand.	38

Table of Figures

Scheme 1.26 Reaction of 1.73 with a strong electrophile, MeOTf, to form 1.74. ¹³⁷	39
Scheme 1.27 General scheme of MLC through the aromatization-dearomatization mechanism.	39
Scheme 1.28 Possible catalytic cycle for the Michael addition of benzyl cyanide with methyl acrylate catalyzed by 1.76. ¹³⁸	41
Scheme 1.29 Undesirable reaction of the doubly deprotonated 1.82 with CO ₂ to form CO ₂ adduct 1.83. ¹³⁹	42
Scheme 1.30 Selective semi-hydrogenation of diphenylacetylene catalyzed by 1.84. ¹²⁶	43
Scheme 1.31 Acceptorless dehydrogenative coupling of ammonia and benzyl alcohol catalyzed by 1.85-1.86. ¹³⁶	43
Scheme 1.32 Formation of lactams from water and amines, and formation of biofuels from ethanol catalyzed by 1.87. ^{139, 140}	43
Scheme 1.33 Dearomatization at the <i>para</i> position of Ni, Pd, and Pt complexes 1.88, 1.92, and 1.95 as well as further reactivities. ⁵³	44
Scheme 1.34 Formation of the cobalt and nickel dimers of acridine-based PNP complexes 1.97 and 1.99. ¹⁴²	45
Scheme 1.35 Formation of the iron and manganese dimers of acridine-based PNP complexes 1.103 and 1.106. ¹⁴²	46
Scheme 1.36 Formation of the dinitrogen diamagnetic complex 1.112 through consecutive 1-electron reductions of 1.110 and 1.111. ¹⁵¹	48
Scheme 1.37 Electrochemical transformation of CO ₂ to CO and H ₂ catalyzed by NNP pincer complexes 1.108-1.111. ¹⁵⁴	48
Scheme 2.1 Ligand-based reduction of the tetramethylated complex 2.1 under electrochemical conditions. ¹⁵⁷	54
Scheme 2.2 Preparation of a new family of bulky, tetramethylated PNP ligand (L2.3-L2.4).	55
Scheme 2.3 Proposed catalytic cycle for C-C and C-B coupling involving a Ni ^I pincer intermediate 2.12. ¹⁸²	57
Scheme 2.4 Proposed catalytic cycle of the alkyl-alkyl Kumada coupling catalyzed by either 1.44 or 2.10. ¹⁶²	58
Scheme 2.5 Homolytic cleavage of H ₂ by a Ni ^I dimer complex 2.5 to form the Ni ^{II} hydride complex 2.13. ¹⁷⁹	59
Scheme 2.6 C-C coupling between a Ni ^I CO adduct 1.67 and MeI to form 1.77-1.79. ¹⁸⁴	60
Scheme 2.7 Reactivity of a Ni ^I NNN pincer complex with O ₂ and further reactivity of the dimeric species 1.80. ¹⁷²	60
Scheme 2.8 Proposed mechanism of methyl-coenzyme M reductase involving Ni ^I and Ni ^{III} centers. ¹⁸⁵	61
Scheme 2.9 Proposed paramagnetic mechanisms for acetyl-Coenzyme A Synthase (ACS) catalyzed acetyl-CoA formation with either initial binding of CO (Path A) or initial binding of Me ⁺ (Path B). ¹⁶⁹	62
Scheme 2.10 Formation of Ni ^{III} species via oxidation of Ni ^{II} halide NCN pincer complexes. ¹⁸⁹	64
Scheme 2.11 2-electrons oxidation of Ni ^{II} bis-carbene pincer complex to Ni ^{IV} . ¹⁹⁰	64
Scheme 2.12 Catalytic cycle for the Kharasch addition of CCl ₄ to alkenes catalyzed by 2.27. ¹⁹¹ Note: Ligand X is Br during first catalytic cycle, however, it is likely to exchange with Cl during subsequent cycles.	65

Scheme 2.13 (top) Preparation of $\text{Me}_4\text{PNP}^{\text{R}}\text{BH}_3$ (L2.3–L2.4) and $\text{Me}_4\text{PNP}^{\text{R}}$ (L2.5–L2.6) ligands. (bottom). ORTEP diagram showing 50% probability anisotropic displacement ellipsoids of non-hydrogen atoms for L2.3, L2.4, and L2.6.	66
Scheme 2.14 Preparation of Ni^{II} cationic PNP complexes 2.32–2.39.	66
Scheme 2.15 Preparation of neutral Ni^{I} complexes 2.40–2.44 via electrochemical or chemical reduction with cobaltocene.	75
Scheme 3.1. Reduction of CO_2 with catecholborane catalyzed by nickel pincer hydride complexes. ²²⁰	113
Scheme 3.2 Selected examples of formylation of amines using CO_2 and Ph_2SiH_2 catalyzed by 3.4. ²¹⁹	114
Scheme 3.3 Selected examples of the hydrogenation of alkenes catalyzed by 3.9. ²²¹	114
Scheme 3.4 Hydrosilylation of benzaldehyde catalyzed by 3.2. ²⁷	114
Scheme 3.5 Reaction of the nickel pincer hydride complex 3.5 with ethylene to form 3.10. ⁵⁹	115
Scheme 3.6 Difference of reactivity between phenylacetylene and palladium or nickel PCOP hydride complexes. ²²²	115
Scheme 3.7 Reactivity of 3.17 towards phenylacetylene to form the phenylacetylene-bound complex 3.18 with elimination of methane. ²²⁷	116
Scheme 3.8 Reactivity of 3.16 towards H_2 to form the hydride 3.20 with elimination of methane. ²²⁶	117
Scheme 3.9 Insertion of CO_2 into the nickel methyl bond of 3.18 to form 3.21. ²²⁷	117
Scheme 3.10 Insertion of CO_2 into the nickel methyl bond of 3.13 to form 3.21. ²²³	117
Scheme 3.11 Reaction of the nickel methyl PCP pincer complex 3.23 with O_2 from air to form a decomposition product. ²²⁸	118
Scheme 3.12 Preparation of Ni^{II} cationic complexes 2.36, 2.38, and 3.24–3.33. ^a Complexes were previously reported. ²²⁹	119
Scheme 3.13 Synthesis of complexes 3.34–3.36.....	123
Scheme 3.14 Reaction of 3.33 with MeLi leading to dearomatization and methylation of the pyridine ring to form 3.37 as a mixture of two isomers.....	126
Scheme 3.15 Reduction of Ni^{II} -Me complex 3.30 to form 3.38.	130
Scheme 3.16 UV-induced reactivity of 3.30.	133

Abbreviations

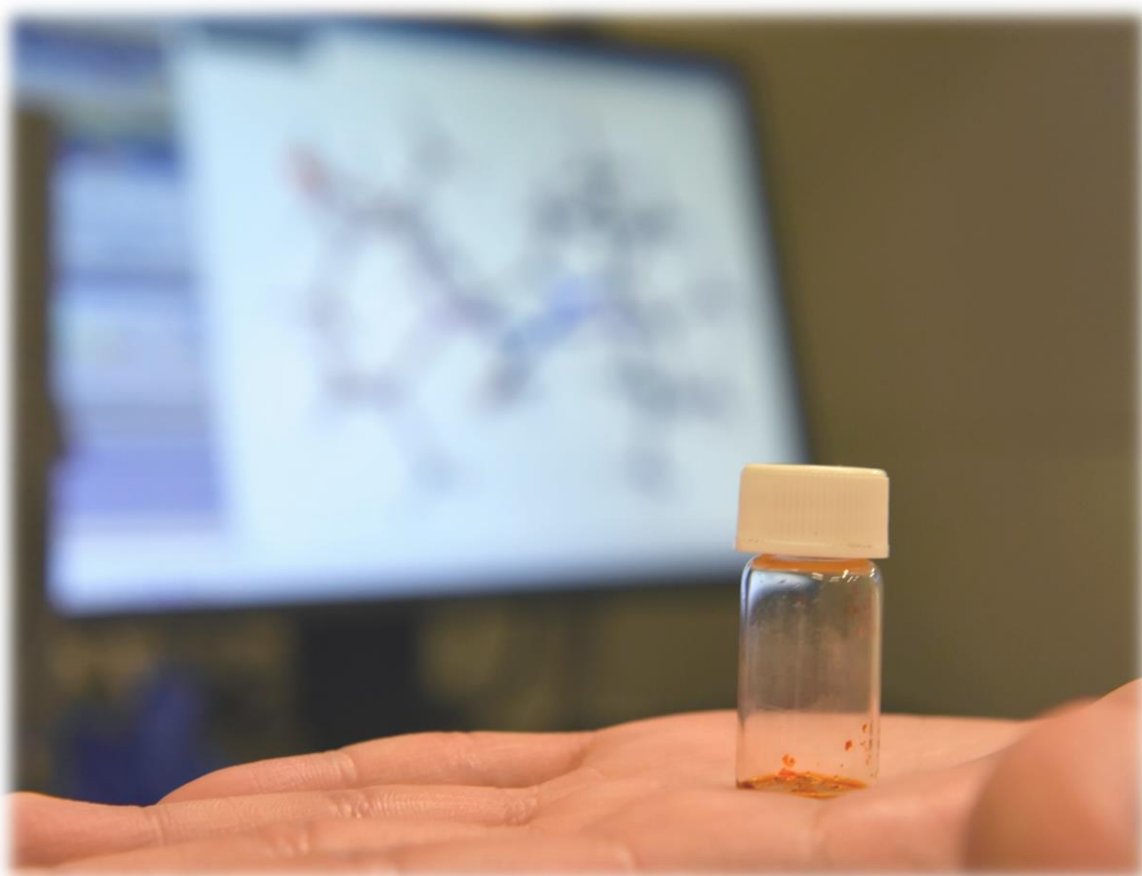
°	Degrees
°C	Degrees Celsius
$^{13}\text{C}\{^1\text{H}\}$ NMR	Carbon nuclei NMR with proton decoupling (spectroscopy)
$^{19}\text{F}\{^1\text{H}\}$ NMR	Fluorine nuclei NMR with proton decoupling (spectroscopy)
^1H NMR	Proton nuclei NMR (spectroscopy)
$^{31}\text{P}\{^1\text{H}\}$ NMR	Phosphorous nuclei NMR with proton decoupling (spectroscopy)
Å	Ångström
ATR	Attenuated-total-reflectance (spectroscopy)
C	Coulombs
CV	Cyclic voltammetry (electrochemistry)
Cy	Cyclohexyl group
d	Doublet (Spectroscopy)
DCM	Dichloromethane
dd	doublet of doublets (spectroscopy)
DEPT-135 NMR	Distortionless Enhancement by Polarization Transfer (Spectroscopy)
DFT	Density functional theory
$E_{1/2}$	Half-wave potential
EDG	Electron-donating group
EPR or ESR	Electron paramagnetic resonance (spectroscopy)
eq.	Equivalent or equivalents
ESI-HRMS	Electron-spray ionization high resolution mass spectrometry
Et	Ethyl group
EWG	Electron-withdrawing group
Fc	Ferrocene
Fc^+	Ferrocenium ion
FT-IR	Fourier-transformed Infrared (spectroscopy)
G	Gauss
G	Ligand Shielding parameter
GC	Glassy carbon disk electrode (electrochemistry)
GC-MS	Gas-chromatography coupled with mass-spectrometry (spectrometry)
Hal	Halogen
hept	heptuplet (spectroscopy)
HOMO	Highest Occupied Molecular Orbital
Hz	Hertz
$i\text{Pr}$	isopropyl group

J_{XY}	Coupling constant between X and Y nuclei (spectroscopy)
K	Kelvins
LCAO	Linear Combination of Atomic Orbital
LUMO	Lowest Unoccupied Molecular Orbital
m	Multiplet (Spectroscopy)
M	Molar concentration or molarity
Me	Methyl group
MLC	Metal-ligand cooperation
MO	Molecular Orbital
mT	Milli-Tesla
NMR	Nuclear Magnetic Resonance (spectroscopy)
OMe	Methoxy group
PC _{sp2} P or PCP	1,3-bis(phosphinobenzene)
PC _{sp3} P	1,5-bis(phosphinopentane)
Ph	Phenyl group
PIMCOP	3-[2-(phosphanyl)-1H-imidazol-1-yl]phenyl phosphinite
POC _{sp2} OP or POCOP	1,3-bis(phosphonitobenzene)
POC _{sp3} OP	1,3-bis(phosphinitopropane)
PONOP	1,3-bis(phosphinitopyridine)
q	Quadruplet (Spectroscopy)
R	Generic group
rt	Room temperature
s	Singlet (Spectroscopy)
S	Spin
SOMO	Singly Occupied Molecular Orbital
str	steradians (unit of the surface of a sphere)
t	Triplet (Spectroscopy)
^t Bu	tert-butyl group
THF	Tetrahydrofuran
tt	triplet of triplets (spectroscopy)
UV-vis	Ultraviolet-visible (Spectroscopy)
v	virtual (spectroscopy)
V or mV	Volts or millivolts (electrochemistry)
δ	Chemical shift (spectroscopy)
τ_4 or τ_4'	Geometrical index for 4-coordinate compounds
τ_5 or τ_5'	Geometrical index for 5-coordinate compounds
Ω°	Exact Ligand Solid Angle
ΔE_p	Peak potential separation (electrochemistry)
ε	molar absorptivity (spectroscopy)
λ_{\max}	Wavelength at maximum absorption (spectroscopy)
μ_{eff}	effective moment (spectroscopy)
μ_B	Bohr's magneton (spectroscopy)

1

Chapter 1

Introduction to Pincer Chemistry



1.1 General introduction and challenges in organometallic chemistry and catalysis

With an increasing world population and demand for energy comes the necessity to invest in and to improve sustainable technologies. As the chemical industry is responsible for many daily necessities such as plastic, drugs, and fuel, it is very important that it moves to utilize cleaner and less wasteful methods and technologies and focuses on the transformation of wastes and use of renewable resources. Catalysis plays a major role in the quest for greater sustainability in the chemical industry, where the catalyst is the main actor. A catalyst is a substance that accelerates the rate of a reaction, while not being consumed throughout the reaction. This makes it possible to recover the intact catalyst at the end of the reaction. By definition, the amount of catalyst is less than that of the substrate and product obtained. Ideally, however, the catalyst is only used in extremely small quantities to produce a high quantity of the desired chemical. Catalyst research is a major and by now well-developed field, where increasingly active and efficient catalysts that are highly stable are often adopted by use in the industry to minimize costs and improve the environmental profile of many bulk scale reactions. Catalysis is divided into two major areas of research depending on whether the reactants and the catalyst are in the same phase (homogeneous catalysis) or in separate phases (heterogeneous catalysis). Homogeneous catalysts are usually well-defined species in the same solution as the reactants, where heterogeneous catalysts can be supported on solid support or deposited onto surfaces.. Heterogeneous catalysts are often cheaper than homogeneous catalysts and are more resistant to degradation at high temperatures (Ex: car mufflers that transform carbon monoxide exhaust to carbon dioxide). In contrast, homogeneous catalysts are preferred for their selectivity and ability to operate under less harsh conditions than heterogeneous catalysts (ex. plastics are

made mostly by homogeneous organometallic catalysts: early transition metal Hf and Zr catalysts are used on multi-ton scale in reactions for which K. Ziegler and G. Natta were awarded the Nobel Prize in chemistry in 1963).^{1, 2}

Most homogeneous and heterogeneous catalysis is metal based, and often involves a transition metal center as the main active site. The popularity of transition metals in catalysis is due to their accessible *d*-orbitals which allow for substrates to effectively coordinate to the metal center and be in closer proximity, or for a free orbital to activate bonds in the substrate. Transition metals can also accommodate a range of metal-based oxidation states, which allows for electron cycling in chemical transformation. For example, the ability of palladium to undergo two-electron oxidations (from Pd⁰ to Pd^{II}, or Pd^{II} to Pd^{IV}) has resulted in an exponential rise of Pd-based catalysts for C-C coupling reactions in organic chemistry,³ for which a Nobel Prize was recently awarded (2010) to R. F. Heck, E.-I. Negishi, and A. Suzuki for their pioneering work in this field. Other notable organometallic Nobel prizes include catalytic asymmetric hydrogenation reactions: in 2001 to W. Knowles, R. Noyori, and B. Sharpless, and for olefin metathesis in 2005 to Y. Chauvin, R. H. Grubbs, and R. F. Schrock.

In transition metal catalysts, design of the ligand framework surrounding the metal plays a crucial role. Homogeneous catalysis typically requires milder conditions compared to many heterogeneous catalytic processes (i.e. lower temperature and pressure), and well-defined nature of many organometallic homogeneous catalysts typically imply that steric and electronic factors can be used to finely tune the reactivity of the catalyst, sometimes leading to the discovery of new selective chemical transformations. This is similar to the chemistry found in metalloenzymes (organometallic proteins evolved by Nature for catalysis), where a change in the coordinating environment of one amino acid can mean the difference between an active catalyst or an inactive one in a mutant. Many metalloenzymes are also capable of transformations, such as methane conversion to methanol or nitrogen to ammonia, that chemists cannot

yet efficiently replicate in the lab. In contrast to natural metalloenzymes, chemists have access to a greater variety of organic scaffolds (ligands) for the metal, or to metals that are rare in the Earth's crust and that were not selected for by evolution, which means that we can often create catalysts that can be more robust under harsher conditions, and discover reactions that are not found in Nature.

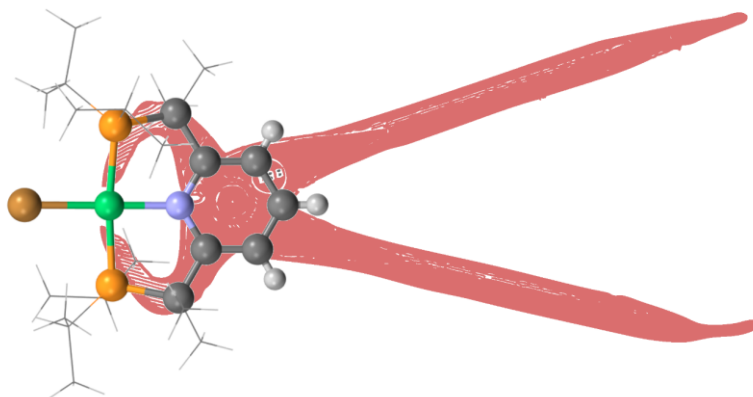


Figure 1.1 Artistic representation of how the term “pincer” was used to represent a tridentate class of ligands based on its usefulness and its ability to bind a metal center similar to how a pincer pinches an object

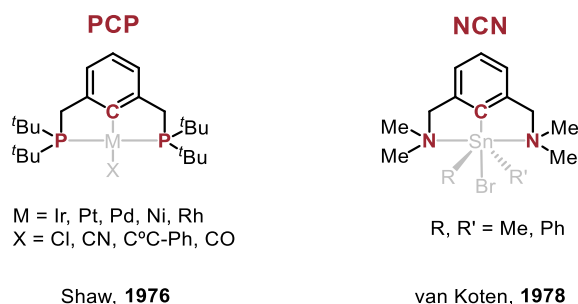
Amongst the class of ligands that are widely used in homogeneous catalysis research is the pincer ligand, a class of ligands that are widely tunable to help stabilize a variety of oxidation states on the metal center. The pincer ligand owes its name to its ability to bind a metal center by three donor atoms in a plane, and its resemblance to the pincer tool (See Figure 1.1). With the ever-increasing price of 2nd and 3rd row transition metals, there is today a greater need to employ cheap 1st-row transition metals instead. These metals were previously not as popular in catalysis since they tended to undergo one-electron oxidation or reduction to form radical species leading to often unselective reactions or paramagnetic intermediates that are difficult to characterize by Nuclear Magnetic Resonance spectroscopy, one of the most widely used tools in organometallic chemistry. The need to develop ligands that can stabilize those earth-abundant metal centers, their promise in catalysis and the resulting advantages in cost, and the

high tunability of pincer ligands is why I have decided to explore the chemistry of nickel pincer complexes in this thesis.

1.2 Pincer Complexes of Late-Transition Metals: Synthesis and Applications

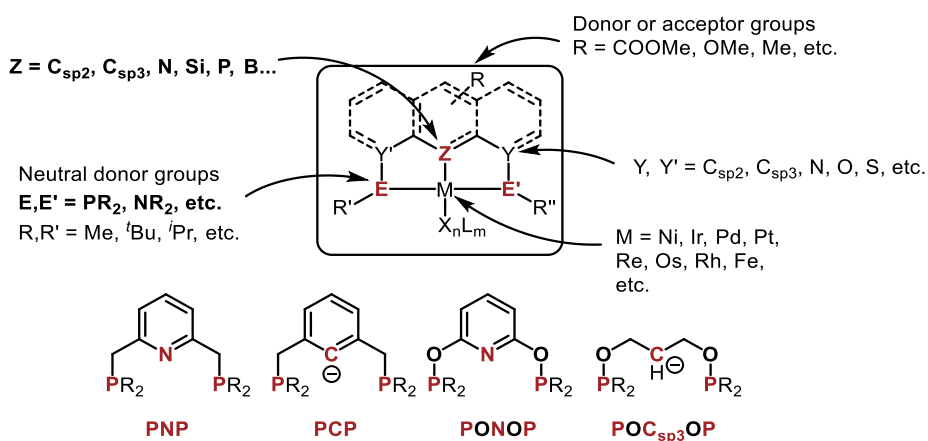
1.1.1 What are Pincer Ligands and Complexes?

Pincer ligands are a class of tridentate ligands that were introduced in the 1970s by the pioneering works of Shaw⁴ and van Koten,^{5, 6} (See Scheme 1.1 for the first examples of pincer complexes). A pincer ligand is usually a tridentate chelating ligand that binds to three adjacent atoms, typically in a meridional (coplanar) fashion, where all three binding atoms and the metal lie in the same plane. This meridional binding fashion brings a lot of stability to the metal complex formed, and the nature of each atom and group binding to the metal center bring a lot of variation in the fine tuning of different properties, either electronic or steric.

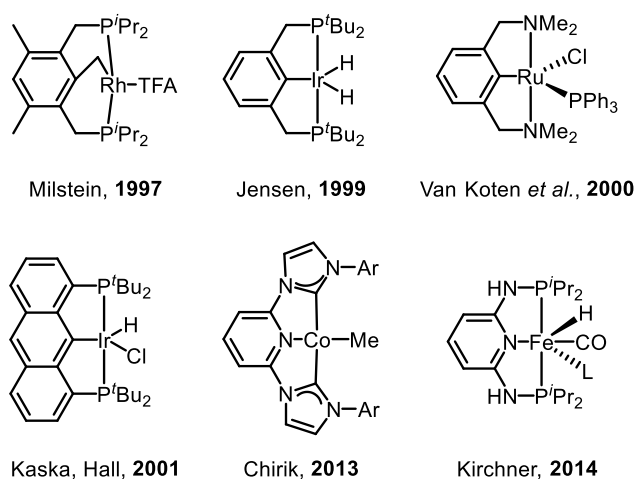


Scheme 1.1 First PCP and NCN pincer complexes by Shaw and van Koten.

Many different types of pincer ligands have been designed ever since based on various types of donor atoms (PCP,⁷⁻²⁰ POCOP,²¹⁻²⁹ POC_{sp3}OP,³⁰⁻³³ POCN,³⁴⁻³⁹ PNP,⁴⁰⁻⁴⁸ PONOP,⁴⁹⁻⁵⁶ NNN,⁵⁷⁻⁵⁹ etc., see Scheme 1.2 for the general framework of pincer ligands and their common designations) and many of them have been able to support transition-metal complexes that features accessible reactive sites (See Scheme 1.3 for typical examples of pincer complexes).



Scheme 1.2 General types of pincer ligands

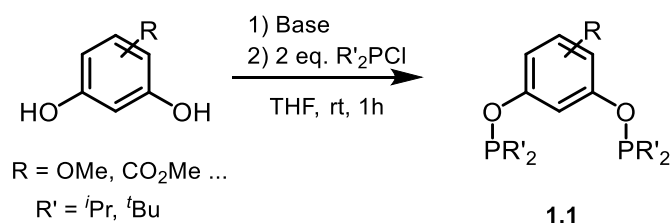
Scheme 1.3 Examples of pincer complexes in the literature⁶⁰⁻⁶⁴

The stability of the pincer ligand depends on the nature of the groups binding to the metal center as well as their steric properties. For example, aromatic PCP or POCOP ligands can form strong metal-carbon σ -bond, which provides enough thermal stability to complexes so that they can survive much higher reaction temperatures than most other pincer ligand frameworks. On the other hand, pincer ligands that contain oxygen or nitrogen atoms are sometimes less stable and more prone to react under aerobic conditions and decompose at higher temperatures. Finally, the often structurally rigid and well-defined nature of the pincer ligands allows for a well-defined coordination environment around the metal center, enabling direct tuning of catalytic properties, and facilitating the rational design of catalytic transformations. Moreover,

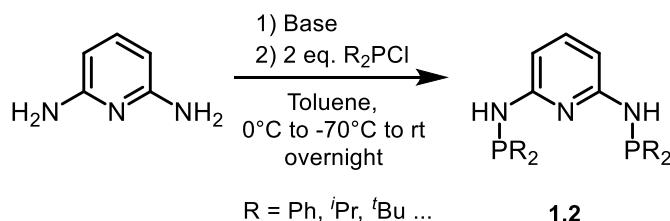
the well-defined coordination properties and good chelating ability of pincer ligands facilitate the study of reaction mechanisms and can allow the isolation of reactive intermediates species.

1.1.2 General Procedures for the Synthesis of Pincer Ligands and Complexes

The syntheses of many symmetrical pincer ligands and complexes are often straightforward and utilize easily available starting materials, starting from accessible organic ligands and cheap metal precursors, while preparation of more complex heterocyclic frameworks or unsymmetrical ligands may require more elaborate multistep procedures. For example, a family of POCOP ligands⁶⁵ (**1.1**, Scheme 1.4) are prepared by a simple deprotonation of commercially available resorcinol (multiple variations are available with electron-withdrawing or electron-donating groups, as well as halides) using a base such as triethylamine. Then, 2 equivalents of dialkylchlorophosphine are added and the reaction is stirred and complete in 1 hour at rt (room temperature). The synthesis of a family of aromatic PN₃P ligands containing NH-arms⁶⁶ (**1.2**, Scheme 1.5) is done in a very similar fashion, but requires a more delicate temperature control.

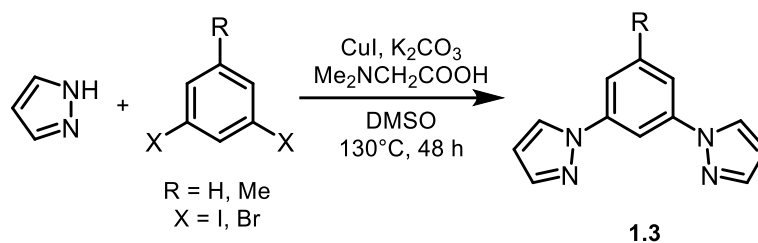


Scheme 1.4 Example of a synthesis of a POCOP ligand.⁶⁵



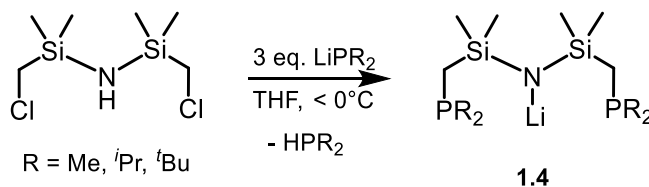
Scheme 1.5 Example of the synthesis of an aromatic PNP ligand.⁶⁶

Some other types of pincer ligands, such as this family of pyrazole-containing NCN ligands⁶⁷ (**1.3**, Scheme 1.6) requires more harsh conditions, but can still be prepared with cheap and commercially-available reagents.



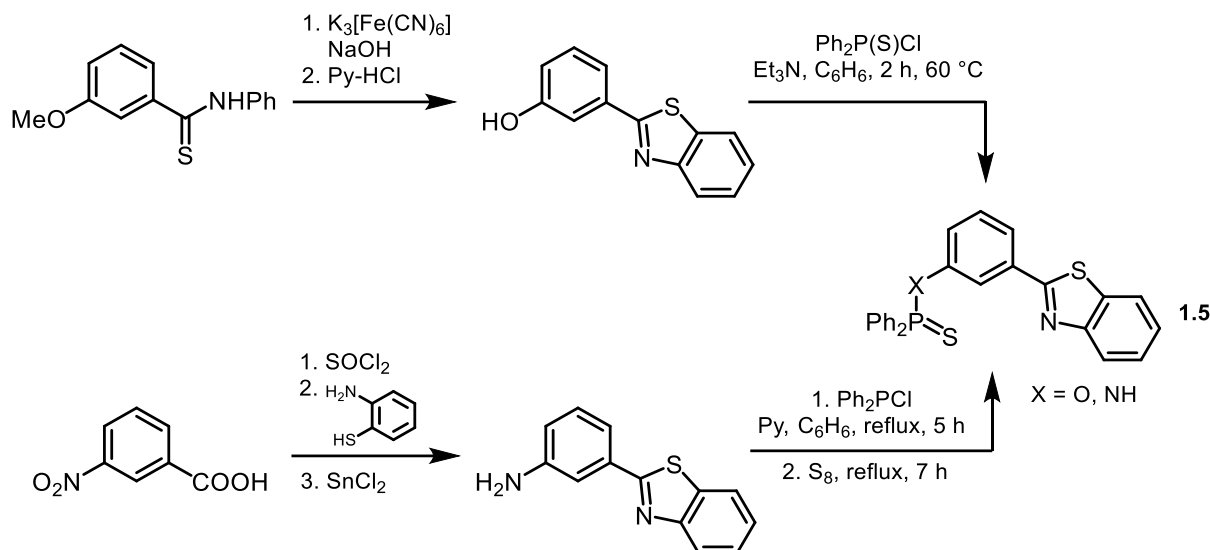
Scheme 1.6 Example of the synthesis of an NCN ligand.⁶⁷

Finally, lithiation may be required for preparation of the anionic form of the pincer ligand to use in the following steps of metalation. One example of such ligand is Fryzuk's aliphatic PNP ligand⁶⁸ (**1.4**, Scheme 1.7) containing disilazane moieties, which requires the use of lithium dialkylphosphanide (R_2PLi) at low temperatures.



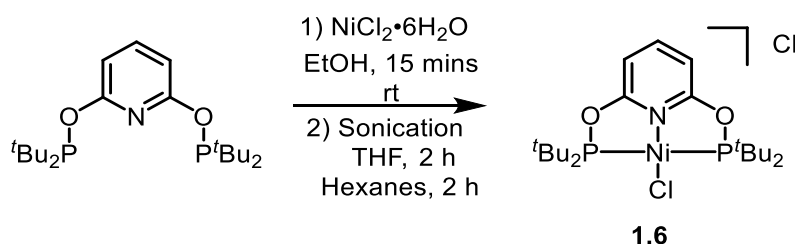
Scheme 1.7 Example of the synthesis of an aliphatic PNP ligand.⁶⁸

Some sulfur- and nitrogen- containing pincer ligands require several steps for their synthesis, especially for unsymmetrical ligands. For example, this SCN ligand⁶⁹ (**1.5**, Scheme 1.8) requires two steps from a commercially available reagent.



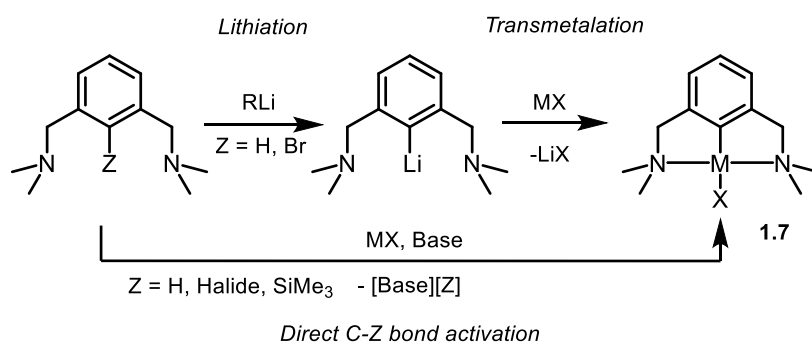
Scheme 1.8 Examples of synthesis of an unsymmetrical SCN pincer ligand.⁶⁹

The procedures for metalation of pincer ligands are usually quite straightforward and involve either the direct addition of a transition metal halide precursor to the pincer ligand under mild conditions when no bond activation is necessary. For example, a PONOP ligand will react at room temperature within 15 minutes with $\text{NiCl}_2 \cdot 6\text{H}_2\text{O}$ in ethanol, followed by sonication in different solvents (THF, hexane) over 4 hours to form $[(\text{PONOP}^{\text{tBu}})\text{NiCl}][\text{Cl}]$ ⁵³ (**1.6**, Scheme 1.9) in 85% yield.



Scheme 1.9 Preparation of a cationic PONOP nickel chloride complex without bond activation on the ligand.⁵³

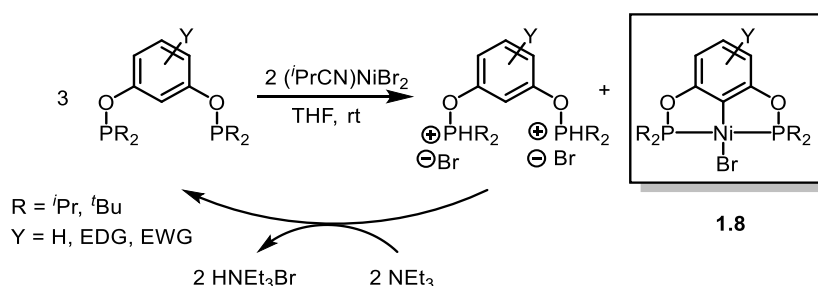
Anionic PCP or NCN-type ligands often require harsher conditions for metalation because they are prepared from the starting material containing a C-Z bond (Z = H, halide, SiMe_3 , etc.) that needs to be activated (either directly, or via prior lithiation followed by transmetalation, see Scheme 1.10).⁷⁰



Scheme 1.10 General scheme of C-Z bond activation with NCN pincer ligands.⁷⁰

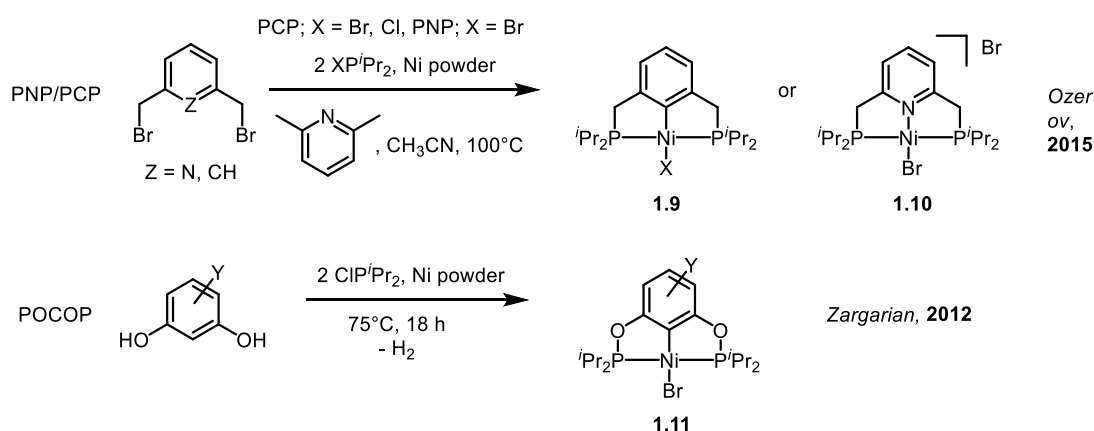
For most NCN pincer ligands, the prior lithiation step from the corresponding halide substituted ligand is necessary and often requires less harsh conditions as the driving force is the removal of the stable lithium halide salt in both steps. The lithiation usually requires low temperatures and strong lithium reagents (such as *n*BuLi, *n*-buthyl lithium) are often used, but the isolation is relatively straightforward. Then, the desired halide salt is used to afford the metalated complex **1.7** as seen in Scheme 1.10. However, this method is not used regularly as it requires an extra step in the synthesis of the metal complex.

Many pincer ligands require C-H or C-halide activation for the metalation step to be successful, and in this case the reaction almost always requires a stoichiometric amount of base and in some cases, high temperatures (See bottom path in Scheme 1.12). For example, a variety of substituted POCOP ligands can be metalated by using a nitrile-solvated nickel(II) bromide precursor, (RCN)_xNiBr₂, and triethylamine in excess to quench a protonated ligand species that is formed during the reaction (See Scheme 1.11).



Scheme 1.11 Synthesis of substituted POCOP Nickel(II) bromide complexes via C-H activation.⁶⁵

Much research has been done in the last decade on the development of one-pot reactions for the synthesis of some pincer ligands and complexes, especially those containing resorcinol or lutidine-based ligands. This research stems from the need for more synthetically straightforward and atom economical reactions that also produce less waste (i.e. ‘greener processes’ where some of the 12 principles of green chemistry are satisfied)⁷¹. Some examples of one-pot synthesis of pincer ligands include the synthesis of PCP, PNP⁷² and POCOP ligands²² (See Scheme 1.12).



Scheme 1.12 Examples of one-pot synthetic procedures for the preparation of PCP, PNP and POCOP Nickel complexes.^{22,72}

1.1.3 Steric and Electronic Properties of Pincer Complexes

Because this thesis is focused specifically on pincer complexes that contain both phosphine and pyridine moieties linked together, it is important to first understand the properties and chemistry of both phosphine and pyridine-donor ligands before discussing the properties of the newly designed pincer ligands. Introducing these concepts will give insights into the tools and techniques available to characterize and modify the steric and electronic properties of multi-dentate pincer ligands.

1.1.3.1 Electronic Properties of Monodentate Phosphine Ligands

Simple alkyl and aryl phosphines mostly interact as a Lewis base with transition metal centers, and act as σ -donor ligands. The lone pair in the filled σ orbital of the phosphine interacts with

the empty metal d orbital, creating a stable bond. However, they also have Lewis π -acidity character (π -acceptor character) as they can accept electron density from filled metal d orbitals. It was previously thought that the empty d orbitals on the phosphine center would act as the acceptor ligands and receive the electronic density from the metal. However, in 1985, a revised view of the bonding was proposed, which states that the acceptor orbital of the phosphine is a combination of a $3d$ orbital with a σ^* orbital. The orbital still contains two acceptor lobes but differs with the $3d$ orbital in that it is antibonding with respect to the P-R bond. (See Figure 1.2).^{73,74-78}

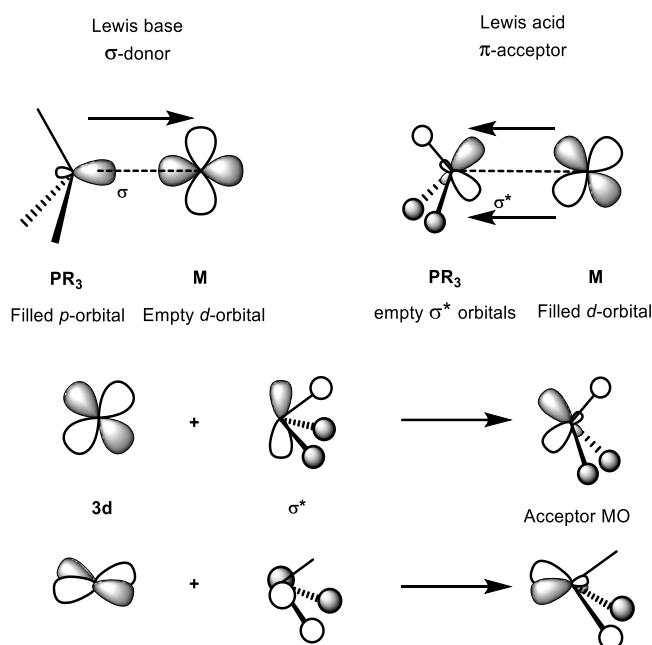


Figure 1.2 Representation of the dual Lewis base (σ -donor) and acid (π -acceptor) character of phosphines.

Because of the dual σ -donor and π -acceptors characters of the phosphine ligands, the nature of the R groups on the phosphine can greatly influence the electronic properties of the ligand. Several methods have been used to quantify the strength of the nature of the substituent on the phosphine, either based on theoretical calculations, or experimentally by analyzing the IR frequency of an IR active transition metal adduct. Using NBO (Natural Bond Order) to analyze the energy of the P-C σ^* orbitals, Leyssens *et al.*⁷⁹ were able to grade the π -accepting ability

of PR_3 ligands ($\text{R} = \text{Ph}, \text{H}, \text{Me}, \text{OMe}, \text{F}, \text{Cl}$) by arbitrarily weighting their π -accepting character versus CO (which was fixed at 100), as well as comparing them with simple amine ligands NR_2 ($\text{R} = \text{Me}, \text{H}, \text{F}$) and pyridine (See Figure 1.3). They were able to grade the π -accepting nature of simple phosphine substituents as follow: $\text{PCl}_3 > \text{PF}_3 > \text{P}(\text{OMe}_3) > \text{PMe}_3 > \text{PH}_3 > \text{PPh}_3$.

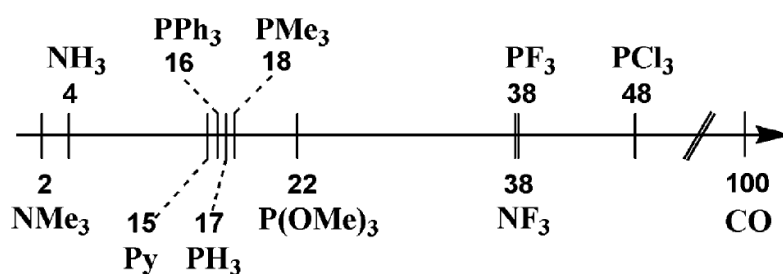


Figure 1.3 Calculated π -acceptor character for P- and N- based ligands, relative to CO. Determined by NBO analysis (Reprinted with permissions from *Organometallics* **2007**, 26, 2637-2645).⁷⁹

Many different approaches have been used to experimentally determine the back-bonding capacity of different phosphine substituents. Infrared (IR) spectroscopy is an important tool when determining the strength of bonds and the electronic nature of complexes. The most widely used method to characterize many electronic properties of the ligand is comparison of stretching frequencies of the CO ligand in carbonyl complexes. It has a very specific frequency range that not many other ligands have, so the region where the CO frequency would appear is often free of overlapping signals. The extremely strong π -backdonation from the metal center to the CO ligand allows for a quite straightforward probe into the electronic properties of a system. Moreover, the preparation of transition metal carbonyl complexes is often simple and straightforward, and present a quite elegant and attractive method to probe the subtle differences in the electronic nature of phosphine substituents. In a fundamental study by Tolman in 1977,⁸⁰ the analysis of nickel carbonyl complexes incorporating simple phosphine and phosphite ligands, $[\text{Ni}(\text{CO})_3\text{L}]$ ($\text{L} = \text{P}^t\text{Bu}_3, \text{PCy}_3, \text{PMe}_3, \text{P}(^4\text{-OMePh})_3, \text{PPh}_3, \text{P}(\text{OMe})_3, \text{P}(\text{OPh})_3, \text{PF}_3$) revealed some trends amongst the substituents of the phosphines, such as: alkyl are stronger σ -donor than aryl

substituents, phosphites are weaker σ -donors than phosphines, that t Bu and cyclohexyl substituents are the strongest donors while fluorine substituted phosphine is the weakest donor (See Table 1.1).

Table 1.1 CO stretching frequencies (ν_{CO}) values for $[\text{Ni}(\text{CO})_3\text{L}]$.^a

L	ν_{CO} (cm^{-1})
P^tBu_3	2056
PCy_3	2056
PMe_3	2064
$\text{P}(4\text{-OMePh})_3$	2066
PPh_3	2069
$\text{P}(\text{OMe})_3$	2079
$\text{P}(\text{OPh})_3$	2085
PF_3	2110

^aAdapted from Organotransition Metal Chemistry⁷³; Original source: Tolman, C.A., *Chem. Rev.* **1997**, 77, 313.⁸⁰

1.1.3.2 Steric Properties of Monodentate Phosphine Ligands

Along with their abilities to modulate the electronic properties of complexes, phosphine ligands are also well known to have a big effect on the steric properties of complexes due to their wide range of substituents and their commercial availabilities. However, the proper effects of the phosphine ligand's sterics were not well explored before the work of Tolman.⁸⁰ Tolman analyzed a large variety of substituted phosphines and phosphites by using their cones angles. The cone angle (later referred to as the "Tolman cone angle") is the angle which is formed between the metal center and the outer edges of the phosphine's substituents, if those substituents were represented as a space-filling model (See Figure 1.4). This method has been widely used for approximation of steric trends in organometallic chemistry, but some drawbacks make it only appropriate for qualitative analysis. Since the cone angle is based on the least hindered conformation of the phosphine in a certain complex, it can vary significantly when the complex has different steric hindrance than the complex for which the cone angle was measured. Finally, the presence of unsymmetrical ligand in the determination of the cone angle is much less straightforward than for symmetrical ligands.⁷³ The Tolman cone angle is also more often used

for monodentate ligands than multidentate ligands, which makes it more difficult to use with pincer complexes, for example.

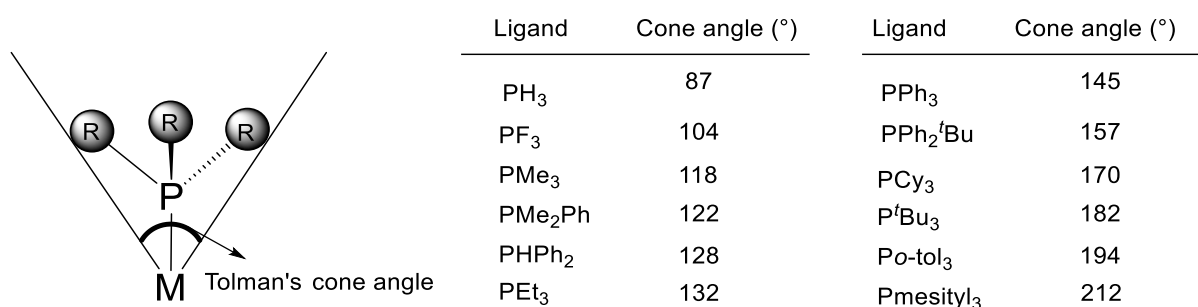


Figure 1.4 Artistic representation of the concept of Tolman's cone angle, and some representative cone angles⁸⁰

1.1.3.3 Electronic properties of Pyridine Ligands

Pyridine is a very common molecule and type of ligand used in transition metal chemistry. Compared to benzene, its closest all-carbon analogue, the presence of a nitrogen brings in interesting properties that benzene does not have. For example, pyridine has a dipole moment of 2.2 Debye, and has an accessible electron pair lying flat in with the pyridine ring. Moreover, the pyridine is relatively electron-deficient compared to benzene. Pyridine can also act as a base due to the presence of the nitrogen atom, on par with other tertiary amines. Although it is a neutral ligand, pyridine is known to bind strongly with metal centers and cause strong overlap from the sp^2 lone pair on N and the empty d orbitals of the metal. Pyridine also has electron-accepting character through back-bonding interactions due to the interaction of filled d orbitals of the metals and delocalized π^* anti-bonding orbitals of the ring (See Figure 1.5)⁸¹

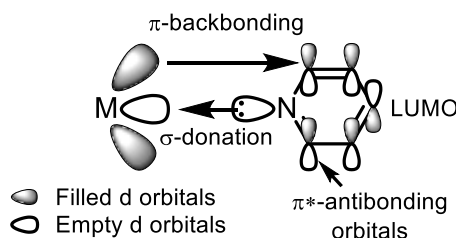


Figure 1.5 Visual representation of σ -donation and π -backbonding orbitals involved in pyridine interaction with transition metal centers.

Because of the substitution of a carbon atom by a nitrogen atom, the aromaticity of the pyridine ring is lowered by about 16 kJ mol^{-1} compared to the benzene ring.⁸² This means that, in principle, pyridine should be able to undergo dearomatization more easily than benzene. However, the stronger aromaticity of benzene compared to pyridine is not the only factor in their stabilities. For example, the presence of the more electronegative nitrogen atom (compared to carbon in benzene) causes the pyridine to be more susceptible towards nucleophilic substitution reactions than benzene (at the *ortho*- and *para*-carbon) while being less susceptible to electrophilic substitution reactions than benzene (at the nitrogen and *meta*-carbon).⁸²

1.1.3.4 How to Quantify the Size of a Multidentate Ligand

Simpler descriptions of the size of a ligand usually fail when a multidentate ligand such as a pincer ligand is involved. This is due to the often-intrinsic enforcement of a certain geometry around the metal center when a multidentate ligand is present, due to steric repulsions or other factors that are not considered with simpler models like the Tolman's cone angle (See Section 1.1.3.2). For this reason, many groups have been working on the development of different description methods of multidentate ligand sterics in complexes, which has given rise to the "solid angles" methods.⁸³⁻⁸⁷ Although the principles of the cone angles and solid angles are closely related, the latter can take into account more of the intrinsic geometries that are caused by repulsion between parts of the same ligand. Whereas the cone angle method takes the edge of the space-filling model of a ligand as two points of a triangle, the solid angles are based on the shadow that is created from the projection of each atom (in a space-filling model) from the metal center on a sphere encompassing the whole complex. Lack in computational power at the time of the discovery of the solid angles made for oversimplified models which lacked descriptors that would consider more intricate factors of multidentate ligands. With the advances in computational analyses came a much more precise description of the solid angles.

The advancement in computer graphics also meant that those solid angles could be easily visualized in a 3D projection on a sphere (See Figure 1.6). In recent years, a more accurate version named the “exact ligand solid angles”, can accurately integrate the occluded area on the projected sphere, which gives an accurate value that can be compared to different systems and allow more accurate quantitative comparisons. This quantitative analytical method for the description of multidentate ligand is now widely used to compare steric properties of more complicated ligands such as tridentate pincer ligands containing multiple sterically complex groups and geometries.

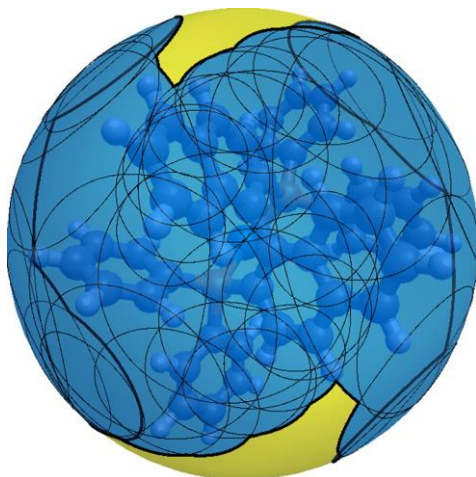


Figure 1.6 The occluded area in blue is used to determine the ligand solid angle of Pd(BINAP) complex. This area is the result of the intricate overlap of many shadow cones (circles) of each individual atom. The yellow part is the area where the ligand is not covering, which is accessible for reactants or other ligands. Reproduced with permission from: Bilbrey J.A., Kazez A.H., Locklin J., and Allen W.D., *J. Chem. Theory Comput.* 2013, 9, 5734-5744

1.1.3.5 Pincer ligands

Having introduced each donor group of pincer ligands separately in the previous section, I will now discuss the electronic and steric properties of pincer ligands, and how modification of the sterics or electronics can affect properties of the resulting complexes. I will also briefly show examples where the fine-tuning of these properties led to an increase in efficiency of the pincer complex in catalysis or enabled different reactivities.

Pincer ligands are perhaps some of the most versatile family of ligands that exist, mainly because of the almost endless ways that one can modify the ligand. Moreover, the preparation of the pincer ligand often uses simple and readily available starting materials, which can also be modified through simple synthetic procedures to introduce functionality. As such, introducing all the possible variations on the pincer framework would be out of the scope of this thesis, and I will try to focus on examples that are somewhat analogous to the pincer ligands studied in Chapter 2 and Chapter 3.

1.1.3.5.1 Electronic Properties of Benzene-Based Pincer Ligands

Previously, I have worked on resorcinol-based POCOP pincer complexes of nickel ($[2,6-(OPR')_2(R_nC_6H_{3-n})Ni^{II}NCMe][OTf]$, R = electron-withdrawing (EWG) or electron-donating group (EDG); $R' = ^iPr, ^tBu$) and studied the influence of the substitution of electron-withdrawing and donating substituents on the resorcinol framework towards the metal center²⁴ (See Figure 1.7), and their application towards the hydroamination of nitriles.²⁵ By analyzing at the IR stretching frequencies of the acetonitrile $C\equiv N$ moiety ($\nu(CN)$), I was able to determine that changing the nature of the backbone substituent can have an important impact on the electron density at the metal center. For example, $\nu(CN)$ of *para*-CO₂Me containing complex **1.12** (2329 cm⁻¹) is shifted to higher energy compared to the *para*-OMe containing complex **1.19** (2293 cm⁻¹), with respective differences compared to the free acetonitrile $\nu(CN)$ (2252 cm⁻¹) of 77 cm⁻¹ and 41 cm⁻¹, respectively. The other complexes **1.13-1.18** and **1.20-1.21** fit relatively well with the respective degree of electron-donating or withdrawing of their substituents (and their respective Hammett coefficients).²⁴

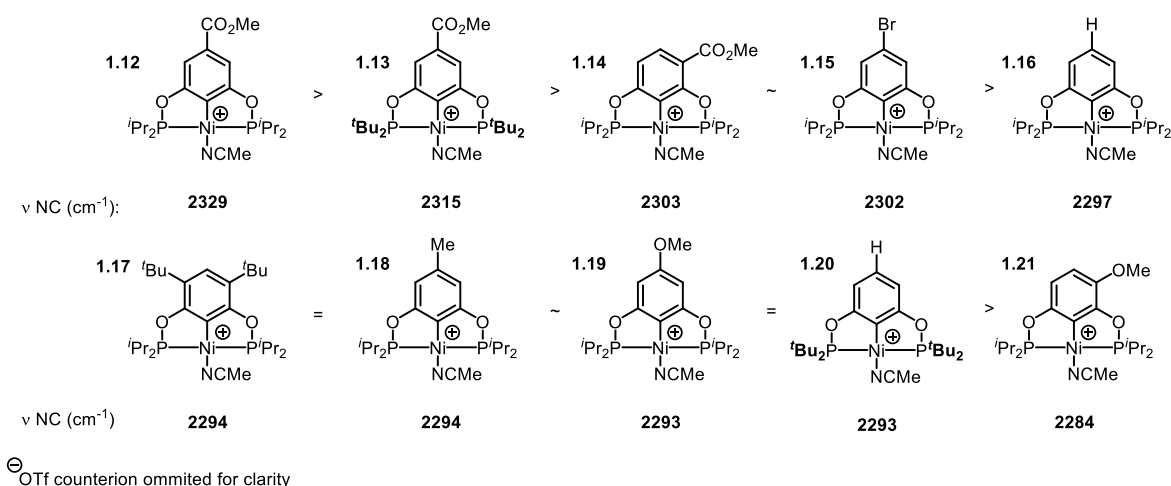
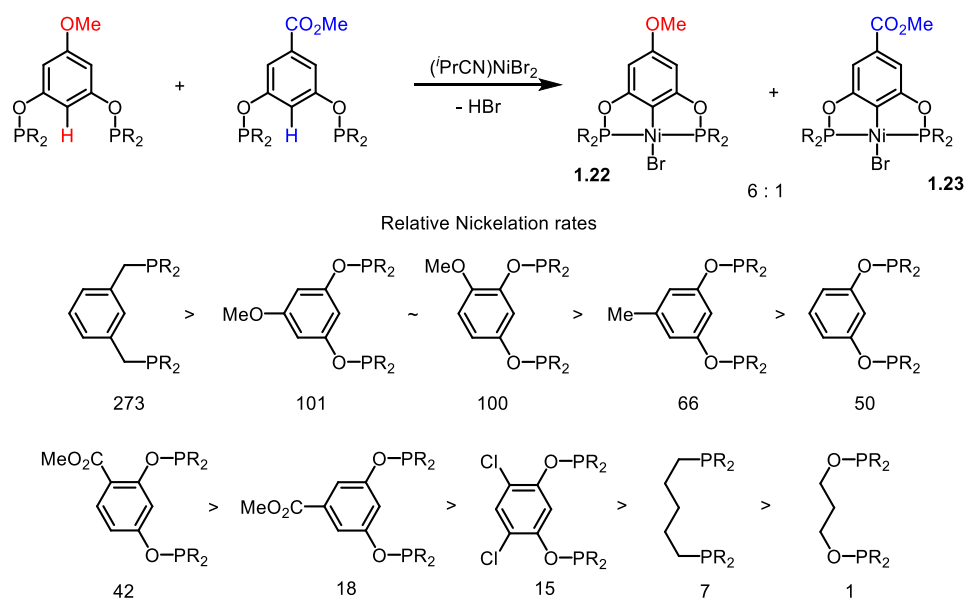


Figure 1.7 Effect of the nature of backbone substituent of POCOP cationic nickel pincer complexes **1.12-1.21** on their IR stretching frequencies of CN bond and on their Ni^{II/III} oxidation potentials.²⁴

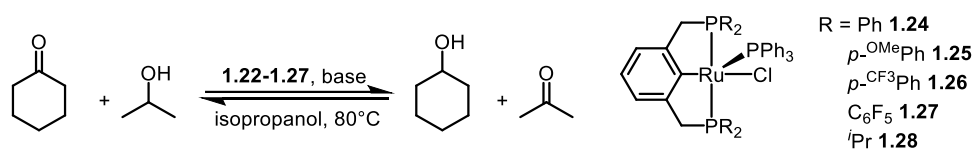
The group of Zargarian⁸⁸ has also studied the effect of those substituents on the rate of nickelation of POCOP pincer ligands with (iPrCN)NiBr₂ (See Scheme 1.13). For example, they found that the rate of complexation for the electron-rich OMe-substituted pincer complex **1.22** was six times higher than the electron-poor CO₂Me-substituted pincer complex **1.23**.⁸⁸ The rate of metalation for the other substituted complexes also matches quite well with respect to their Hammett coefficients.



Scheme 1.13 Relative metalation rates for a wide range of aliphatic and aromatic POCOP and PNP pincer ligands.⁸⁸

The group of van Koten, in 2007, studied the electronic effects of different substituents at the phosphine donors of ruthenium PCP pincer complexes (**1.24-1.28**) on hydrogen transfer catalysis by changing different ligands on the phosphine groups⁸⁹ (See Table 1.2). From their analysis, they found that the more electron-poor *para*-CF₃Ph phosphine substituted catalyst **1.26** gave much higher TOF at 20% conversion (and did not require basic pretreatment) compared to the more electron-rich *para*-OMePh phosphine substituted catalyst **1.25**. Moreover, the electron-poor complex **1.27** gave poor conversion because of the presence of *ortho*-fluoro substituents which are causing *ortho*-hindrance.⁸⁹

Table 1.2. Hydrogen transfer reaction of cyclohexanone catalyzed by different Ru^{II} PCP pincer complexes **1.24-1.28** with varying degree of electronic properties on the phosphine moieties.^{89 a}



entry	Catalyst precursor	TOF(h ⁻¹) ^b	conversion (%) / t (min)
1	1.22	33 600	98/10
2	1.23	8000	96/30
3	1.24	35 700	98/10
4	1.25	41	98/780
5	1.26	980	98/300

^a Reaction conditions: 2.0 mmol of cyclohexanone; catalyst concentration = 0.1 mol%; 2mL of isopropanol; [base]:[catalyst] = 20:1; *T* = 82 °C; N₂ atmosphere. Pretreatment of catalyst with base for 1h. ^b Turnover frequency (TOF) calculated at 20% conversion.

1.1.3.5.2 Electronic Properties of Pyridine-Containing Pincer Ligands

The combination of the σ -donor and π -acceptor properties of both the pyridine and phosphine moieties (and further modulation on the pyridine ring with substituents) allows an incredible variety of pincer ligands to be prepared. Although anionic pincer frameworks such as benzene containing PCP ligands are usually more thermally stable than pyridine or amine-based pincer

ligands because of the stronger metal-carbon interactions, they are often more difficult to prepare because of the C-H activation step required, or prior lithiation or derivatization of the pincer ligand before metalation.

Moreover, as discussed previously, the pyridine ring in pyridine based PNP pincer ligands are easier to dearomatize than the benzene rings in PCP pincer ligands. The increased susceptibility towards deprotonation of pyridine-based ligands compared to their benzene-based analogues are the key factor in the surge of popularity of pyridine-based ligands in catalysis because of the enormous potential of catalysis and reactivity through aromatization-dearomatization pathways in “metal-ligand cooperativity” (MLC, see the later section 1.1.8).

1.1.3.5.3 Geometry, Conformation and Size of Pincer Ligands

The size of a pincer ligand has important effects on the stability and the reactivity of the resulting complex. For example, the size of the ring formed by the pincer arm can drastically influence the stability of the pincer complex. Usual pincer arms are comprised of 5-membered rings, which confer the rigid, planar geometry that pincer complexes usually adopt. The planar nature of the pincer ligand favors the optimal overlap between each atom and the metal center, and thus is the most stable conformation in most cases. However, the aromatic or aliphatic nature of the pincer complex, the nature of the metal center, and the coordinating atoms can also influence the geometries that a pincer complex can adopt. One example is the PSiP pincer ligand system, where Ru and Ir will adopt *fac* configurations (monomer **1.29** or dimer **1.30**) and can exist as an equilibrium between the two configurations, *mer*-**1.31** and *fac*-**1.31** (See Figure 1.8).⁹⁰

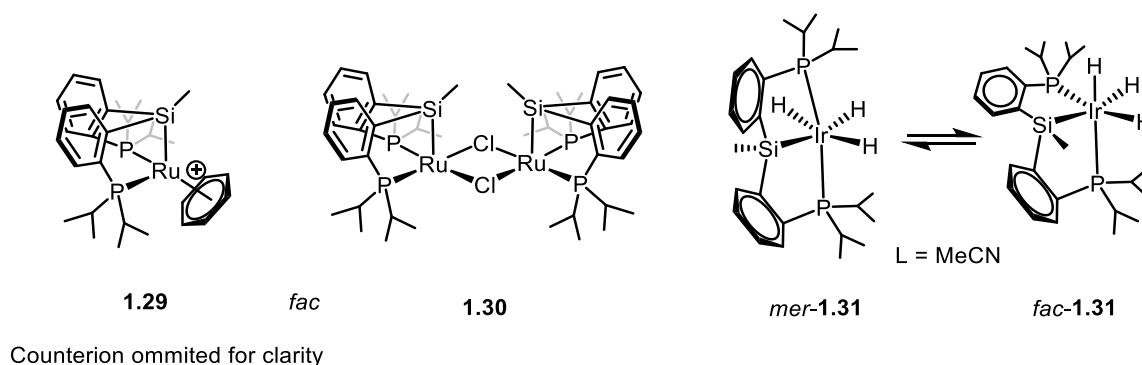


Figure 1.8 Examples of unusual *fac* geometries for Ru and Ir PSiP pincer complexes **1.29-1.31**.⁹⁰

Although very limited in the literature, some examples of 6-membered pincer complexes have been reported, either on only one side or on both. The ligands themselves often adopt a twisted geometry to compensate for the increased ring size, but often the geometry around the metal center is the usual geometry for the specific metal center (i.e. square-planar for 4-coordinated $M^{II} d^8$ systems, etc.). Compared to similar 5-membered ring pincer complexes, the 6-membered rings often show longer metal-central atom distances (i.e. complex **1.32** with 2.155 Å vs complex **1.33** with 2.488 Å, see Figure 1.9),^{91, 92} and even lability of one or both pincer arms during catalysis (See complex **1.36-1.38** in Scheme 1.14).

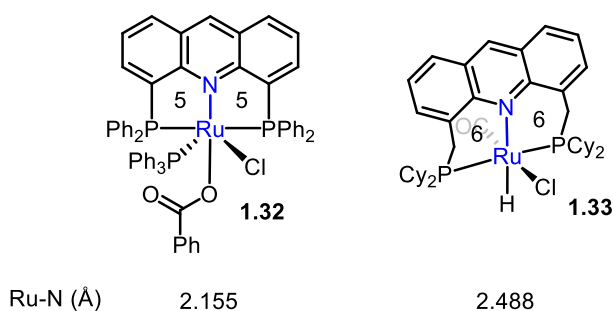
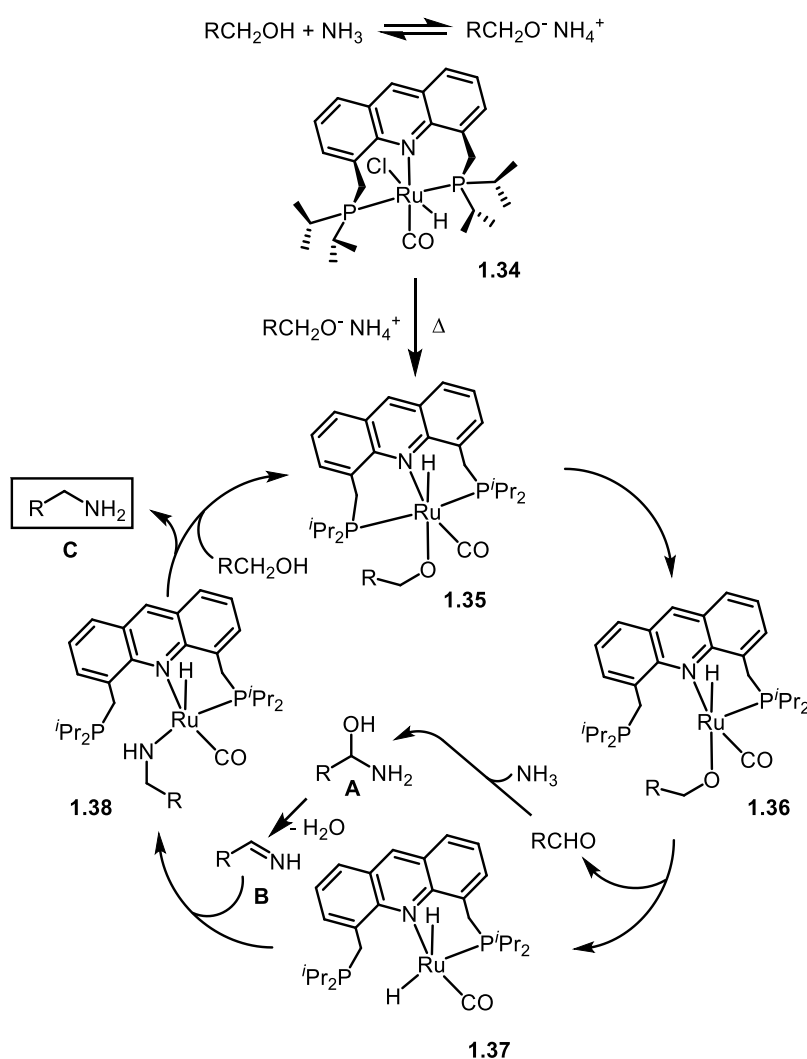


Figure 1.9 Example of Ru-N bond elongation when increasing pincer from 5-membered ring to 6-membered ring.^{91, 92}

An example of the lability of the 6-membered ring pincer's arm during catalysis comes from the group of Milstein when they studied the application of **1.34** in the direct amination of alcohols with ammonia⁹³ (See Scheme 1.14). A proposed mechanism involves the following: upon activation of the starting Ru^{II} pre-catalyst with the alkoxide formed by deprotonation of the

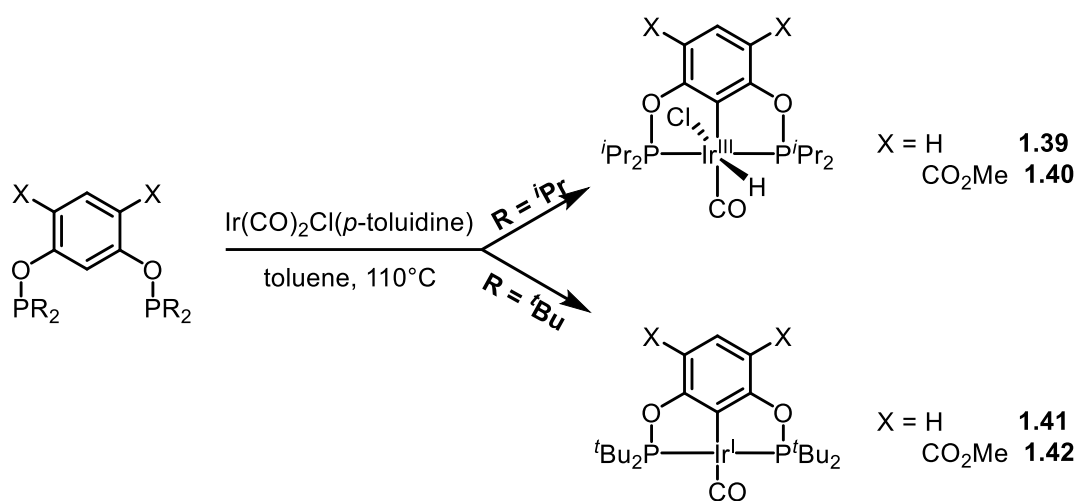
alcohol with ammonia under reflux, the alkoxide-bound complex **1.35** is formed. One of the pincer's phosphine arms de-coordinates from the ruthenium center, and then the alkoxide species undergoes dehydrogenation to form an aldehyde and generates the dihydride species **1.37**. The aldehyde then reacts with a molecule of ammonia and forms the hemiaminal intermediate species **A** which loses water to form the terminal imine **B**. This terminal imine **B** then gets reduced by the ruthenium dihydride species **1.37** and binds to the ruthenium center to form **1.38**, where the final amine **C** is formed and **1.35** is regenerated upon reaction with alcohol.



Scheme 1.14 Proposed mechanism for the direct amination of alcohols with ammonia catalyzed by **1.34**.⁹³

Although 6-membered pincer complexes are sometimes not as stable as their 5-membered counterparts are, they still show catalytic activity often on par with their 5-membered analogues, but their examples are much scarcer in the literature (one example is presented later, see complex **1.47** in Scheme 1.17, Section 1.1.4).

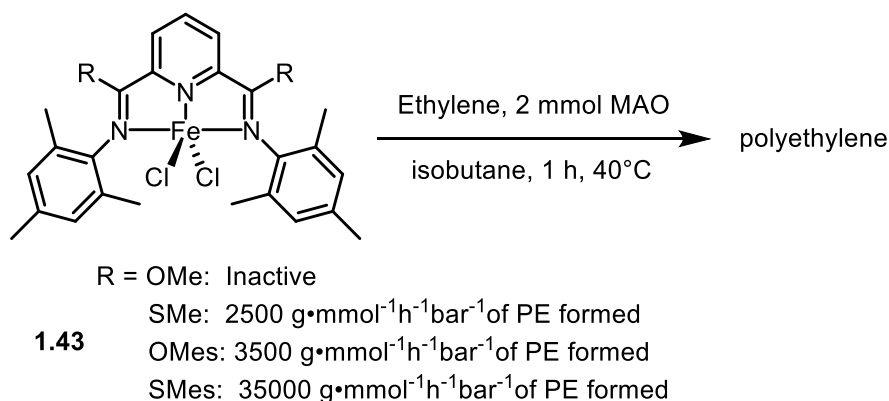
In 2015, the group of Goldberg and Heinekey studied the steric impact of phosphine substituents in POCOP pincer complexes of iridium and found out that changing phosphine groups from *i*Pr to *t*Bu has an important effect on the complexation and oxidation state of the iridium metal center.⁹⁴ They found that the presence of a less bulky *i*Pr substituted phosphine on the POCOP backbone, independent of the substitution on the benzene framework, caused the formation of an iridium center in the +3 oxidation state (complexes **1.39-1.40**), while the presence of a bulkier *t*Bu substituent on the phosphines gave only the final complex where the iridium center was in the +1 oxidation state (complexes **1.41-1.42**).⁹⁴



Scheme 1.15 Effect of the size of phosphine substituents on the oxidation state of the iridium center.⁹⁴

Interestingly, a study done in 2004 by the group of Willams on the polymerisation of ethylene with an iron NNN pincer complex found that varying the size as well as electronic properties of the substituents on the pincer's arms affects the catalytic activity significantly. They found that changing the R substituent from thiomethane (MeS) to 2,4,6-trimethylbenzenethiol (MesS)

in the a bis(iminopyridine) iron dichloride pincer complex **1.43** can dramatically increase the activity of the complex in the polymerization of ethylene, from producing $2750 \text{ g} \cdot \text{mmol}^{-1} \text{ h}^{-1} \text{ bar}^{-1}$ to $35000 \text{ g} \cdot \text{mmol}^{-1} \text{ h}^{-1} \text{ bar}^{-1}$ of polyethylene. However, the effect does not only come from the steric properties, but also from the difference in electronic properties of oxygen and sulfur atoms in the ligand (Scheme 1.16)



Scheme 1.16 Electronic and steric effects of substituents on the pincer arms of **1.43** on the polymerization of ethylene.⁹⁵

1.1.4 Catalysis and Small Molecule Activation by Nickel Pincer Complexes

The application of pincer complexes, especially in catalysis, has been the topic of many great reviews and books over the last few decades. These often focus on pincer complexes with specific metals: Mn,^{96, 97} Fe,^{98, 99} Co,^{96, 100} Ni,¹⁰¹ Ru,^{102, 103} Rh,¹⁰⁴ Pd,¹⁰⁵ Os,¹⁰⁶ Ir,^{107, 108} Pt.^{70, 109}

First-row transition metals are often much lower in cost than their 2nd or 3rd row analogues because of their much higher natural availability. They are also sometimes less toxic than their heavier analogues. Because of these reasons, they are often used in many different types of catalysis, with different efficiencies. They have been used in the last decades in competition with the more traditional precious metal catalysts. In this chapter, I will focus on a few selected applications of first-row transition metal complexes, in particular of nickel, as they are more relevant to this thesis.

1.1.4.1 Catalysis by nickel pincer complexes

Although not as earth abundant as iron (which is the most abundant transition metal in the earth's crust), nickel is still the 6th most abundant transition metal. Nickel has been used for thousands of years, mainly due to its ease of extraction and purification from ore mining. Nickel pincer complexes have been widely used as catalyst in a wide variety of catalytic reactions, and although they often don't show the same level of activity as Group 10 heavier analogues (Pd, Pt), their low price and environmental impact allows for higher catalyst loading and an overall more cost-effective solution in many cases. Examples of catalysis include C-X and C-C cross coupling, hydrosilylations, hydroamination or alkoxylation, and many others, with an important emphasis on C-C cross coupling reactions.

In 2009, the group of Hu prepared a NNN pincer nickel chloride complex (complex **1.44**), nicknamed "Nickamine", which turned out to be quite active in Sonogashira coupling and in direct alkylation of terminal alkynes amongst other reactions (See Figure 1.10).^{110, 111}

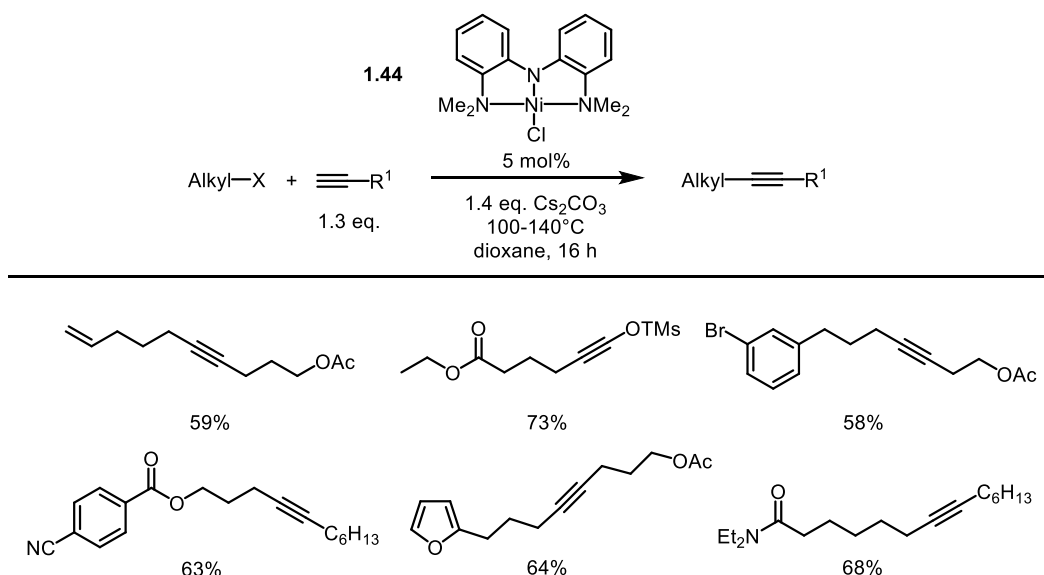


Figure 1.10 Selected scope of the direct alkylation of terminal alkynes catalyzed by **1.44**.^{110, 111}

A more recent example by the group of Sun involves a nickel pincer complex (complex **1.45**) in transfer hydrogenation of ketones.¹¹²

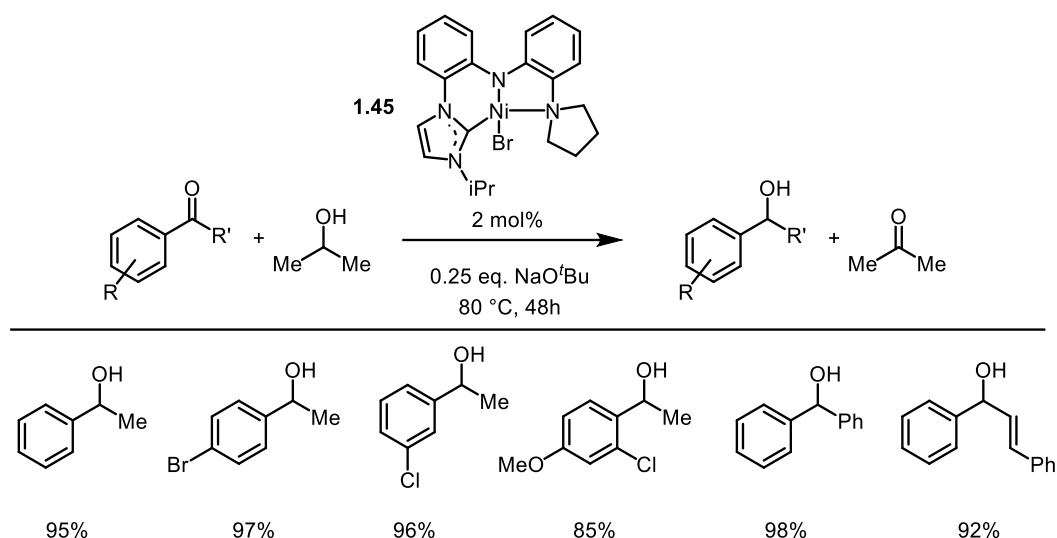
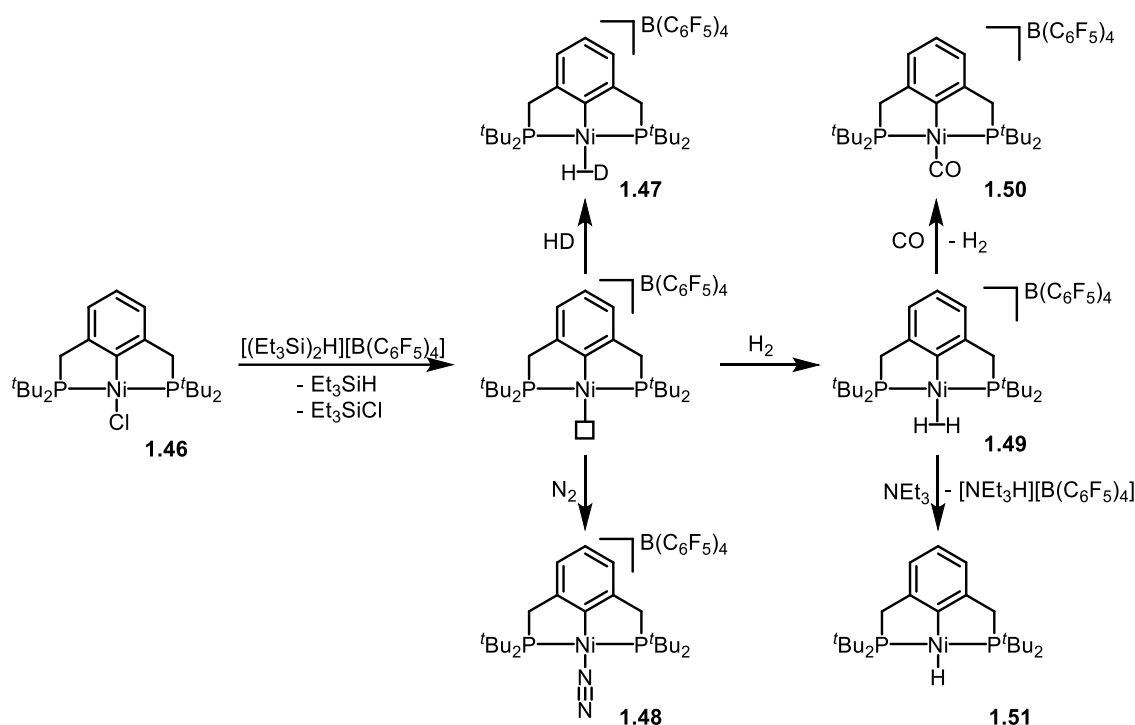


Figure 1.11 Selected examples for the transfer hydrogenation of ketones catalyzed by **1.45**.¹¹²

1.1.4.2 Small Molecule Activation by Nickel Pincer Complexes

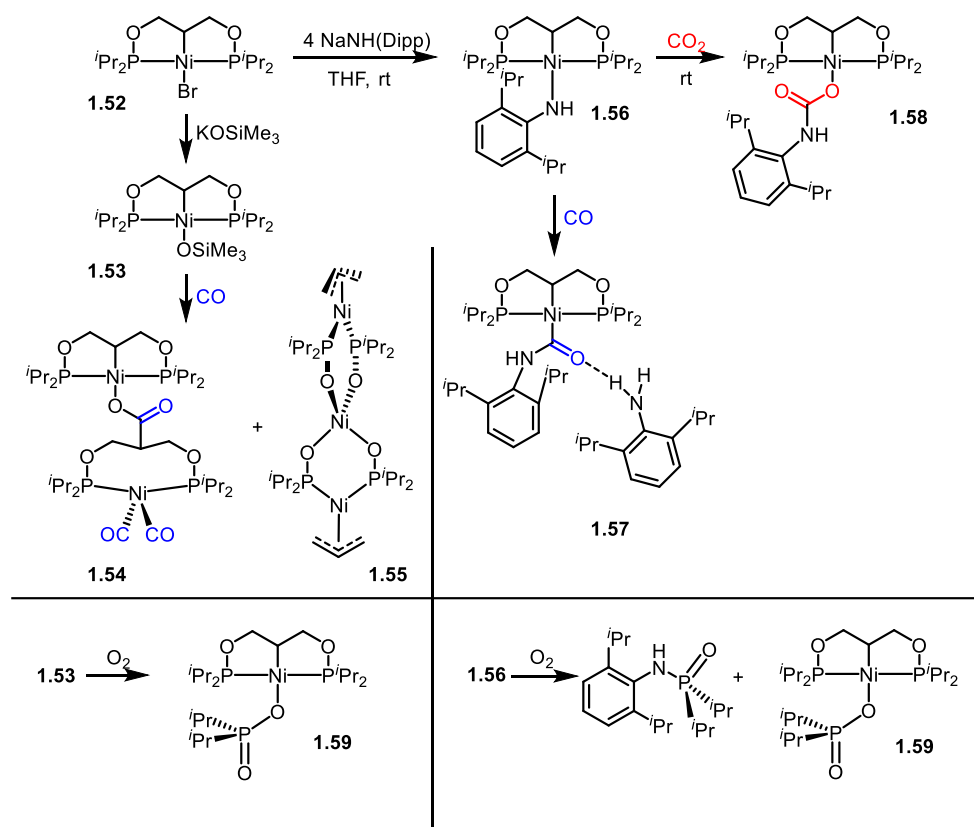
Small molecules often play an important part in catalysis. The activation step is often a key step in catalytic cycles and the isolation and characterization of the products of small molecule activation can help elucidate elementary steps of organic transformations. In this section, I will focus on examples of nickel pincer complexes that involve CO₂, CO, H₂, and O₂ as they are relevant to the studies in this thesis.

In 2012, the group of Heinekey was able to isolate and characterize adducts of H₂, HD, and CO of an aromatic PCP pincer complex by abstracting the chloride atom on **1.46** using a strong halide abstracting compound [(Et₂Si)₂H][B(C₆F₅)₄] and forming a transient cationic pincer complex¹¹³ (See Scheme 1.17). The deeply colored cationic complex was then reacted with N₂ to form the dinitrogen adduct **1.48**. They also reacted the same complex with H₂, forming a rare H₂ adduct with a nickel pincer complex (complex **1.49**). The H₂ bound on the nickel center could be exchanged by CO to form the cationic complex **1.50**. Finally, in the presence of triethylamine, the H₂ adduct **1.49** was deprotonated, forming the neutral hydride nickel complex **1.51**.



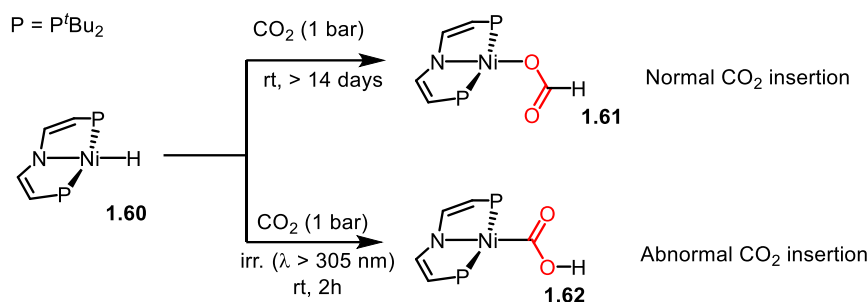
Scheme 1.17 Activation of small molecules at the nickel center of **1.46** after chloride atom abstraction.¹¹³

In 2014, the group of Zargarian³¹ studied the fate of some aliphatic POCOP nickel pincer complexes when reacted with CO and CO₂ (see Scheme 1.18). They first prepared the amine-bound **1.56** by reaction of the bromo precursor **1.52** with an excess of NaNH(Dipp). They also studied their previously reported siloxide complex **1.53**.²⁹ Compared to the siloxide complex, the amine complex **1.56** is much more stable and insertion of CO₂ and CO proceed as expected in the Ni-N bond to form complexes **1.58** and **1.57**, respectively. Complex **1.57** has an additional free H₂N(Dipp) amine that interacts through a NH---OC hydrogen bond with the bound moiety. The siloxide complex **1.53** is, however, much less stable. In the presence of CO, **1.53** forms at least two decomposition products (**1.54** and **1.55**). Finally, when either the amine-bound complex **1.56** or the siloxide species **1.53** was reacted in the presence of O₂, they both formed complex **1.59** which is an adduct with a phosphinate ligand that most likely comes from a complex sequence of decomposition events.³¹



Scheme 1.18 Reactions of **1.52**, **1.53** and **1.56** towards CO_2 , CO and O_2 and their decomposition products.^{31, 32}

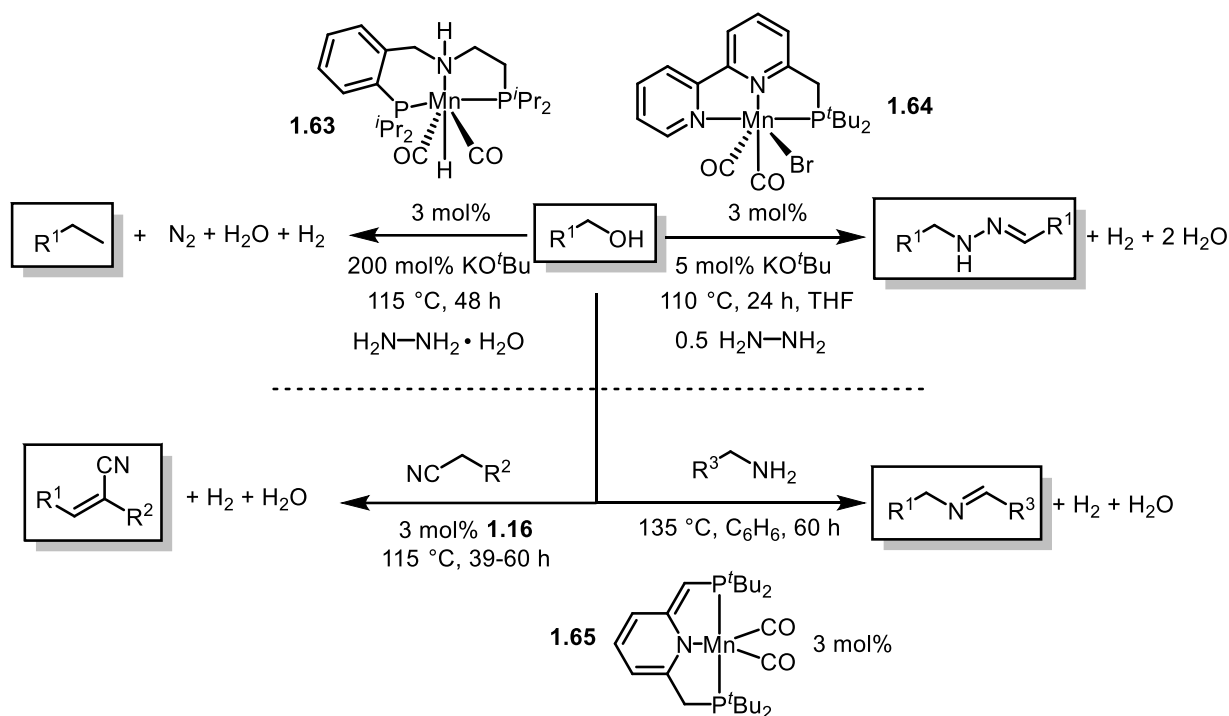
The reverse water-gas shift (RWGS) reaction has been a very attractive route for the transformation of CO_2 for a long time. However, research into the utilization of molecular catalysts is difficult because the usual reactivity of metal hydrides with CO_2 does not follow the mechanism of the RWGS reaction. The usual pathway for the insertion of CO_2 in a M-H bond is through the formation of metal formate species ($\text{MO}(\text{O})\text{CH}$), while a hydroxycarbonyl species ($\text{MC}(\text{O})\text{OH}$), which is the key intermediate in CO-selective catalysis, has never been observed until recently by the group of Schneider.¹¹⁴ In their article, they were able to isolate the “abnormal” CO_2 insertion product (See complex **1.62** under abnormal CO_2 insertion in Scheme 1.19) into a Ni-H bond using photochemical conditions, while thermal conditions alone gave the “normal” CO_2 insertion product (See complex **1.61** under normal CO_2 insertion in Scheme 1.19) but only after two weeks at room temperature.



Scheme 1.19 Normal and abnormal insertion of CO_2 into Ni-H bond of **1.60**.¹¹⁴

1.1.5 Catalysis by Manganese Pincer Complexes

Although manganese complexes were widely used previously in oxidation catalysis, their use in reduction catalysis, hydrogenation, dehydrogenation, and “hydrogen borrowing” reactivity was essentially overlooked until recently when Mn pincer complexes have gained a significant interest for their application in catalysis. Manganese pincer complexes are now used as catalysts in (de)hydrogenation reactions,¹¹⁵⁻¹¹⁹ electrocatalytic CO_2 reduction,¹²⁰⁻¹²³ alcohol deoxygenation,^{124, 125} and other reactions. Manganese PNP and PNN complexes have been widely used in those type of catalysis and remain a robust and versatile family of complexes. Recently, Milstein has reported that an aliphatic PNP manganese pincer (complex **1.63**) catalyzes the deoxygenation of alcohols and the coupling of nitriles, whereas an aromatic PNP complex (complex **1.64**) is shown to catalyze the coupling of hydrazines to alcohols, and an aromatic PNN complex (complex **1.65**) catalyzes an α -olefination of nitriles (See Scheme 1.20).¹²⁴⁻¹²⁷

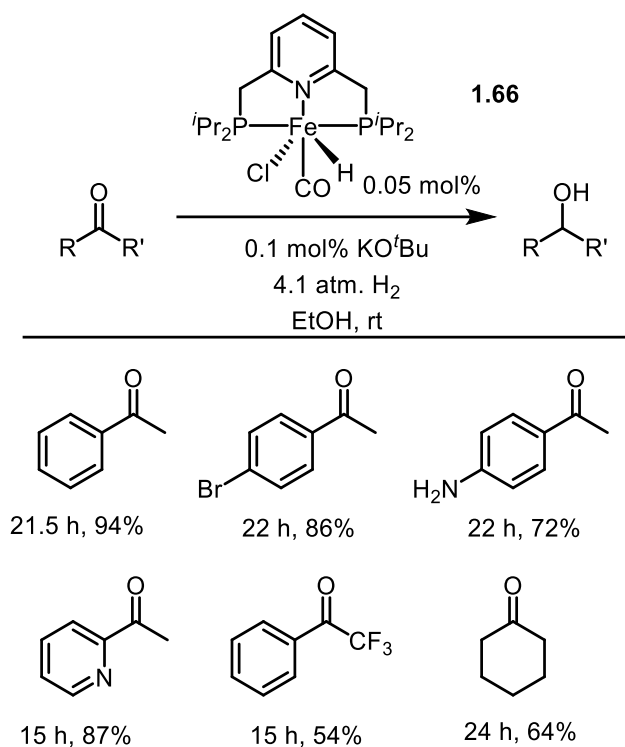


Scheme 1.20 Examples of manganese pincer catalyzed reactions involving an alcohol.¹²⁴⁻¹²⁷

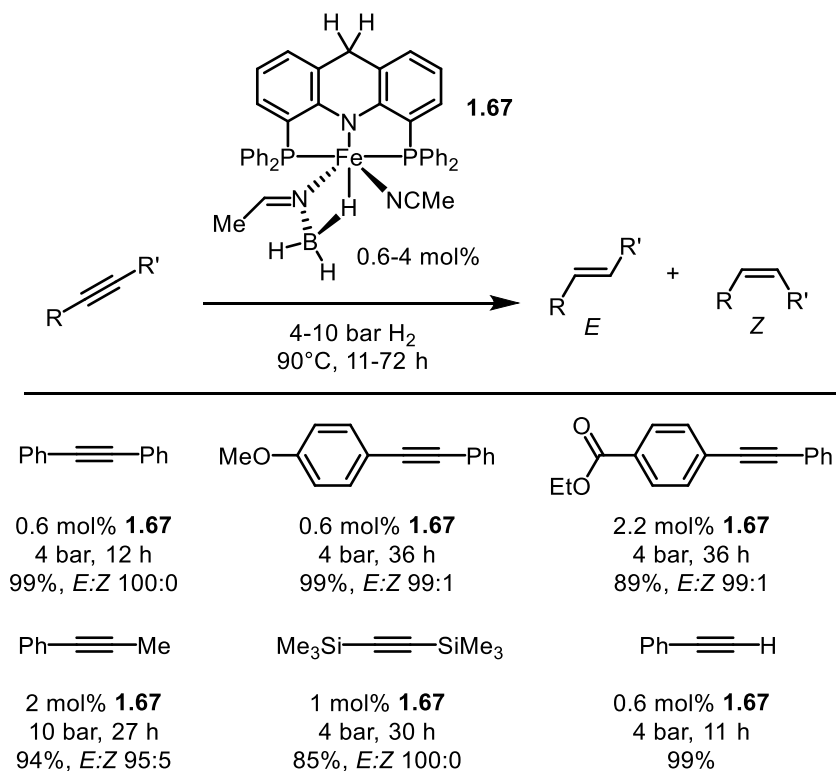
1.1.6 Catalysis by Iron Pincer Complexes

Iron is one of the most well studied metal in catalysis due to its low cost, lack of toxicity and extremely high abundance in the earth's crust. Iron pincer complexes are well known, and their catalytic activity is widely described in hydrogenation and dehydrogenation of many functional groups. They have a high affinity to form hydride species and activate H_2 , and as such, many complexes have been isolated and characterized.

Examples of hydrogenation reactions catalyzed by iron pincer complexes includes the work done by the group of Milstein on the hydrogenation of ketones in 2015 with the iron PNP pincer complex **1.66**^{98, 128} shown in Scheme 1.21. They were able to hydrogenate a variety of substituted benzophenones, 2-acetylpyridine, as well as cyclohexanone in moderate to good yields. The same group in 2013 also studied the *E*-selective semihydrogenation of alkynes to form alkenes catalyzed by the PNP complex **1.67**, and obtained good yields on a variety of alkynes (See Scheme 1.22).^{98, 128}

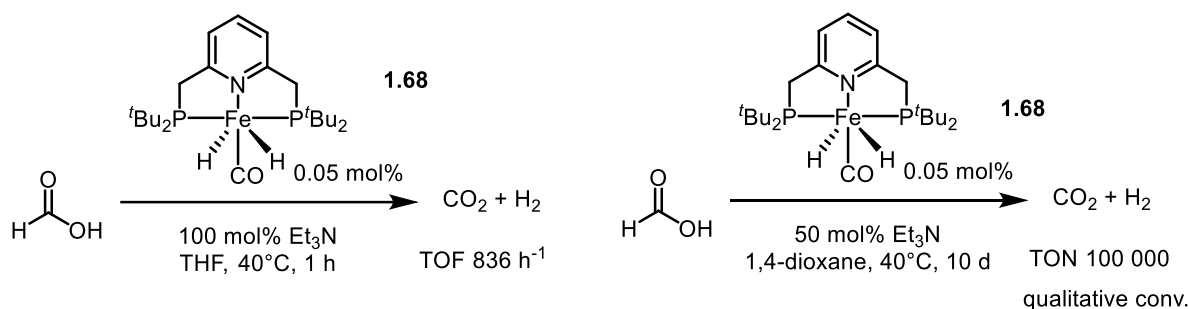


Scheme 1.21 Selected example of the hydrogenation of ketones with KO^tBu catalyzed by **1.66**^{98, 129}



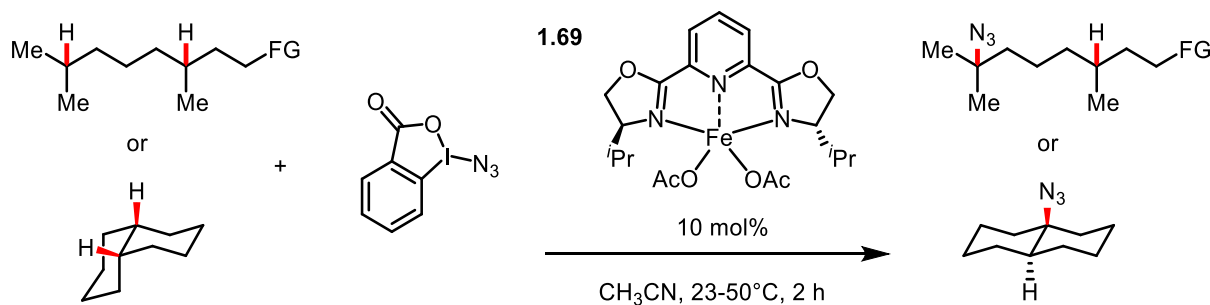
Scheme 1.22 Selected examples of *E*-selective semihydrogenation of Alkynes catalyzed by **1.67**.^{98, 128}

The group of Milstein in 2011 also showed that the dehydrogenation of formic acid to CO₂ and H₂ was possible under mild conditions, although using stoichiometric amount of base. They obtained a highly active catalyst with a TOF of 836 h⁻¹ in the first hour of reaction, while they obtained complete conversion and a TON of 100 000 after 10 days by using a substoichiometric amount of base.¹³⁰



Scheme 1.23 Examples of the dehydrogenation of formic acid to CO₂ and H₂ catalyzed by **1.67**.¹³⁰

Other notable examples of iron pincer catalyzed reactions include C-H azidations¹³¹ (Complex **1.69**, Scheme 1.24), C-H deuteration and tritiation of pharmaceutical compounds¹³² and trans-formation of glycerol to lactic acid.¹³³



Scheme 1.24 Iron pincer-like complex **1.75** for C-H azidation¹³¹

1.1.7 Catalysis by Cobalt Pincer Complexes

Cobalt pincer complexes have been receiving a lot of attention in recent years with pioneering work by the groups of Milstein, Kirchner, Chirik, Kempe, Beller, and others. Cobalt pincer

complexes are known to catalyze (de)hydrogenations reactions, hydroboration, and hydrosilylation reactions.¹³⁴ Some reviews have been published in recent years that cover most cobalt pincer catalysis.^{96, 100}

Some examples of hydrogenations include the work of the group of Hanson in 2012, where they prepared a new aliphatic PNP cobalt catalyst (complex **1.69**) which could easily hydrogenate ketone, aldehyde, and imine substrates.¹³⁴ In the presence of 1 to 4 atm of H₂ and 1 equivalent of the strong acid H[BAr^F₄](Et₂O)₂, complex **1.69** could hydrogenate ketones in good to moderate yields, either aromatic (entry 1, Table 1.3, 89% isolated yield) or aliphatic (entry 3, Table 1.3, 66% GC yields). The reaction was not selective in the presence of a terminal alkene however, and both the ketone and alkene moieties were hydrogenated (entry 3, Table 1.3). They also hydrogenated aldehydes (entries 4 and 5, 96% and 92% isolated yield, Table 1.3) and imines in good yields (entries 6 and 7, 84% and 88% isolated yield, Table 1.3). Although they used a low catalyst loading of 2 mol%, the use of a stoichiometric amount of a strong acid H[BAr^F₄](Et₂O)₂ could make this reaction less applicable for industrial applications.

Table 1.3 Selected examples of ketones, aldehydes, and imine hydrogenations using catalyst **1.69**.¹³⁴

1.69

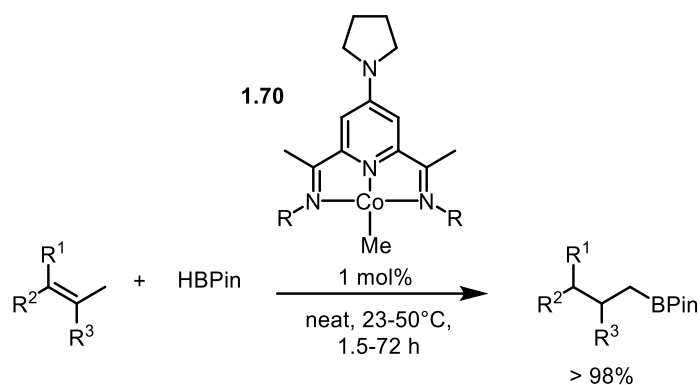
2 mol%

$$\begin{array}{c}
 \text{R}^1-\text{C}(=\text{O})-\text{R}^2 \quad \text{or} \quad \text{R}^3-\text{C}(\text{N}=\text{R}^4)=\text{H} \\
 \xrightarrow[\text{THF, 1 atm H}_2, 25-60^\circ\text{C, 24 h}]{\text{H}[\text{BAR}^{\text{F}}_4](\text{Et}_2\text{O})_2} \\
 \text{R}^1-\text{CH}(\text{OH})-\text{R}^2 \quad \text{or} \quad \text{R}^3-\text{CH}(\text{NH}-\text{R}^4)-\text{H}
 \end{array}$$

Entry	Substrate	Product	<i>t</i> [h]	Yield [%] (NMR) {GC}
1 ^[a]			24	89 (98)
2 ^[b]			48	97 (99)
3 ^[c]			65	{99}
4 ^[a]			24	96 (>99)
5 ^[d]			64	92 (>99)
6 ^[d]			42	84 (89)
7 ^[d]			48	88 (98)

[a] Conditions: Substrate (0.5 mmol), THF (2 mL), H₂ (1 atm), 25°C. [b] *T* = 60°C. [c] *T* = 25°C, H₂ (4 atm). [e] *T* = 60°C, H₂ (4 atm).

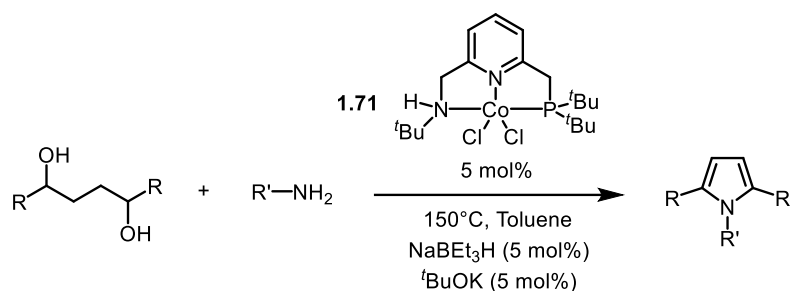
Cobalt pincer complexes are also used in hydroboration and hydrosilylations reactions, with pioneering work done by the group of Chirik. One example of an efficient catalyst for hydroboration of hindered alkenes is a modified NNN pincer cobalt methyl complex **1.70** with a *para* substituted pyrrolidine group, which helps to increase the yields of the reactions. With this cobalt NNN pincer complex, Chirik obtained full conversion for many sterically hindered alkenes, from the simple tetramethylated ethylene (entry 3, Table 1.4, > 98% conversion) to the more complicated alkene (1*S*,5*S*)-2,6,6-trimethylbicyclo[3.1.1]hept-2-ene (entry 5, Table 1.4, >98% conversion).¹³⁵

Table 1.4 Hydroboration of sterically hindered alkenes catalyzed by **1.70**.¹³⁵

Entry	Substrate	Product	T [°C]	Conversion [%] (isolated yield)
1			23 ^[a]	>98 (75)
2			23 ^[a]	>98 (74)
3			50 ^[b]	>98 (55)
4			50 ^[b]	70 (55)
5			50 ^[b]	>98 (67) (dr = 62 :38)
6			23 ^[c]	>98
7			23 ^[a]	88

[a] Conditions : 1 mol% **1.70** for 24 h. [b] 5 mol% **1.70** for 72 h. [c] 1 mol% **1.70** for 72 h,

Another notable example of catalysis using a cobalt pincer complex comes from the group of Milstein with his PNN ligand complex **1.71**. Milstein showed that heterocyclic compounds can be prepared catalytically via some dehydrogenative reactions (See Table 1.5).¹³⁶

Table 1.5. Selected examples of dehydrogenative coupling of diols and amines catalyzed by **1.71**.¹³⁶

Entry	Diol	Amine	<i>t</i> [h]	Yield of pyrrole [%]
1			24	88 ^[a]
2			24	90 ^[a]
3			24	70 ^[a]
4			36	56 ^[b]
5			24	58 ^[b]

Conditions: diol (0.5 mmol), amine (0.5 mmol), toluene (2 mL), and 4Å molecular sieves heated in a closed Schlenk tube for the specified time. [a] Yield of isolated product. [b] Yield determined by GC.

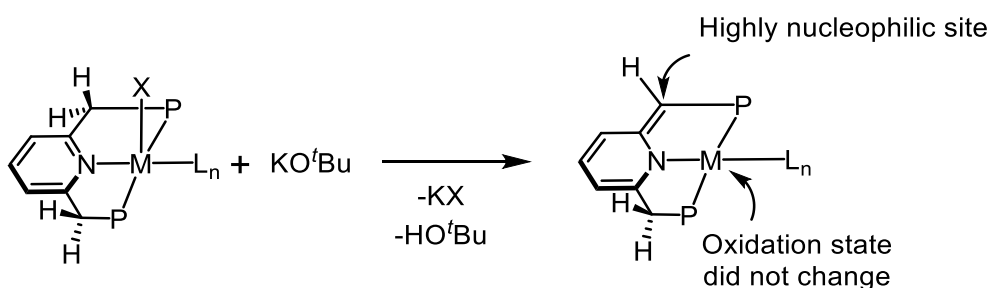
1.3 Ligand Centered Reactivity in Pincer Complexes

Although pincer ligands have been used as stable chelating ligands in catalysis for many decades, they have gained popularity in recent years because of the pioneering work by Milstein where he found that some pincer ligands, notably of the PNP and PNN family, exhibit ligand-centered reactivity in addition to metal-centered reactivity. In multiple cases, this ligand-centered reactivity plays an important role in catalysis and allows for the activation of reactants and small molecules for further reactivity. In most cases this reactivity is desired and is an important step in the catalytic cycle. However, in some cases, reactivity at the arm can be irreversible and lead to the formation of undesirable side products or inactive catalytic species.

This section will introduce the concept of “metal-ligand cooperativity” (MLC), the application of its concept in catalysis, and will show an example of when this reactivity may be undesirable.

1.1.8 Deprotonation of Pyridine-Based Pincer Ligands

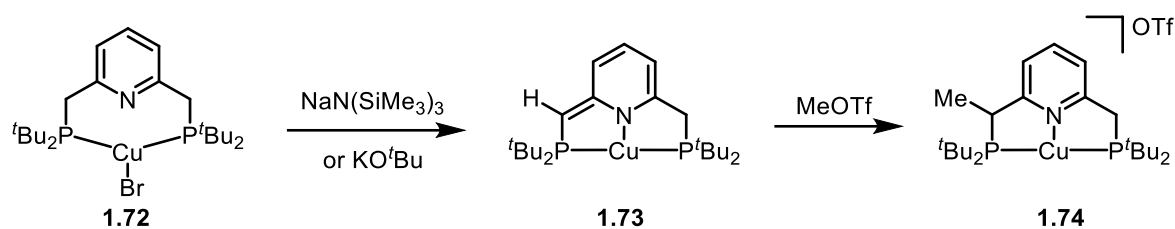
As discussed in the previous sections 1.1.3.3 and 1.1.3.5.2, pyridine does not have the same degree of aromaticity as benzene and should be easier to dearomatize. Because of this, pyridine-based pincer ligands (especially with phosphinomethylene arms) are much more prone to dearomatization than their benzene PCP analogues. This fact, combined with the easily deprotonated methylene moieties of the pyridine-based PNP pincers led to the development of the concept of MLC. For example, in the presence of a strong base such as KO^tBu, a pincer ligand can undergo dearomatization via deprotonation of a methylene arm by the tert-butoxide anion, forming a highly nucleophilic site on the arm. At the same time, the potassium cation abstracts the X group on the metal center, leading to the dearomatized species without any change in oxidation state of the metal (See Scheme 1.25).



Scheme 1.25 General scheme for the formation of a dearomatized lutidine-based PNP pincer ligand.

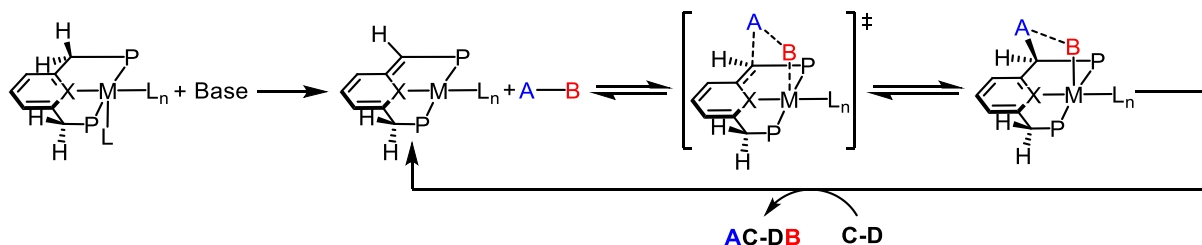
To prove the nucleophilic nature of the deprotonated methylene moiety on the pincer arm, the group of van der Vlugt in 2009 prepared the T-shaped copper complex **1.73**¹³⁷ by reacting chelated complex **1.72** with very strong bases (NaN(SiMe₃)₃, KO^tBu). To test its nucleophilicity, they reacted **1.73** with methyl triflate (MeOTf), a strong methylating agent and a strong electrophile, and they observed the formation of the mono-methylated PNP Cu complex **1.74**

(Scheme 1.26). Moreover, DFT analysis show that the HOMO of the dearomatized complex **1.73** has a strong contribution on the dearomatized $=C(H)-P$ moiety.



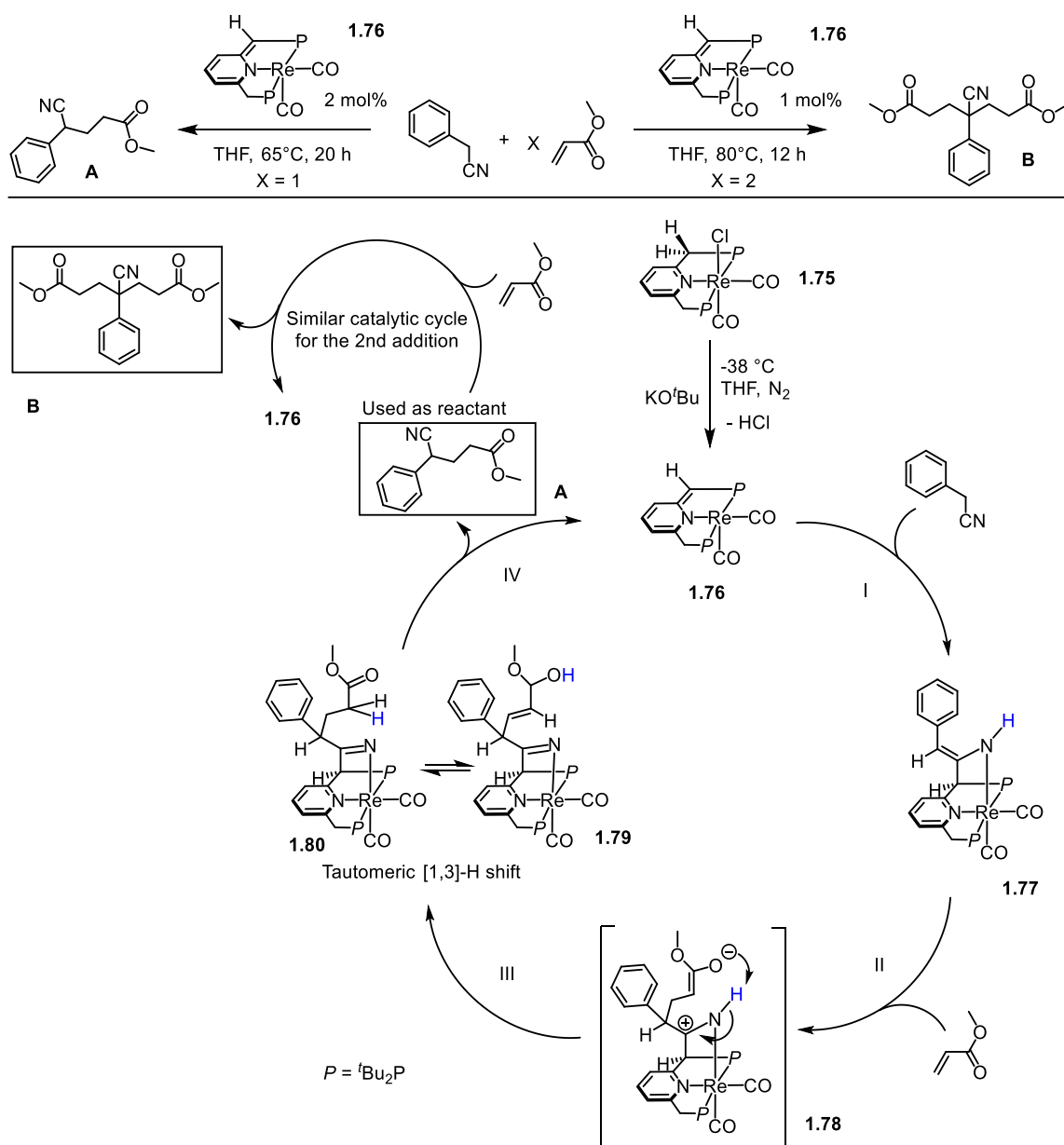
Scheme 1.26 Reaction of **1.73** with a strong electrophile, $MeOTf$, to form **1.74**.¹³⁷

The ability of pyridine PNP and PNN-type pincer ligands to undergo deprotonation/dearomatization has led to discovery of new types of bond activation via MLC, which eventually found application in hydrogenation/dehydrogenation catalysis, in particular. Scheme 1.27 presents a general scheme of the MLC through aromatization-dearomatization in catalysis. For example, the methylene protons of the linker in a pincer ligand are first removed by deprotonation with a base with concomitant abstraction of an X group (Scheme 1.25). The dearomatized species can then be used to activate a molecule A-B by coordination through both the metal center and the ligand, which weakens the A-B bond. In some cases, The A-B bond gets cleaved, and the A moiety stays on the ligand while the B moiety stays on the metal center. In other cases, the A-B bond is still present (see Scheme 1.28). Those complexes can then be further reacted with a second molecule C-D, leading to the expulsion of a final product AC-DB and dearomatization of the pincer ligand to regenerate the original active catalyst.



Scheme 1.27 General scheme of MLC through the aromatization-dearomatization mechanism.

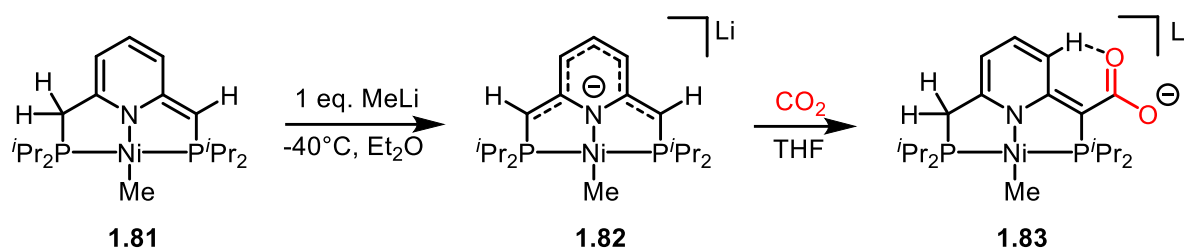
One example of MLC through aromatization-dearomatization is shown in Scheme 1.28 where catalyst **1.76**, formed by deprotonation of the aromatic PNP pincer catalyst **1.75** with KO^tBu, reacts with benzyl cyanide and 1 or 2 equivalents of methyl acrylate to form the mono-addition product **A** or the bis-addition product **B**.¹³⁸ The catalyst **1.76** first binds benzyl cyanide in Step I to form an enamido species **1.77**, then is attacked by methyl acrylate to give an intermediate species **1.78** which then rearranges to a ketimide species **1.79**. Complex **1.79** undergoes a tautomeric [1,3]-hydrogen shift to form **1.80** which eliminates the product **A**. When a second equivalent of methyl acrylate is used, the product **A** is used as the starting reagent and undergoes a similar catalytic cycle to produce **B**.



Scheme 1.28 Possible catalytic cycle for the Michael addition of benzyl cyanide with methyl acrylate catalyzed by **1.76**.¹³⁸

In some instances, MLC can lead to irreversible change on the ligand, which is unproductive in catalysis. In a study by the group of Milstein and co-workers in 2012, the authors found that reacting a doubly deprotonated species **1.82** with CO_2 irreversibly formed species **1.83** where a CO_2 molecule is attached to the pincer arm.¹³⁹ The formation of the doubly deprotonated complex **1.82** is formed by reacting the deprotonated methyl species **1.81** with 1 equivalent of

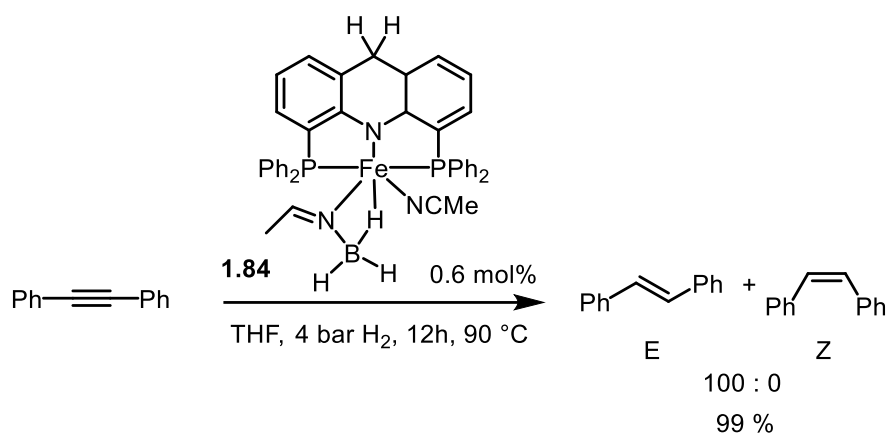
MeLi. In solution, if MeLi is used in excess compared to the starting deprotonated species in the presence of CO₂, this could be an important deactivation pathway for catalysis.



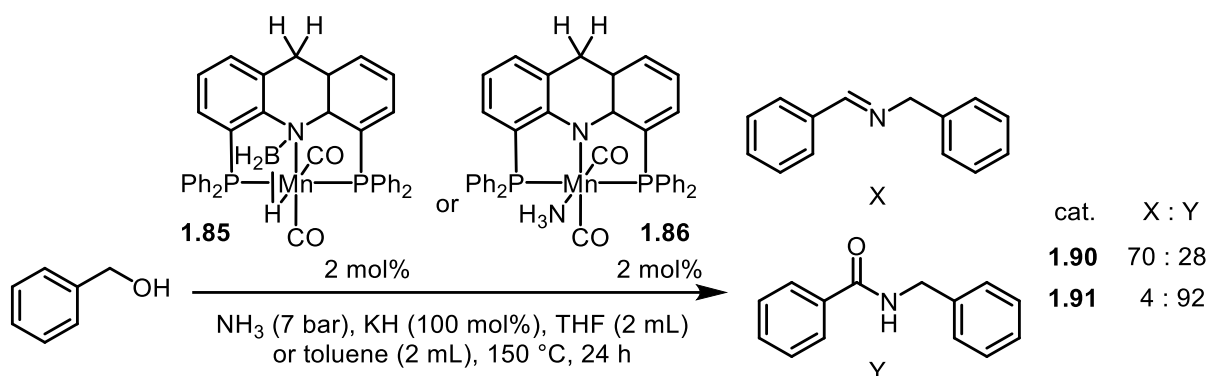
Scheme 1.29 Undesirable reaction of the doubly deprotonated **1.82** with CO₂ to form CO₂ adduct **1.83**.¹³⁹

1.1.9 Reactivity at the *Para*-Position of Pyridine-Based Pincer Ligands

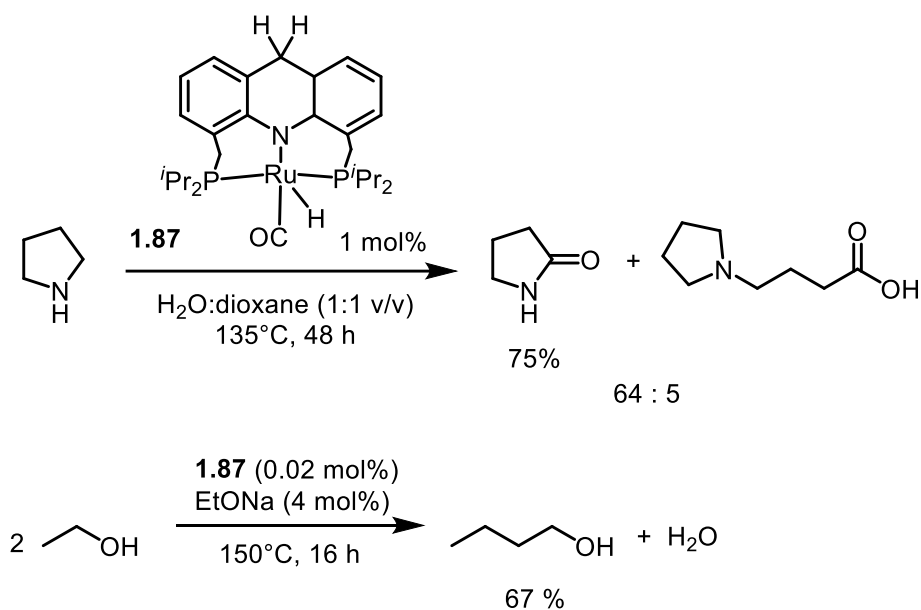
As was previously discussed in Sections 1.1.3.3, 1.1.3.5.2, and 1.1.8, pyridine-based pincer ligands have a propensity to be easily dearomatized. Under strong reductive conditions, the pyridine ring itself can become dearomatized if the pincer's arm has no available sites for deprotonation. This is often a beneficial property because it allows the pincer ligand to change from a neutral to an anionic ligand, which can help stabilizing higher oxidation state species and increase the stability of the complex by a stronger M-N bond. Most of the research done on this type of reactivity are done on acridine-based pincer ligands (a pincer ligand that contains a pyridine ring fused within two benzene rings) and are mostly spearheaded by the group of Milstein,¹⁴⁰⁻¹⁴² but some contributions by the groups of Yip,¹⁴³ and Hofmann⁹¹ are also known. These dearomatization of the pyridine backbone at the *para*-position have been shown to be important in multiple catalytic reactions such as in hydrogenation reactions (Scheme 1.30),¹²⁸ in acceptorless dehydrogenative couplings (Scheme 1.31),^{144, 145} in the amination of alcohols,⁹¹ in the formation of lactams (Scheme 1.32 (top)),¹⁴⁶ and in the formation of biofuels from ethanol (Scheme 1.32 (bottom)).¹⁴⁷



Scheme 1.30 Selective semi-hydrogenation of diphenylacetylene catalyzed by **1.84**.¹²⁶

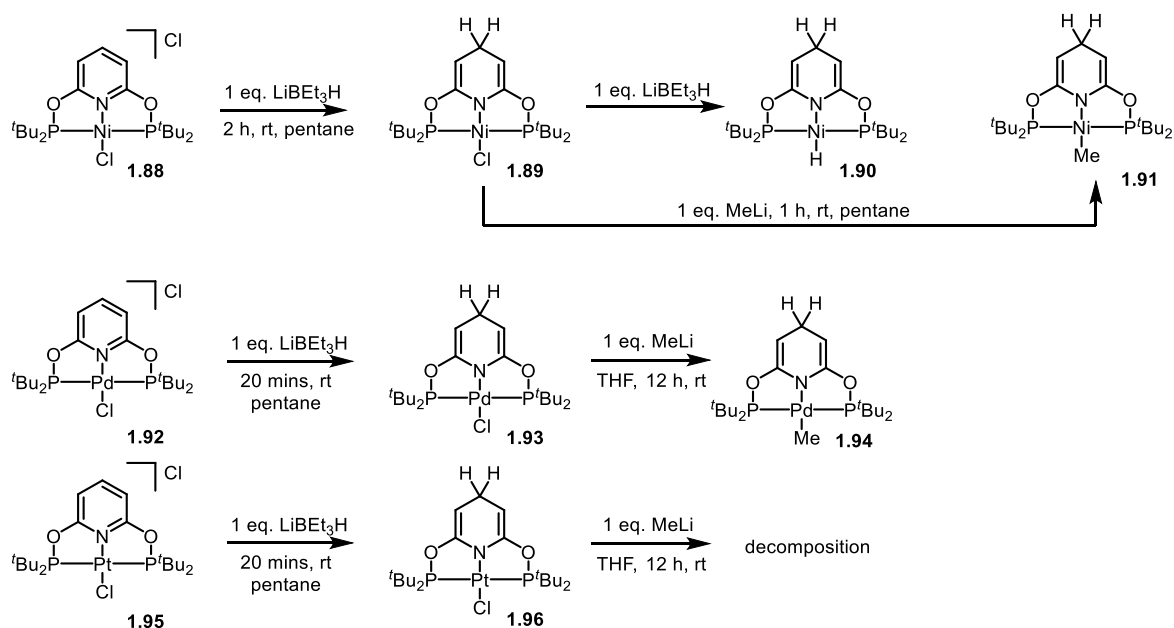


Scheme 1.31 Acceptorless dehydrogenative coupling of ammonia and benzyl alcohol catalyzed by **1.85-1.86**.¹³⁶



Scheme 1.32 Formation of lactams from water and amines, and formation of biofuels from ethanol catalyzed by **1.87**.^{139, 140}

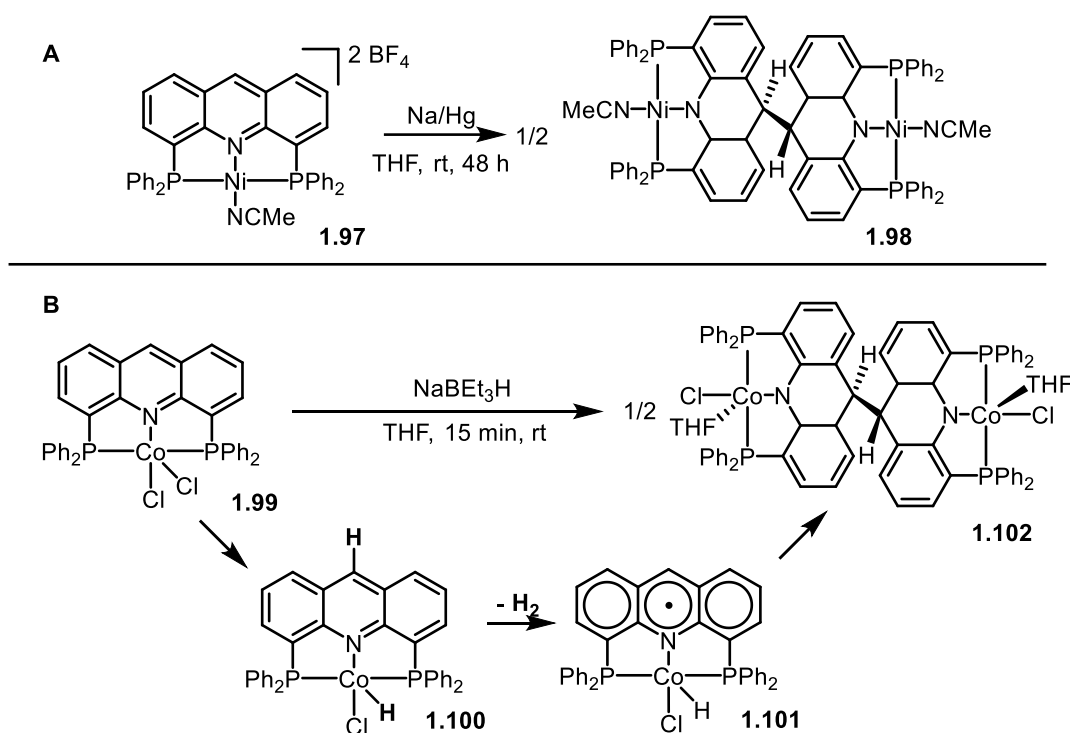
The group of Jones in 2011 showed the dearomatization of pyridine-based PONOP pincer complex was possible by reacting the halide precursors with LiEt_3H (super hydride), a strong reductant and hydride source.⁵³ Scheme 1.33 shows the reaction of different metal PONOP complexes. For example, the Ni^{II} chloride PONOP complex **1.88** was reacted with 1 equivalent of LiEt_3H to furnish the dearomatized species at the *para*-position, complex **1.89**. Complex **1.89** was then further reacted with 1 equivalent of LiEt_3H , which furnished the hydride species **1.90**. Complex **1.89** can also be further reacted with MeLi to form a Ni^{II} -Me species **1.91**. Similar reaction with the palladium complex **1.92** and platinum complex **1.95** gives the dearomatized species **1.93** and **1.96**, respectively. Reaction of the palladium complex **1.93** with MeLi gives the expected methyl species **1.94**, but reaction of the platinum complex **1.96** only furnishes decomposition products upon reactivity with MeLi .⁵³



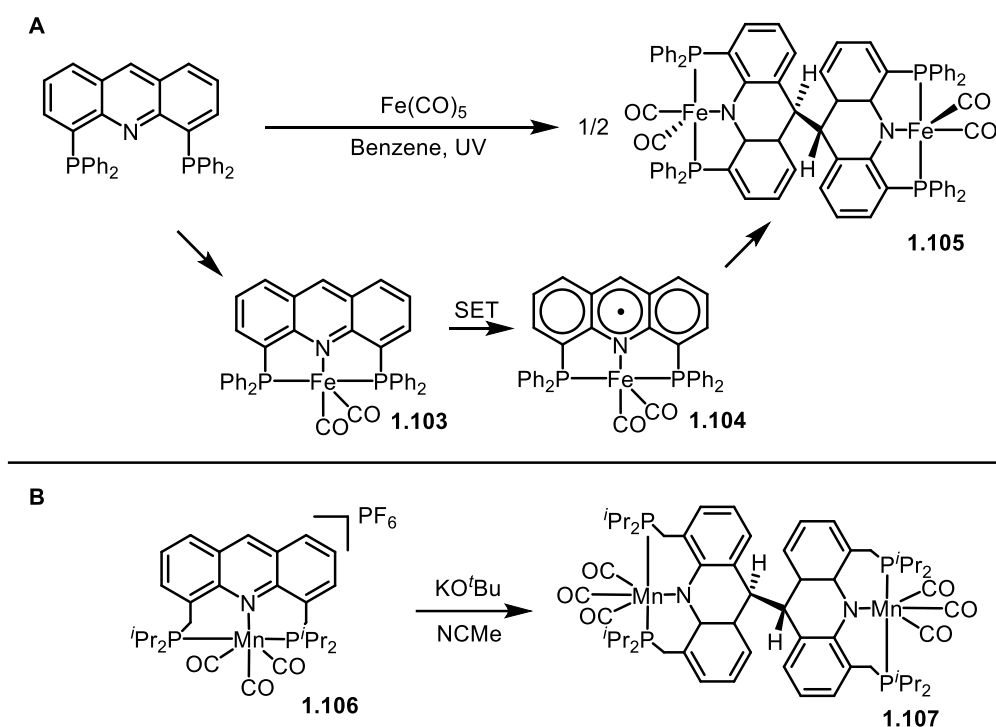
Scheme 1.33 Dearomatization at the *para* position of Ni, Pd, and Pt complexes **1.88**, **1.92**, and **1.95** as well as further reactivities.⁵³

Finally, a very recent article by the group of Milstein studied different metal complexes of acridine pincer ligand and their behavior. Depending on the metal center, different conditions are used to form a radical on the ligand at the *para*-position. In the case of nickel, a strong

reductant (Na/Hg, sodium-mercury amalgam) is needed to dearomatize the ligand of complex **1.97** to form the dimer **1.98** (Scheme 1.34, A). For the cobalt species **1.99**, NaBEt₃H is used which they propose acts as a chloride abstracting agent and hydride source to form the Co(H)(Cl) intermediate **1.100**. Then, homolytic cleavage of the hydride and the hydrogen on the acridine ligand forms a radical species **1.101** and loss of H₂. This radical intermediate then reacts with another of the same radical species to form the dimer **1.102** (Scheme 1.34, B). This also presents a relatively rare example of redox-noninnocence of the pincer ligand heterocyclic framework (*vide infra*).¹⁴²



Scheme 1.34 Formation of the cobalt and nickel dimers of acridine-based PNP complexes **1.97** and **1.99**.¹⁴²



Scheme 1.35 Formation of the iron and manganese dimers of acridine-based PNP complexes **1.103** and **1.106**.¹⁴²

In contrast, the iron dimer **1.107** was obtained through a different mechanism. The authors reacted $\text{Fe}(\text{CO})_5$ and the acridine ligand under UV irradiation and propose that a $\text{Fe}(0)$ species **1.103** is formed, which then would form the radical species **1.104** via electron transfer from the $\text{Fe}(0)$ center to the acridine ligand and form the dimer **1.105** in the presence of another radical species **1.104** (Scheme 1.35, A). Finally, they studied the reactivity of a manganese PNP acridine pincer complex **1.106** and found that the use of KO^tBu forms the dimer complex **1.107** (Scheme 1.35, B).¹⁴²

1.1.10 Redox Active Pincer Ligands

Classical reduction and oxidation (redox) chemistry that features transition metal coordination complexes usually involves the transition metal center only, and the ligand acts as a spectator without direct involvement in the reaction (also termed “innocent”). However, a growing number of systems have been found or designed to involve the ligand itself in the redox processes, hence the term redox non-innocent ligand has been designed for those systems. Figure 1.12

presents some examples of usual classes of redox non-innocent ligands include catecholates (complex **1.108**),¹⁴⁸ dithiolates (complex **1.109**),¹⁴⁹ and tetra-amido macrocycles (complex **1.110**)¹⁵⁰ to name a few.

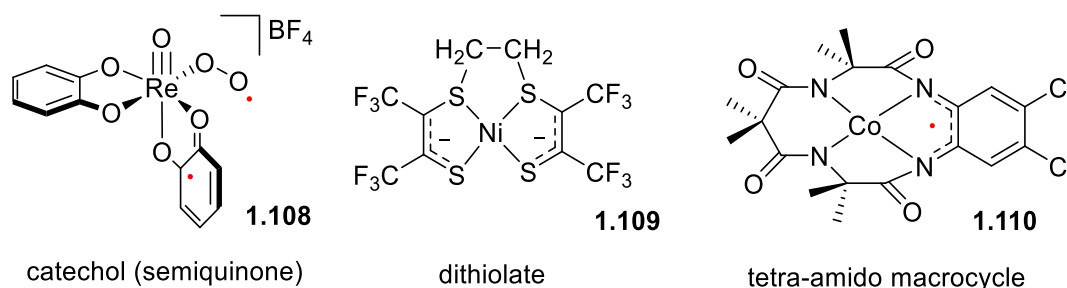
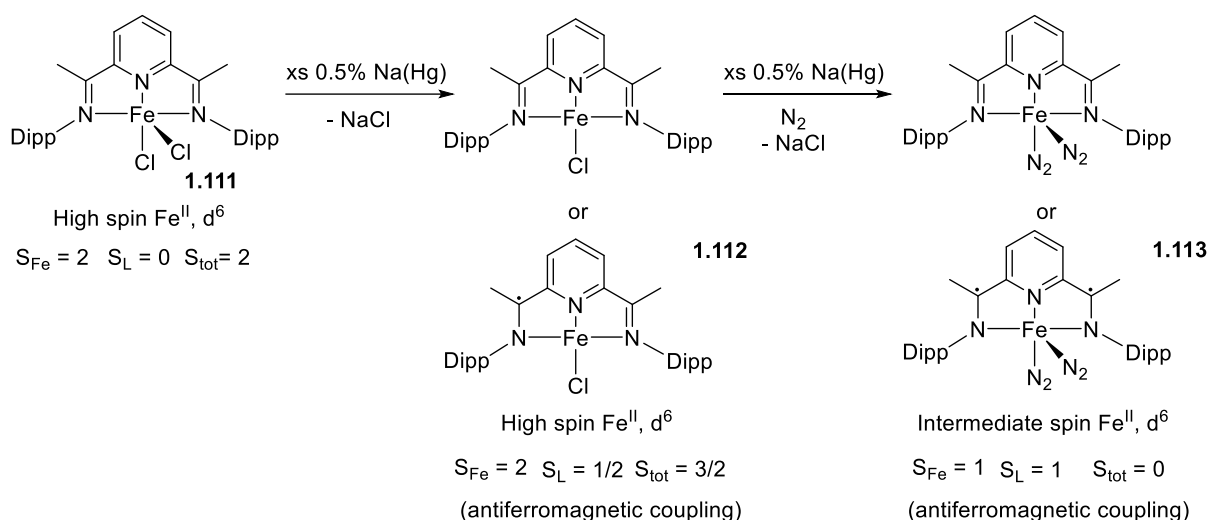


Figure 1.12 Examples of redox active ligands in the literature.^{148, 149,150}

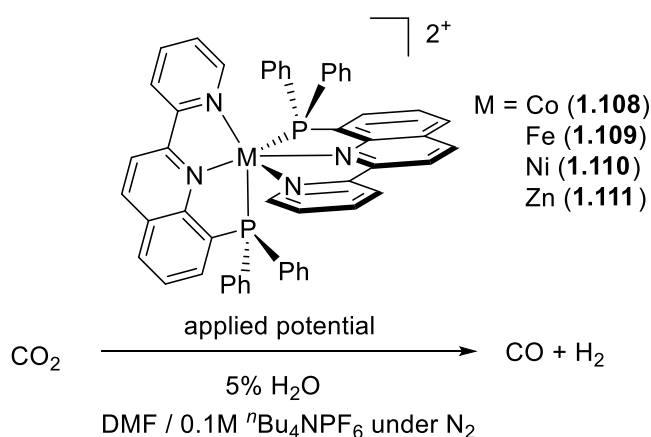
Compared to those examples, pincer ligands have rarely been used as redox non-innocent ligands, especially when the pyridine-based framework is used. Below I will introduce some of the few exceptional examples of pyridine-based ligand that are used as redox non-innocent ligands in catalysis.

One of the exceptional examples of a pyridine diimine based NNN redox non-innocent pincer ligand in catalysis comes from the group of Chirik. Through high quality crystal structures and DFT analysis, they proposed that the ligand, rather than the metal center, is reduced in complex **1.111** when a strong reductant was used. When an excess of reducing agent is used, complex **1.112** is formed where a radical is on the ligand. Addition of more reducing agent under an N₂ atmosphere forms the diradical bis(dinitrogen) complex **1.113**. Although the ligand is reduced, because of antiferromagnetic coupling of iron (with an intermediate spin state with $S_{\text{Fe}} = 1$ and oxidation state of +2) and the ligand diradical triplet spin state (both the triplet ($S_{\text{L}} = 1$) and singlet ($S_{\text{L}} = 0$) of the ligand are nearly isoenergetic), complex **1.113** is diamagnetic with a total spin state of $S = 0$.¹⁵¹ They then studied the complex in catalysis such as the $[2\pi+2\pi]$ cycloadditions of α,ω -dienes¹⁵² or in hydrogen-assisted enyne cyclization¹⁵³ and they proposed that a similar paramagnetic complex ligand-based radical species is involved in the catalysis.



Scheme 1.36 Formation of the dinitrogen diamagnetic complex **1.112** through consecutive 1-electron reductions of **1.110** and **1.111**.¹⁵¹

Other examples of pyridine-containing redox-active pincer ligand comes from the work of the group of Jurss, where NNP pincer complexes (Co, Fe, Zn and Ni) are active in the electrocatalytic transformation of CO_2 to CO and H_2 in the presence of water.¹⁵⁴ The complexes in their inactive states are dimers of NNP pincer ligands, but after a few redox cycles, one of the ligands dissociates to possibly form a monomeric species which was suggested as the active species in the reactions (See Scheme 1.37). The author suggests that the ligand itself gets reduced by one electron and that the reduced ligand is part of the active catalytic system.¹⁵⁴



Scheme 1.37 Electrochemical transformation of CO_2 to CO and H_2 catalyzed by NNP pincer complexes **1.108**-**1.111**.¹⁵⁴

Thesis Outline

The development of organometallic chemistry and catalysis by PNP pincer complexes, especially by late transition metals, has been historically dominated by the concept of Metal-Ligand Cooperation (MLC), inspired by the studies of pincer complexes with precious metals such as Ru, Rh, Pt in small molecule activation and hydrogenation/dehydrogenation catalysis. However, a recent computational and experimental study has brought to light that the accepted MLC mechanism (through aromatization-dearomatization) for such widely studied reactions as the ruthenium PNN catalyzed alcohol (de)hydrogenation might not necessarily involve the dearomatization of active catalytic species under the reaction conditions, while the pincer ligand framework is still required to support an active catalyst.^{155, 156} Comparatively, the mechanisms of the reactions catalyzed by first-row transition metals complexes are often more difficult to explore due to the instability of many reaction intermediates. Therefore, it is important to explore new pincer ligands that can retain their tridentate chelating framework under reaction conditions, while the ability to undergo classical MLC pathways are blocked. Such ligands and their complexes could potentially show new types of metal-centered and ligand centered reactivities, increase the stability of reactive first-row transition metal intermediates and expand the library of the currently known pincer ligands.

In **Chapter 2**, I will introduce a new family of pyridine-based PNP pincer ligands that are based on the classic PNP framework and study how the modified ligand influences the behavior of nickel complexes and describe examples of mostly metal-based reactivity. The newly developed PNP pincer ligands remains unreactive under reductive conditions and allows the stabilization of unusual oxidation state of the metal center.

In **Chapter 3**, I will show that by blocking classical modes of MLC, it is possible to induce new types of ligand-based reactivity on the PNP pincer framework. I will explain how changes

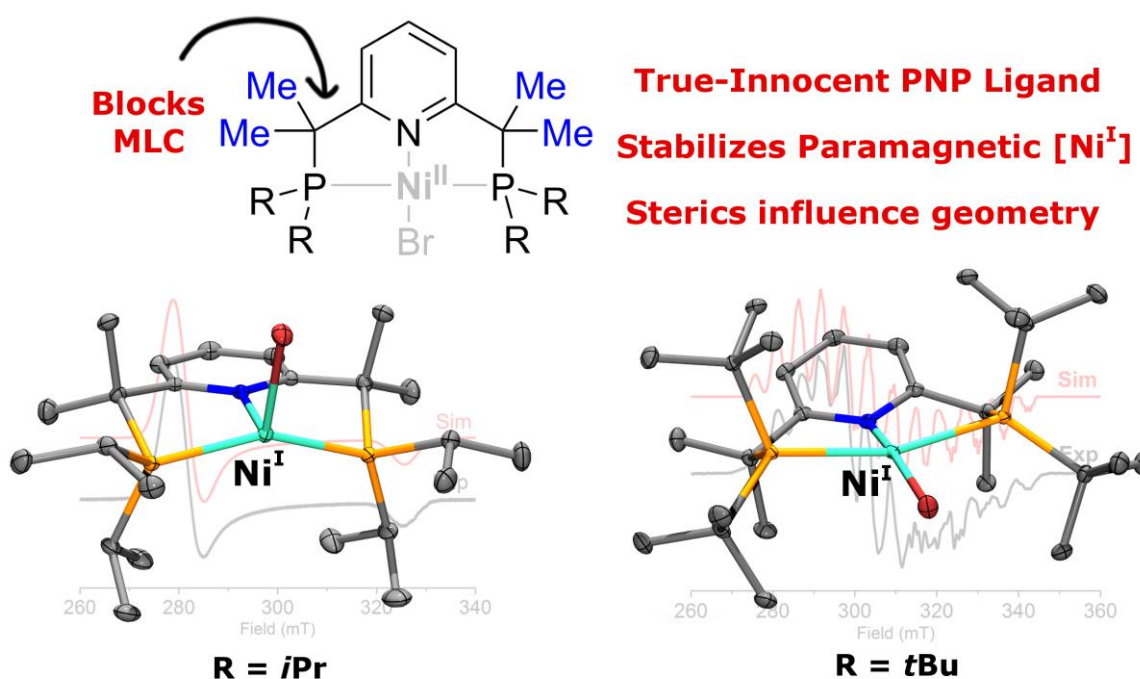
in the electronics and steric properties of the complex can lead to switching from metal-based reactivity to ligand-based reactivity.

Declaration of Contribution from Co-authors

The following chapter contains contributions from Dr. Eugene Khaskin, Dr. Robert R. Fayzullin and Pr. Dr. Julia R. Khusnutdinova as described below. Pr. Dr. Julia R. Khusnutdinova guided the project and helped with analysis of experimental and computational data. Dr. Eugene Khaskin initially developed the synthesis of the ligands and prepared the first complexes with the family of ligands and provided advice and guidance regarding ligand synthesis. Dr. Robert R. Fayzullin finalized every X-ray structural measurement to publication level. The author performed synthesis and characterization of all complexes described within this chapter, performed DFT and ORCA calculations, and analyzed and simulated all reported spectra.

2 Chapter 2:

Stabilization of Reactive Nickel(I) Species



The content described in this chapter is partially reported in the following publication. Reprinted and adapted with permission from: Lapointe, S.; Khaskin E.; Fayzullin R. R.; Khusnutdinova J. R. *Organometallics* **2019**, 38 (7), 1581-1594. Copyright **2019** American Chemical Society

2.1 Development of New Me₄PNP Pincer Ligands and Their Nickel(II) and Nickel(I) Complexes

2.1.1 Design of New, Bulky, and Electron-Rich Me₄PNP Ligands

As discussed previously in Section 1.2, pincer complexes often are susceptible to reactivity at the ligand, which can cause problems if the aim is to focus on metal-centered reactivity. Some of the most often reactive sites in pincer ligands are the methylene units on the pincer's arms, such as those found in classical pyridine-based PNP ligands, which are also some of the most well-known ligands to undergo MLC through dearomatization-aromatization mechanism. Those can be easily deprotonated and cause dearomatization of the pincer framework, enabling reactivity at the ligand itself, which can be undesirable and lead to irreversible decomposition or modification of the pincer ligand framework. The dimerization of a pincer complex is another factor that can cause a complex to be inactive towards metal-centered reactivity, and even prevent catalysis. The most chemically simple answer to both problems is a relatively straightforward one: a simple substitution of the reactive hydrogens on the pincer's arm with more inert and bulkier methyl groups (Figure 2.1). Such methylation strategy will essentially block possible deprotonation of the ligand arms and help increase steric bulk around the metal center.

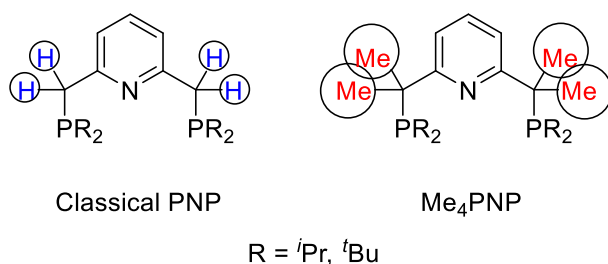
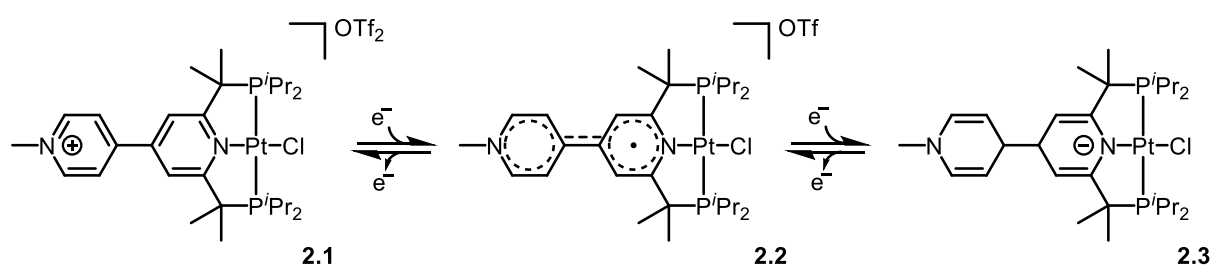


Figure 2.1 Classical PNP and Me₄PNP ligand systems.

As discussed previously in Section 1.1.8, the group of van der Vlugt in 2009 has shown that partial methylation of the pincer framework of the dearomatized complex **1.73** is possible by

using the strong methylating agent MeOTf to form the aromatized PNP complex **1.74**, although no further reactivities or attempts to fully methylate the pincer ligand was reported (see Scheme 1.26 in Section 1.1.8).¹³⁷

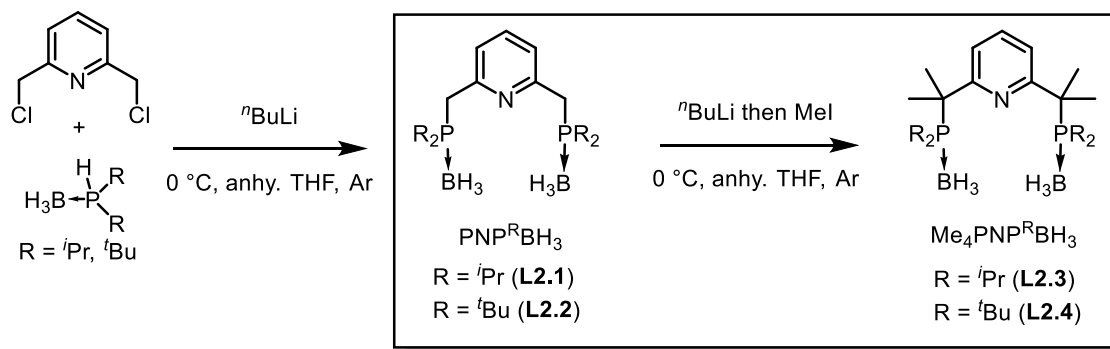
Although the methylation of the pincer arm has a single precedent in 2014 by the group of Nishibayashi using an analogous substituted PNP pincer framework,¹⁵⁷ their studies show that the complex still undergoes ligand-centered reduction even in the presence of the methyl group on the arms and without change in the oxidation state of the platinum metal center due to the presence of a redox-active methylpyridinium substituent. The presence of a redox-active *para*-substituent does not allow for direct comparison of the reactivity with the classical PNP pincer ligands.



Scheme 2.1 Ligand-based reduction of the tetramethylated complex **2.1** under electrochemical conditions.¹⁵⁷

The preparation of the new family of bulky tetramethylated ligands (**L2.3** and **L2.4**) is relatively straightforward and can be done in one step from the non-methylated ligand (**L2.1** and **L2.2**). The non-methylated ligand is prepared by a new synthetic pathway that takes advantage of the protecting BH₃ moiety to prevent decomposition of the ligand. The protected phosphines HPR₂-BH₃ are prepared in a single step from the commercially available chlorophosphine using LiAlH₄ or NaBH₄ depending on the nature of the starting chlorophosphine.^{158,159} Then, reacting those protected phosphine with the commercially available 2,6-bis(chloromethyl)pyridine in the presence of the strong base ^{*n*}BuLi readily affords the protected, non-methylated phosphines **L2.1-2.2**. The ligands **L2.3-2.4** are then prepared by the simple subsequent reaction

of 1 equivalent of $n\text{BuLi}$ and 1 equivalent of methyl iodide (MeI) for 6 consecutive additions of both reagents. Simple quenching and extraction give pure white crystalline powders of **L2.3-2.4** in near quantitative yields. Simple deprotection using pyrrolidine affords the deprotected ligand that can further be reacted with a metal precursor to give the desired metal complex.



Scheme 2.2 Preparation of a new family of bulky, tetramethylated PNP ligand (**L2.3-L2.4**).

With my experience and interest in nickel chemistry, I sought to investigate how this new family of methylated PNP pincer ligands could help stabilize reactive nickel species including nickel in unusual oxidation states of +1, +3 and +4 (compared to the more stable 0 and +2 oxidation states). Stabilizing those unusual oxidation state species and possible other reactive species through the modification of the classical pyridine-based PNP pincer ligand (and by association, the modification of analogous systems) could open a completely new set of reactivities in well-known and well-studied systems (Figure 2.1).

In the course of this work, I have found that although, not unexpectedly, methylated Me_4PNP pincer ligands could not stabilize high oxidation states of Ni, I was able to obtain unusually stable, relatively rare paramagnetic Ni^{I} pincer complexes. Therefore, in the following section, I will mostly focus on properties, reactivity and importance of Ni^{I} complexes in organometallic chemistry.

2.1.2 Nickel(I) Pincer Complexes in the Literature

There is currently growing evidence that paramagnetic transition complexes play more important role in catalysis and small molecule activation than previously expected, in particular, in the area of C-C bond coupling catalyzed by first row transition metals.¹⁶⁰⁻¹⁶⁴ In particular, organometallic chemistry of Ni has been previously dominated by studying these complexes in the most stable +2 and 0 oxidation states, while much less research has been done on paramagnetic nickel complexes in +1 and +3 oxidation states or highly reactive Ni(+4) species. However, with the advance of modern equipment and techniques (ultrafast spectroscopy, modern EPR, etc.), analyzing paramagnetic and short-lived species has made the routine analysis of nickel in those unusual oxidations a more common occurrence. Nowadays, research in nickel complexes with +1 oxidation state has grown and such complexes have been shown to play important role in catalysis and small molecule activation.¹⁶⁵⁻¹⁶⁹ Of particular interest is the occurrence of Ni^I species in biological systems and their importance in key biological pathways, as will be discussed later in Section 2.1.5.

Along with the advances in Ni^I chemistry came the development of pincer complexes of Ni^I. As pioneers of this field, the groups of Gade,¹⁷⁰⁻¹⁷³ Lee,¹⁷⁴⁻¹⁷⁷ Mindiola,¹⁷⁸ and Walter,¹⁷⁹ are the few groups who successfully isolated and characterized Ni^I complexes with pincer ligands (complexes **2.4-2.11**, see Figure 2.2).

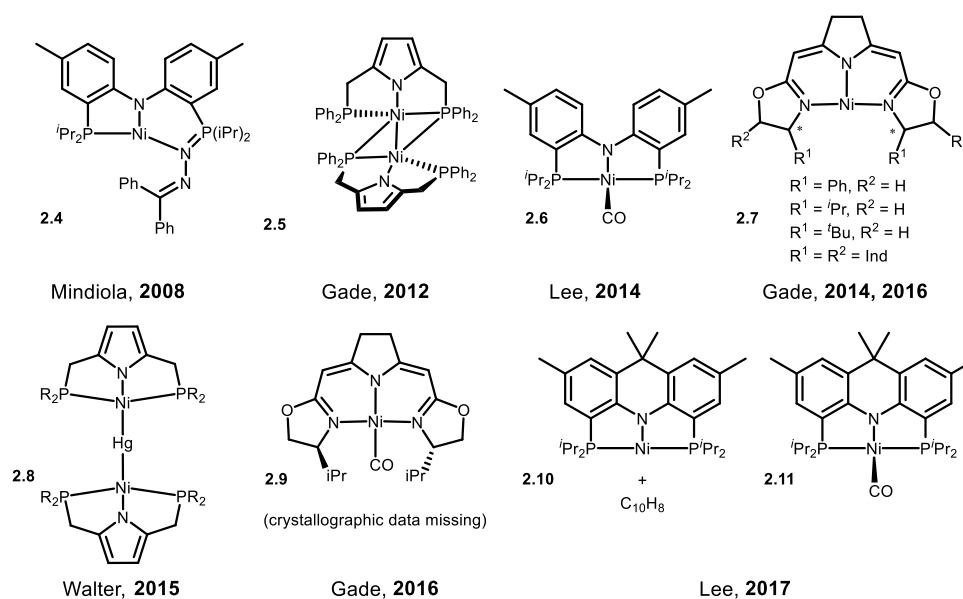
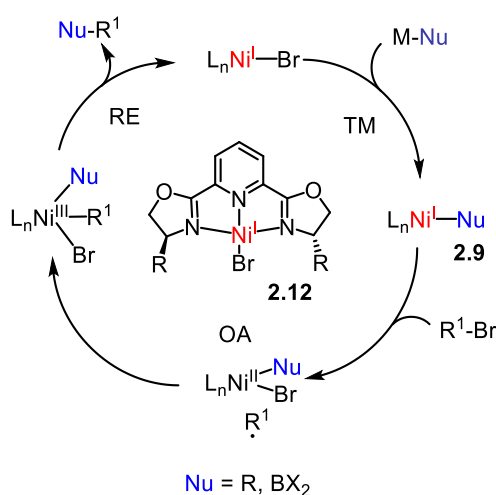


Figure 2.2 All structurally characterized Ni^I pincer and pincer-like complexes to date.^{170, 173, 176-181}

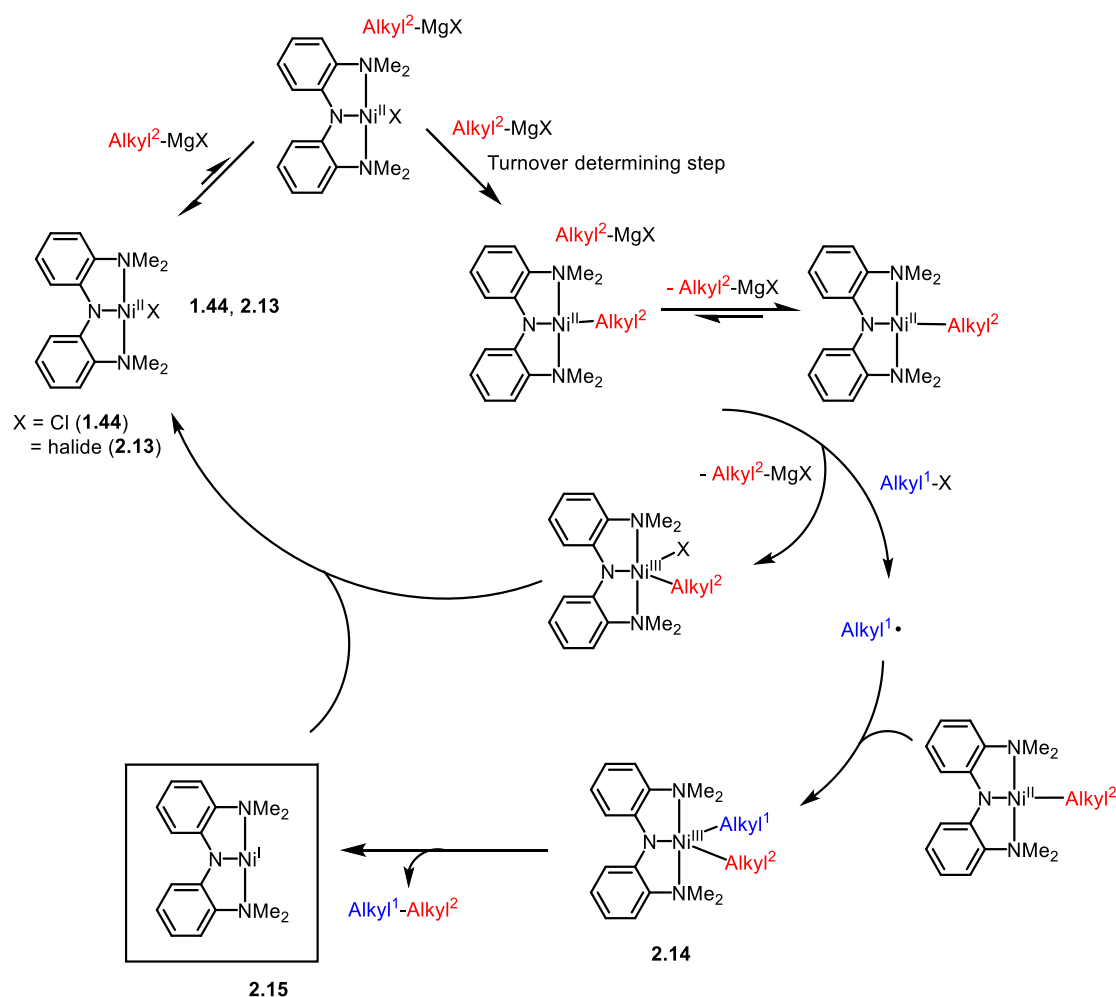
2.1.3 Application of Nickel(I) Pincer Complexes in Catalysis

Pincer complexes of Ni^I have been proposed to play an important role in catalysis, especially in C-C coupling reactions. The group of Fu¹⁸² have proposed that a Ni^I pincer (complex **2.12**) is involved in the reaction mechanism of C-B and C-C coupling of alkyl electrophiles (primary, secondary or tertiary) with bis(pinacolato)diboron or hexylzinc(II) iodide (See Scheme 2.3), although the reactive Ni^I or Ni^{III} intermediates have not been isolated.¹⁸²



Scheme 2.3 Proposed catalytic cycle for C-C and C-B coupling involving a Ni^I pincer intermediate **2.12**.¹⁸²

In 2013 the group of Hu reported the alkyl-alkyl Kumada coupling reaction catalyzed by the Ni^{II} NNN pincer complex **2.13**. In the proposed catalytic cycle, a short-lived Ni^{I} T-shaped species **2.15** is proposed to be involved at the last step, although this species is not isolated or characterized. This Ni^{I} intermediate **2.15** reacts with a Ni^{III} intermediate **2.14** to regenerate the Ni^{II} starting catalyst **2.13**.¹⁶²



Scheme 2.4 Proposed catalytic cycle of the alkyl-alkyl Kumada coupling catalyzed by either **1.44** or **2.10**.¹⁶²

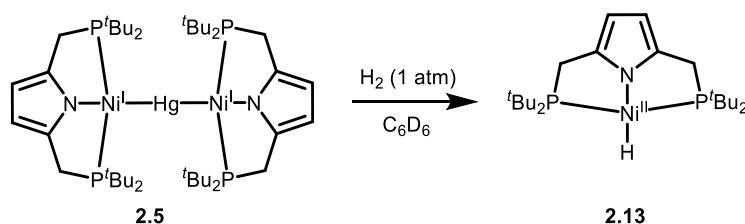
2.1.4 Application of Nickel(I) Pincer Complexes in Small Molecule Activation

The involvement of Ni^{I} complexes in catalysis sparked the interest towards studying its reactivity in small molecule activation, which may help to shed light on the mechanisms of elementary steps of the catalytic reactions. Highly reducing ability and metalloradical Ni^{I} species

make them interesting for studying activation of CO₂, H₂ and especially O₂, which has a biradical nature. Several selected examples will be described below, while a comprehensive review covers many other examples of small molecule activation at Ni^I centers.¹⁸³

2.1.4.1 Activation of H₂ with Nickel(I) Pincer Complexes

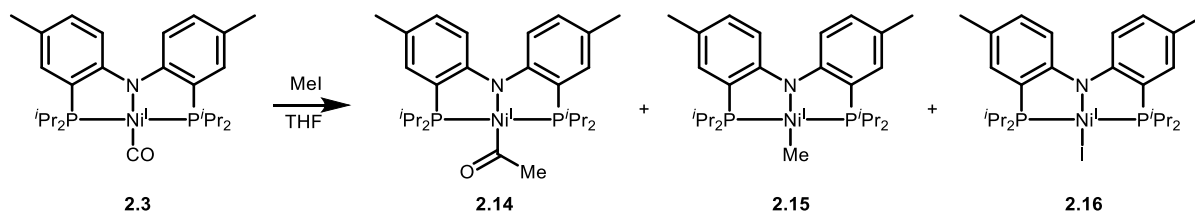
Activation of H₂ is fundamentally important for studying application of transition metal complexes as hydrogenation catalysts. Generation of Ni^{II} hydride species via homolytic activation of H₂ is an interesting strategy to potentially enable catalysis via Ni^I/Ni^{II} cycle. One example of a pincer complex that was shown to activate H₂ is the mercury dimer complex **1.69** containing a pyrazole backbone. In the presence of H₂, complex **1.69** forms a Ni^{II} hydride species (**1.76**) through homolytic cleavage of H₂ (see Scheme 2.5).¹⁷⁹



Scheme 2.5 Homolytic cleavage of H₂ by a Ni^I dimer complex **2.5** to form the Ni^{II} hydride complex **2.13**.¹⁷⁹

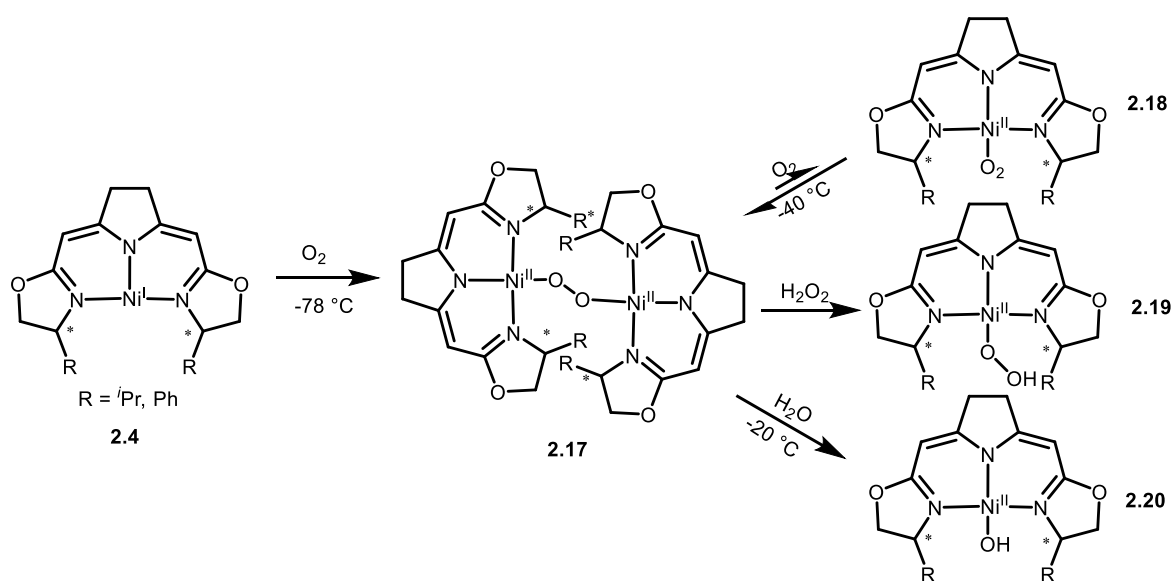
2.1.4.2 Activation of CO with Nickel(I) Pincer Complexes

In 2015, the group of Lee studied the reactivity of the Ni^I-CO complex **2.3** in the presence of MeI and saw that it formed multiple activation products (Scheme 2.6).¹⁸⁴ One of those was the C-C coupling product between the bound CO and the methyl group (complex **2.14**), proposed to go through a radical mechanism. Other products include the formation of a Ni^{II} methyl (complex **2.15**) and a Ni^{II} iodide adduct (complex **2.16**).



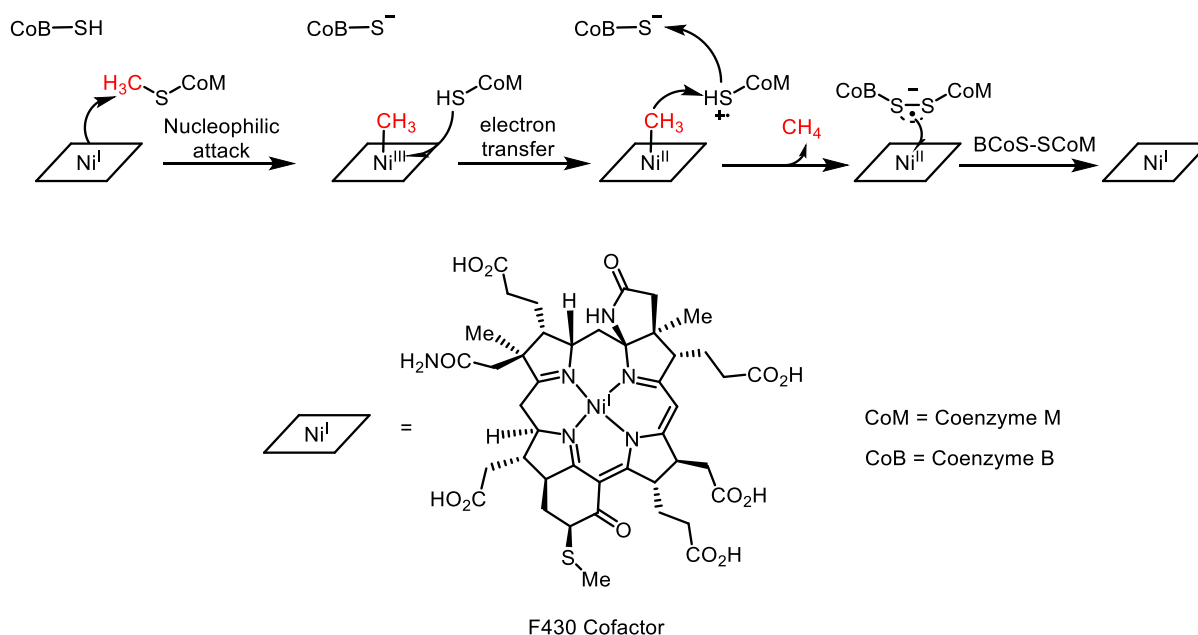
Scheme 2.6 C-C coupling between a Ni^I CO adduct **1.67** and MeI to form **1.77-1.79**.¹⁸⁴**2.1.4.3 Activation of O₂ with Nickel(I) Pincer Complexes**

Considering usually highly reducing nature and radical nature of Ni^I species, facile activation of O₂ by Ni^I could be expected. O₂ can be activated with an NNN pincer Ni^I species at low temperature. The group of Gade in 2015 reported the isolation and characterization of an oxo dimer (**2.17**) and a superoxo monomeric species (**2.18**) by EPR from the reaction of the NNN pincer complex **2.4** with O₂.¹⁷² The oxo dimer can undergo further reactivity with H₂O₂ to form the hydroperoxo species **2.19**, and with H₂O to form the hydroxo species **2.20** (See Scheme 2.7).¹⁷² All those reactions are done at low temperature as the complexes show decomposition at room temperature.

**Scheme 2.7** Reactivity of a Ni^I NNN pincer complex with O₂ and further reactivity of the dimeric species **1.80**.¹⁷²**2.1.5 Nickel(I) Species as Key Intermediates in Biological Systems**

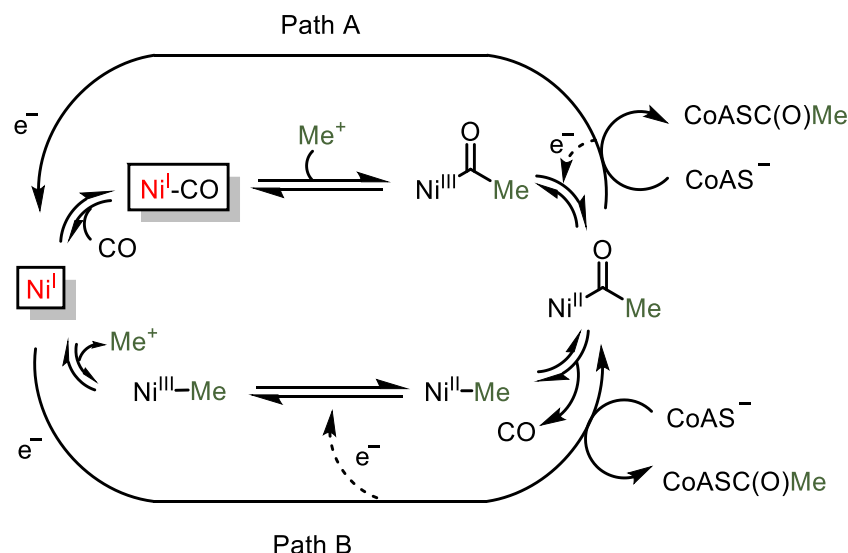
Because of their reactivity with small molecules, it is no surprise then that metalloradical centers are present in biological systems. For example, the nickel hydrocorphinate F₄₃₀, which is the active site of the methyl-coenzyme reductase (MCR), has a Ni^I at its core which catalyzes

the last step of methane synthesis by activating the methyl group of a methyl-coenzyme M and being oxidized to a Ni^{III} center (Scheme 2.8).¹⁸⁵



Scheme 2.8 Proposed mechanism of methyl-coenzyme M reductase involving Ni^{I} and Ni^{III} centers.¹⁸⁵

A second example of the possible involvement of a Ni^{I} center in enzymatic systems is in the acetyl-coenzyme A synthase (Scheme 2.9). One of the possible mechanism involves a $[\text{NiFe}]$ core where one of the step is the reduction of the Ni^{II} center to Ni^{I} , with either the coordination of CO followed by a transfer of CH_3^+ , or the initial formation of a $\text{Ni}^{\text{III}}\text{-CH}_3$ species with a subsequent insertion of CO in the Ni-C bond. The exact mechanism is still not known but there is evidence pointing that both mechanisms are present randomly, and they both form the same product.^{183, 186}



Scheme 2.9 Proposed paramagnetic mechanisms for acetyl-Coenzyme A Synthase (ACS) catalyzed acetyl-CoA formation with either initial binding of CO (Path A) or initial binding of Me^+ (Path B).¹⁶⁹

2.1.6 Geometry and Electronics of Nickel(I) Pincer Complexes

Two main geometries are commonly featured by monomeric pincer complexes of Ni^{I} : T-shaped and distorted seesaw geometries, with different degree of variation from the ideal geometries. For example, Ni^{I} complex **2.6** has a geometrical index τ_4' of 0.36, which is in between a seesaw geometry ($\tau_4' \sim 0.24$)¹⁸⁷ and an ideal tetrahedral geometry ($\tau_4' = 1.00$),¹⁸⁷ but closer to the former, while complex **2.11** is even more distorted with a τ_4' of 0.49.

Although complex **2.9** in Figure 2.2 shown previously appears to be drawn as a square planar structure, no crystallographic data for this compound was reported. However, the dimeric Ni^{I} species bridged with a mercury atom (complex **2.8**) has a distorted square planar geometry, with an average τ_4' value of 0.13 for both nickel centers (ideal square planar $\tau_4' = 0.00$).¹⁷⁹

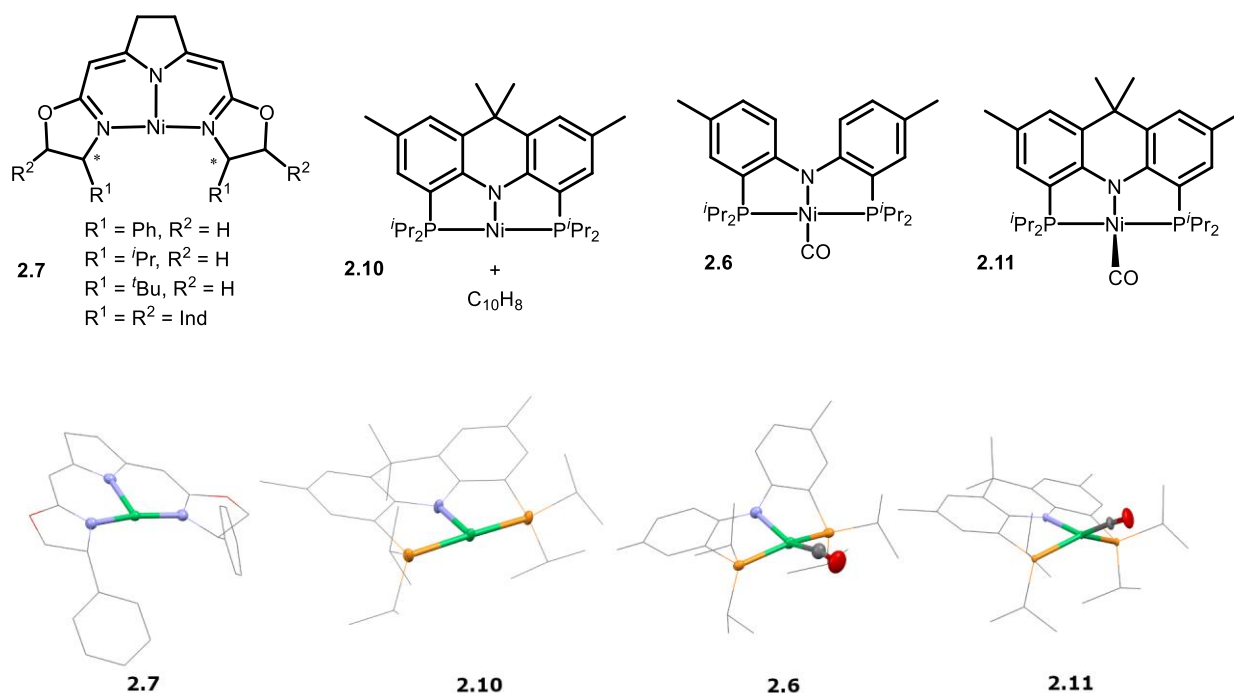


Figure 2.3 Selected examples of Ni^I pincer complexes **2.6-2.7** and **2.10-2.11**, and their crystal structures to emphasize their geometry around the metal center.^{173, 176, 177}

This varying degree of distortion in the geometries of the Ni^I pincer complexes signifies that most of those complexes have slightly different frontier orbital arrangement, although their SOMO are usually $d_{x^2-y^2}$ in nature (Figure 2.4).

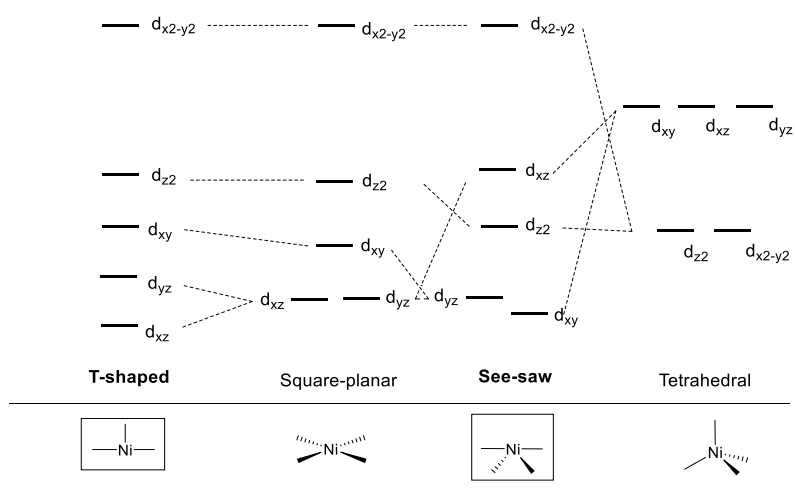
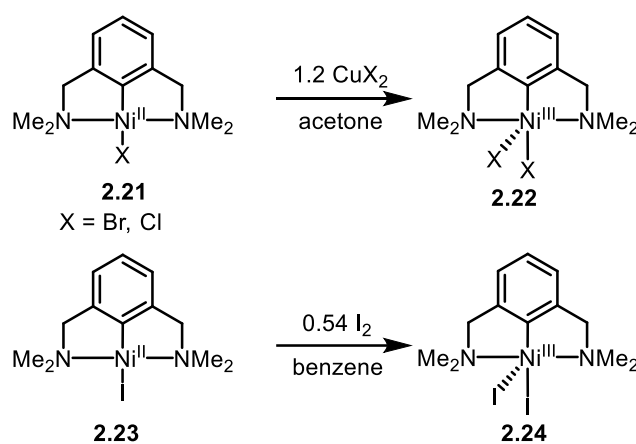


Figure 2.4 Examples of the d -orbital splitting diagram for nickel complexes in different geometries. Pincer complexes of nickel in +1 oxidation states are usually found in T-shaped geometries or in between square-planar and tetrahedral as a seesaw geometry. The seesaw diagram is based on a reported Ni^{II}-methyl complex with a close to ideal seesaw geometry.¹⁸⁸

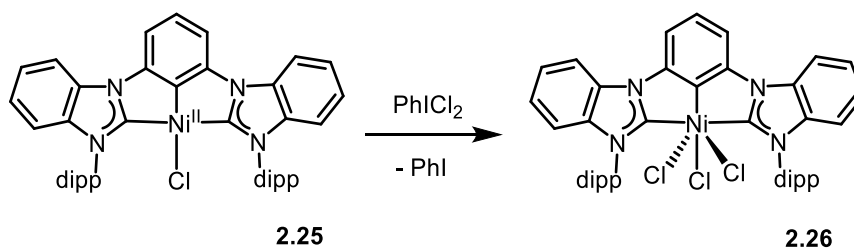
2.1.7 Nickel Pincer Complexes in Other Unusual Oxidation States

High oxidation state transition metal complexes are often proposed as intermediates of catalytic reactions and many efforts have been made to isolate and characterize such high oxidation state species. One of the earlier research came from the group of van Koten in 1988¹⁸⁹ with their research on the stabilization of nickel complexes in the +3 oxidation state with an NCN ligand (Scheme 2.10). They were able to oxidize simple Ni^{II} halide complexes **2.21** or **2.23** to the respective Ni^{III} species (complexes **2.22** and **2.24**) by either CuX₂ (X = Br, Cl) for bromide or chloride Ni^{II} species, or I₂ for the iodide Ni^{II} species.



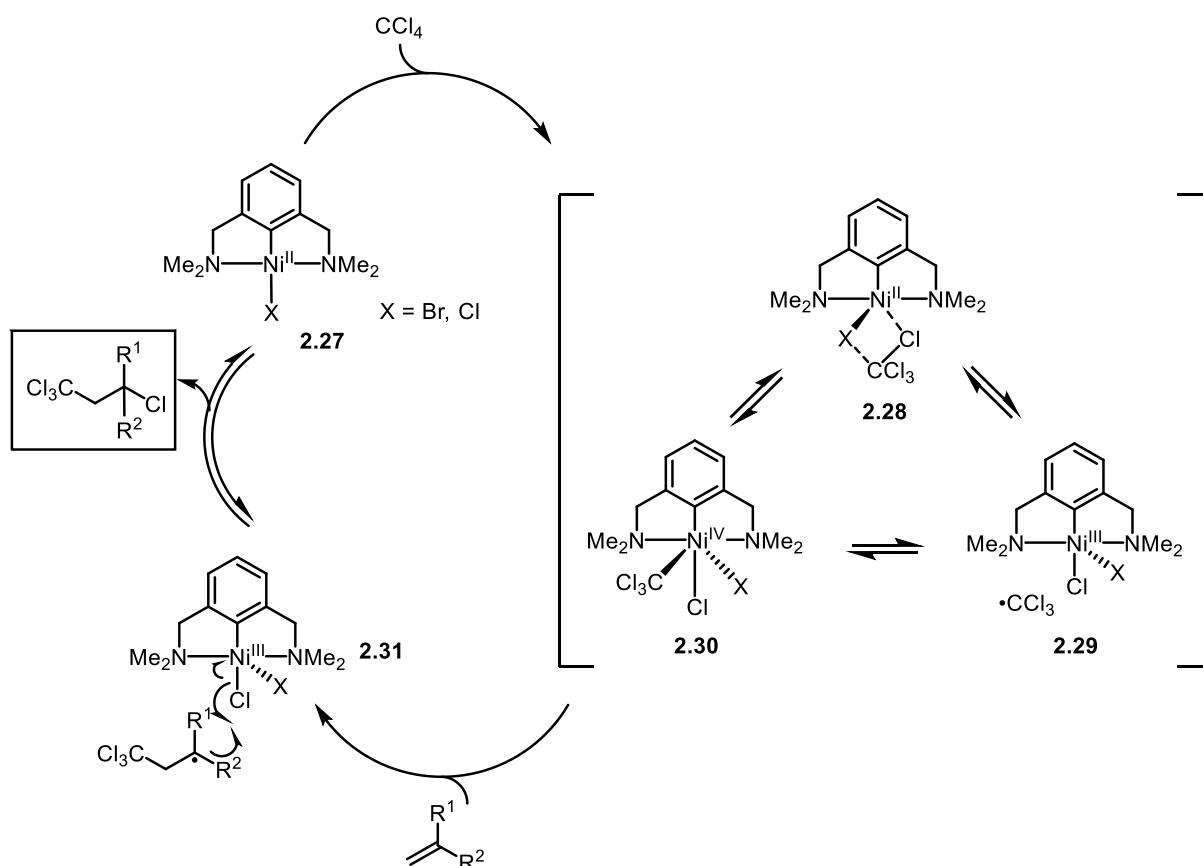
Scheme 2.10 Formation of Ni^{III} species via oxidation of Ni^{II} halide NCN pincer complexes.¹⁸⁹

In the field of pincer complexes, there are very few examples of an isolated Ni^{IV} species. One of those is complex **2.26** with a bis(carbene) pincer ligand. The group of Fout in 2016 showed that a two electrons oxidation from a Ni^{II} halide species **2.25** with PhICl₂ to form the corresponding stable Ni^{IV} halide species **2.26** (Scheme 2.11).¹⁹⁰



Scheme 2.11 2-electrons oxidation of Ni^{II} bis-carbene pincer complex to Ni^{IV}.¹⁹⁰

An example of a system that involves multiple high oxidation states of a nickel pincer complexes is in the Kharasch addition of CCl_4 to alkenes (Scheme 2.12).¹⁹¹ Although not popular nowadays because of the toxicity of the CCl_4 used, it still is an interesting way to form chlorinated alkanes from alkenes. The starting Ni^{II} bromide complex, when reacting with CCl_4 will interconvert between Ni^{II} (**2.27**), Ni^{III} (**2.29**) and Ni^{IV} (**2.30**) species. The $\text{Cl}_3\text{C}\cdot$ radical formed from the formation of the Ni^{III} species **2.28** will then react with an alkene to form the alkene radical species, which will also react with the Ni^{III} species and abstract a Cl atom to form the final product, regenerating the Ni^{II} species **2.27**.

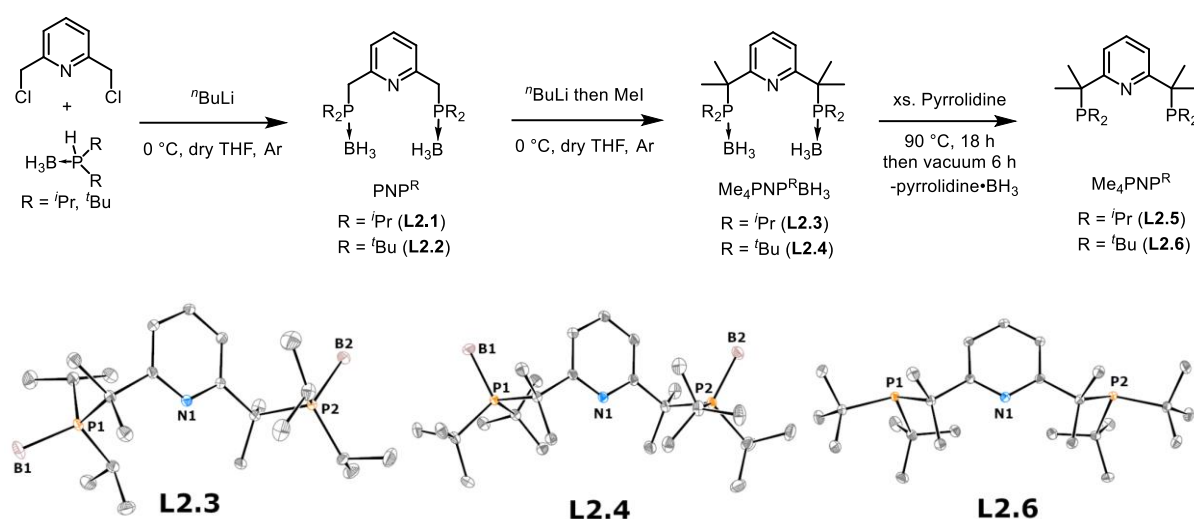


Scheme 2.12 Catalytic cycle for the Kharasch addition of CCl_4 to alkenes catalyzed by **2.27**.¹⁹¹ Note: Ligand X is Br during first catalytic cycle, however, it is likely to exchange with Cl during subsequent cycles.

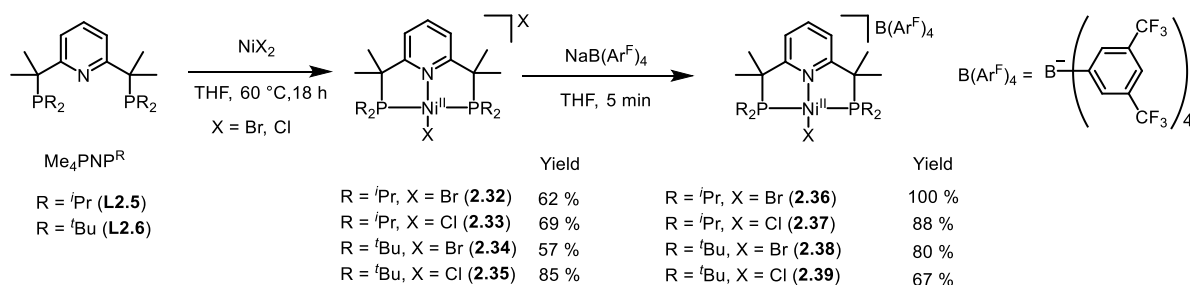
2.2 Results and Discussion

2.2.1 Synthesis of Ligands and Nickel(II) Halide Complexes.

The bulky PNP ligands were synthesized as described above by modification of the synthetic procedure for the previously reported unsubstituted $\text{PNP}^{\text{R}}\text{BH}_3$ ligands **L2.1** and **L2.2** ($\text{R} = i\text{Pr}$, $t\text{Bu}$),¹⁹² which also differs from a procedure for similar previously reported methylated ligands.¹⁹³ They were prepared in good yields and can be scaled up to a few grams (See Section 2.4). The ORTEP of the ligands can be seen in Scheme 2.13 (bottom))



Scheme 2.13 (top) Preparation of $\text{Me}_4\text{PNP}^{\text{R}}\text{BH}_3$ (**L2.3–L2.4**) and $\text{Me}_4\text{PNP}^{\text{R}}$ (**L2.5–L2.6**) ligands. (bottom). ORTEP diagram showing 50% probability anisotropic displacement ellipsoids of non-hydrogen atoms for **L2.3**, **L2.4**, and **L2.6**.



Scheme 2.14 Preparation of Ni^{II} cationic PNP complexes **2.32–2.39**.

The tetramethylated $\text{Me}_4\text{PNP}^{\text{R}}\text{BH}_3$ ligands **L2.3** and **L2.4** were deprotected by reaction with pyrrolidine at 90 °C for 18 hours, while evaporation under low pressure at 60 °C for 4–6 hours

following the reaction allows for a thorough removal of the pyrrolidine-BH₃ complex formed and the excess pyrrolidine (See Scheme 2.13). The resulting deprotected ligands (Me₄PNP^R ligands **L2.5** and **L2.6**) were isolated in a pure form and characterized by NMR spectroscopy, and X-ray diffraction for Me₄PNP^{tBu} (**L2.6**). The deprotected ligand Me₄PNP^{iPr} (**L2.5**) is a viscous substance that is unstable in air, and Me₄PNP^{tBu} (**L2.6**) is a crystalline solid. Both protected forms are crystalline and can be kept for months under air without degradation. The deprotected ligands were reacted in situ with anhydrous Ni^{II} dihalides in THF at 60 °C overnight to afford complexes [Me₄PNP^{iPr}NiBr]Br (**2.32**), [Me₄PNP^{iPr}NiCl]Cl (**2.33**), [Me₄PNP^{tBu}NiBr]Br (**2.34**), and [Me₄PNP^{tBu}NiCl]Cl (**2.35**) in 57% to 85% yield (See Scheme 2.2). The halide counterion can be replaced using sodium tetrakis[3,5-bis(trifluoromethyl)phenyl]borate (NaB(Ar^F)₄) via salt metathesis to afford complexes [Me₄PNP^{iPr}NiBr]B(Ar^F)₄ (**2.36**), [Me₄PNP^{iPr}NiCl]B(Ar^F)₄ (**2.37**), [Me₄PNP^{tBu}NiBr]B(Ar^F)₄ (**2.38**), and [Me₄PNP^{tBu}NiCl]B(Ar^F)₄ (**2.39**) in 67% to quantitative yield (See Scheme 2.14). Changing the redox-active halide counterion to B(Ar^F)₄⁻ in complexes **2.36–2.39** allowed for facile characterization of the nickel complex via electrochemical methods.

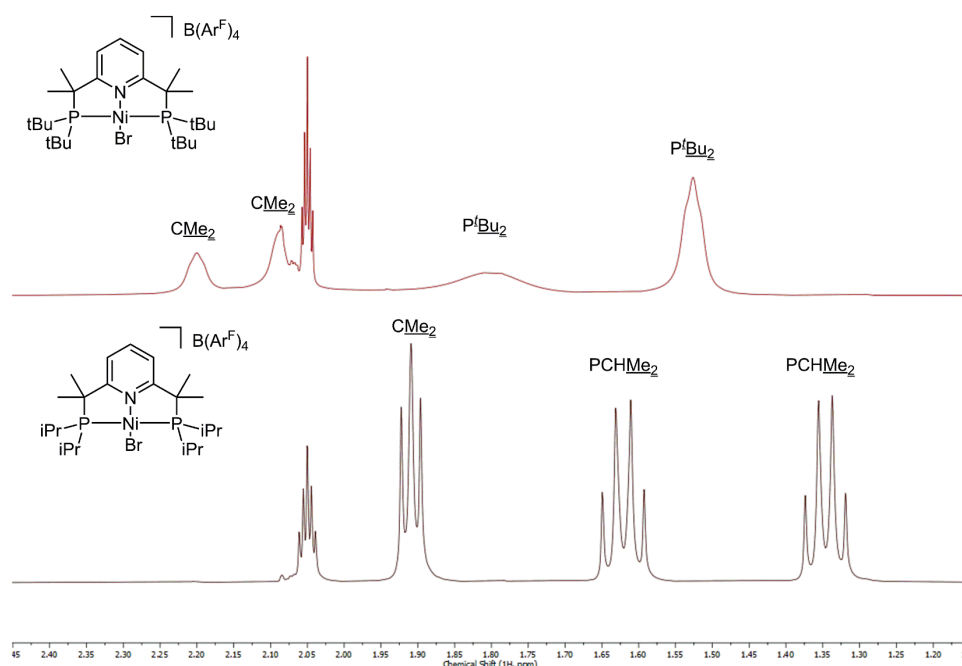


Figure 2.5 Stacked ^1H NMR spectra of **2.36** and **2.38** to show broadening of signals of $t\text{Bu}$ groups from hindered rotation.

^1H NMR spectra of bis(isopropyl)phosphine-based complexes (**2.32–2.33** and **2.36–2.37**) exhibit two overlapping doublets corresponding to Me groups of the CMe_2 arms with splitting to the phosphorus atom, suggesting a lack of a mirror plane through the coordination plane of the square planar Ni complexes (Figure 2.5) This is also consistent with their solid-state structures (vide infra). Methyl groups of isopropyl groups also appear as two sets of multiplets showing splitting to the phosphorus atom. In comparison, complexes with bis(tertbutyl)phosphine donors (**2.34–2.35** and **2.38–2.39**) show broadened signals for $t\text{Bu}$ groups and Me groups of the ligand arm in ^1H NMR spectrum due to hindered rotation. Comparison between the aliphatic region of **2.36** and **2.38** is shown in Figure 2.5. Moreover, variable temperature NMR study of complex **2.38** in CD_2Cl_2 reveals that a broadened signal of one of the $t\text{Bu}$ groups resolves into three separate signals of Me groups, while the other broad singlet the $t\text{Bu}$ group remains unresolved even at $-60\text{ }^\circ\text{C}$ (see Figure 2.6)

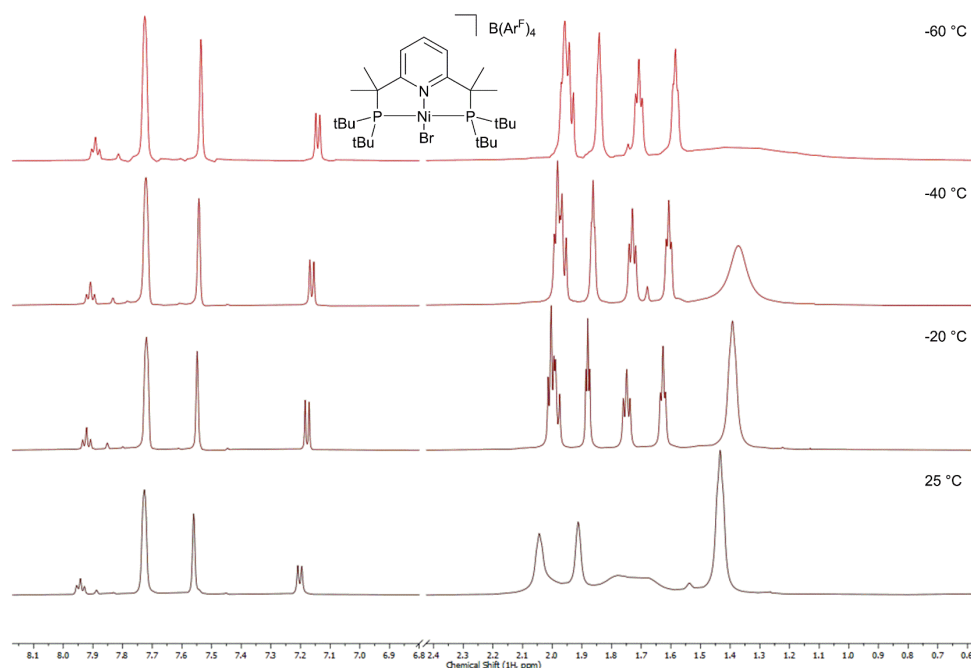


Figure 2.6 Variable temperature NMR of **2.38** from 25 °C to -60 °C in CD_2Cl_2 .

2.2.2 Solid State Structure of Nickel(II) Complexes

All the complexes shown in Scheme 2.14 were analyzed by X-ray diffraction, and their crystals were grown by different methods using either THF, acetone or benzene at rt or -30 °C. Table 2.1 lists the Ni-ligand bond lengths and Ni centered bond angles for complexes **2.32–2.39**, showing almost ideal square planar geometry ($\tau_4' = 0.03\text{--}0.07$; ideal square planar $\tau_4' = 0.00$) around the metal center for this series of Ni^{II} complexes. The ORTEP diagrams of complexes **2.32–2.35** are presented in Figure 2.7, while those of complexes **2.36–2.39** are presented in Figure 2.8.

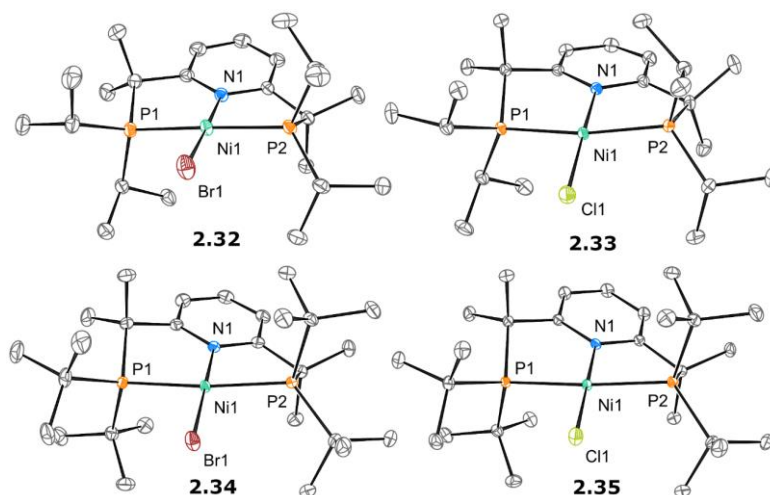


Figure 2.7 ORTEP diagrams for the cationic parts of complexes **2.32-2.35** with the thermal ellipsoids set at 50% probability level. Hydrogen atoms, counterions and solvent molecules are omitted for clarity.

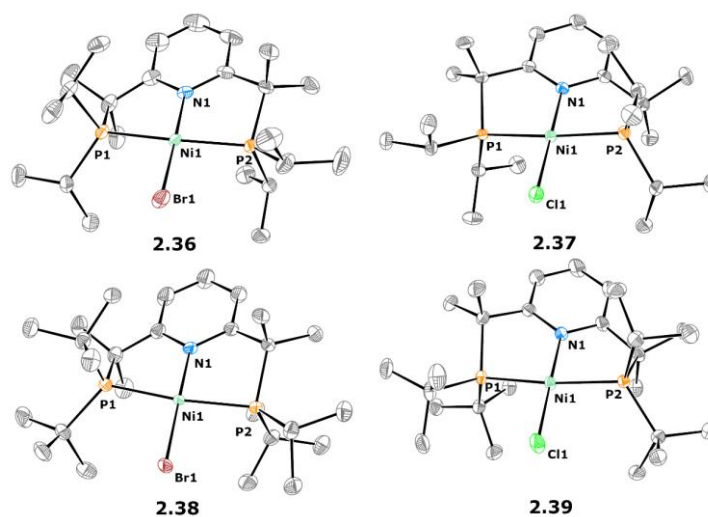


Figure 2.8 ORTEP diagrams for the cationic parts of complexes **2.36-2.39** with the thermal ellipsoids set at 50% probability level. Hydrogen atoms, counterions and solvent molecules are omitted for clarity. Only the main disordered component of **2.38** is shown.

Table 2.1 Bond distances [Å] and angles [deg] for complexes **2.32–2.39**. The atom numbering corresponds to that of Figures 2.7-2.8.

Complex	Ni1–N1	Ni1–Hal	Ni1–P1	Ni1–P2	∠ P1–Ni1–P2	∠ N1–Ni1–Hal	$\tau_4'^a$	τ_4
2.32	1.918(2)	2.3015(4)	2.1880(6)	2.1924(6)	171.36(3)	176.49(6)	0.07	0.09
2.33	1.9153(7)	2.1658(2)	2.1922(2)	2.1861(2)	171.336(10)	176.52(2)	0.07	0.09
2.34	1.9222(19)	2.3070(3)	2.2394(6)	2.2413(6)	171.68(2)	179.45(6)	0.04	0.06
2.35	1.9166(8)	2.1643(3)	2.2220(3)	2.2201(3)	171.405(11)	179.51(3)	0.04	0.06
2.36^b	1.9095(13)	2.2827(2)	2.1786(4)	2.1805(4)	172.320(18)	176.66(4)	0.06	0.08
2.37^b	1.9135(11)	2.1548(3)	2.1763(3)	2.1779(3)	173.359(14)	179.34(3)	0.03	0.05
2.38^c	1.9236(15)	2.2877(12)	2.2324(12)	2.2454(13)	171.87(5)	178.84(7)	0.04	0.07
2.39	1.9119(9)	2.1531(3)	2.2333(3)	2.2275(3)	172.587(12)	179.29(3)	0.04	0.06

^a Geometrical index τ_4' and τ_4 for the nickel centers is calculated according to refs.^{187, 194, 195}. ^b There are two complexes in the asymmetric unit; data are tabulated for the first one. ^c Data are listed for the main disordered component.

The geometry index for 4-coordinate complexes, τ_4' , varies within 0.03 and 0.07, which is close to the ideal square planar value of $\tau_4' = 0.00$.¹⁹⁵ Complexes **2.32–2.39** show insignificant variations in the Ni–N_{py} bond lengths depending on the nature of the halogen on the Ni center (1.9034(11) to 1.9236(15) Å) and the Ni-halogen bond length varies only slightly between the same halogen-containing complexes (2.2827(2) to 2.3070(3) Å for Br, 2.1462(3) to 2.1658(2) Å for Cl-containing complexes).

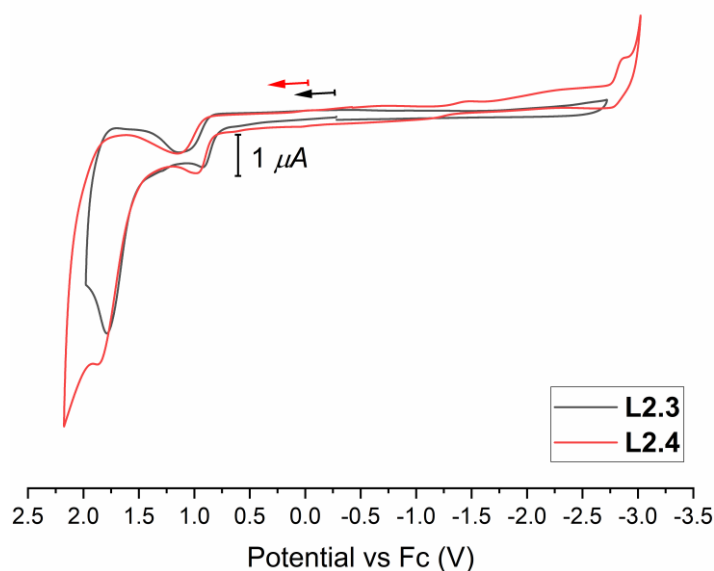
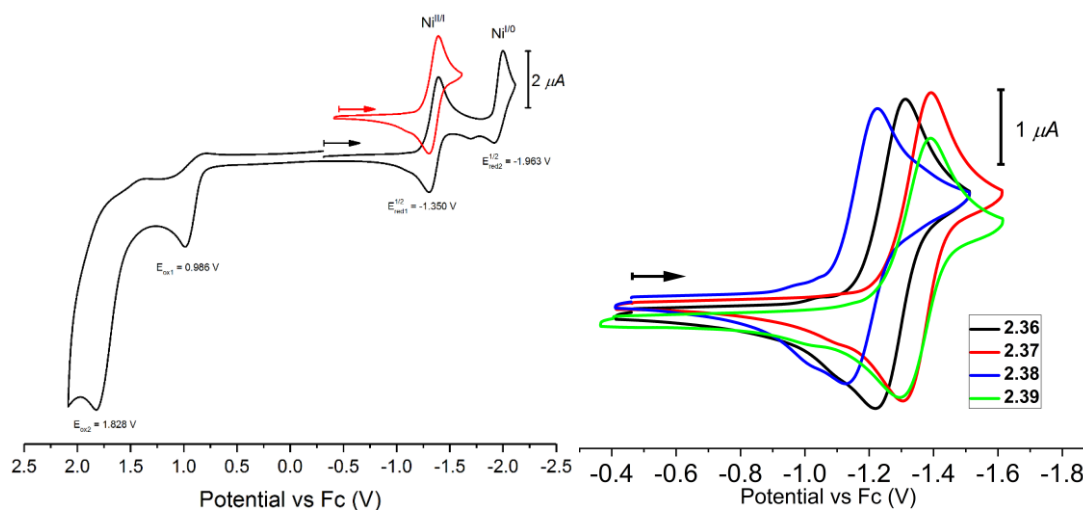
2.2.3 Electrochemical Properties of Nickel(II) Complexes

To test the stability of the bulky PNP framework and the possibility of oxidation or reduction of its associated nickel complexes, we studied the redox properties of the Me₄PNPBH₃ protected ligand and Ni^{II} complexes with the B(Ar^F)₄[−] counterion, using cyclic voltammetry in MeCN solution with ⁿBu₄NPF₆ as the electrolyte. The protected ligands show two irreversible oxidation peaks in acetonitrile (See Table 2.2 and Figure 2.9). For the ⁱPr-containing ligand **L2.3**, the first oxidation appears at 0.92 V and the second at 1.78 V, while the ^tBu-containing ligand **L2.4** has the the oxidation potentials of 1.16 V and 1.87 V. No reduction waves are observed up to -2.5 V vs. Fc for both ligands. Complexes **2.36–2.39** exhibit quasi-reversible reduction

Table 2.2 Redox potentials for **L2.3** and **L2.4**.

Ligands	E _{ox} (V)	E _{red} (V)
L2.3	1.78, 0.92	N/A
L2.4	1.87, 1.16	-2.85

N/A: not applicable

**Figure 2.9** Full cyclic voltammogram of ligands **L2.3** (black line) and **L2.4** (red line). See caption of Figure 2.10 for experimental details.**Figure 2.10** (left) Full cyclic voltammogram of **2.37**. (right) Cyclic voltammogram of complexes **2.36–2.39**. Experimental conditions for both figures: 1 mM solution of complexes 2.36–2.39 in 0.1 M ⁿBu₄NPF₆/MeCN solution at 23 °C (scan rate 0.1 V s⁻¹; 1.0 mm GC disk working electrode; the arrow indicates the initial scan direction). Left figure: Red trace is a CV recorded in a shorter range to estimate reversibility of Ni^{III/I} wave; the curve was translated upwards in the vertical direction for clarity.

waves (See Figure 2.10 and Table 2.3) with redox potential ranging from -1.17 to -1.35 V vs. Fc and a peak-to-peak separation between 90 and 99 mV. We assign this wave to Ni^{II/I} reduction, which is confirmed by further studies (vide infra). Generally, the Ni^{II/I} reduction potentials $E_{1/2}$ of complexes containing a chloride, such as **2.37** ($E_{1/2}$ = -1.35 V) or **2.39** ($E_{1/2}$ = -1.34 V), are more negative than those of complexes containing a bromide ligand, such as **2.36** ($E_{1/2}$ = -1.27 V) and **2.38** ($E_{1/2}$ = -1.17 V). All complexes also show irreversible oxidation waves around 0.93–1.45 V. However, considering that the protected ligands also feature an irreversible oxidation wave at 0.98 V and 1.16 V vs. Fc for the ⁱPr-containing ligands **L2.3** and **L2.4**, respectively, it likely corresponds to ligand oxidation. Accordingly, attempted detection of Ni^{III} intermediates by EPR spectroscopy during one-electron electrochemical or chemical oxidation of complex **2.36** did not lead to any detectable paramagnetic species, and no single product could be isolated.

Table 2.3 Electrochemical properties of complexes **2.36–2.39** (V vs. Fc)

Complexes	$E_{1/2}$ for Ni ^{II/I} vs. Fc ^a (ΔE_p) ^b
2.36	-1.27 V (94 mV)
2.37	-1.35 V (90 mV)
2.38	-1.17 V (99 mV)
2.39	-1.34 V (95 mV)

^aMeasured vs. Fc⁺/Fc by CV in 0.1 M ⁿBu₄NPF₆/MeCN, scan rate 100 mV s⁻¹. ^b ΔE_p is the peak potential separation calculated as difference between forward and reverse peak potentials.

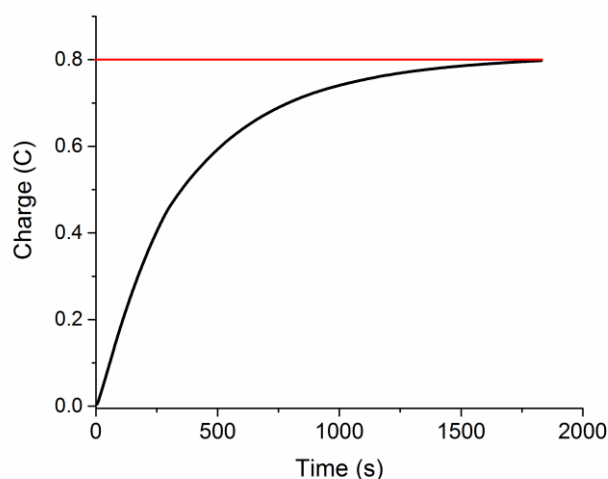
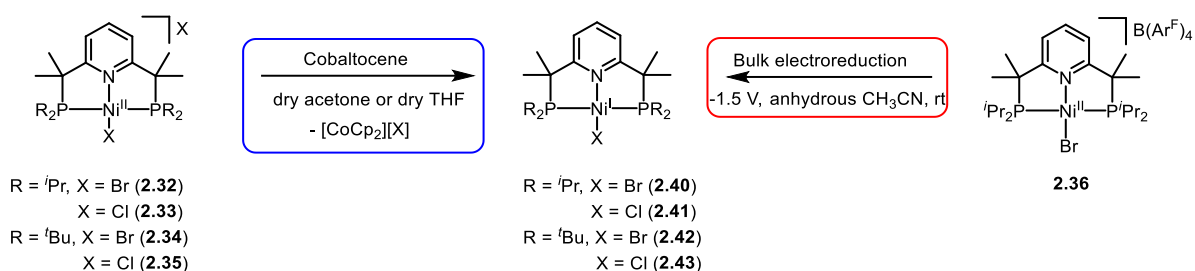


Figure 2.11 Charge – time dependence during coulometry experiment performed using bulk electroreduction of **2.36** in anhydrous acetonitrile with a fixed potential of -1.5 V.

Coulometric study of the reduction of complex **2.36** confirmed that the reduction wave corresponds to a one-electron process, with the experimental charge of 0.800 C that is close to the theoretical charge of 0.776 C for a one electron reduction process (See Figure 2.11). Such reversible reduction waves suggested that stabilization of the uncommon Ni^{I} oxidation state might be possible and led us to further investigate one-electron reduction chemistry of Me_4PNP nickel halide complexes. A second irreversible reduction wave is observed at around -2.0 V for all complexes, which likely corresponds to the $\text{Ni}^{\text{I/0}}$ reduction (see the linked Appendix of Chapter 2 for the experimental details).

2.2.4 Synthesis of Nickel(I) Complexes and Their Characterization in Solution

Following the cyclic voltammetry analysis, we performed bulk electrolysis of a 1 mM solution of **2.36** in anhydrous acetonitrile, which led to a gradual change of the solution color from orange to dark brown (Scheme 2.15). An aliquot of the solution obtained via electroreduction of **2.36** was analyzed by EPR spectroscopy (See Figure 2.12 complex **2.40**, dashed lines), which showed a nearly axial signal with g values significantly deviating from 2 (*vide infra*), suggesting significant metal-centered radical character (See Figure 2.12 and Table 2.4).



Scheme 2.15 Preparation of neutral Ni^{I} complexes **2.40**–**2.44** via electrochemical or chemical reduction with cobaltocene

In order to isolate the reduction product in pure form, we attempted chemical reduction of complex **2.32** with 1 equivalent of cobaltocene in anhydrous acetone solution at room temperature (See Scheme 2.15). Gratifyingly, chemical reduction led to the formation of a dark-red solution, from which crystalline product **2.40** was isolated in 79% yield. The EPR spectrum of crystalline **2.40** dissolved in acetone was essentially identical to that obtained by electrochemical reduction (see Figure 2.12, complex **2.40**, solid lines).

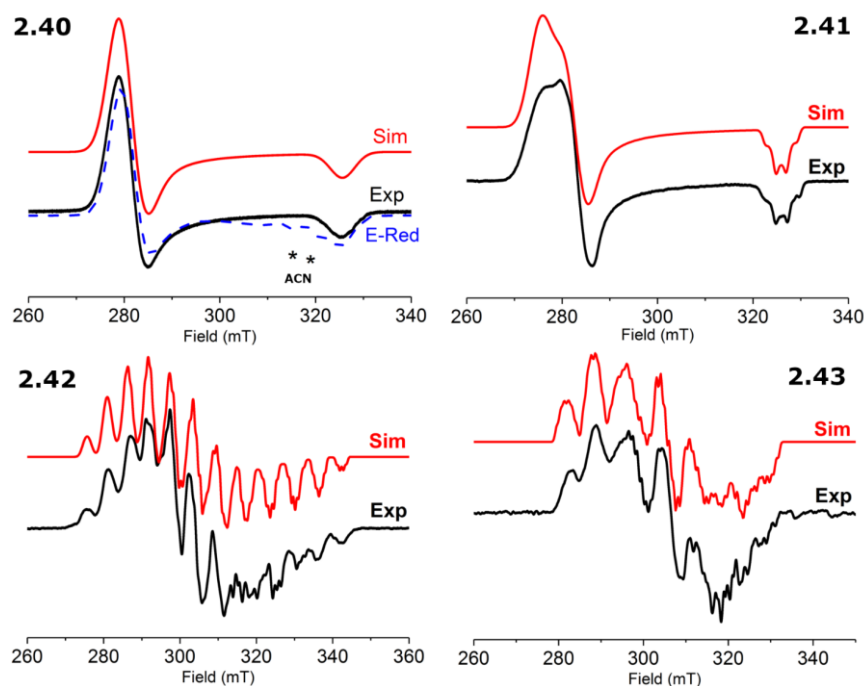


Figure 2.12 Experimental (black line) and simulated (red line) EPR spectra of Ni^{I} complexes (top left) isolated complex **2.40** in solid black line, and the product of electroreduction of **2.36** in dashed blue line; (top right) isolated complex **2.41**; (bottom left) isolated complex **2.42**; (bottom right) isolated complex **2.43**. See Table 2.4 for simulated and experimental parameters.

Table 2.4 Selected EPR parameters^a and effective magnetic moment μ_{eff} in solution for Ni^{I} complexes **2.40**-**2.43**.

Complex	g_x, g_y, g_z^b	g_{iso}	$A_{xx} \text{ (G)}^b$	$A_{yy} \text{ (G)}^b$	$A_{zz} \text{ (G)}^b$	$\mu_{\text{eff}} (\mu_B)^c$
2.40	2.316, 2.309, 1.993	2.206	n.d.	n.d.	n.d.	2.07
2.41	2.355, 2.293, 1.990	2.213	n.d.	n.d.	$A_{zz}^{\text{P}} = 18.7;$ $A_{zz}^{\text{N}} = 9.34$	2.18
2.42	2.240, 2.150, 1.983	2.124	$A_{xx}^{\text{Br}} = 57.5;$ $A_{xx}^{\text{P}} = 49.8;$ $A_{xx}^{\text{N}} = 7.77.$ $A_{xx}^{\text{Cl}} = 10.7;$	$A_{yy}^{\text{Br}} = 60.4;$ $A_{yy}^{\text{P}} = 51.8;$ $A_{yy}^{\text{N}} = 8.48.$ $A_{yy}^{\text{Cl}} = 11.3;$	$A_{zz}^{\text{Br}} = 62.3;$ $A_{zz}^{\text{P}} = 55.6;$ $A_{zz}^{\text{N}} = 9.31.$ $A_{zz}^{\text{Cl}} = 12.0;$	1.94
2.43	2.250, 2.120, 2.000	2.123	$A_{xx}^{\text{P}} = 44.5;$ $A_{xx}^{\text{N}} = 7.56.$	$A_{yy}^{\text{P}} = 67.4;$ $A_{yy}^{\text{N}} = 8.02.$	$A_{zz}^{\text{P}} = 71.4;$ $A_{zz}^{\text{N}} = 8.50.$	1.82

^aMeTHF/acetone glass or frozen acetone, 84-95 K. ^bFrom simulated spectra. For complex **2.40**, simulation cannot provide reliable superhyperfine splitting constants for g_x and g_y components due to signal broadening.

^cEvans method, acetone- d_6 solvent, 298 K.

In a similar way, chemical reduction of complexes **2.33–2.35** with cobaltocene in dry acetone at room temperature led to the formation of complexes **2.41–2.43**, which were isolated as crystalline samples in 65-85% yields by slow evaporation of concentrated acetone solution at -30°C. The complexes were characterized by UV-vis, FT-IR, EPR spectroscopy, and X-ray diffraction (*vide infra*).

The EPR spectrum of isolated bromo-complex **2.40** reveals a rhombic signal with g_x and g_y values that are close to each other, without discernible superhyperfine splitting due to signal broadening. This signal broadening might be due to unresolved splitting from Br and P nuclei similar to other reported Ni^I complexes.¹⁹⁶ By comparison, EPR spectra of the analogous chloro-complex **2.41** shows a rhombic signal (Figure 2.12, top right), with $g_x = 2.355$; $g_y = 2.293$ and $g_z = 1.990$. Superhyperfine splitting was observed for the g_z component, which could be simulated as splitting from two phosphorus atoms and one nitrogen donor, with superhyperfine splitting constants of 18.7 G and 9.34 G, respectively.

Interestingly, *t*Bu substituted complexes **2.42** and **2.43** feature a more complex EPR signal pattern, which shows distinct splitting from the pincer ligand donor atoms as well as the halogen. The spectra could be simulated as rhombic signals showing splitting from nitrogen and two phosphorus atoms and with a contribution from bromide for complex **2.42** or chloride for complex **2.43** (Figure 2.12, bottom left). The g values and superhyperfine splitting constants for complexes **2.40–2.43** are summarized in Table 2.4. In all cases, EPR spectroscopy confirms the $S = \frac{1}{2}$ spin state for complexes **2.40–2.43**, while the g_{iso} values (2.123–2.213) suggest metal-loradical character, consistent with our DFT studies (*vide infra*).

Visually, the EPR signal for complex **2.40** has a nearly axial symmetry and could be simulated both as a rhombic or axial signal. However, comparison of the RMSD (root-mean-square deviation) for the rhombic model compared to the axial model in the experimental EPR spectrum was smaller for rhombic model, which is why we report the signal as rhombic (See Table 2.5)

Table 2.5 Comparison between rhombic and axial signal simulation and RMSD values compared to the experimental spectrum for complex **2.40**

Signal shape	g_x, g_y, g_z	RMSD
Axial	$g_x = 2.313$	0.011042
	$g_y = 2.313$	
	$g_z = 1.991$	
Rhombic	$g_x = 2.316$	0.007737
	$g_y = 2.309$	
	$g_z = 1.993$	

To support the interpretation of the experimental EPR spectra, we simulated the EPR spectrum for complexes **2.40-2.43** using both ORCA¹⁹⁷ and the Easyspin¹⁹⁸ module of Matlab.¹⁹⁹ Preliminary g tensor values and hyperfine coupling A values were obtained from ORCA from optimized geometries of complexes **2.40-2.43**. Then, those values were inserted into Easyspin and simulated to obtain the DFT-optimized EPR spectrum shown in Figure 2.13.

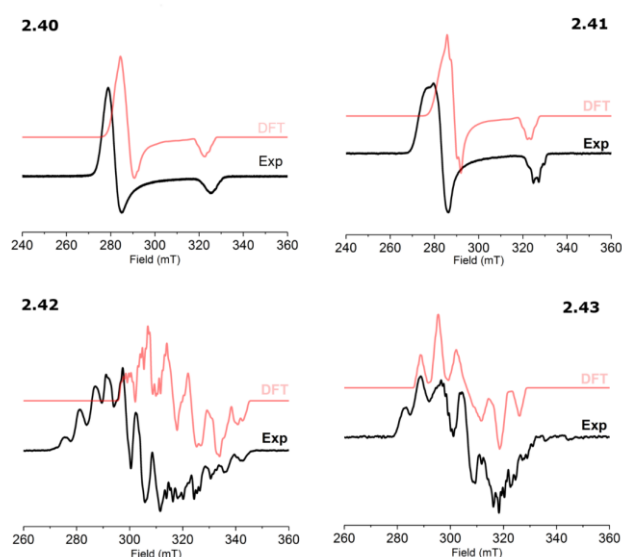


Figure 2.13 Comparison of experimental spectra and EPR spectra simulated in EasySpin using g tensor and A values calculated in ORCA.

Although there are discrepancies in the g tensor and hyperfine coupling A values from the simulated ORCA and experimental values, the general signal shape, especially for **2.40** and **2.41**, match quite well with the experimental data. Even for complexes **2.42** and **2.43**, the shape is somewhat closely related. In the case of **2.40**, the DFT-optimized spectra also show a preference for a rhombic signal with DFT-optimized g tensor g_x , g_y , and g_z values of 2.280, 2.258, and 2.008, respectively (See Table 2.6).

Table 2.6 ORCA-calculated EPR parameters for complexes **2.40–2.43**.

Complex	g_x, g_y, g_z	A_{xx} (G)	A_{yy} (G)	A_{zz} (G)
2.40	2.280, 2.258, 2.008	$A_{xx}^{Br} = 14.4;$ $A_{xx}^P = 25.6;$ $A_{xx}^N = 8.92.$	$A_{yy}^{Br} = 1.42;$ $A_{yy}^P = 20.7;$ $A_{yy}^N = 7.00.$	$A_{zz}^{Br} = -3.23;$ $A_{zz}^P = 21.5;$ $A_{zz}^N = 7.78.$
2.41	2.286, 2.246, 2.009	$A_{xx}^{Cl} = 3.34;$ $A_{xx}^P = 25.2;$ $A_{xx}^N = 8.87.$	$A_{yy}^{Cl} = 0.54;$ $A_{yy}^P = 20.5;$ $A_{yy}^N = 7.02.$	$A_{zz}^{Cl} = -0.90;$ $A_{zz}^P = 21.3;$ $A_{zz}^N = 7.78.$
2.42	2.186, 2.111, 2.037	$A_{xx}^{Br} = 68.0;$ $A_{xx}^P = 70.1;$ $A_{xx}^N = 10.1.$	$A_{yy}^{Br} = 26.4;$ $A_{yy}^P = 65.1;$ $A_{yy}^N = 8.04.$	$A_{zz}^{Br} = 26.9;$ $A_{zz}^P = 66.8;$ $A_{zz}^N = 7.94.$
2.43	2.195, 2.116, 2.033	$A_{xx}^{Cl} = 15.6;$ $A_{xx}^P = 73.4;$ $A_{xx}^N = 10.2.$	$A_{yy}^{Cl} = 6.78;$ $A_{yy}^P = 68.3;$ $A_{yy}^N = 8.13.$	$A_{zz}^{Cl} = 6.91;$ $A_{zz}^P = 70.2;$ $A_{zz}^N = 7.94.$

Simulated hyperfine coupling constants and g tensors were obtained using the following parameters: a spin-unrestricted Kohn-Sham (UKS) approach with the UB3LYP functional and 6-311++G**basis set and a tight SCF convergence criteria in vacuo.

We then analyzed the magnetic moment of complexes **2.40–2.43** in an acetone solution using the Evan's method at room temperature (see Table 2.4) and obtained that the effective magnetic moment values (μ_{eff}) were found to be in a range from 1.82 to 2.18 μ_B depending on the complex (usual range for d^9 complexes is 1.7–2.2 μ_B), consistent with the presence of one unpaired electron.

2.2.5 Solid-State Structures of Nickel(I) Complexes.

The different EPR signal symmetry and splitting patterns in the case of t Bu and i Pr substituted complexes suggested that the geometry around the metal center might also show significant differences depending on the steric environment of the phosphine donors. We were able to

grow single crystals of Ni^I complexes, **2.40** and **2.41** (red crystals), **2.42** (dark orange), and **2.43** (dark red crystals), which were analyzed by X-ray diffraction. Analysis of the crystal structures confirmed that complexes **2.40–2.41** and **2.42–2.43** have very different geometry around the metal center, consistent with their different EPR spectral patterns. As shown in Figure 2.14 and Table 2.7, Ni^I complexes containing ⁱPr groups on the phosphine donor have a very unusual seesaw-like geometry ($\tau_4' = 0.59$ and 0.60 for **2.40** and **2.41**, respectively) with the halide ligand present above the plane formed by the Ni atom with PNP pincer ligand. Thus, the N_{py}–Ni–Hal (Hal = Br, Cl) angles for **2.40** and **2.41** were found to be $109.65(3)^\circ$ and $110.76(3)^\circ$, respectively. Coordination of the ⁱPr ligand **L2.5** is not planar and shows P1–Ni1–P2 angles of $149.357(13)^\circ$ and $148.029(13)^\circ$ for complexes **2.40** and **2.41**, respectively. By contrast, ^tBu substituted complexes **2.42** and **2.43** display a distorted square planar geometry ($\tau_4' = 0.14$) with the halide present *trans* to pyridine and N_{py}–Ni–Hal (X = Br, Cl) angles of $173.54(3)^\circ$ and $173.88(2)^\circ$, respectively.

Table 2.7 Selected bond distances [Å] and angles [deg] for complexes **2.40–2.43**

Complex	Ni1–N1	Ni1–Hal	Ni1–P1	Ni1–P2	∠ P1–Ni1–P2	∠ N1–Ni1–Hal	τ_4'	τ_4
2.40	1.9821(10)	2.48133(19)	2.2030(3)	2.1952(3)	149.357(13)	109.65(3)	0.59	0.72
2.41^a	1.9833(9)	2.3414(3)	2.2066(3)	2.1976(3)	148.029(13)	110.76(3)	0.60	0.72
2.42	2.0973(9)	2.51129(18)	2.3021(3)	2.3024(3)	161.830(12)	173.54(3)	0.14	0.17
2.43	2.1176(7)	2.3723(2)	2.2943(2)	2.2960(2)	161.509(9)	173.88(2)	0.14	0.17

^a The bond distances and angles are those of the major disordered component.

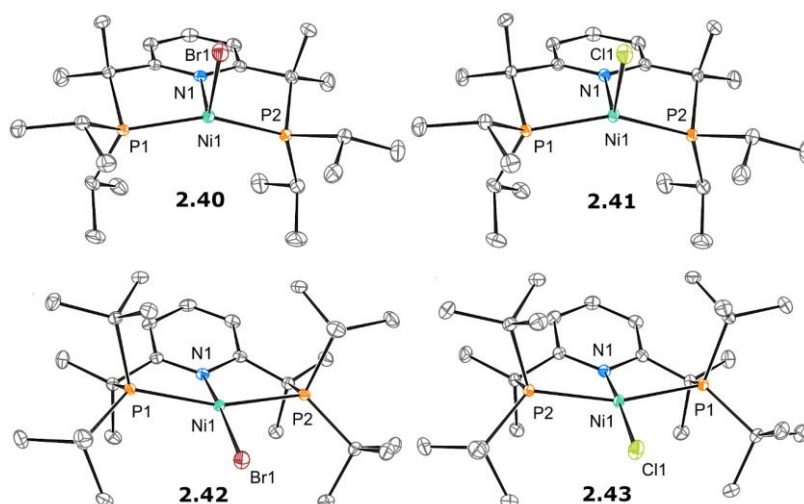


Figure 2.14 ORTEP diagrams of complexes **2.40–2.43** with the thermal ellipsoids set at 50% probability level.

Hydrogen atoms, solvent molecules and a minor disordered component for **2.41** are omitted for clarity.

All the Ni^{I} complexes show elongation of the Ni–Hal bond compared to the corresponding Ni^{II} precursors. Ni^{I} bromide complexes **2.40** and **2.41** have Ni1–Br1 bond lengths 0.17 and 0.20 Å longer than their Ni^{II} bromo analogues **2.32** and **2.33**. The same trend is repeated in chloro-containing complexes **2.41** and **2.43** with respect to **2.33** and **2.35**. No significant differences in the ligand C–C or C–P bond lengths are present between the complexes **2.32–2.35** and **2.40–2.43**, giving credence to the initial vision of designing the ligand system with a view to limit ligand-centered reactivity.

2.2.6 Computational Analysis of the Nickel(I) Complexes

The metalloradical nature of the Ni^{I} complexes was further confirmed by DFT studies, which showed that the spin density is mainly localized on the metal. Figure 2.15 shows the Mulliken atomic spin density plot for the optimized geometries for complexes **2.40–2.43**, with 85–89% of spin density present at the Ni center, consistent with d^9 configuration. At the same time, Mulliken spin density at the halogen atoms was found to be slightly higher for square-planar complexes **2.42** and **2.43** than in bent complexes **2.40** and **2.41**.

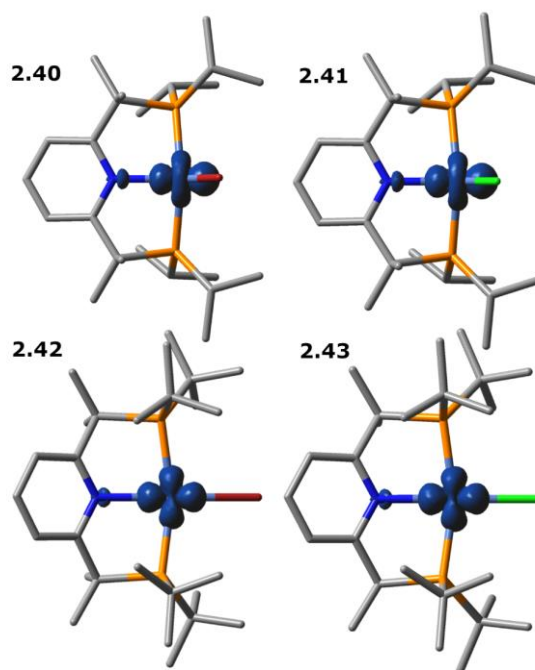


Figure 2.15 Mulliken atomic spin density plots of **2.40-2.43** (DFT-optimized geometries, B3LYP, lanl2dz/6-311++G**). (a) Ni 88.8%, Br 1.2%, P 1.7%, N 3.4%; (b) Ni 87.9%, Cl 1.2%, P 2.4%, N 3.4%; (c) Ni 86.8%, Br 4.1%, P 0.9%, N 1.8%; (d) Ni 85.2%, Cl 3.8%, P 1.8%, N 1.4%.

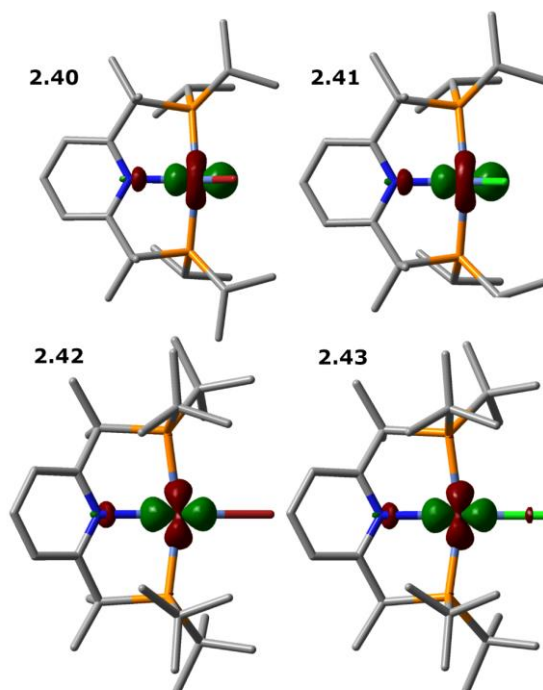


Figure 2.16 The SOMO representation of **2.40-2.43** (DFT-optimized geometries, B3LYP, lanl2dz (Ni, Br, Cl)/6-311++G**).

Table 2.8 LCAO-MO analysis of the SOMO using Chemissian (highest contributions are shown).²⁰⁰

Complex	Highest contributors to the SOMO (coefficient)				
2.40	Ni - $d_{x^2-y^2}$ (0.70)	Ni - d_{yz} (0.43)	P2 - 7s (0.35)	P1 - 7s (0.35)	Ni - 3s (0.30)
2.41	Ni - $d_{x^2-y^2}$ (0.77)	Ni - 3s (0.43)	Ni - d_{z^2} (0.37)	P1 - p_z (0.23)	P2 - p_z (0.23)
2.42	Ni - $d_{x^2-y^2}$ (0.81)	P1 - p_z (0.48)	P2 - p_z (0.48)	P1 - p_x (0.42)	P2 - p_x (-0.42)
2.43	Ni - $d_{x^2-y^2}$ (0.80)	P2 - p_z (0.55)	P1 - p_z (0.55)	Ni - 3 p_y (0.34)	C - 5s (0.33)

The Natural Population Analysis (NPA), Mulliken population and LCAO-MO analyses reveal that the SOMO has essentially a $d_{x^2-y^2}$ character in all the complexes (Figure 2.16, Table 2.8, Table 2.9, and Table 2.10), which resembles the Ni^I complexes reported by Lee and Gade.^{65,176}

Table 2.9 Natural population analysis for Ni center for complexes **2.40-2.41**

2.40			2.41		
Angular momentum type	Orbital type (AO) ^a	Orbital occupancy	Angular momentum type	Orbital type (AO)	Orbital occupancy
s	core (3s)	1.99681	s	core (3s)	1.99665
s	valence (4s)	0.35867	s	valence (4s)	0.34772
p _x	core (3p)	1.99888	p _x	core (3p)	1.99884
p _x	valence (4p)	0.27604	p _x	valence (4p)	0.27271
p _y	core (3p)	1.99914	p _y	core (3p)	1.99902
p _y	valence (4p)	0.1911	p _y	valence (4p)	0.16138
p _z	core (3p)	1.9994	p _z	core (3p)	1.99948
p _z	valence (4p)	0.20478	p _z	valence (4p)	0.21506
d _{xy}	valence (3d)	1.97044	d _{xy}	valence (3d)	1.97149
d _{xz}	valence (3d)	1.96262	d _{xz}	valence (3d)	1.96058
d _{yz}	valence (3d)	1.73366	d _{yz}	valence (3d)	1.94549
$d_{x^2-y^2}$	valence (3d)	1.36187	$d_{x^2-y^2}$	valence (3d)	1.25043
d _{z²}	valence (3d)	1.88887	d _{z²}	valence (3d)	1.77974

^aRydberg-type orbitals have been omitted for clarity as they do not present significant contribution.

Table 2.10 Natural population analysis for Ni center for complexes **2.42-2.43**

2.42			2.43		
Angular momentum type	Orbital type (AO) ^a	Orbital occupancy	Angular momentum type	Orbital type (AO)	Orbital occupancy
s	core (3s)	1.99668	s	core (3s)	1.9966
s	valence (4s)	0.33781	s	valence (4s)	0.33021
p _x	core (3p)	1.99929	p _x	core (3p)	1.99926
p _x	valence (4p)	0.17575	p _x	valence (4p)	0.17769
p _y	core (3p)	1.99935	p _y	core (3p)	1.99932
p _y	valence (4p)	0.14221	p _y	valence (4p)	0.12832
p _z	core (3p)	1.99923	p _z	core (3p)	1.9992
p _z	valence (4p)	0.08952	p _z	valence (4p)	0.08872
d _{xy}	valence (3d)	1.9682	d _{xy}	valence (3d)	1.96773
d _{xz}	valence (3d)	1.94814	d _{xz}	valence (3d)	1.94617
d _{yz}	valence (3d)	1.91255	d _{yz}	valence (3d)	1.90133
<i>d_{x²-y²}</i>	valence (3d)	1.23263	<i>d_{x²-y²}</i>	valence (3d)	1.243
d _{z²}	valence (3d)	1.94963	d _{z²}	valence (3d)	1.94735

^aRydberg-type orbitals have been omitted for clarity as they do not present significant contribution.

In combination with higher calculated spin density at the halogen atoms, this is also in accordance with more pronounced superhyperfine splitting from halogens observed in EPR spectra of square planar complexes **2.42-2.43** compared to bent complexes **2.40-2.41**. In Lee's case, T-shaped complexes could be obtained for Ni complexes bearing anionic PNP ligands having a central amide donor, where no ligands were present in the *trans* position to that amide. Addition of CO or PMe₃ to their complexes lead to the formation of complexes where the CO or PMe₃ ligands deviate from the (PNP)Ni plane. Such deviations helped to diminish the antibonding interactions in the SOMO, which has the character of a singly-occupied *d_{x²-y²}* orbital.¹⁷⁶ Similarly, the formation of bent geometries in **2.40** and **2.41** by bending of the N_{Py}-Ni-Hal (Hal = Br, Cl) plane and the elongation of Ni-Hal bond might be driven by the minimization of antibonding interactions in our system.

Energy minimization of ¹Pr complexes **2.40** and **2.41** with an enforced square planar geometry relaxed to an energy minimum where the bent structure was obtained, while the geometry of

the more sterically hindered ^tBu complexes **2.42** and **2.43** remained square planar after optimization of the structures with halide ligand forced into bent position. This is likely due to the steric clash between the bulky ^tBu groups and Me groups on the phosphine and ligand arm, respectively, which prevents the formation of the bent structure.

2.2.7 Geometrical Analysis of the Nickel(I) Complexes

To rationalize and as alternative to visualize that the Ni-halogen bond is out of the plane in ⁱPr-containing complexes, we calculated the exact solid angles of the DFT-optimized geometries of Ni^I complexes, the solid-state complexes, as well as their fragments from which halogen was removed (to see visualization for a tentative structure with halogen atoms removed, see figures 4.124 to 4.127 in the linked Appendix of Chapter 2).. As an alternative to the Tolman cone angle, especially for rotationally hindered or highly asymmetric ligands, the exact ligand solid angle (Ω°) should be able to describe the steric hindrance of our ligand system in a quantitative and visual manner. Moreover, we can calculate an easily interpretable parameter (G) that describes ligand shielding as a simple percentage of the maximum solid angle of 4π steradians (str, $G = 100\Omega^\circ/4\pi$) which is described and advocated both by Guzei and Wendt,²⁰¹ as well as by Allen.⁸⁷

Table 2.11 Exact ligand solid angle parameters from the **DFT-optimized** geometry Ni^I complexes with and without the halogen^a

Entry	Complex	Exact solid angles $\Omega^\circ / \text{str}^b$	G % ^{b,c}
1	2.40	10.34 (10.89)	82.3 (86.7)
2	2.40 w/out Br	8.43 (9.09)	67.1 (72.4)
3	2.41	10.09 (10.92)	80.3 (86.9)
4	2.41 w/out Cl	8.50 (9.18)	67.7 (73.1)
5	2.42	10.65 (11.31)	84.7 (90.0)
6	2.42 w/out Br	8.98 (9.77)	71.4 (77.8)
7	2.43	10.52 (11.38)	83.7 (90.6)
8	2.43 w/out Cl	9.09 (9.90)	72.3 (78.7)

^a Complexes **2.40-2.43**: Calculated for DFT-optimized structures, B3LYP, lanl2dz/6-311++G**. Complexes “without”: Calculated for fragments of DFT-optimized structures with halide atom artificially removed; after removing halogen, no further geometry optimization was carried out. ^b The values in parenthesis were calculated using the Bondi radii for all atoms,²⁰² while the values outside the parentheses were calculated using the zero energy point radii.²⁰¹ ^c Ligand shielding parameters.

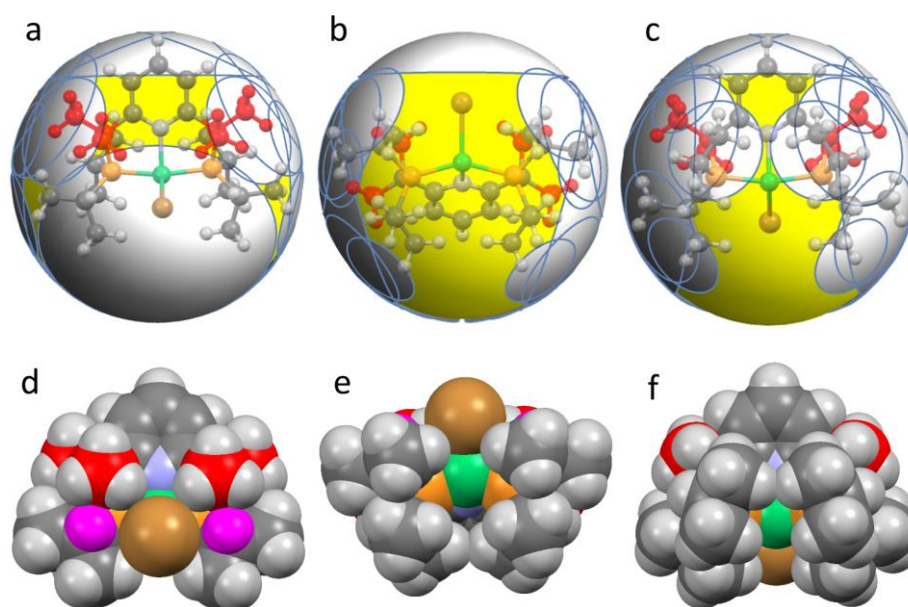


Figure 2.17 Selected ligand solid angle representations (gray area) of the optimized structure of **2.40** (a-c). Corresponding space filling model representation of the optimized structure of **2.40** (d-f). Nickel atom, green, phosphorous atoms, light orange, bromide atom, light brown. Atoms highlighted in red are the methyl groups on the ligand arms; the isopropyl C-H hydrogen is highlighted in magenta. Zero energy radii were used for computation.

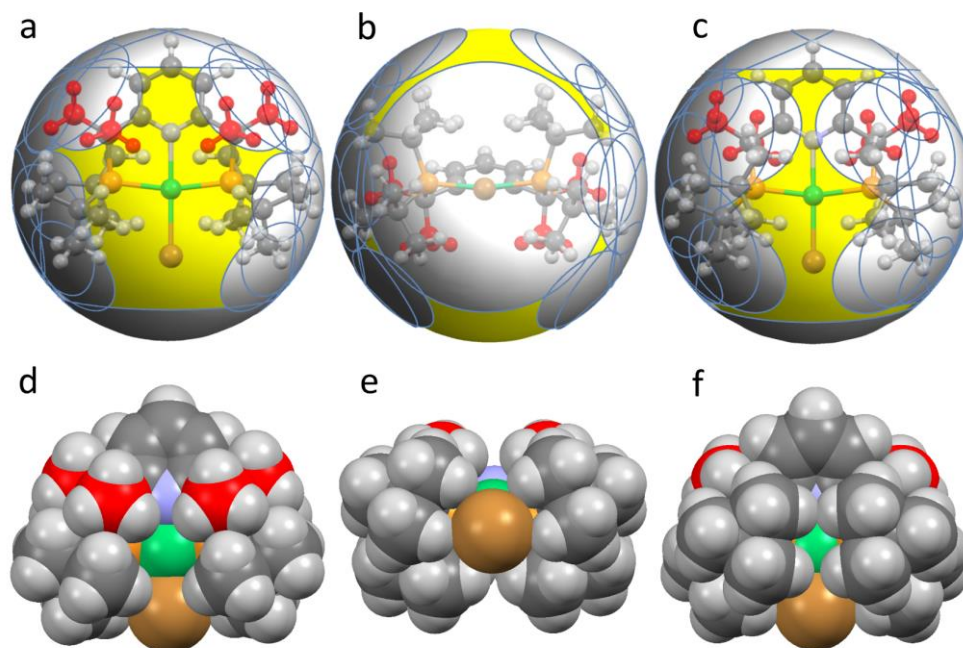


Figure 2.18 Selected ligand solid angle representations (gray area) of the optimized structure of **2.42** (a-c). Corresponding space filling model representation of the optimized structure of **2.42** (d-f). Nickel atom, green, phosphorous atoms, light orange, bromide atom, light brown.

The results of the exact solid angle (Ω°) calculations and of the ligand shielding parameter (G) are reported in Figure 2.17. An overlay of a ball-and-stick representation of the calculated geometry, or of the experimental X-ray coordinates on the sphere created by the exact ligand solid angle method are shown in Figure 2.17 and Figure 2.18, and Figures 4.130 to 4.159 in the linked Appendix of Chapter 2.

The ^tPr-containing complexes **2.40-2.41** have exact solid angles of 10.34 and 10.09 str, which correspond to a ligand shielding (G) of 82.3 and 80.3 % for DFT-optimized structures. In contrast, both the ^tBu containing complexes **2.42-2.43** have higher exact solid angles (Ω°) of 10.65 and 10.52 str, which corresponds to higher ligand shielding of 84.7 and 83.7%, respectively. Although the exact ligand angles or the ligand shielding parameter by itself might seem to show only a small difference between ^tPr and ^tBu containing complexes, it is a useful way to visualize the voids available in the complexes, alternative to space filling models (Figure 2.17). For example, comparison of the solid angle representation of complexes **2.40-2.41** shows that while

for the ⁱPr-substituted **2.40**, the void is available to bind Br in the position bent from the plane of (PNP)Ni fragment; such binding would not be possible for ^tBu-substituted **2.41** due to steric clash between Me groups of the CMe₂ arm (shown in red) and ^tBu groups on the phosphines.

Table 2.12 Exact ligand solid angle parameters from the **X-ray coordinates** for Ni^I complexes with and without the halogen^a

Entry	Complexes	Exact solid angles (Ω°) ^b / str .	G ^{b,c} / %
1	2.40	10.74 (11.20)	85.5 (89.1)
2	2.40 w/out Br	8.76 (9.37)	69.7 (74.6)
3	2.41	10.42 (11.18)	82.9 (89.0)
4	2.41 w/out Cl	8.74 (9.35)	69.5 (74.4)
5	2.42	10.74 (11.30)	85.5 (89.9)
6	2.42 w/out Br	9.00 (9.72)	71.6 (77.3)
7	2.43	10.57 (11.34)	84.1 (90.3)
8	2.43 w/out Cl	9.07 (9.81)	72.2 (78.1)

^a Complexes **2.40-2.43**: Calculated for DFT-optimized structures, B3LYP, lanl2dz/6-311++G**₂. Complexes “without”: Calculated for fragments of DFT-optimized structures with halide atom artificially removed; after removing halogen, no further geometry optimization was carried out. ^b The values in parenthesis were calculated using the Bondi radii for all atoms,²⁰² while the values outside the parentheses were calculated using the zero energy point radii.²⁰¹ ^c Ligand shielding parameters.

To estimate steric requirements of new bulky PNP ligands in these complexes, we also compared exact solid angles for both ligands with ⁱPr and ^tBu substituents by calculating Ω° and *G* parameters for a hypothetical (Me₄PNP^R)Ni (R = ^tBu, ⁱPr) fragment where halide was removed from DFT-optimized structures and X-ray coordinates (Table 2.11 and Table 2.12 entries 2, 4, 6, and 8). These parameters are only used as an estimation of the system under consideration as not all possible conformers of the ligands were considered. This gives *G* values, considering both zero-energy point radii and Bondi radii, of 67.1–74.6% for ⁱPr-substituted ligand and expectedly larger values, 71.4–78.1%, for ^tBu-substituted ligand, meaning that these new bulky ligands occupy as much as approximately 67–78% of the total unit sphere.

Overall, this analysis shows that not only steric parameters of ^tBu- and ⁱPr-substituted ligands are different, but also greater steric hindrance of the ^tBu-substituted ligand likely makes the bent position above coordination plane of the (PNP)Ni fragment unavailable for binding of the

additional ligand, leading to an enforced square planar coordination mode for ^tBu-containing complexes **2.42-2.43**.

2.3 Conclusion of Chapter 2

By designing a ligand that is both bulky and blocks possible MLC via dearomatization on the pincer arm, we were able to stabilize and fully characterize unusual Ni^I species, which are usually difficult to isolate. We first investigated the redox properties of the Ni^{II} complexes and found that the reduction of Ni^{II} to Ni^I is both reversible and easily accessible by reductants such as cobaltocene. We also investigated the EPR spectra of each Ni^I species and found that both their shape, g values and hyperfine coupling constants vary significantly when changing from the less bulky ⁱPr complexes **2.40-2.41** to the bulkier ^tBu complexes **2.42-2.43**. Solid-state structural analysis revealed that the geometry around the metal center is completely different for **2.40-2.41** (distorted seesaw) than **2.42-2.43** (distorted square planar). Spin density and orbital analysis of the complexes has shown that all complexes are essentially metalloradical in nature with the SOMO that has mostly a $d_{x^2-y^2}$ character, similar to previously reported Ni^I complexes with anionic PNP ligands. Interestingly, having bulkier ^tBu substituents on the phosphine donors results in a dramatic geometry difference for the reduced Ni^I complexes; calculations of steric environment around the complex show that this difference, which is reflected in EPR spectra, is brought about by steric and not electronic effects.

2.4 Experimental Section

Solvents and reagents: Unless otherwise indicated, all solvents and reagents were used as received. Non-deuterated solvents were taken from a solvent purification system (MBRAUN SPS). Acetone- d_6 was vacuum distilled over dried magnesium sulfate at low temperature. All other deuterated solvents were added to activated 3 Å molecular sieves. Diisopropylchlorophosphine, ditertbutylchlorophosphine, anhydrous nickel(II) chloride, and cobaltocene were purchased from Sigma-Aldrich; BH_3 -THF and anhydrous nickel(II) bromide 99% were purchased from Acros Organics; *n*-Butyl lithium and 2,6-bis(chloromethyl)pyridine were purchased from Kanto Chemical Co., Inc. The reported yields are based on isolated solids. The preparation of $\text{PH}^t\text{Bu}_2\text{-BH}_3$ and $\text{PH}^i\text{Pr}_2\text{-BH}_3$ was reported elsewhere.^{158,159}

Nuclear Magnetic Resonance (NMR) spectroscopic analyses: NMR spectra were recorded using JEOL ECZR-400 MHz or ECZR-600 MHz. Chemical shifts are reported in ppm (δ) and referenced internally to the residual solvent signals (^1H and ^{13}C : 7.26 and 77.16 ppm for CDCl_3 ; 2.05 and 29.84 ppm for acetone- d_6 ; 1.94 and 1.32 ppm for CD_3CN). The signal abbreviation is as follow: d, doublet, t, triplet, v, virtual, q, quartet, br, broad, m, multiplet.

A typical Evans measurement was done in coaxial tube containing the solvent and the internal standard, and a ^1H NMR was recorded.²⁰³ Diamagnetic corrections were applied for the ligands and metal center.^{204, 205}

Fourier transform infrared (FT-IR) spectroscopic analyses: FTIR spectra were recorded for crystalline samples under an Ar atmosphere on a Cary 630 with an attenuated-total-reflection (ATR) module. IR spectroscopy abbreviations are as follows: w (weak), m (medium), s (strong); sh (shoulder). FT-IR measurements were performed between 4000 cm^{-1} and 650 cm^{-1} at a resolution of 2 cm^{-1} . UV-vis measurements were carried at 298 K in air in a 10^{-4} M CH_2Cl_2

solution for all Ni^{II} complexes, while measurements for complexes **2.40** to **2.43** were carried at 298 K under N_2 atmosphere in a closed-cap cell with 10^{-4} M anhydrous THF solutions.

Electrochemical analyses: Electrochemical-grade tetrabutylammonium hexafluorophosphate ($n\text{Bu}_4\text{NPF}_6$) from Sigma-Aldrich was used as the supporting electrolyte. Cyclic voltammetry and control potential electrolysis experiments were performed on an ALS CHI 660E electrochemical workstation. The cyclic voltammetry measurements were carried out at 298 K using solutions containing 10^{-4} M solution of the complexes or ligands in 0.1 M $n\text{Bu}_4\text{PF}_6$ in anhydrous CH_3CN as the electrolyte under a N_2 atmosphere. A glassy carbon disk electrode ($d = 1.0$ mm) or a Pt gauze were used as working electrodes for cyclic voltammetry and for controlled potential electrolysis, respectively. A non-aqueous Ag-wire reference electrode assembly was filled with 0.01M AgNO_3 in 0.1 M $n\text{Bu}_4\text{NPF}_6/\text{MeCN}$ solution as a reference electrode. A Pt-wire or a Pt gauze were used as an auxiliary electrode for cyclic voltammetry and for the controlled potential electrolysis experiments, respectively. The reference electrodes were calibrated against FeCp_2 (Fc), where the Fc/Fc^+ couple vs $\text{Ag}/\text{AgNO}_3/\text{MeCN}$ nonaqueous reference is 102 mV in 0.1 M $n\text{Bu}_4\text{NPF}_6/\text{MeCN}$. Coulometric study was carried out on 5 mL of a 10^{-3} M solution of **2.36** in anhydrous acetonitrile. Bulk electroreduction of **2.36** was carried using a fixed -1.5 V voltage and the charge was measured over time until less than 1% of the remaining current was present. The theoretical charge expected from one-electron reduction is 0.771 C and the observed charge at the end of the bulk electroreduction was 0.800 C.

Electron Paramagnetic Resonance (EPR) spectroscopic analyses: X-band EPR spectra were recorded on an X-band JEOL JES-X330 instrument using liquid nitrogen-cooled cryostat in 5 mm diameter quartz tubes. In a typical EPR experiment a 1 mM solution of the isolated or in situ generated (in case of electroreduction) Ni^{I} complex in acetone, Me-THF or mixture of acetone-MeTHF was placed into 5 mm diameter quartz EPR tube, precooled in liquid nitrogen and then quickly inserted into a pre-cooled EPR cavity. Simulation of the experimental EPR

spectrum were done using the Easyspin¹⁹⁸ package in Matlab R2015b¹⁹⁹. “Pepper” function was used for spectra simulation; g values and superhyperfine splitting constants were optimized using least-square fitting procedure in EasySpin (esfit function, Levenberg/Marquardt algorithm). The superhyperfine coupling constants and g tensor values are reported in the main text of the article.

X-ray diffraction studies: The X-ray diffraction data for the single crystals were collected on a Rigaku XtaLab PRO instrument (κ -goniometer) with a PILATUS3 R 200K hybrid pixel array detector using MoK α (0.71073 Å) radiation monochromated by means of multilayer optics. The performance mode of a MicroMaxTM-003 microfocus sealed X-ray tube was 50 kV, 0.60 mA. The diffractometer was equipped with a Rigaku GN2 system for low temperature experiments. Suitable crystals of appropriate dimensions were mounted on loops in random orientations. Preliminary unit cell parameters were determined with three sets of a total of 10 narrow frame scans. The data were collected according to recommended strategies in an ω -scan mode. Final cell constants were determined by global refinement of reflections from the complete data sets using the Lattice wizard module. Images were indexed and integrated with “smart” background evaluation using the *CrysAlis*^{Pro} data reduction package (1.171.39.7b, 1.171.39.20a or 1.171.39.46, Rigaku Oxford Diffraction). Analysis of the integrated data did not show any decay. Data were corrected for systematic errors and absorption using the AB-SPACK module: Numerical absorption correction based on Gaussian integration over a multifaceted crystal model and empirical absorption correction based on spherical harmonics according to the point group symmetry using equivalent reflections. The GRAL module and the ASSIGN SPACEGROUP routine of the *WinGX* suite were used for analysis of systematic absences and space group determination.

The structures were solved by the direct methods using *SHELXT*-2018/2²⁰⁶ and refined by the full-matrix least-squares on F^2 using *SHELXL*-2018/3²⁰⁷, which uses a model of atomic scattering based on spherical atoms. Calculations were mainly performed using *Olex2* (v 1.2.10)²⁰⁸ and the *WinGX*-2018.3 suite of programs.²⁰⁹ Non-hydrogen atoms were refined anisotropically. The positions of the hydrogen atoms at boron atoms B1 and B2 were determined by difference Fourier maps, and these atoms were refined isotropically. The positions of hydrogen atoms of methyl groups were found using rotating group refinement with idealized tetrahedral angles. The other hydrogen atoms were inserted at the calculated positions and refined as riding atoms.

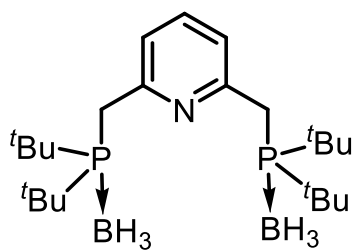
The absolute structure of the studied crystal **2.34** was determined by Parsons' method;²¹⁰ The Flack parameter was equal to 0.000(2) and calculated using 4617 selected quotients. Complexes **2.33** and **2.35** crystallize as hydrates (1:1); complexes **2.34**, **2.42**, and **2.43** crystallize as solvates with acetone (1:1). Some trifluoromethyl groups of tetrakis[3,5-bis(trifluoromethyl)phenyl]borate and the framework of the mentioned anion for **2.38** are found to be disordered. Complex **2.32** was refined with positional disorder of the bromide anion. Disorder of both the Cl anion and the water molecule over two positions was observed in the case of structure **2.33**. The Ni–Hal moieties of complexes **2.38** and **2.41** were disordered into two positions as well. The disorder was resolved using free variables and reasonable restraints on geometry and anisotropic displacement parameters. All the compounds studied have no unusual bond lengths and angles.

Detailed information about crystal structure determination can be accessed via supplementary cif files. The crystallographic data for the investigated compounds have been deposited in the Cambridge Crystallographic Data Centre as supplementary publication numbers CCDC 1885748 (**L2.3**), 1885747 (**L2.4**), 1885755 (**L2.6**), 1885758 (**2.32**), 1885751 (**2.33**), 1885754 (**2.34**), 1885752 (**2.35**), 1885750 (**2.36**), 1885757 (**2.37**), 1885759 (**2.38**), 1885756 (**2.39**), 1885745 (**2.40**), 1885749 (**2.41**), 1885746 (**2.42**), 1885753 (**2.43**).

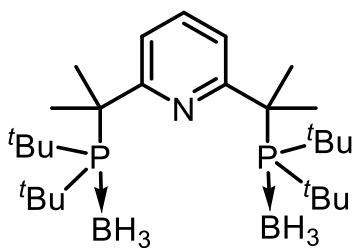
Computational analyses: DFT calculations were performed using Gaussian 09 rev. E.01²¹¹ using unrestricted or restricted open-shell B3LYP^{212, 213} functional. For C, H, N, P, 6-311++G** basis set was used; for Ni and halogens, LANL2DZ with ECP was used. For geometry optimizations, unrestricted calculations (UB3LYP) were performed using X-ray coordinates as a starting point; vibrational frequencies calculations were used to confirm the absence of imaginary frequencies. For analysis of SOMO, full population analysis was used using restricted open-shell formalism (ROB3LYP) and single point calculations using optimized geometries. The assignment of the SOMO as having essentially $d_{x^2-y^2}$ character was confirmed by NBO (Natural Bond Order) and NPA (Natural Population) analysis (NBO v. 3.0 incorporated in Gaussian 09 package).

The Cartesian coordinates of the geometry-optimized structures for complexes **2.40-2.43** are available in xyz format in the linked Appendix of Chapter 2 and at <https://pubs.acs.org/doi/10.1021/acs.organomet.9b00026>

The exact ligand solid angles were determined from both experimental X-ray coordinates as well as optimized geometries. A Mathematica²¹⁴ package, FindSolidAngle, written by the group of W. D. Allen⁸⁷ and freely available at www.ccqa.uga.edu, was used to compute the Ω° and Θ° parameters and produce the figures. The solid angles were computed using both the van der Waals atomic radii of Bondi and the zero energy point radii. However, the figures were prepared using the zero energy point radii. The atomic radii of Bondi that were used for the computation are as follow : $r(\text{\AA}) = 1.80, 1.20, 1.70, 1.55, 1.75$, and 1.85 for P, H, C, N, Cl, and Br respectively.²⁰² The zero energy point radii used for the computation are as follow : $r(\text{\AA}) = 1.801, 1.000, 1.539, 1.521, 1.599$, and 1.845 P, H, C, N, Cl, and Br respectively.²⁰¹

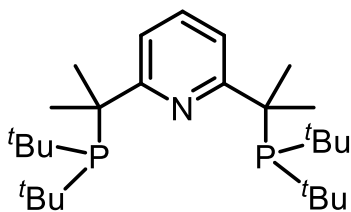
2.4.1 2,6-Bis(di-*tert*-butylphosphinomethyl)pyridine Boron Trihydride Adduct, L2.2.

Although this ligand was previously reported,²¹⁵ an alternative procedure was used to give the desired product that does not require further purification. In a flame-dried 500 mL round-bottom flask under Ar was added the precursor $\text{P}^t\text{Bu}_2\text{-BH}_3$ previously synthesized¹⁵⁸ (10.00 g, 62.48 mmol, 2.22 equiv) followed by 200 mL of dry THF, after which the temperature was lowered to 0°C. After 10 minutes of stirring, a 2.6 M solution of *n*-butyl lithium (26.24 mL, 68.66 mmol, 2.44 equiv). The reaction was stirred for 3 hours at room temperature, and 2,6-bis(chloromethyl)pyridine (4.955 g, 28.14 mmol, 1.00 equiv) was added, then the reaction was left to stir at room temperature overnight. Water was added to quench the reaction, and the aqueous phase was extracted with 3 portions of 150 mL of diethyl ether. The combined organic phases were washed with a saturated sodium hydrogen carbonate solution, then with a saturated brine solution. The organic phases were combined, dried over magnesium sulfate, filtered and evaporated under reduced pressure to afford a white crystalline solid (11.83 g, 88 %). Crystals suitable for X-ray analysis were obtained by slow evaporation of the ligand in THF at room temperature. ^1H NMR (400 MHz, CDCl_3): δ 0.15-0.76 (br m, 6H, P-BH_3), 1.25 (d, $J_{\text{PH}} = 12.9$ Hz, 36H, Me of ^tBu), 3.26 (d, $J_{\text{PH}} = 12.2$ Hz, $\text{P-CH}_2\text{C}_{\text{py}}$), 7.43 (d, $J_{\text{HH}} = 7.6$ Hz, 2H, $\text{C}_{\text{py-Hmeta}}$), 7.51 (dd, $J_{\text{HH}} = 8.5$ Hz, $J_{\text{PH}} = 6.8$ Hz, 1H, $\text{C}_{\text{py-Hpara}}$). $^{13}\text{C}\{^1\text{H}\}$ (101 MHz, CDCl_3): δ 28.27 (Me of ^tBu), 28.94 (vd, $J_{\text{PC}} = 23.4$ Hz, $\text{P-CH}_2\text{C}_{\text{py}}$), 32.85 (vd, $J_{\text{PC}} = 25.2$ Hz, C_{quat} of ^tBu), 123.77 ($\text{C}_{\text{py,meta}}$), 135.98 ($\text{C}_{\text{py,para}}$), 154.54 ($\text{C}_{\text{py,ortho}}$). $^{31}\text{P}\{^1\text{H}\}$ NMR (162 MHz, CDCl_3): δ 47.40, 47.76.

2.4.2 [2,6-Bis(2-di-*tert*-butylphosphino-2-propyl)pyridine Boron Trihydride Adduct,**L2.4.**

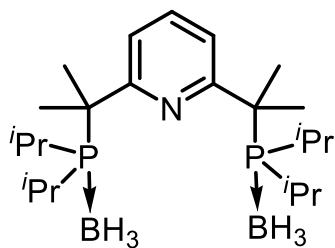
L2.2 (1.00 g, 2.36 mmol, 1.00 equiv) was added into a dry 250 mL round-bottom flask under Ar, to which was later added 100 mL of dry THF, and the entire solution was then cooled to 0 °C with an ice bath. Then, successively and with 2 minutes between

each addition, a 2.6 M solution of *n*-butyl lithium (0.9 mL, 2.4 mmol, 1.00 equiv) was slowly added, followed by iodomethane (147 μ L, 2.4 mmol, 1.00 equiv) for a total of 6 additions of both reagents. The reaction was further stirred at room temperature for 10 minutes and was quenched with 50 mL of water. The aqueous phase was separated and washed with 3 portions ethyl acetate (note: washing with diethyl ether gives similar yields if the extraction is done quickly). The organic phases were then washed with a saturated solution of sodium hydrogen carbonate followed by a saturated brine solution. The organic phases were combined, dried over magnesium sulfate, filtered, and concentrated under reduced pressure. The resulting slightly off-white solid was washed 3 times with a minimal amount of hexanes (1–2 mL) and the liquid was carefully decanted using a Pasteur pipet. The solid was then dried again under reduced pressure to afford a white solid (0.96 g, 85%). ^1H NMR (600 MHz, CDCl_3) δ 0.41–0.71 (br m, 6H, P–BH₃), 1.05–1.48 (br m, 36H, Me of *t*Bu), 1.92 (br s, 12H, PC–(CH₃)₂C_{py}), 7.57 (t, $J_{\text{HH}} = 8.0$ Hz, 1H, C_{py}–H_{para}), 7.90 (d, $J_{\text{HH}} = 8.0$ Hz, 2H, C_{py}–H_{meta}). $^{13}\text{C}\{^1\text{H}\}$ NMR (151 MHz, CDCl_3) δ 28.46 (d, $J_{\text{PC}} = 36.6$ Hz, C_{quat} of *t*Bu), 30.24 (br, Me of *t*Bu), 36.91 (d, $J_{\text{PC}} = 19.5$ Hz, P–C(CH₃)₂C_{py}), 45.68 (d, $J_{\text{PC}} = 14.7$ Hz, PC–(CH₃)₂C_{py}), 125.16 (C_{py,meta}), 135.59 (C_{py,para}), 161.19 (C_{py,ortho}). $^{31}\text{P}\{^1\text{H}\}$ NMR (162 MHz, CDCl_3) δ 63.99, 63.66. UV–vis (CH_2Cl_2 , $[1 \cdot 10^{-4} \text{ M}]$), λ_{max} , nm (ϵ , $\text{L} \cdot \text{mol}^{-1} \cdot \text{cm}^{-1}$): 263 (10500), 269 (12100), 276 (10000). Anal. Calcd. For $\text{C}_{27}\text{H}_{57}\text{B}_2\text{NP}_2$: C, 67.66; H, 12.06; N, 2.92. Found: C, 67.59; H, 12.01; N, 3.20.

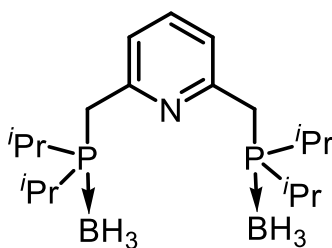
2.4.3 2,6-Bis(2-(di-*tert*-butylphosphino-2-propyl)pyridine, L2.6.

L2.4 (500 mg, 1.04 mmol) was put into a dry 100 mL Schlenk flask under Ar, to which 20 mL of pyrrolidine was then added in a N₂ glovebox. The solution was stirred at 90 °C for 18h followed by a thorough evaporation under reduced pressure (0.3 Torr) for at least 6 h to remove all traces of the pyrrolidine-BH₃ adduct and unreacted pyrrolidine (use of a second trap is recommended as pyrrolidine is corrosive), giving an off-white solid as the product (450mg, 96%). Colorless crystals suitable for X-ray diffraction study were grown by slow evaporation of a concentrated solution of the ligand in C₆D₆ under N₂. ¹H NMR (400 MHz, C₆D₆) δ 1.19 (d, *J*_{HP}= 10.0 Hz, 36 H, Me of *t*Bu), 1.83 (d, *J*_{HP} = 6.9 Hz, 12 H, PC-(CH₃)₂C_{py}), 7.17 (t, *J*_{HH}= 7.9 Hz, 1 H (overlaps with C₆D₆), C_{py}-H_{para}), 7.59 (d, *J*_{HH}= 7.9 Hz, 2H, C_{py}-H_{meta}). ¹³C{¹H} NMR (101 MHz, C₆D₆): δ 29.35 (br, PC-(CH₃)₂C_{py}), 32.46 (d, *J*_{PC}= 13.8 Hz, Me of *t*Bu), 35.10 (d, *J*_{PC}= 34.7 Hz, C_{quat} of *t*Bu), 45.31 (P-C(CH₃)₂C_{py}), 121.24 (d, *J*_{PC}= 16.2 Hz, C_{py,meta}), 135.03 (C_{py,para}), 167.30 (d, *J*_{PC}= 14.6 Hz, C_{py,ortho}). ³¹P{¹H} NMR (162 MHz, C₆D₆): δ 69.55.

2.4.4 2,6-Bis(di-isopropylphosphinomethyl)pyridine Boron Trihydride Adduct, L2.1.

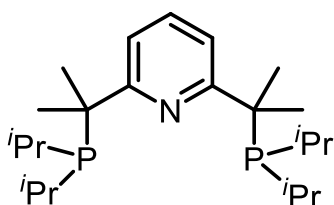


The analogous procedure to prepare **L2.2** was used to prepare this ligand. PH^{*i*}Pr₂-BH₃ (10.0 g, 76.9 mmol, 2.44 equiv), a 2.6 M solution of *n*-butyl lithium in *n*-hexane (26 mL, 69 mmol, 2.2 equiv) and 2,6-bis(chloromethyl)pyridine (4.95 g, 28.1 mmol, 1.00 equiv) was used to afford a white solid (10.47 g, 99 %). ¹H NMR (400 MHz, CDCl₃) δ 0.01–0.68 (br, m, 6H, P-BH₃), 1.13–1.19 (m, 12 H, PCH-CH₃), 2.03–2.16 (m, 4H, P-CHCH₃), 3.18 (d, *J*_{HH} = 11.24 Hz, 4H, P-CH₂C_{py}), 7.20 (d, *J*_{HH} = 7.7 Hz, 2H, C_{py}-H_{meta}), 7.56 (t, *J*_{HH} = 7.7 Hz, 1H, C_{py}-H_{para}). ¹³C{¹H} NMR (101 MHz, CDCl₃) δ 17.13 (d, *J*_{PC}= 36.9 Hz, PCH-CH₃), 21.87 (d, *J*_{PC} = 31.4 Hz, P-CHCH₃), 30.54 (d, *J*_{PC} = 26.5 Hz, P-CH₂C_{py}), 123.12 (C_{py,meta}), 136.79 (C_{py,para}), 154.43 (d, *J*_{PC}= 5.7 Hz, C_{py,ortho}). ³¹P{¹H} NMR (162 MHz, CDCl₃) δ 35.90, 36.38.

2.4.5 2,6-Bis(2-(di-isopropylphosphino-2-propyl)pyridine Boron Trihydride Adduct, L2.3

This ligand was prepared following the same procedure as for the preparation of **L2.4**. **L2.1** (1.00 g, 2.74 mmol), a 2.6 M solution of *n*-butyl lithium in *n*-hexane (1.05 mL, 2.74 mmol, 1.00 equiv) and iodomethane (171 μ L, 2.74 mmol, 1.00 equiv) were used to prepare

the ligand, affording a white crystalline solid (0.96 g, 83%). ^1H NMR (400 MHz, CDCl_3) δ 0.11–0.59 (br m, 6H, P–BH₃), 0.87 (dd, $J_{\text{HP}} = 13.0$ Hz, $J_{\text{HH}} = 7.1$ Hz, 12H, PCH–CH₃), 1.17 (dd, $J_{\text{HP}} = 13.9$ Hz, $J_{\text{HH}} = 7.2$ Hz, 12H, PCH–CH₃), 1.73 (d, $J_{\text{HP}} = 12.6$ Hz, 12H, P–(CH₃)₂C_{py}), 2.13–2.27 (m, 4H, P–CHCH₃), 7.46 (d, $J_{\text{HH}} = 8$ Hz, 2H, C_{py}–H_{meta}), 7.65 (t, $J_{\text{HH}} = 8$ Hz, 1H, C_{py}–H_{para}). $^{13}\text{C}\{^1\text{H}\}$ NMR (101 MHz, CDCl_3) δ 18.34 (PCH–CH₃), 19.23 (PCH–CH₃), 22.14 (d, $J_{\text{PC}} = 28$ Hz, P–CHCH₃), 26.66 (PC–(CH₃)₂C_{py}), 41.35 (d, $J_{\text{PC}} = 21.7$ Hz, P–C(CH₃)₂C_{py}), 121.28 (C_{py,meta}), 136.89 (C_{py,para}), 167.77 (C_{py,ortho}). $^{31}\text{P}\{^1\text{H}\}$ NMR (162 MHz, CDCl_3): δ 50.78, 50.29. ESI–HRMS (m/z) calculated for $[\text{C}_{23}\text{H}_{49}\text{NB}_2\text{P}_2 + \text{H}^+] = 424.3599$. Found for $[\text{C}_{23}\text{H}_{50}\text{NB}_2\text{P}_2 + \text{H}^+] = 424.3603$. UV–vis (CH_2Cl_2 , $[1 \cdot 10^{-4} \text{ M}]$), λ_{max} , nm (ϵ , $\text{L} \cdot \text{mol}^{-1} \cdot \text{cm}^{-1}$): 269 (7670). Anal. Calcd. For $\text{C}_{23}\text{H}_{49}\text{B}_2\text{NP}_2$: C, 65.27; H, 11.66; N, 3.31. Found: C, 65.22; H, 11.79; N, 3.84.

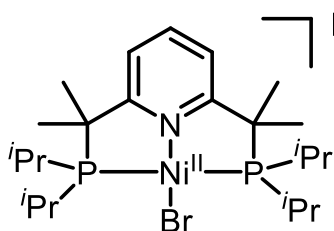
2.4.6 2,6-Bis(2-(di-isopropylphosphino-2-propyl)pyridine, L2.5.

L2.3 (40 mg, 0.095 mmol) was put into a dry 50 mL Schlenk flask under Ar, and 10 mL of pyrrolidine was added under N_2 . The solution was stirred at 90 $^\circ\text{C}$ for 18h followed by a thorough evaporation under reduced pressure (0.3 Torr) for at least 6 hours to re-

move all traces of the pyrrolidine- BH_3 adduct and unreacted pyrrolidine (use of a second trap is recommended as pyrrolidine is corrosive), giving a viscous colorless oil as the product (38 mg, 100%). ^1H NMR (400 MHz, C_6D_6) δ 0.90 (dd, $J_{\text{HP}} = 10.1$ Hz, $J_{\text{HH}} = 7.1$ Hz, 12H, PCH–

$\underline{\text{CH}}_3$), 1.15 (dd, $J_{\text{HP}} = 14.2$ Hz, $J_{\text{HH}} = 7.3$ Hz, 12H, $\text{PCH}-\underline{\text{CH}}_3$), 1.65 (d, $J_{\text{HH}} = 10.1$ Hz, 12H, $\text{PC}-(\underline{\text{CH}}_3)_2\text{C}_{\text{py}}$), 1.75–1.87 (m, 4H, $\text{P}-\underline{\text{CH}}\text{CH}_3$), 7.13 (s, 3H, $\text{C}_{\text{py}}-\underline{\text{H}}_{\text{meta}} + \text{C}_{\text{py}}-\underline{\text{H}}_{\text{para}}$). $^{13}\text{C}\{^1\text{H}\}$ NMR (101 MHz, C_6D_6) δ 20.36 (d, $J_{\text{PC}} = 9.9$ Hz, $\text{PCH}-(\underline{\text{CH}}_3)_2$), 22.68 (d, $J_{\text{PC}} = 23.3$ Hz, $\text{P}-\underline{\text{CH}}(\text{CH}_3)_2$), 23.48 (d, $J_{\text{PC}} = 22.1$ Hz, $\text{PCH}-(\underline{\text{CH}}_3)_2$), 27.53 (d, $J_{\text{PC}} = 13.7$ Hz, $\text{PC}-(\underline{\text{CH}}_3)_2\text{C}_{\text{py}}$), 41.49 (d, $J_{\text{PC}} = 24.3$ Hz, $\text{P}-\underline{\text{C}}(\text{CH}_3)_2\text{C}_{\text{py}}$), 118.58 (d, $J_{\text{PC}} = 8.1$ Hz, $\underline{\text{C}}_{\text{py,meta}}$), 135.67 ($\underline{\text{C}}_{\text{py,para}}$), 165.71 (d, $J_{\text{PC}} = 5.0$ Hz, $\underline{\text{C}}_{\text{py,ortho}}$). $^{31}\text{P}\{^1\text{H}\}$ NMR (162 MHz, C_6D_6) δ 43.46.

2.4.7 [(Me₄PNP^{*i*Pr})Ni^{II}Br][Br], 2.32.

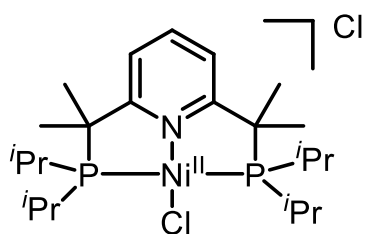


L2.3 (400 mg, 1.01 mmol) was added to a pre-dried Schlenk flask under Ar, and approximately 15 mL of pyrrolidine was added to this flask inside a glovebox after which time it was sealed and taken outside. The reaction was stirred for 24 hours

at 100 °C and then the pyrrolidine was evaporated under reduced pressure (0.3 Torr) for at least 6 hours (use of a second trap is recommended, as pyrrolidine is corrosive). The resulting deprotected ligand was a viscous oil that was taken back inside a glovebox and used directly without isolation for the metalation reaction, assuming a 100% conversion to deprotected form. Then, 20 mL of dry THF was added to the oil, followed by anhydrous nickel(II) bromide (232 mg, 1.06 mmol, 1.05 equiv). The mixture was stirred and heated at 60 °C overnight. After cooling, a cannula filtration was performed to remove the dark solution and give a solid that was washed two times with *n*-hexane and evaporated under reduced pressure to give a brown-orange powder (388 mg, 62%). Orange crystals suitable for X-ray diffraction were obtained by slow crystallization from an acetone solution of **2.1** at -30 °C. ^1H NMR (400 MHz, CDCl_3) δ 1.23–1.29 (m, 12H, $\text{PCH}-\underline{\text{CH}}_3$), 1.55–1.60 (m, 12H, $\text{PCH}-\underline{\text{CH}}_3$), 1.83–1.86 (m, 12H, $\text{PC}-\underline{\text{CH}}_3\text{C}_{\text{py}}$), 2.52–2.65 (m, 4H, $\text{P}-\underline{\text{CH}}\text{CH}_3$), 7.74 (d, $J_{\text{HH}} = 7.8$ Hz, 2H, $\text{C}_{\text{py}}-\underline{\text{H}}_{\text{meta}}$), 8.54 (t, $J_{\text{HH}} = 8.1$ Hz, 1H, $\text{C}_{\text{py}}-\underline{\text{H}}_{\text{para}}$). $^{13}\text{C}\{^1\text{H}\}$ NMR (101 MHz, CDCl_3) δ 19.26, ($\text{PCH}-\underline{\text{CH}}_3$), 19.79 ($\text{PCH}-\underline{\text{CH}}_3$), 23.45 (vt, $J_{\text{PC}} = 10.8$ Hz, $\text{P}-\underline{\text{CH}}\text{CH}_3$), 28.35 ($\text{PC}-(\underline{\text{CH}}_3)_2\text{C}_{\text{py}}$), 50.44 (vt, $J_{\text{PC}} = 8.1$ Hz, $\text{P}-\underline{\text{C}}(\text{CH}_3)_2\text{C}_{\text{py}}$),

121.76 (vt, $J_{\text{PC}} = 4.4$ Hz, $\underline{\text{C}}_{\text{py},\text{meta}}$), 145.20 ($\underline{\text{C}}_{\text{py},\text{para}}$), 172.74 (vt, $J_{\text{PC}} = 7.2$ Hz, $\underline{\text{C}}_{\text{py},\text{ortho}}$). $^{31}\text{P}\{^1\text{H}\}$ NMR (162 MHz, CDCl_3) δ 73.82. UV-vis (CH_2Cl_2 , $[1 \cdot 10^{-4}$ M]), λ_{max} , nm (ϵ , $\text{L} \cdot \text{mol}^{-1} \cdot \text{cm}^{-1}$): 261 (10100), 303 (3400), 347 (8240), 468 (1130). ATR-IR (cm^{-1}): 3039 (w), 2965 (m), 2896 (w), 2872 (w), 1589 (m), 1559 (w), 1455 (s), 1389 (s), 1367 (s), 1292 (s), 1241 (s), 1164 (w), 1133 (w), 1096 (w), 1034 (m), 1012 (w), 928 (m), 888 (m), 831 (s), 752 (w), 715 (w), 664 (s). ESI-HRMS (m/z) calculated for $[\text{C}_{23}\text{H}_{43}\text{NNiP}_2\text{Br}]^+ = 534.15$. Found for $[\text{C}_{23}\text{H}_{43}\text{NNiP}_2\text{Br}]^+ = 534.1367$. Anal. Calcd. For $\text{C}_{23}\text{H}_4\text{Br}_2\text{NP}_2\text{Ni}$: C, 44.99; H, 7.06; N, 2.28. Found: C, 44.98; H, 7.04; N, 2.33.

2.4.8 $[(\text{Me}_4\text{PNP}^{\text{iPr}})\text{Ni}^{\text{II}}\text{Cl}][\text{Cl}]$, **2.33**.

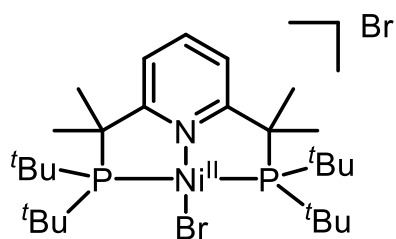


The procedure to prepare **2.32** was also used to prepare **2.33**. **L2.3** (500 mg, 1.18 mmol), and anhydrous nickel(II) chloride (153 mg, 1.18 mmol, 1.00 equiv) were used to afford a light-yellow powder (427 mg, 69% yield). Orange crystals suitable

for X-ray diffraction studies were obtained by vapor diffusion of hexanes into a concentrated solution of **2.33** in benzene at rt. Although stable under air, the product is highly hygroscopic, and as it was taken out of, and used outside the glovebox, water molecules were present in the elemental analysis and NMR, as well as in the X-ray structure. ^1H NMR. (400 MHz, acetone- d_6) δ 1.34 (d, $J_{\text{HH}} = 7.0$ Hz, 12H, $\text{PCH}-\underline{\text{CH}}_3$), 1.60 (d, $J_{\text{HH}} = 7.0$ Hz, 12H, $\text{PCH}-\underline{\text{CH}}_3$), 1.92 (br s, 12H, $\text{P}-\text{C}(\underline{\text{CH}}_3)_2\text{C}_{\text{py}}$), 2.61–2.72 (hept, $^3J_{\text{HH}} = 7$ Hz, 4H, $\text{P}-\underline{\text{CH}}\text{CH}_3$), 7.78 (d, $J_{\text{HH}} = 7.7$ Hz, 2H, $\text{C}_{\text{py}}-\underline{\text{H}}_{\text{meta}}$), 8.35 (t, $J_{\text{HH}} = 7.7$ Hz, 1H, $\text{C}_{\text{py}}-\underline{\text{H}}_{\text{para}}$). $^{13}\text{C}\{^1\text{H}\}$ NMR (101 MHz, acetone- d_6) δ 19.26 ($\text{PCH}-\underline{\text{CH}}_3$), 19.63 ($\text{PCH}-\underline{\text{CH}}_3$), 23.67 ($\text{P}-\underline{\text{CH}}(\text{CH}_3)_2$), 28.17 ($\text{PC}-\underline{\text{CH}}_3$), 50.52 ($\text{P}-\underline{\text{C}}(\text{CH}_3)_2\text{C}_{\text{py}}$), 122.20 ($\underline{\text{C}}_{\text{py},\text{meta}}$), 144.76 ($\underline{\text{C}}_{\text{py},\text{para}}$), 174.23 ($\underline{\text{C}}_{\text{py},\text{ortho}}$). Water present in hygroscopic sample of **2.2** was detected by NMR and X-ray. $^{31}\text{P}\{^1\text{H}\}$ NMR (162 MHz, CDCl_3) δ 71.38. UV-vis (CH_2Cl_2 , $1 \cdot 10^{-4}$ M]), λ_{max} , nm (ϵ , $\text{L} \cdot \text{mol}^{-1} \cdot \text{cm}^{-1}$): 259 (5430), 305 (3520), 338 (6970), 452 (903). ATR-IR (cm^{-1}): 2963 (m), 2871 (m), 1592 (w), 1563 (w), 1454 (s), 1387

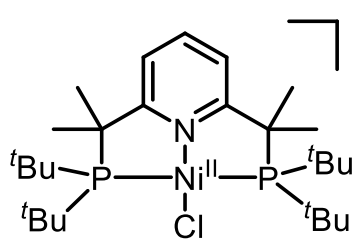
(m), 1638 (m), 1268 (w), 1167 (w), 1126 (w), 1099 (w), 1072 (w), 1032 (m), 931 (m), 884 (m), 828 (m), 759 (m), 696 (w), 665 (s). ESI–HRMS (m/z) calculated for $[\text{C}_{23}\text{H}_{43}\text{NNiP}_2\text{Cl}]^+ = 488.1904$. Found for $[\text{C}_{23}\text{H}_{43}\text{NNiP}_2\text{Cl}]^+ = 488.1895$. Anal. Calcd. For $\text{C}_{23}\text{H}_{43}\text{Cl}_2\text{NP}_2\text{Ni} \cdot \text{H}_2\text{O}$: C, 50.86; H, 8.35; N, 2.58 (according to X–ray, one water molecule per complex present in the crystalline sample of **2.33**). Found: C, 49.74; H, 8.13; N, 2.69. Deviation of %C could be due to hygroscopic nature of complex.

2.4.9 $[(\text{Me}_4\text{PNP}^{\text{tBu}})\text{Ni}^{\text{II}}\text{Br}][\text{Br}]$, **2.34**.



The analogous procedure to prepare **2.32** was used to prepare **2.34**. **L2.4** (359 mg, 0.749 mmol) and anhydrous nickel(II) bromide (164 mg, 0.749 mmol, 1.00 equiv) are reacted to afford a dark red powder (288 mg, 57%). Red crystals suitable

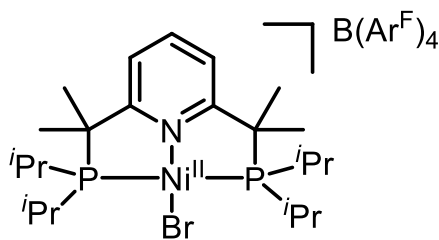
for X-ray diffraction were obtained by slow evaporation of an acetone solution of **2.34** at rt. ^1H NMR (400 MHz, acetone- d_6) δ 1.51–1.54 (br m, 18H, Me of ^tBu), 1.65–1.92 (br m, 18H, Me of ^tBu), 2.08–2.12 (br m, 6H, $\text{P}-\text{C}(\underline{\text{H}}_3)_2\text{C}_{\text{py}}$), 2.18–2.21 (br m, 6H, $\text{P}-\text{C}(\underline{\text{H}}_3)_2\text{C}_{\text{py}}$), 7.73 (d, $J_{\text{HH}} = 8$ Hz, 2H, $\text{C}_{\text{py}}-\underline{\text{H}}_{\text{meta}}$), 8.34 (tt, $J_{\text{HH}} = 8.0$ Hz, $J_{\text{HP}} = 1.6$ Hz, 1H, $\text{C}_{\text{py}}-\underline{\text{H}}_{\text{para}}$). $^{13}\text{C}\{^1\text{H}\}$ NMR (101 MHz, acetone- d_6) δ 24.98 ($\text{P}-\text{C}(\underline{\text{C}}\text{H}_3)_2\text{C}_{\text{py}}$), 32.20 (Me of ^tBu), 32.89 (br, Me of ^tBu), 36.00 ($\text{P}-\text{C}(\underline{\text{C}}\text{H}_3)_2\text{C}_{\text{py}}$), 40.11 (C_{quat} of ^tBu), 41.52 (C_{quat} of ^tBu), 53.32 ($\text{P}-\underline{\text{C}}(\text{CH}_3)_2\text{C}_{\text{py}}$), 121.93 ($\underline{\text{C}}_{\text{py,meta}}$), 145.04 ($\underline{\text{C}}_{\text{py,para}}$), 173.87 ($\underline{\text{C}}_{\text{py,ortho}}$). $^{31}\text{P}\{^1\text{H}\}$ (162 MHz, acetone- d_6) δ 87.00. ATR–IR (cm^{-1}): 3425 (w), 3377 (w), 2959 (m), 2903 (m), 2114 (w), 2080 (w), 1593 (m), 1457 (m), 1395 (s), 1365 (m), 1168 (s), 1019 (m), 935 (m), 919 (m), 829 (m), 806 (m), 767 (m), 745 (m). UV–vis (CH_2Cl_2 , $[1 \cdot 10^{-4} \text{ M}]$), λ_{max} , nm (ϵ , $\text{L mol}^{-1} \text{ cm}^{-1}$): 263 (15600), 363 (8820). 505 (1740). Anal. Calcd. For $\text{C}_{27}\text{H}_{51}\text{NP}_2\text{NiBr}_2$: C, 48.39; H, 7.67; N, 2.09. Found: C, 47.95; H, 7.29; N, 2.19.

2.4.10 [(Me₄PNP^{tBu})Ni^{II}Cl][Cl], **2.35.**

The same procedure to prepare **2.34** was used to prepare **2.35**.

L2.4 (500 mg, 1.04 mmol), and anhydrous nickel(II) chloride (135 mg, 1.04 mmol, 1.00 equiv) was used to afford a bright orange powder (516 mg, 85% yield). Yellow crystals suitable

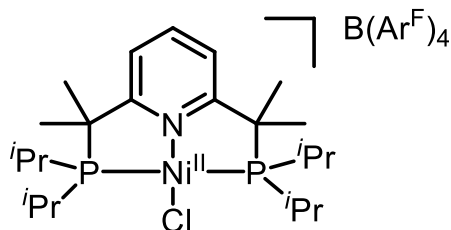
for X-ray diffraction studies were obtained by vapor diffusion of hexanes into a concentrated THF solution of **2.35** at rt. ¹H NMR (600 MHz, acetone-*d*₆) δ 1.43–1.61 (br m, 18H, Me of ^tBu), 1.65–1.91 (br m, Me of ^tBu), 2.06–2.13 (br m, 6H, P-C(CH₃)₂C_{py}), 2.14–2.24 (br m, 6H, P-C(CH₃)₂C_{py}), 7.77 (d, *J*_{HH} = 8.0 Hz, 2H, C_{py}-H_{meta}), 8.35 (t, *J*_{HH} = 8.0 Hz, C_{py}-H_{para}). ¹³C{¹H} NMR (151 MHz, acetone-*d*₆) δ 24.61 (PC-(CH₃)₂C_{py}), 31.89 (br, Me of ^tBu), 35.93 (br, PC-(CH₃)₂C_{py}), 39.95 (br, C_{quat} of ^tBu), 40.64 (br, C_{quat} of ^tBu), 52.82 (vt, *J*_{PC} = 5.4 Hz, P-C(CH₃)₂C_{py}), 121.86 (C_{py,meta}), 145.10 (C_{py,para}), 174.17 (C_{py,ortho}). ³¹P{¹H} (262 MHz, acetone-*d*₆) δ 83.63. ATR-IR (cm⁻¹): 2977 (m), 2962 (m), 2906 (m), 2872 (m), 1596 (w), 1565 (w), 1459 (s), 1395 (m), 1363 (s), 1276 (m), 1172 (s), 1136 (w), 1106 (w), 1067 (s), 1020 (m), 923 (m), 831 (w), 810 (m), 761 (m), 710 (w), 662 (w). UV-vis (CH₂Cl₂, [1·10⁻⁴ M]), λ_{max}, nm (ε, L mol⁻¹ cm⁻¹): 256 (7620), 308 (sh, 2980), 351 (9580), 481 (1360). ESI-HRMS (*m/z*) calculated for [C₂₇H₅₁NNiP₂Cl]⁺ = 544.2533. Found for [C₂₇H₅₁NNiP₂Cl]⁺ = 544.2520. Anal. Calcd. For C₂₇H₅₁NP₂NiCl₂ + 1 H₂O: C, 54.12; H, 8.91; N, 2.34. Found: C, 54.08; H, 8.90; N, 2.44. According to X-ray analysis, one water molecule per complex was present in crystalline sample of **2.35**.

2.4.11 [(Me₄PNP^{iPr})Ni^{II}Br][B(3,5-CF₃C₆H₃)₄], **2.36.**

To a solution of **2.32** (10.0 mg, 0.0163 mmol) in 10 mL of dry THF in a N₂ glovebox at room temperature was added sodium tetrakis[3,5-bis(trifluoromethyl)phenyl]borate (14.7 mg, 0.0163 mmol, 1.00 equiv), and the

solution was agitated by hand for 5 minutes. Then, the solution was filtered through a small Celite plug and concentrated under reduced pressure to afford a light orange solid (24 mg, 100%). Orange crystals suitable for X-ray diffraction analysis were obtained from vapor diffusion of hexanes into a concentrated THF solution of **2.36** at rt. ^1H NMR (400 MHz, acetone- d_6) δ 1.31–1.36 (m, 12H, PCH-**CH**₃), 1.58–1.64 (m, 6H, PCH-**CH**₃), 1.89–1.91 (m, 12H, PC-**CH**₃C_{py}), 2.68–2.78 (m, 4H, P-**CH**CH₃), 7.66 (br m, 6H total, BC_{Ar}-**H**_{para} (4H) + C_{py}-**H**_{meta} (2H)), 7.78 (br m, 8H, BC_{Ar}-**H**_{ortho}), 8.31 (tt, $J_{\text{HH}} = 8.0$ Hz, $J_{\text{PH}} = 1.3$ Hz, 1H, C_{py}-**H**_{para}). $^{13}\text{C}\{^1\text{H}\}$ NMR (101 MHz, acetone- d_6) δ 19.31 (PCH-**C**₃), 19.91 (PCH-**C**₃), 24.08 (vt, $J_{\text{PC}} = 11.2$ Hz, P-**C**CH₃), 28.29 (PC-(**C**₃)₂C_{py}), 51.08 (vt, $J_{\text{PC}} = 8.4$ Hz, P-**C**(CH₃)₂C_{py}), 118.46 (m, B-**C**_{Ar,para}), 121.85 (vt, $J_{\text{PC}} = 4.4$ Hz, **C**_{py,meta}), 125.37 (q, $J_{\text{CF}} = 273.1$ Hz, BC_{Ar,meta}-**C**F₃), 130.02 (m, B-**C**_{Ar,meta}CF₃), 135.53 (B-**C**_{Ar,ortho}), 144.45 (**C**_{py,para}), 162.59 (dd, $J_{\text{BC}} = 50.0$ Hz, B-**C**_{Ar,ipso}), 174.36 (vt, $J_{\text{PC}} = 7.1$ Hz, **C**_{py,ortho}). $^{31}\text{P}\{^1\text{H}\}$ NMR (162 MHz, acetone- d_6) δ 74.73. ^{19}F NMR (376.2 MHz, acetone- d_6) δ -63.13. ATR-IR (cm⁻¹): 2972 (w), 1610 (w), 1459 (w), 1353 (m), 1272 (s), 1115 (s), 885 (m), 839 (m), 715 (m), 682 (m), 668 (m). UV-vis (CH₂Cl₂, [1·10⁻⁴ M]), λ_{max} , nm (ϵ , L mol⁻¹ cm⁻¹): 262 (13100), 279 (sh, 7120), 307 (3030), 348 (7300), 469 (1040). Anal. Calcd. For C₅₅H₅₅NP₂NiBrBF₂₄: C, 47.27; H, 3.97; N, 1.00. Found: C, 45.38; H, 3.45; N, 1.38. Despite multiple attempts, we were unable to obtain satisfactory elemental analysis for this compound.

2.4.12 [(Me₄PNPⁱPr)^{II}NiCl][B(3,5-CF₃C₆H₃)₄], **2.37**.

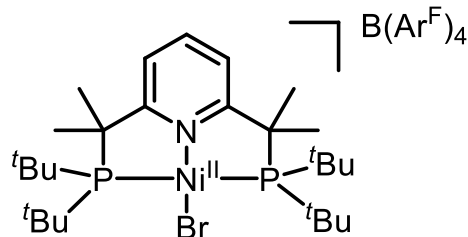


To a solution of **2.33** (100 mg, 0.190 mmol) in 10 mL of dry THF in a N₂ glovebox at room temperature was added sodium tetrakis[3,5-bis(trifluoromethyl)phenyl]borate (169 mg, 0.190 mmol, 1.00 equiv), and the

solution was stirred for 1 h. The reaction mixture was filtered through a small celite plug and concentrated under reduced pressure. The solid was then washed with approximately 3 mL of

diethyl ether and filtered on a short celite plug to afford an orange solid (226 mg, 88 %). Crystals suitable for X-ray diffraction were obtained by vapor diffusion of hexanes into a concentrated THF solution of **2.37** at rt. ^1H NMR (400 MHz, acetone- d_6) δ 1.30–1.35 (m, 12H, PCH- $\underline{\text{CH}_3}$), 1.56–1.62 (m, 12H, PCH- $\underline{\text{CH}_3}$), 1.88–1.90 (m, 12 H, PC- $\underline{\text{CH}_3}\text{C}_{\text{py}}$), 2.57–2.70 (m, 4H, P- $\underline{\text{CHCH}_3}$), 2.77 (br s, 1H, $\underline{\text{HDO}}$), 2.81 (br s, 1.5H, $\underline{\text{H}_2\text{O}}$) 7.62 (d, $J_{\text{HH}} = 8.1$ Hz, $\text{C}_{\text{py}}-\underline{\text{H}_{\text{meta}}}$), 7.64 (br s, 4H, $\text{BC}_{\text{Ar}}-\underline{\text{H}_{\text{para}}}$), 7.75–7.76 (m, 8H, $\text{BC}_{\text{Ar}}-\underline{\text{H}_{\text{ortho}}}$), 8.26 (tt, $J_{\text{HH}} = 7.9$ Hz, $J_{\text{HP}} = 1.3$ Hz, 1H, $\text{C}_{\text{py}}-\underline{\text{H}_{\text{para}}}$). $^{13}\text{C}\{^1\text{H}\}$ NMR (101 MHz, acetone- d_6) δ 19.20 (PCH-($\underline{\text{CH}_3}$) $_2$), 19.59 (PCH-($\underline{\text{CH}_3}$) $_2$), 23.66 (vt, $J_{\text{PC}} = 10.6$ Hz, P- $\underline{\text{CH}}(\text{CH}_3)_2$), 28.12 (PC-($\underline{\text{CH}_3}$) $_2\text{C}_{\text{py}}$), 50.52 (vt, $J_{\text{PC}} = 8.30$ Hz, P- $\underline{\text{C}}(\text{CH}_3)_2\text{C}_{\text{py}}$), 118.46 (m, B- $\underline{\text{C}_{\text{Ar,para}}}$), 121.85 (vt, $J_{\text{PC}} = 3.03$ Hz, $\underline{\text{C}_{\text{py,meta}}}$), 125.37 (q, $J_{\text{CF}} = 273.2$ Hz, $\text{BC}_{\text{Ar,meta}}-\underline{\text{CF}_3}$), 130.01 (qdd, $J_{\text{CF}} = 31.0$ Hz; $J_{\text{CB}} = 5.3$ Hz; $J_{\text{CF}} = 2.8$ Hz, B- $\underline{\text{C}_{\text{Ar,meta}}}\text{CF}_3$), 135.53 (B- $\underline{\text{C}_{\text{Ar,ortho}}}$), 144.40 ($\underline{\text{C}_{\text{py,para}}}$), 162.59 (dd, $J_{\text{BC}} = 50.0$ Hz, B- $\underline{\text{C}_{\text{Ar,ipso}}}$), 174.45 (vt, $J_{\text{PC}} = 7.47$ Hz, $\underline{\text{C}_{\text{py,ortho}}}$). $^{31}\text{P}\{^1\text{H}\}$ NMR (162 MHz, acetone- d_6) δ 72.23. ^{19}F NMR (376.2 MHz, acetone- d_6) δ -63.14. ATR-IR (cm^{-1}): 2974 (w), 1606 (w), 1465 (w), 1394 (w), 1354 (m), 1273 (s), 1160 (m), 1119 (s), 1035 (w), 931 (w), 885 (m), 838 (w), 813 (w), 752 (w), 713 (m), 670 (m). UV-vis (CH_2Cl_2 , [$1 \cdot 10^{-4}$ M]), λ_{max} , nm (ϵ , $\text{L mol}^{-1} \text{cm}^{-1}$): 260 (12500), 279 (sh, 6100), 307 (sh, 5650), 339 (11000), 454 (1410). ESI-HRMS (m/z) calculated for $[\text{C}_{23}\text{H}_{43}\text{NNiP}_2\text{Cl}]^+ = 488.1904$ and for $[\text{C}_{32}\text{H}_{12}\text{BF}_{24}]^- = 863.0643$. Found for $[\text{C}_{23}\text{H}_{43}\text{NNiP}_2\text{Cl}]^+ = 488.1900$ and for $[\text{C}_{32}\text{H}_{12}\text{BF}_{24}]^- = 863.0643$. Anal. Calcd. For $\text{C}_{55}\text{H}_{55}\text{BClF}_{24}\text{NNiP}_2$: C, 48.83; H, 4.10; N, 1.04. Found: C, 48.5; H, 4.07; N, 1.15.

2.4.13 $[(\text{Me}_4\text{PNP}^{\text{tBu}})\text{Ni}^{\text{II}}\text{Br}][\text{B}(\text{3,5-}\text{CF}_3\text{C}_6\text{H}_3)_4]$, **2.38**.

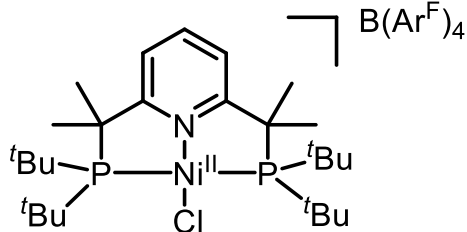


2.3 (20.0 mg, 0.0298 mmol) was dissolved in dry toluene in a 20 mL vial in the Ar glovebox. A few drops of anhydrous CH_2Cl_2 were added to facilitate dissolution. Sodium tetrakis[3,5-bis(trifluoromethyl)phenyl]borate

(26.4 mg, 0.298 mmol, 1.00 equiv) was added and the mixture agitated for 5 minutes. The

solution was filtered through a short celite plug, then concentrated to give a light pink solid (35 mg, 80 %). Red crystals suitable for X-ray diffraction studies were obtained by liquid diffusion of pentane into a concentrated THF solution of **2.38** at -30 °C. ^1H NMR (600 MHz, acetone- d_6) δ 1.48–1.56 (br m, 18H, Me of $t\text{Bu}$), 1.70–1.87 (br m, 18H, Me of $t\text{Bu}$), 2.07–2.11 (br m, 6H, PC-(CH_3) C_{py}), 2.17–2.22 (br m, 6H, PC-(CH_3) C_{py}), 7.64 (d, $J_{\text{HH}} = 7.9$ Hz, 2H, $\text{C}_{\text{py}}-\text{H}_{\text{meta}}$), 7.66 (br s, 4 H, $\text{BC}_{\text{Ar}}-\text{H}_{\text{para}}$), 7.77–7.78 (br m, 8H, $\text{BC}_{\text{Ar}}-\text{H}_{\text{ortho}}$), 8.28 (t, $J_{\text{HH}} = 7.9$ Hz, 1H, $\text{C}_{\text{py}}-\text{H}_{\text{para}}$). $^{13}\text{C}\{^1\text{H}\}$ NMR (151 MHz, acetone- d_6) δ 24.87 (PC-(CH_3) C_{py}), 32.20 (Me of $t\text{Bu}$), 33.04 (br, Me of $t\text{Bu}$), 36.07 (PC-(CH_3) C_{py}), 40.15 (C_{quat} of $t\text{Bu}$), 41.62 (C_{quat} of $t\text{Bu}$), 53.28 (vt, $J_{\text{PC}} = 4.4$ Hz, P- $\text{C}(\text{CH}_3)_2\text{C}_{\text{py}}$), 118.46 (m, B- $\text{C}_{\text{Ar,para}}$), 121.60 (br, $\text{C}_{\text{py,meta}}$), 125.38 (q, $J_{\text{CF}} = 272.0$ Hz, $\text{BC}_{\text{Ar,meta}}-\text{CF}_3$), 130.01 (qdd, $J_{\text{CF}} = 31.7$ Hz; $J_{\text{CB}} = 5.2$ Hz; $J_{\text{CF}} = 2.6$ Hz, B- $\text{C}_{\text{Ar,meta}}$ CF_3), 135.54 (B- $\text{C}_{\text{Ar,ortho}}$), 144.64 ($\text{C}_{\text{py,para}}$), 162.61 (q, $J_{\text{BC}} = \text{Hz}$, 50.0 Hz, B- $\text{C}_{\text{Ar,ipso}}$), 174.14 ($\text{C}_{\text{py,ortho}}$). $^{31}\text{P}\{^1\text{H}\}$ NMR (243 MHz, acetone- d_6) δ 87.28. $^{19}\text{F}\{^1\text{H}\}$ NMR (565 MHz, acetone- d_6) δ -63.15. ATR-IR (cm^{-1}): 3005 (w), 2976 (w), 2914 (w), 1605 (w), 1482 (w), 1397 (w), 1353 (m), 1273 (s), 1121 (s), 1017 (w), 928 (w), 888 (m), 838 (w), 806 (w), 746 (w), 714 (m), 871 (m). UV-vis (CH_2Cl_2 , [$1 \cdot 10^{-4}$ M]), λ_{max} , nm (ϵ , $\text{L mol}^{-1} \text{cm}^{-1}$) : 263 (9860), 363 (4370), 505 (811). ESI-HRMS (m/z) calculated for $[\text{C}_{27}\text{H}_{51}\text{NNiP}_2\text{Br}]^+ = 588.2028$ and for $[\text{C}_{32}\text{H}_{12}\text{BF}_{24}]^- = 863.0643$ Found for $[\text{C}_{27}\text{H}_{51}\text{NNiP}_2\text{Br}]^+ = 588.2014$ and for $[\text{C}_{32}\text{H}_{12}\text{BF}_{24}]^- = 863.0569$. Anal. Calcd. For $\text{C}_{59}\text{H}_{63}\text{B}_1\text{Br}_1\text{F}_{24}\text{N}_1\text{P}_2\text{Ni}_1$: C, 48.76; H, 4.37; N, 0.96. Found: C, 48.66; H, 4.34; N, 1.12.

2.4.14 $[(\text{Me}_4\text{PNP}^{t\text{Bu}})\text{Ni}^{\text{II}}\text{Cl}][\text{B}(\text{3,5-}\text{CF}_3\text{C}_6\text{H}_3)_4]$, **2.39**.

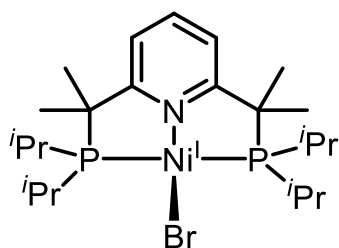


To a solution of **2.35** (100 mg, 0.172 mmol) in 10 mL of anhydrous THF in a N_2 glovebox at room temperature was added sodium tetrakis[3,5-bis(trifluoromethyl)phenyl]borate (152 mg, 0.172 mmol, 1.00 equiv),

and the solution was stirred for 1 h. The reaction mixture was filtered through a small Celite

plug and concentrated under reduced pressure. The solid was subsequently washed with approximately 3 mL of diethyl ether and filtered on a short celite plug to afford an orange solid (163 mg, 67 %). Red crystals suitable for X-ray diffraction studies were obtained by vapor diffusion of hexane into a concentrated THF solution of **2.39** at rt. ^1H NMR (600 MHz, acetone- d_6) δ 1.44–1.61 (br m, 18H, Me of $t\text{Bu}$), 1.64–1.91 (br m, 18H, Me of $t\text{Bu}$), 2.05–2.11 (br m, 6H, PC-($\underline{\text{CH}_3}$) $_2\text{C}_{\text{py}}$), 2.15–2.23 (br m, 6H, PC-($\underline{\text{CH}_3}$) $_2\text{C}_{\text{py}}$), 7.60 (d, $J_{\text{HH}} = 8.1$ Hz, 2H, $\text{C}_{\text{py}}-\underline{\text{H}_{\text{meta}}}$), 7.66 (br s, 4 H, $\text{BC}_{\text{Ar}}-\underline{\text{H}_{\text{para}}}$), 7.77–7.79 (m, 8H, $\text{BC}_{\text{Ar}}-\underline{\text{H}_{\text{ortho}}}$), 8.25 (tt, $J_{\text{HH}} = 8.1$ Hz, $J_{\text{HP}} = 1.1$ Hz, 1H, $\text{C}_{\text{py}}-\underline{\text{H}_{\text{para}}}$). $^{13}\text{C}\{^1\text{H}\}$ NMR (151 MHz, acetone- d_6) δ 24.53 (br, PC-($\underline{\text{CH}_3}$) $_2\text{C}_{\text{py}}$), 31.89 (br, Me of $t\text{Bu}$), 36.04 (br, PC-($\underline{\text{CH}_3}$) $_2\text{C}_{\text{py}}$), 40.03 (br, C_{quat} of $t\text{Bu}$), 40.79 (br, C_{quat} of $t\text{Bu}$), 52.77 (vt, $J_{\text{PC}} = 4.8$ Hz, P- $\underline{\text{C}}(\text{CH}_3)_2\text{C}_{\text{py}}$), 118.43–118.49 (m, B- $\underline{\text{C}_{\text{Ar,para}}}$), 121.39 (br, $\underline{\text{C}_{\text{py,meta}}}$), 125.40 (q, $J_{\text{CF}} = 272.0$ Hz, $\text{BC}_{\text{Ar}}-\underline{\text{CF}_3}$), 130.04 (qdd, $J_{\text{CF}} = 31.7$ Hz; $J_{\text{CB}} = 5.2$ Hz; $J_{\text{CF}} = 2.7$ Hz, B- $\underline{\text{C}_{\text{Ar,meta}}}\text{CF}_3$), 135.56 (B- $\underline{\text{C}_{\text{Ar,ortho}}}$), 144.59 ($\underline{\text{C}_{\text{py,para}}}$), 162.62 (dd, $J_{\text{BC}} = 49.83$ Hz, B- $\underline{\text{C}_{\text{Ar,ipso}}}$), 174.46 ($\underline{\text{C}_{\text{py,ortho}}}$). $^{31}\text{P}\{^1\text{H}\}$ NMR (242.95 MHz, acetone- d_6) δ 83.92. $^{19}\text{F}\{^1\text{H}\}$ NMR (564.73 MHz, acetone- d_6) δ -63.14. ATR-IR (cm^{-1}): 2975 (w), 2912 (w), 1743 (w), 1606 (w), 1569 (w), 1486 (w), 1396 (w), 1353 (m), 1273 (s), 1119 (s), 1018 (w), 929 (w), 887 (m), 837 (w), 806 (w), 745 (w), 713 (m), 672 (m). UV-vis (CH_2Cl_2 , $[1 \cdot 10^{-4} \text{ M}]$), λ_{max} , nm (ϵ , $\text{L mol}^{-1} \text{ cm}^{-1}$): 261 (15700), 278 (sh, 7590), 309 (sh, 4260), 351 (14000), 481 (1910). ESI-HRMS (m/z) calculated for $[\text{C}_{27}\text{H}_{51}\text{NNiP}_2\text{Cl}]^+ = 544.2533$ and for $[\text{C}_{32}\text{H}_{12}\text{BF}_{24}]^- = 863.0643$ Found for $[\text{C}_{23}\text{H}_{43}\text{NNiP}_2\text{Cl}]^+ = 544.2525$ and for $[\text{C}_{32}\text{H}_{12}\text{BF}_{24}]^- = 863.0638$. Anal. Calcd. For $\text{C}_{59}\text{H}_{63}\text{BClF}_{24}\text{NNiP}_2$: C, 50.29; H, 4.51; N, 0.99. Found: C, 48.93; H, 4.15; N, 1.10.

2.4.15 ($\text{Me}_4\text{PNP}^{i\text{Pr}}$) $\text{Ni}^{\text{I}}\text{Br}$, **2.40**.

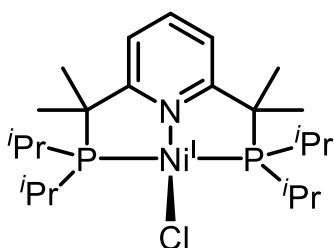


Method 1: Chemical Reduction Using CoCp_2 To a solution of **2.32** (50.0 mg, 0.081 mmol) in dry acetone was added cobaltocene (15.4 mg, 0.081 mmol, 1.00 equiv) at room temperature. The solution turns dark red immediately and after 5 minutes of stirring,

the solution was filtered through a short Celite plug. The acetone was evaporated to afford a red solid (34.5 mg, 79% yield). Red crystals suitable for X-ray diffraction studies were obtained by cooling down a solution of **2.40** in acetone- d_6 at $-30\text{ }^{\circ}\text{C}$ under N_2 . Crystals of the complex in an acetone or mixture was characterized by EPR spectroscopy (see main text). ^1H NMR (400 MHz, C_6D_6) δ 44.01 (br), 34.38 (br, s), 5.02 (br, s), 4.02 (br, s), 1.56 (s), -0.20 (br, s), -51.45 (br, s). ATR-IR (cm^{-1}): 3055 (w), 2954 (s), 2923 (m), 2866 (s), 2717 (w), 2110 (w), 2073 (w), 1888 (w), 1809 (w), 1709 (w), 1581 (w), 1559 (w), 1452 (s), 1382 (m), 1296 (w), 1231 (m), 1183 (w), 1156 (w), 1084 (w), 1035 (m), 1003 (m), 954 (w), 928 (w), 867 (m), 808(s), 746 (s), 663 (s). UV-vis (THF, $[1 \cdot 10^{-4}\text{ M}]$), λ_{max} , nm (ϵ , $\text{L mol}^{-1}\text{ cm}^{-1}$): 237 (9630), 263 (10700), 298 (sh, 6650), 464 (1430), 529 (941).

Method 2: Generation of Ni^{I} Complex by Electrochemical Reduction and Coulometric Analysis. Ni^{I} complex **2.40** was prepared via bulk electrolysis at the same time as a coulometric analysis was performed. A voltage of -1500 mV was applied (using an Ag/AgNO_3 reference electrode, a platinum gauze working electrode and a platinum gauze counter-electrode) to a yellow solution of **2.36** ($1 \cdot 10^{-3}\text{ M}$ using $0.1\text{ M } n\text{Bu}_4\text{NPF}_6$ in dry CH_3CN as the electrolyte). The voltage was applied for 1830 s, until the current measured was less than 1% of the starting current (charge measured = 0.800 C , theoretical charge for 1 electron reduction = 0.771 C). At that point the solution had become brown. The nature of the product formed was confirmed by comparing its low temperature EPR spectra and g tensor values with those from the chemically reduced **2.40** (see main text).

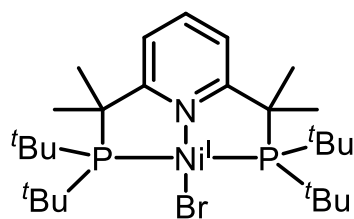
2.4.16 ($\text{Me}_4\text{PNP}^{\text{iPr}}$) $\text{Ni}^{\text{I}}\text{Cl}$, **2.41**.



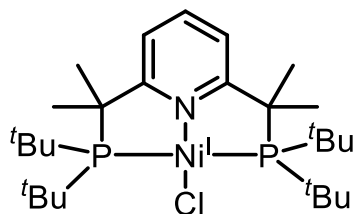
The complex was prepared via method 1 described for the preparation of complex **2.40** above, using the following quantities: **2.33** (70.0 mg, 0.133 mmol) and cobaltocene (25.2 mg, 0.133 mmol, 1.00 equiv) gave a dark red powder (55.4 mg, 85%). Red crystals

of **2.41** were obtained in the same way as described in method 1 for the preparation of **2.40**. The complex solution in 20% acetone/MeTHF was analyzed by EPR spectroscopy (See main text). ^1H NMR (400 MHz, C_6D_6): δ 44.07 (br), 36.64 (br, s), 4.77 (br, s), 3.92 (br, s), 3.11 (s), 0.30 (br, s), -51.52 (br, s). ATR-IR (cm^{-1}): 3069 (w), 2983 (m), 2960 (m), 2943 (m), 2922(m), 2893 (m), 1712 (w), 1584 (w), 1539 (w), 1464 (m), 1451 (m), 1413 (m), 1388 (m), 1380 (m), 1364 (w), 1234 (w), 1220 (w), 1188 (w), 1156 (w), 1109 (w), 1087 (w), 1040 (m), 1016 (w), 996 (m), 958 (w), 950 (w), 925 (w), 895 (w), 879 (m), 810 (m), 779 (s), 753 (s), 732 (w), 668 (s). UV-vis (THF, $[1 \cdot 10^{-4} \text{ M}]$), λ_{max} , nm (ϵ , $\text{L mol}^{-1} \text{ cm}^{-1}$): 233 (19200), 260 (16200), 294 (sh, 9680), 338 (9440), 480 (1070). Anal. Calcd. For $\text{C}_{23}\text{H}_{43}\text{ClNNiP}_2$: C, 56.41; H, 8.85; N, 2.86. Found: C, 55.81 H, 7.75; N, 2.27.

2.4.17 ($\text{Me}_4\text{PNP}^{\text{tBu}}$) $\text{Ni}^{\text{I}}\text{Br}$, **2.42**.



The complex was prepared following the method 1 used to prepare complex **2.40** using the following quantities: **2.34** (40.0 mg, 0.060 mmol) and cobaltocene (11.3 mg, 0.060 mmol, 1.00 equiv) and gave a red powder (26.1 mg, 65% yield). Dark orange crystals of complex **2.42** were obtained by crystallization of a concentrated solution in acetone- d_6 at -30°C under N_2 . The complex solution in 20% acetone/MeTHF was analyzed by EPR spectroscopy (See main text). ^1H NMR (400 MHz, C_6D_6): δ 11.12 (br, s), 5.24 (br, s), 1.97 (br, s), -51.50 (br, s). ATR-IR (cm^{-1}): 3329 (w), 3057 (w), 2991 (m), 2955 (m), 2891 (m), 2864 (m), 2708 (w), 2656 (w), 2111 (w), 1701 (w), 1558 (w), 1486 (m), 1443 (m), 1388 (s), 1359 (m), 1251 (w), 1217 (w), 1172 (m), 1106 (m), 995 (m), 947 (w), 931 (w), 891 (w), 858 (w), 808 (m), 776 (s), 757 (s), 726 (w), 680 (w). UV-vis (THF, $[1 \cdot 10^{-4} \text{ M}]$), λ_{max} , nm (ϵ , $\text{L mol}^{-1} \text{ cm}^{-1}$): 261 (12000), 328 (8840), 499 (1100).

2.4.18 (Me₄PNP^{*t*Bu})Ni^ICl, **2.43.**

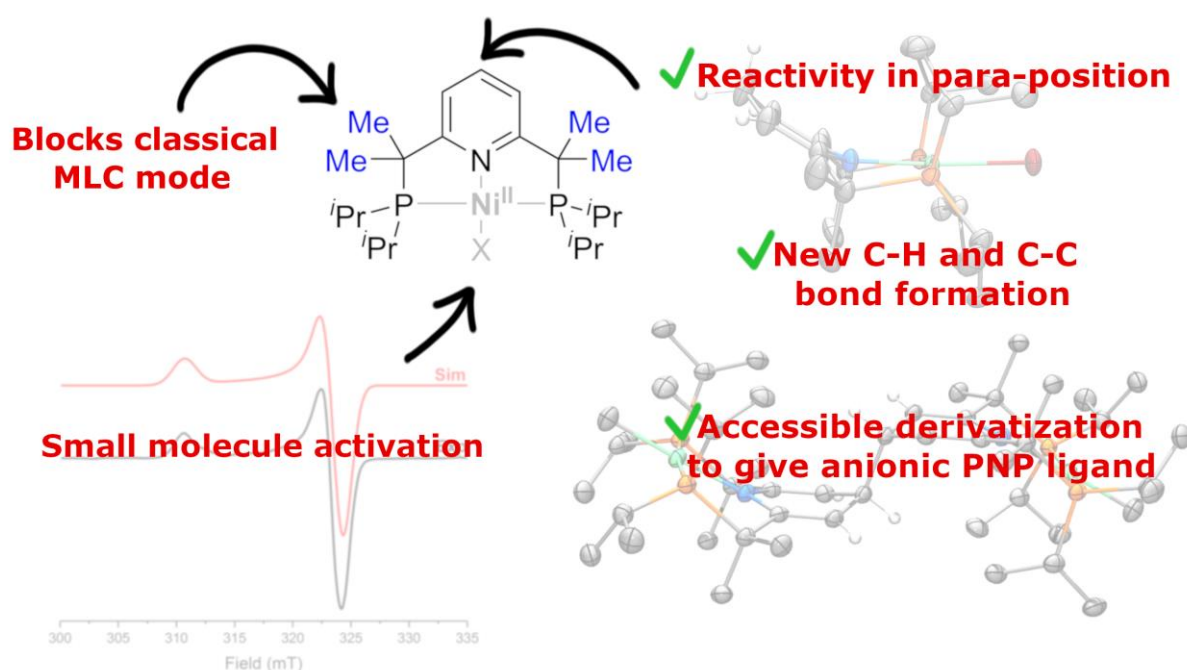
The complex was prepared via method 1 described for the preparation of complex **2.40** above, except that a 2 h mixing time was needed, using the following quantities: **2.35** (25.0 mg, 0.043 mmol) and cobaltocene (8.1 mg, 0.043 mmol, 1.00 equiv). A dark red powder (20.7 mg, 88 % yield) was obtained. Dark red crystals of **2.43** were obtained in the same way as described in method 1 for the preparation of **2.40**. The complex solution in 35% acetone/MeTHF was analyzed by EPR spectroscopy (See main text). ¹H NMR (400 MHz, C₆D₆) δ 12.09 (br, s), 6.23 (br, s), -51.52 (br, s). ATR-IR (Solid state, cm⁻¹): 3057 (w), 2979 (m), 2960 (m), 2894 (m), 2872 (m), 1702 (m), 1595 (m), 1579 (w), 1563 (w), 1470 (m), 1461 (m), 1450 (m), 1409 (w), 1395 (m), 1364 (m), 1253 (m), 1212 (w), 1196 (w), 1171 (m), 1137 (m), 1107 (m), 1018 (m), 987 (w), 978 (m), 932 (w), 903 (w), 891 (w), 831 (m), 806 (s), 763 (m), 758 (m), 746 (m), 724 (w), 661 (m), 654 (m). UV-vis (THF, [1·10⁻⁴ M]), λ_{max}, nm (ε, L mol⁻¹ cm⁻¹): 267 (12800), 334 (3220), 462 (508).

Declaration of Contribution from Co-Authors

The following chapter contains contributions from Dr. Eugene Khaskin, Dr. Robert R. Fayzullin and Pr. Dr. Julia R. Khusnutdinova as described below. Pr. Dr. Julia R. Khusnutdinova guided the project and helped with analysis of experimental and computational data. Dr. Eugene Khaskin initially developed the synthesis of the ligands. Dr. Robert R. Fayzullin finalized every X-ray structural measurement to publication level. The author performed synthesis and characterization of all complexes described within this chapter, performed DFT calculations, and analyzed and simulated most reported spectra, with the help of Pr. Dr. Julia R. Khusnutdinova.

3 Chapter 3:

Changing Metal-Centered Reactivity to Ligand-Centered Reactivity by Modifying Electronics and Sterics at the Nickel Center



Part of this content was published in the following article. Reprinted and adapted with permissions from: Lapointe, S.; Khaskin E.; Fayzullin R. R.; Khusnutdinova J. R. *Organometallics* **2019**, 38 (22), 4433-4447. Copyright **2019** American Chemical Society

3.1 Introduction to Nickel Hydride and Methyl Pincer Complexes

Following the work done in Chapter 2 on halide complexes of Ni^{II} and their reactivity towards reductants, I decided to alter the ligands at the metal center, which may affect its reactivity and electronic properties. Changing halide to hydride or methyl on the nickel center can open a lot of diverse reactivity, as they both are known to react with small molecules, particularly for hydride species. They are also known to be catalytically relevant reactive species, as will be discussed below. Moreover, methyl species can show interesting reduction or oxidation behaviors, which sometimes differ from their halide analogues.

3.1.1 Nickel Hydride Pincer Complexes and their Reactivity

Many examples of nickel pincer hydrides exist in the literature, and Figure 3.1 shows selected examples of pincer nickel hydride complexes.

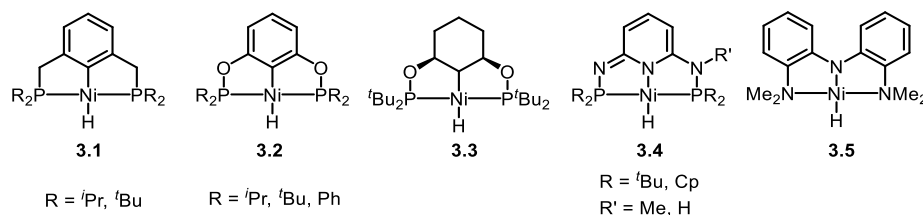
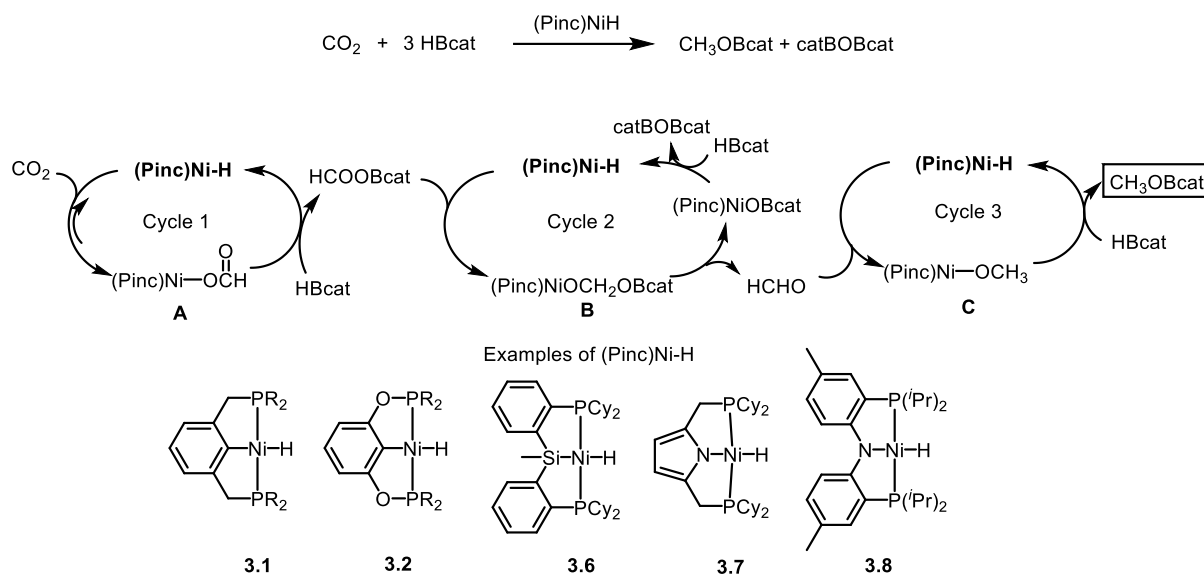


Figure 3.1 Examples of pincer nickel hydride complexes in the literature.^{27, 59, 216-219}

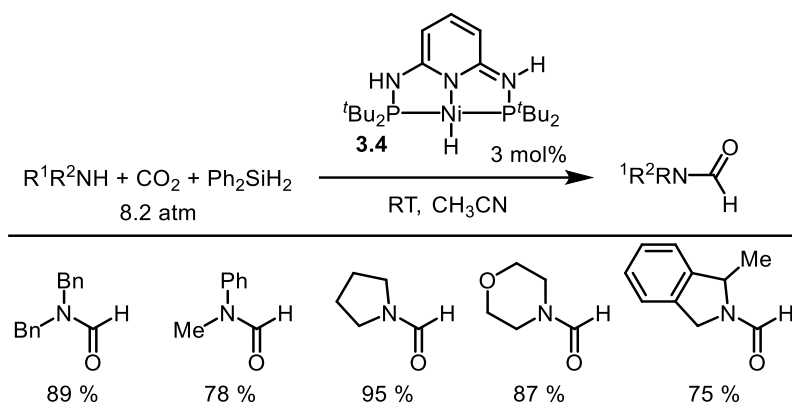
Small molecules, such as CO₂, are well-known to insert into the nickel hydride bond, forming nickel formate species which is one of the steps in the reduction of CO₂ to methanol in the presence of a hydrogen donor. One of the possible hydrogen donors in CO₂ reduction chemistry is catecholborane, which forms CH₃OBcat, a product one step away from the formation of methanol. The general scheme of CO₂ reduction to CH₃OBcat is shown in Scheme 3.1 with examples of nickel hydride pincers that can catalyze the reactions. The conversion of CO₂ to the methanol precursor CH₃OBcat involves three parallel catalytic cycles, forming a formate species **A** via reaction with CO₂, which forms HCO₂Bcat by reaction with 1 equivalent of HBcat. That HCO₂Bcat species reacts with the regenerated hydride species to form an alkoxy species **B**. This

species then releases formaldehyde and forms an oxyborane species that also reacts with HBcat to regenerate the hydride catalyst and form an inactive borane species catBOBcat. The formaldehyde previously formed again reacts with the hydride catalyst to form a methoxy species **C** that finally reacts with a third equivalent of HBcat to give CH₃OBcat as the desired methanol precursor.²²⁰

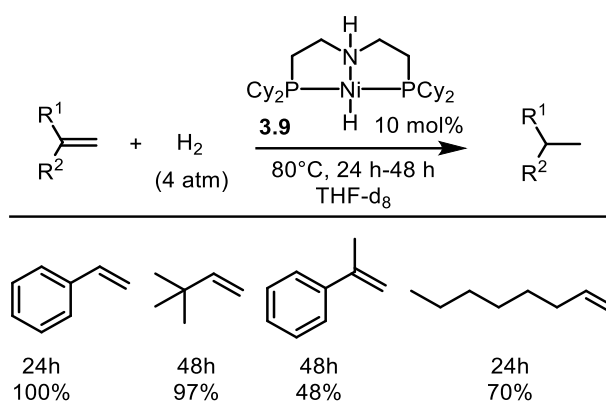


Scheme 3.1. Reduction of CO₂ with catecholborane catalyzed by nickel pincer hydride complexes.²²⁰

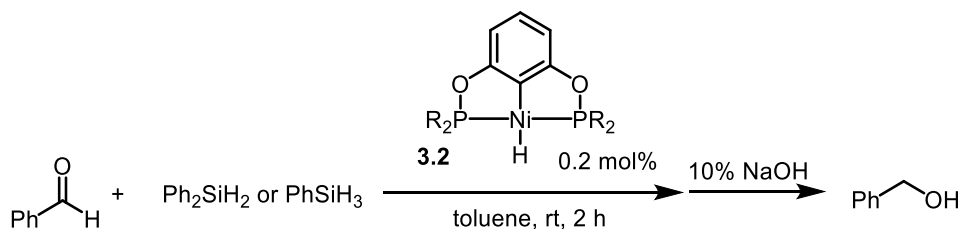
Nickel pincer hydrides are also used as catalysts for other reactions, such as formylation of amines²¹⁹ (Scheme 3.2), alkene hydrogenation²²¹ (Scheme 3.3) and hydrosilylation of benzaldehyde²⁷ (Scheme 3.4).



Scheme 3.2 Selected examples of formylation of amines using CO_2 and Ph_2SiH_2 catalyzed by **3.4**.²¹⁹

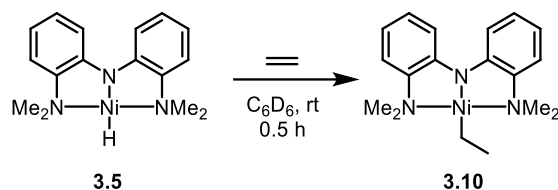


Scheme 3.3 Selected examples of the hydrogenation of alkenes catalyzed by **3.9**.²²¹



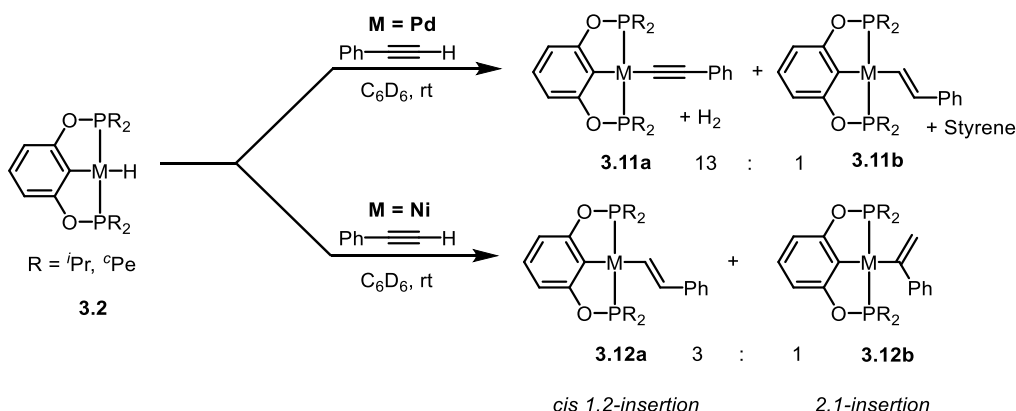
Scheme 3.4 Hydrosilylation of benzaldehyde catalyzed by **3.2**.²⁷

Ethylene and phenylacetylene are also known to insert into nickel hydride bonds of pincer complexes. For example, the group of Hu in 2012 reported the insertion of ethylene into the nickel hydride bond of **3.5** to form the ethyl bound complex **3.10** quickly at room temperature⁵⁹ (Scheme 3.5).



Scheme 3.5 Reaction of the nickel pincer hydride complex **3.5** with ethylene to form **3.10**.⁵⁹

In the case of phenylacetylene, the reactivity with nickel pincer hydrides differs from the reactivity of the analogous palladium complex. For example, in 2015 the group of Guan studied the reaction of a POCOP palladium hydride species with phenylacetylene and obtained mostly an alkynyl product (**3.11a**) with a small amount of the (*E*)-alkenyl product (**3.11b**), whereas the reaction of the nickel pincer hydride with the same ligand resulted in either the 2,1-insertion product (**3.12a**) or the *cis* 1,2-insertion product (**3.12b**) with a different ratio depending on the nature of the phosphine substituent (See Scheme 3.6).²²²



Scheme 3.6 Difference of reactivity between phenylacetylene and palladium or nickel PCOP hydride complexes.²²²

3.1.2 Nickel Methyl Pincer Complexes and Their Reactivities

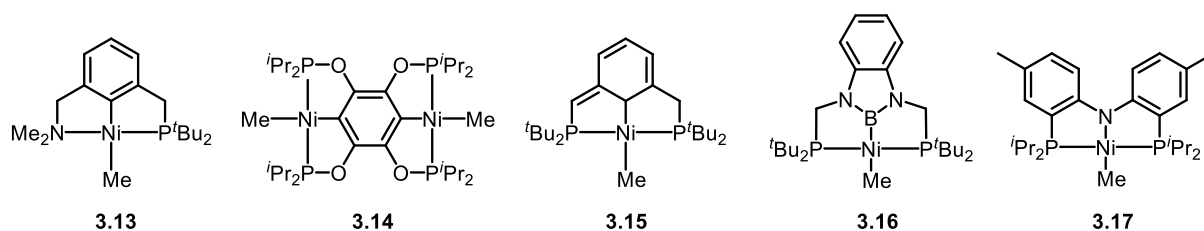
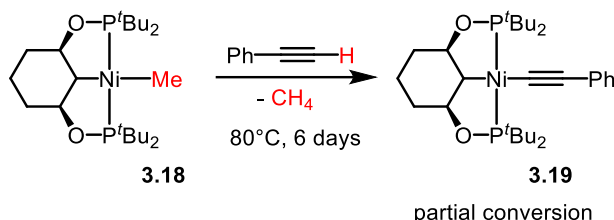


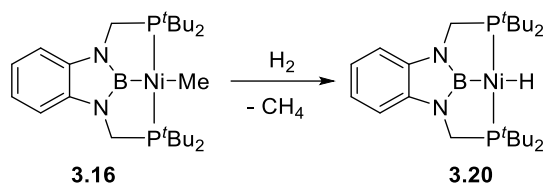
Figure 3.2 Examples of pincer nickel methyl complexes in the literature.^{177, 223-226}

Methyl pincer complexes of nickel are relatively common (see examples in Figure 3.2) and can easily be prepared via methylation of the halide precursor via MeLi at low temperatures in high purity. Nickel methyl complexes are proposed to be intermediates in C-C coupling reactions¹⁶², as well as showing some reactivity with small molecules such as CO₂, CO and acetylene, and generally found to be less reactive than their hydride analogues. For example, complex **3.15** reacts with phenylacetylene to form the alkynyl complex **3.19** with the formation of methane, but the complex does not show full conversion even after 6 days at 80 °C²²⁷ (Scheme 3.7).



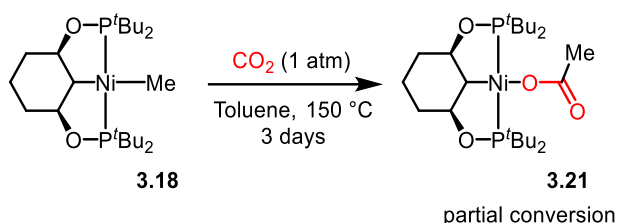
Scheme 3.7 Reactivity of **3.17** towards phenylacetylene to form the phenylacetylene-bound complex **3.18** with elimination of methane.²²⁷

In comparison, the analogous hydride species **3.3** shown in Figure 3.1 gives multiple phosphorus-containing products, with **3.19** being only a minor product. Similarly to the reactivity seen in Scheme 3.7, reaction of the pincer nickel methyl complex **3.16** with H₂ also gave back the hydride species **3.20** and methane²²⁶ (Scheme 3.8).



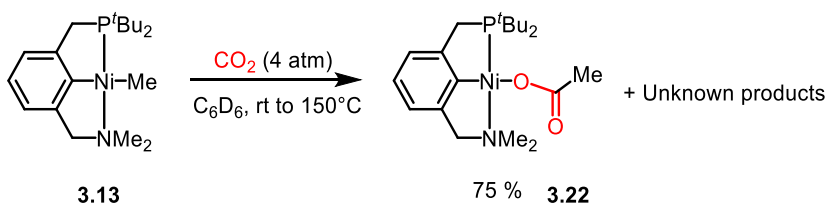
Scheme 3.8 Reactivity of **3.16** towards H_2 to form the hydride **3.20** with elimination of methane.²²⁶

A stark reactivity contrast can be observed when comparing rates of insertion of CO_2 . For example, the nickel pincer hydride complex **3.3** inserts CO_2 at room temperature in under 1 hour, while the methyl complex **3.18** requires heating at 150°C and only partial conversion to **3.21** is seen after 3 days (Scheme 3.9).



Scheme 3.9 Insertion of CO_2 into the nickel methyl bond of **3.18** to form **3.21**.²²⁷

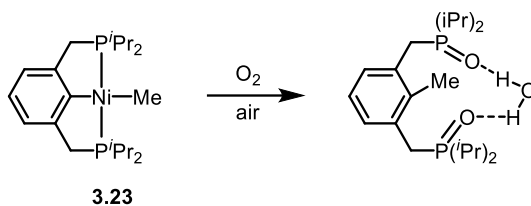
Insertion of CO_2 is also possible with aromatic PCN nickel complex **3.13**. In this case, the reaction requires temperatures up to 150°C and 4 atmospheres of CO_2 (compared to 1 atmosphere for **3.21**) to form **3.22** with some other unidentified products.²²³



Scheme 3.10 Insertion of CO_2 into the nickel methyl bond of **3.13** to form **3.21**.²²³

Literature examples of reaction between nickel methyl pincer complexes and oxygen are much less prevalent than with CO_2 or CO. For example, in 2012 the group of Cámpora let the nickel methyl PCP pincer complex **3.23** crystallize in air and the product of the reductive coupling of

methyl group and the benzene pincer ligand, with oxidized phosphines on the arm, was obtained²²⁸ (complex **3.23**, Scheme 3.11).

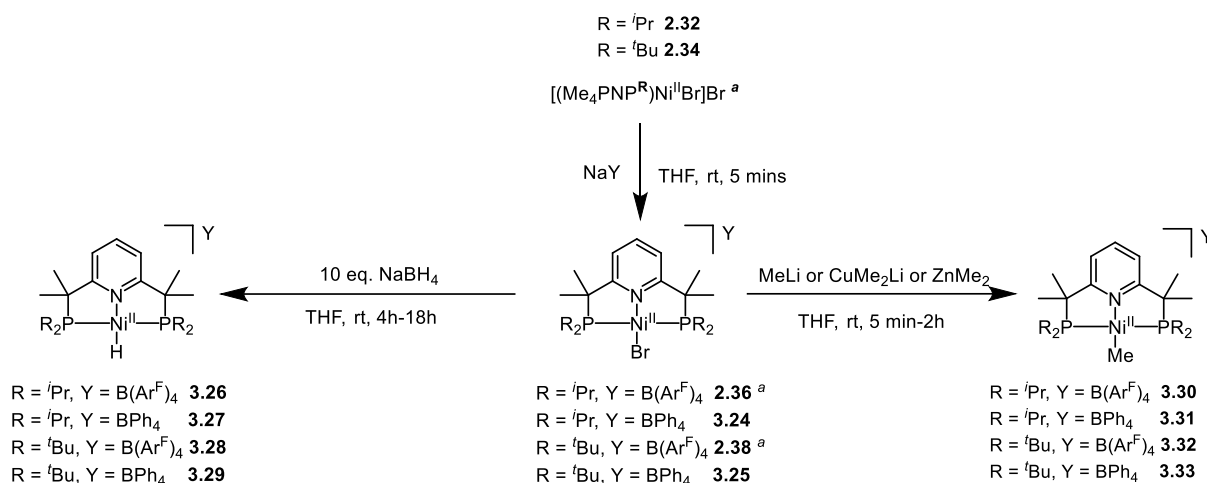


Scheme 3.11 Reaction of the nickel methyl PCP pincer complex **3.23** with O₂ from air to form a decomposition product.²²⁸

3.2 Results and Discussion

3.2.1 Synthesis and Characterization of Nickel(II) Complexes

The Ni^{II} complexes were prepared by reacting the Ni^{II} bromo complexes [(Me₄PNP^R)NiBr]Br (R = *i*Pr (**2.32**), *t*Bu (**2.34**))²²⁹ with either sodium tetraphenylborate (NaBPh₄) or NaB(Ar^F)₄ in anhydrous THF to form [(Me₄PNP^R)NiBr]BPh₄ (R = *i*Pr (**3.24**), *t*Bu (**3.25**)) or previously reported [(Me₄PNP^R)NiBr]B(Ar^F)₄ (R = *i*Pr (**2.36**), *t*Bu (**2.38**))²²⁹ (Scheme 3.12). Reacting these complexes with 10 equivalents of NaBH₄ in anhydrous THF over 4–18 h produced the hydride complexes [(Me₄PNP^R)NiH]BPh₄ (R = *i*Pr (**3.27**), *t*Bu (**3.29**)), and [(Me₄PNP^R)NiH]B(Ar^F)₄ (R = *i*Pr (**3.26**), *t*Bu (**3.28**)) in high yields. Reacting complexes **2.36**, **2.38** and **3.24–3.25** with either MeLi, lithium dimethylcuprate (CuMe₂Li), or dimethylzinc (ZnMe₂) over a 5 minutes to 2 hour period formed the methyl complexes [(Me₄PNP^R)NiMe]BPh₄ (R = *i*Pr (**3.31**), *t*Bu (**3.33**)), and [(Me₄PNP^R)NiMe]B(Ar^F)₄ (R = *i*Pr (**3.30**), *t*Bu (**3.32**)) in 80% to 97% yield (Scheme 3.12).



Scheme 3.12 Preparation of Ni^{II} cationic complexes **2.36**, **2.38**, and **3.24–3.33**. ^a Complexes were previously reported.²²⁹

The use of mild methylating reagent, such as ZnMe_2 , resulted in clean and selective formation of the desired Ni-Me complexes after 2 h, and the same complex could be obtained by a reaction with CuMe_2Li after a shorter reaction time of only 5 min, albeit in a less selective manner. Although Ni-Me complex formation was also observed by using a more powerful methylating agent MeLi after ca. 1 h of reaction time, this reagent was the least selective amongst the three.

The ^1H NMR spectra for hydride complexes **3.26–3.29** show a hydride signal in the highly up-field region of -18 ppm as a triplet due to splitting from two phosphorus atoms ($J_{\text{HP}} \approx 55$ Hz) (See Figure 3.3 and Figure 3.4). The methyl complexes **3.30–3.33** show the characteristic Me group signal from around 0 to -0.23 ppm split by two P atoms. The $^{13}\text{C}\{^1\text{H}\}$ spectra for the methyl complexes show the Ni- $\underline{\text{C}}\text{H}_3$ signal from -16 to -21 ppm. As observed previously for the halogen species, complexes that have bulky $\textit{t}\text{Bu}$ groups show broadened signals in ^1H NMR for the arm and phosphine methyl groups, caused by the hindered rotation of $\textit{t}\text{Bu}$ groups around the phosphine atom due to crowding from the methylated ligand arms.

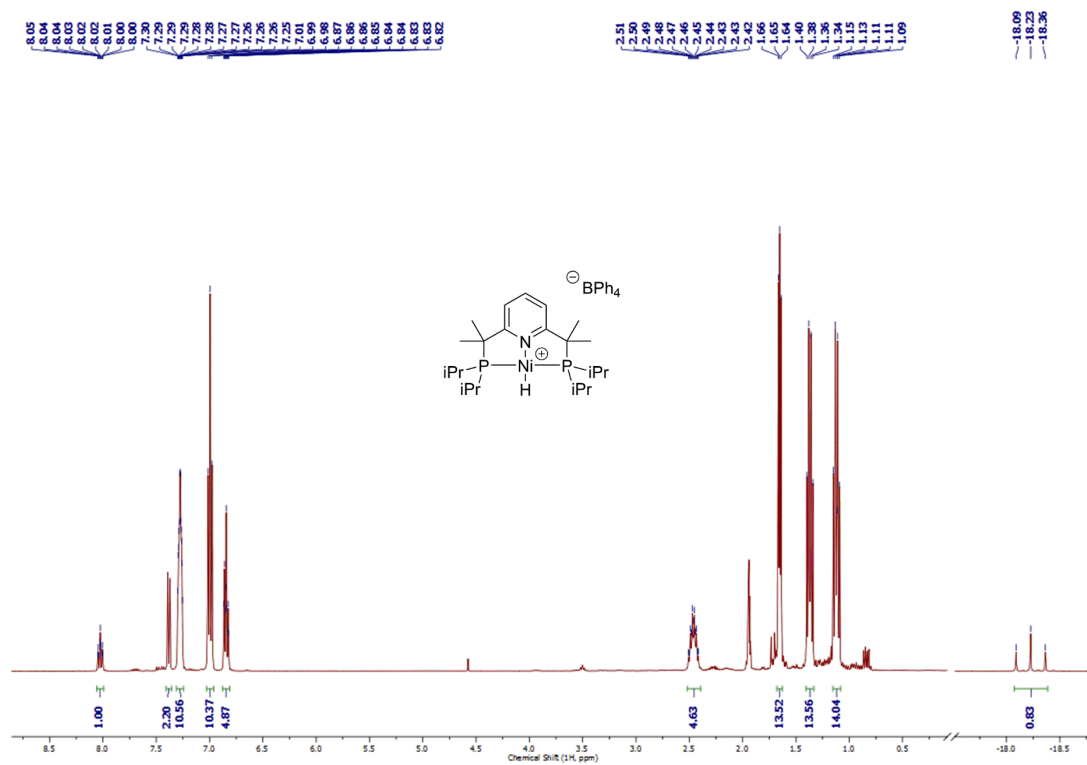


Figure 3.3 ¹H NMR spectrum of complex **3.27** with the characteristic hydride signal (400 MHz, CD₃CN).

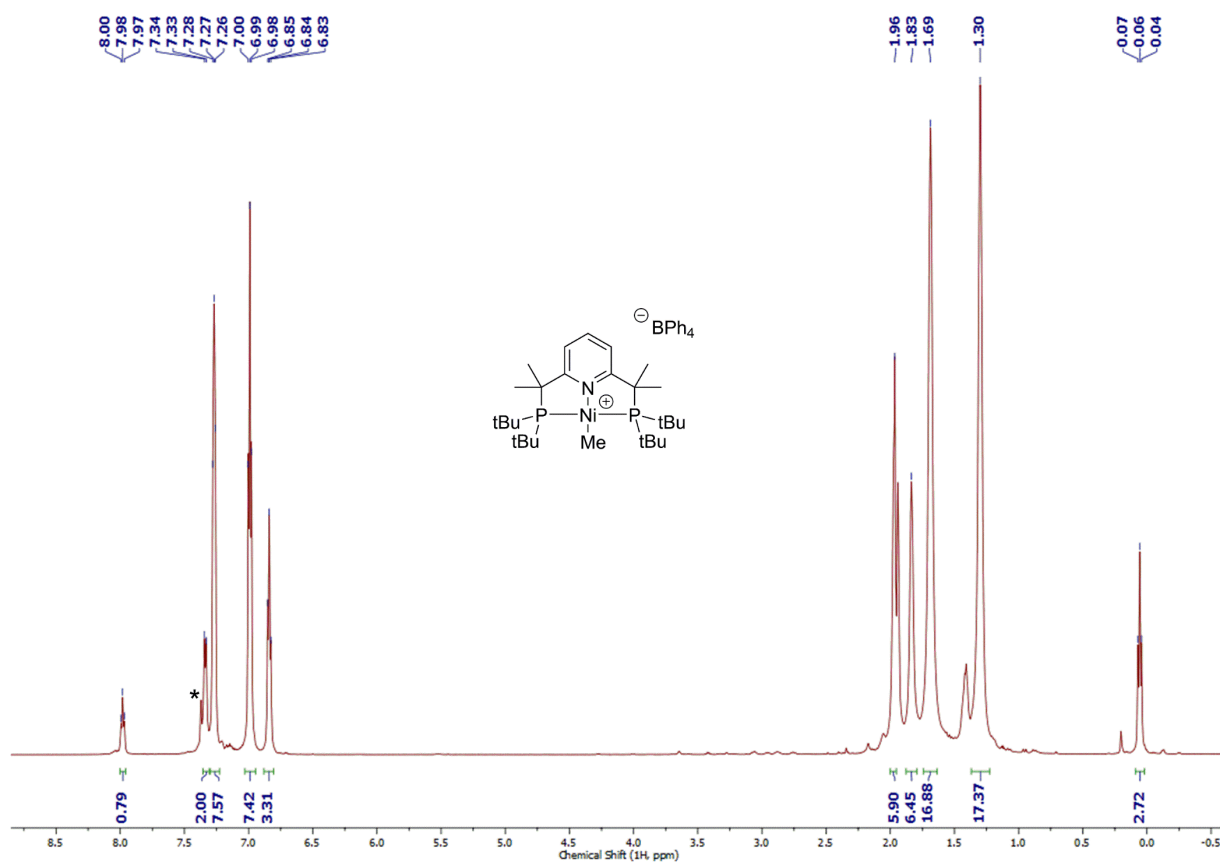


Figure 3.4 ^1H NMR spectrum of complex **3.33** with the characteristic methyl signal (600 MHz, CD_3CN) *Traces of C_6H_6 .

Most complexes in this study have been analyzed by X-ray diffraction studies, NMR, HRMS and elemental analysis. Structural data for the complexes reported in Table 3.1 show almost ideal square planar geometry around the nickel center. The ORTEP diagrams of complexes **3.26**, **3.28**, **3.30**, and **3.32** are shown in Figure 3.5. All aromatized ^iPr complexes show an “up-down” conformation in the crystals where one of the methyl groups on the arms is over the pyridine plane while the other is under the plane. This is also the case for all ^tBu -substituted complexes except for complex **3.25** (see below).

Table 3.1 Bond distances [\AA] and angles [deg] for complexes **2.36**, **2.38**, and **3.1–3.10** according to XRD data.^a

Complex	Ni1–N1	Ni1–X	Ni1–P1	Ni1–P2	\angle P1–Ni1–P2	\angle N1–Ni1–X	$\tau_4'^b$	τ_4^b
2.36 ^d	1.9095(13)	2.2827(2)	2.1786(4)	2.1805(4)	172.320(18)	176.66(4)	0.06	0.08
3.24	1.9133(11)	2.2932(2)	2.1833(4)	2.1863(4)	173.064(15)	179.60(4)	0.03	0.05
2.38 ^{c,e}	1.9236(15)	2.2877(12)	2.2324(12)	2.2454(13)	171.87(5)	178.84(7)	0.04	0.07
3.25 ^{e,f}	1.924(7)	2.2981(9)	2.2314(17)	2.2418(17)	171.40(7)	178.6(4)	0.05	0.07
3.26	1.9234(10)	1.45(2)	2.1424(3)	2.1366(3)	175.547(14)	179.3(8)	0.02	0.03
3.27	1.9193(12)	1.367(19)	2.1297(4)	2.1468(4)	176.300(19)	178.7(8)	0.03	0.03
3.28 ^d	1.9228(19)	1.34(3)	2.1430(6)	2.1452(6)	176.43(3)	179.9(18)	0.01	0.02
3.29	1.9182(8)	1.469(15)	2.1555(2)	2.1574(2)	174.368(10)	178.4(6)	0.04	0.05
3.30	1.9567(9)	1.9471(11)	2.1691(3)	2.1619(3)	170.614(12)	178.03(5)	0.06	0.08
3.31	1.9626(8)	1.9547(10)	2.1790(3)	2.1704(3)	170.919(10)	179.03(4)	0.04	0.07
3.32	1.9610(14)	1.9520(18)	2.2252(5)	2.2110(5)	171.544(19)	179.39(8)	0.04	0.06
3.33	1.9515(13)	2.0012(15)	2.2085(4)	2.2072(5)	170.554(19)	178.30(7)	0.05	0.08

^aAtom numbering corresponds to that of Figure 3.5; X = Br, H or Me. ^bGeometrical indexes τ_4' and τ_4 for the nickel centers are calculated according to refs.^{187, 194} ^cComplexes were previously reported.²²⁹ ^dThere are two complexes in the asymmetric cell ($Z' = 2$); data are tabulated for the first one. ^eData are listed for the main disordered component. ^fData are tabulated for the experiment collected using MoK α radiation.

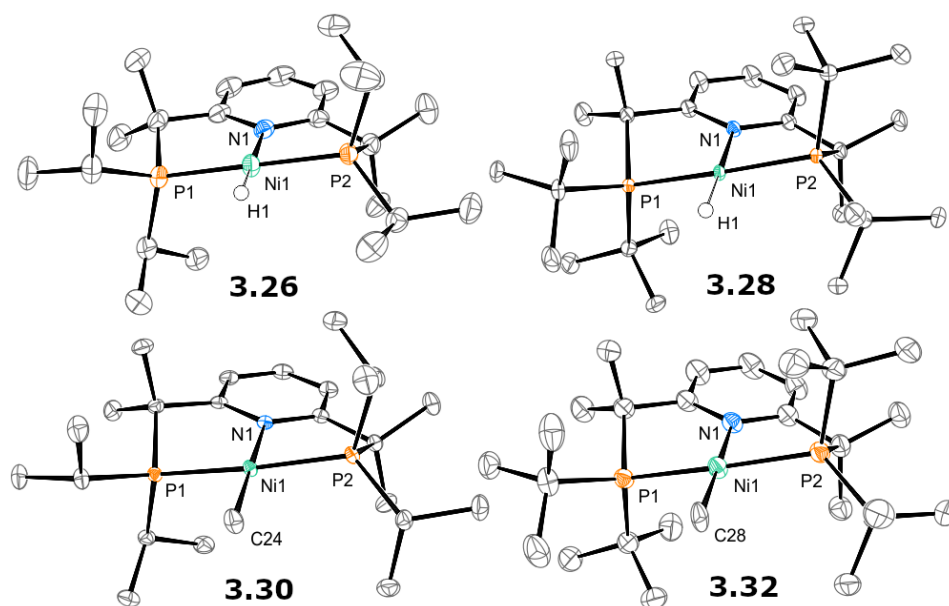


Figure 3.5 ORTEP diagrams of complexes **3.26-3.32** with the thermal ellipsoids set at 50% probability level. Most hydrogen atoms except for those on the nickel center, a minor disorder component for **3.30**, and counterions are omitted for clarity.

As a result of multiple crystallization attempts, we were only able to obtain the structure of **3.25** in the “up-up” conformation for both components of disorder, where two methyl groups are located over the pyridine plane, even though the very closely related complex with a $B(Ar^F)_4$ counterion crystallizes in the “up-down” conformation.²²⁹ DFT analysis of the geometry-optimized structures show that “up-up” and “up-down” complexes are expected to have only a minor energy difference in vacuo, with the “up-up” isomer being only 2.11 kcal mol⁻¹ higher in energy than the “up-down” isomer, well within the limits of error expected from DFT and also susceptible to small solid state energy differences due to crystal packing (see the linked Appendix of Chapter 3 for details). Nevertheless, we cannot completely exclude the presence of an undetected disordered component with the “up-down” conformation in the crystals.

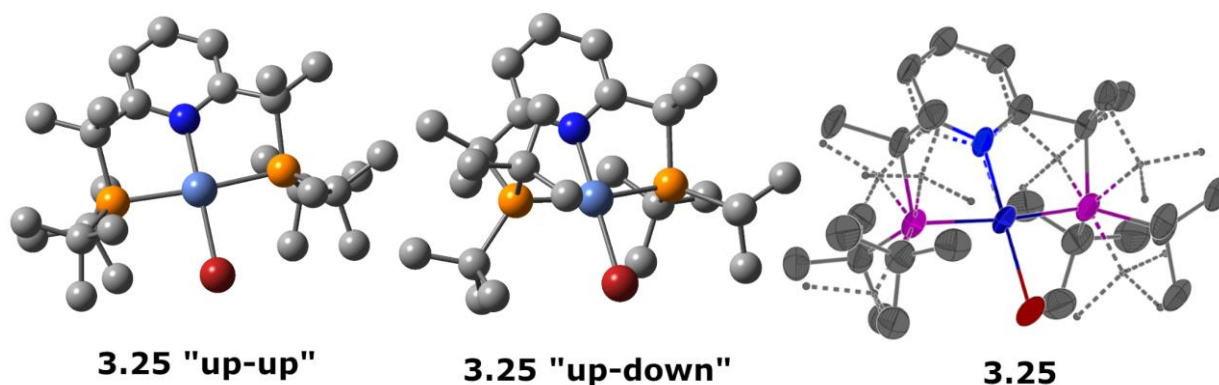
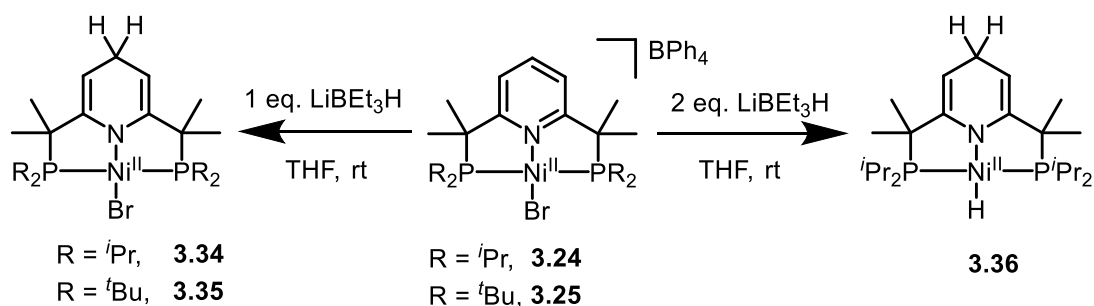


Figure 3.6 (left) DFT-optimized structures of **3.25** without the counterion in the “up-up” and (middle) “up-down” conformations. (right) ORTEP diagram of complex **3.25** with disordered component in dashed lines. Ellipsoids are shown at 50% probability. Hydrogen atoms and the counterion has been omitted for clarity. The major disordered component is shown in the ellipsoid representation, while the minor disordered component is shown in the dashed wireframe representation. DFT-optimized geometries done in vacuo at B3LYP level of theory with 6-311G** basis set with LANL2DZ ECP approximations for Ni and Br atoms.

3.2.2 Reactivity of Nickel(II) Complexes Leading to Pyridine Ring Dearomatization.

Interestingly, while screening various hydride sources for the formation of Ni hydride complexes, we found that the reaction of bromide complexes **3.24** and **3.25** with lithium triethylborohydride (LiBEt₃H, Superhydride) leads to ligand-based reactivity to give complexes **3.34**–**3.35** as major products, in which the pyridine ring is reduced, as evidenced from single crystal X-ray diffraction and NMR studies, while the Ni–Br bond remains intact (Scheme 3.13).



Scheme 3.13 Synthesis of complexes **3.34**–**3.36**

This reactivity resembles reduction of the pyridine ring in PONOP complexes with Superhydride reported by Jones et al.⁵³ and shows that in the presence of a strong reductant, the pyridine ring in our new, sterically-hindered PNP ligands displays non-innocent character.

Complex **3.34** was isolated in 87% yield while complex **3.35** was isolated in 77% yield, and they were both characterized by NMR, X-ray diffraction and HRMS. For complex **3.35**, 0.8 equivalents of Superhydride was used instead of 1 equivalent because it furnished product of the higher purity, whereas unreacted starting material can be easily removed by filtration in diethyl ether.

When ⁱPr-substituted complex **3.24** was treated with 2 equivalents of LiBEt₃H, a new dearomatized hydride complex **3.34** was formed as a major product and characterized by NMR spectroscopy. Notably, when the ^tBu-substituted analogue **3.25** was reacted with 2 equivalents of LiBEt₃H under the same conditions, a mixture of complex **3.35** as a major product and a presumed dearomatized hydride species as a minor product was observed by NMR spectroscopy (See Figure 5.58 in the linked Appendix of Chapter 3). The lower reactivity of the ^tBu-substituted analog compared to **3.24** is likely due to a combination of steric and electronic factors preventing further nucleophilic substitution with LiBEt₃H.

The X-ray diffraction study of complexes **3.34** and **3.35** revealed that the atom C3 deviates from the plane defined by atoms C1, C2, C4, C5, and N1 by 0.317(2) Å and 0.4470(15) Å, respectively, highlighting the loss of aromaticity of the heterocyclic moiety. The Ni1–N1 bond lengths for complexes **3.34** and **3.35** of 1.8768(15) Å and 1.8810(12) Å, respectively, are shorter than in their parent complexes **3.24** and **3.25**, with the Ni1–N1 bond lengths of 1.9133(11) Å and 1.924(7) Å, respectively. The dearomatization of the pyridine ring can be seen by the shorter bond length for C1–C2 and C4–C5 compared to C2–C3 and C3–C4. For complex **3.34**, the C1–C2 and C4–C5 bond lengths have a double bond character with 1.337(3) and 1.338(3) Å bond distances, while C2–C3 and C3–C4 have a single bond character with distances of 1.498(3) and

1.497(3) Å. Similar bond lengths are present in complex **3.35**, with C1–C2, C4–C5 displaying double-bond character with 1.3386(19) and 1.3437(19) Å, respectively, while C2–C3, C3–C4 have single-bond character with 1.5060(19) and 1.5055(19) Å, respectively. The dearomatization of the pyridine ring is also evident from solution NMR spectra of **3.34–3.35**, which shows upfield shifts for the heterocycle protons that now appear in the range of 2.8 to 4.2 ppm.

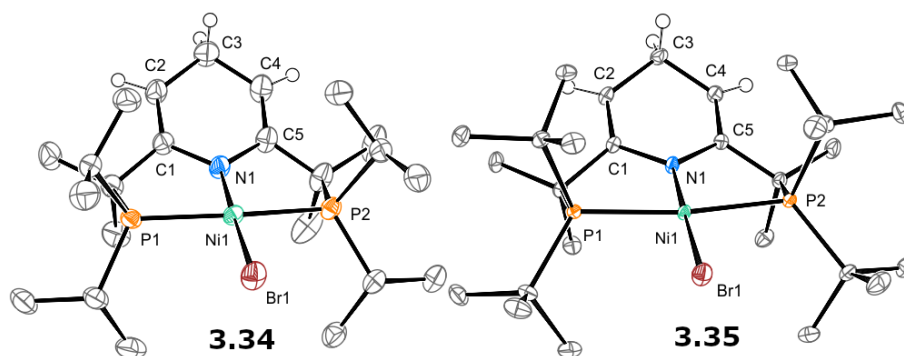


Figure 3.7 ORTEP diagrams of complexes **3.34–3.35** with the thermal ellipsoids set at 50% probability level. Hydrogen atoms except for those on the heterocycle are not shown. Complex **3.34** has two complexes in the asymmetric unit, only the first component is shown. Only the main component of the disorder is shown for complex **3.35**.

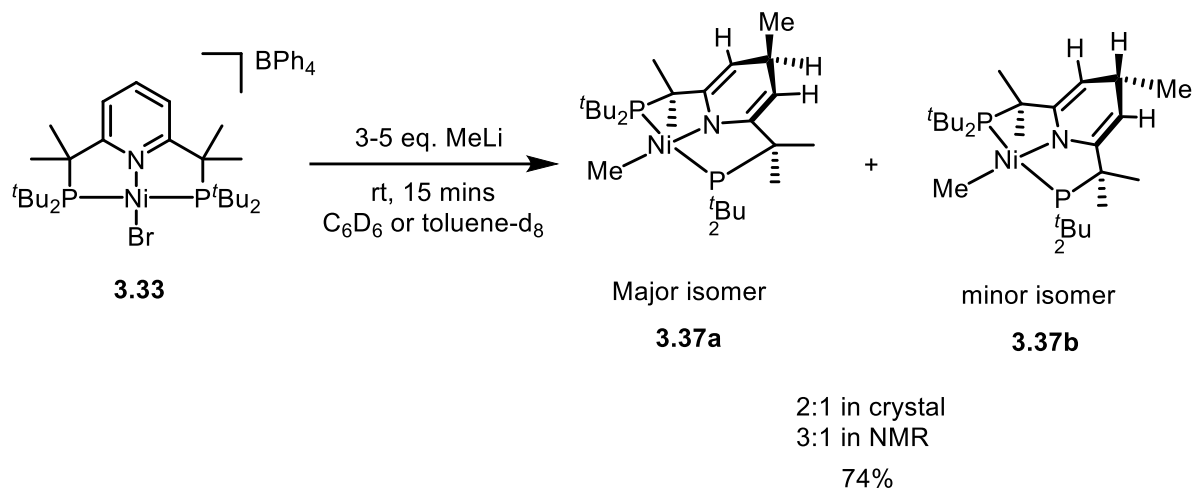
Table 3.2 Bond distances [Å] and angles [deg] for complexes **3.34–3.37** according to XRD data.^a

Complex	Ni1–N1	Ni1–X	Ni1–P1	Ni1–P2	C1–C2	C2–C3	∠ P1–Ni1–P2	∠ N1–Ni1–X	τ_4^a	τ_4^b
3.34^c	1.8768(15)	2.3370(3)	2.1821(5)	2.1857(5)	1.337(3)	1.498(3)	170.67(2)	176.60(5)	0.07	0.09
3.35^d	1.8810(12)	2.3071(3)	2.2297(4)	2.2205(4)	1.3386(19)	1.5060(19)	170.621(15)	178.29(4)	0.05	0.08
3.38^e	1.9028(17)	1.954(2)	2.1510(6)	2.1585(6)	1.343(3)	1.509(3)	171.19(2)	177.29(9)	0.06	0.08

^aAtom numbering corresponds to that of Figure 3.7 and Figure 3.10; X = Br or Me. ^bGeometrical indexes τ_4^a and τ_4^b for the nickel centers are calculated according to refs.^{187,194} ^cThere are two complexes in the asymmetric cell ($Z' = 2$); data are tabulated for the first one. ^dData are listed for the main disordered component; a hydride species is present as the minor disordered component with occupancy of 0.3331(10), and the Ni1–H1 bond length is 1.52(2) Å (see Supp. Info). ^eThe asymmetric cell contains half of the molecule ($Z' = 0.5$); C3–C3ⁱ 1.570(4) Å.

Interestingly, not only the reaction of LiBEt₃H can lead to pyridine-ring dearomatization. In the process of making **3.33** using MeLi, we accidentally used an extra equivalent of methyl lithium to exchange the bromide with a methyl group. Interestingly, addition of 3 or even 5 equivalents of

MeLi gives a new pink solid in 74% yield, corresponding to the dearomatized species **3.37** where both the nickel and the *para*-position of the dihydropyridine ring is methylated (See Scheme 3.14)



Scheme 3.14 Reaction of **3.33** with MeLi leading to dearomatization and methylation of the pyridine ring to form **3.37** as a mixture of two isomers.

Complex **3.37** is obtained as a mixture of isomers **3.37a** and **3.37b** in a 3:1 ratio by NMR (disordered as a 2:1 ratio in the crystal structure). The structure of the main isomer, **3.37a** is tentatively assigned based on NMR integrations and signals, and the bent structure is determined by the X-ray diffraction studies. The dearomatized complex **3.37** differs in its geometry to the closely related, non-methylated bis(tert-butylphosphine)-substituted complex **3.35** in that the dearomatized pyridine ring of both complexes (and of the two isomers) are bent in different directions. For **3.35**, the absence of significant steric hindrance on the heterocyclic ring allows the complex to bend *towards* the two methyl groups on the arms present in the “axial” position (the “axial” methyl groups are those that are pointing “up” almost parallel to each other). On the other hand, the heterocyclic rings in the isomers of **3.37** are bending *away* from the “axial” methyl groups on the arms due to the increase in steric hindrance on the heterocyclic ring by the introduction of the methyl group (See **Figure 3.8**). In the case of the minor isomer **3.37b**, the bending of the reduced pyridine ring is more accentuated due to the orientation of the methyl

group at the *para*-position towards the axial methyl groups in order to reduce the steric hindrance. On the other hand, the major isomer **3.37a** has a less pronounced bending of the aromatic ring because the methyl group on the *para*-position is oriented away from the methyl groups.

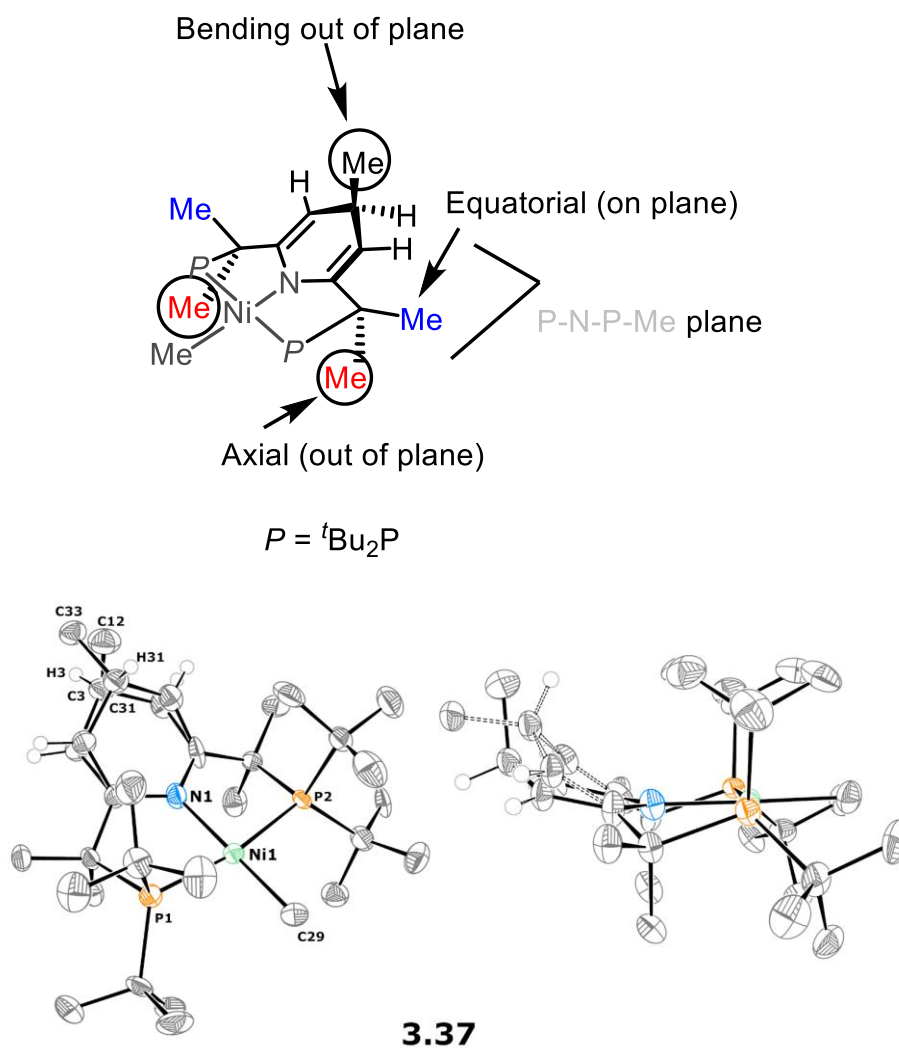


Figure 3.8 (top) Description of equatorial and axial description of methyl groups compared to the P-N-P-Me plane. (bottom) ORTEP diagram of complex **3.37** in two different orientations. The major isomer has the dearomatized pyridine ring shown in hard black lines, while the minor isomer has the dearomatized pyridine ring shown in dashed bonds. Ellipsoids are drawn at 50% probability. Hydrogens, except those on the dearomatized pyridine rings were omitted.

The propensity of our bulky ligands for reduction at the *para*-position is a feature that was originally not entirely desirable as the ligands were usually designed to prevent metal-ligand cooperation/dearomatization pathways, but also not entirely unexpected due to Jones' earlier PONOP

report.⁵³ However, as mentioned previously, it was possible to obtain all the non-dearomatized hydride species with a less reducing NaBH₄ reagent cleanly. It is worth to consider that the Superhydride reduction of the pyridine ring in the *para*-position eventually provides a pathway for in situ formation of an anionic PNP ligand, which, as suggested by previous literature, might eventually enable different reactivity pathways as compared to neutral PNP ligands.^{175, 230} Such pyridine reduction reactivity also resembles the NAD⁺/NADH redox couple in biological systems and NADH-model compounds that are used as a reservoir of hydride ions.²³¹⁻²³³ Careful choice of the reactant and proper stoichiometry when preparing the methyl complexes is also important, as excess of powerful reagents such as MeLi can also cause dearomatization. The *para*-position reactivity of the hydrides suggested that we may be able to get different outcomes upon electrochemical or chemical reduction of complexes **3.30–3.33** as compared to the halogen complexes and their associated stable and unreactive Ni^IX **2.40–2.43** (X= Br , Cl) species earlier reported by us.²²⁹

3.2.3 Reactivity of Nickel(II) Methyl Complexes with Strong Reductants Leading to Dimerization at the *Para* Position

Accordingly, we next studied the reactivity of Ni^{II} methyl complexes with strong chemical reductants. Previously, we reported that Ni^{II} bromide and chloride complexes could be reduced by cobaltocene to form stable paramagnetic Ni^I complexes. In the case of Ni^{II}–Me complexes, cobaltocene was not a sufficiently strong reductant and no reduced product could be observed. Cyclic voltammetry studies gave us more insight into the different reactivity of these complexes when compared to their halide counterparts (Figure 3.9, a). For example, the reduction potential of complex **3.30** (–1.72 V) is much more negative than the reduction potential of cobaltocene, at around –1.33 V (in CH₂Cl₂)²³⁴. The reduction wave of complex **3.30** is electrochemically irreversible ($\Delta E_p = 0.54$ V), suggesting that a Ni^I–Me species might be unstable after generation, or that it undergoes significant changes upon oxidation.²³⁵

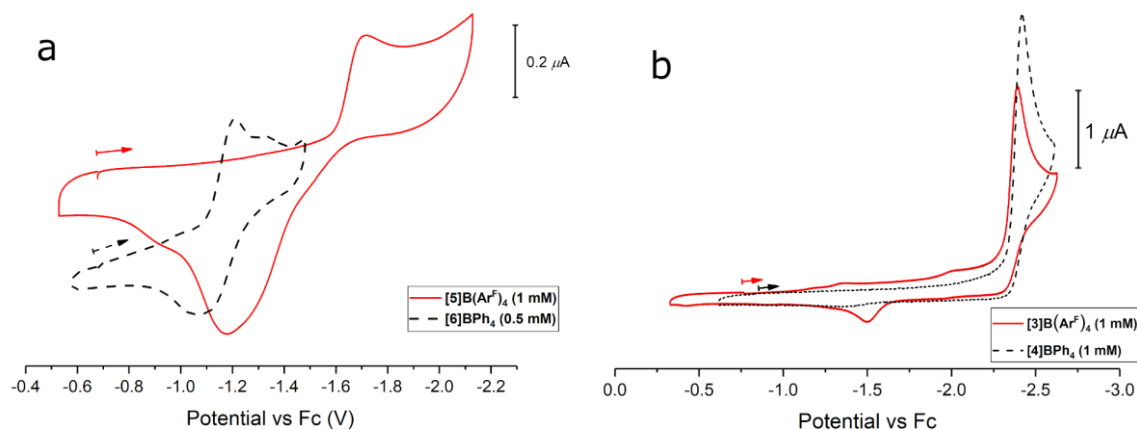


Figure 3.9 Cyclic voltammograms of Ni methyl and hydride complexes in the cathodic region: a) complexes **3.7** (1 mM; red line) and **3.33** (0.5 mM, dashed black line); b) complexes **3.26** (1 mM; red line) and **3.29** (1 mM; dashed black line). Experimental conditions: 0.1 M $n\text{Bu}_4\text{NPF}_6/\text{MeCN}$ solution at 23 °C, scan rate 0.1 V s^{-1} , 1.0 mm GC disk working electrode; the arrow indicates initial scan direction.

The cyclic voltammogram of **3.33** showed a quasi-reversible reduction wave at a less negative potential (−1.21 V) indicating that the presence of bulky $t\text{Bu}$ -substituents might contribute to greater stabilization of the initial reduced product, at least on the electrochemical timescale.

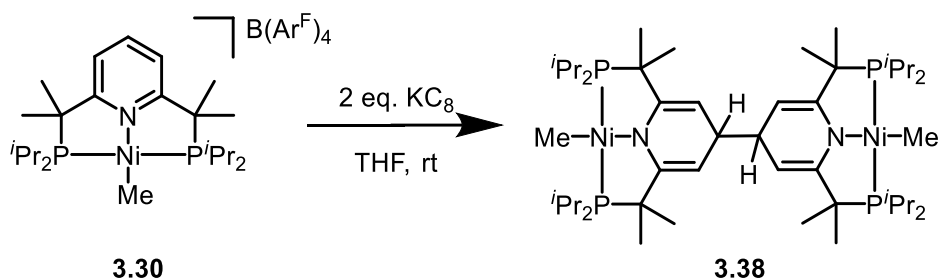
Table 3.3 Electrochemical properties of complexes **3.26**, **3.29**, **3.30** and **3.33**.^a

Complex	E_{pf} (V) ^b	E_{pr} (V) ^c	ΔE (V) ^d	$E_{1/2}$ (V) ^e
3.26	−2.389	−	−	−
3.29	−2.422	−	−	−
3.30	−1.720	−1.180	0.540	−
3.33	−1.209	−1.075	0.134	−1.142

^aCyclic voltammograms for complexes **3.26** (1 mM), **3.29** (1 mM), **3.30** (1 mM) and **3.33** (0.5 mM) in a 0.1 M solution of $n\text{Bu}_4\text{NPF}_6$ as supporting electrolyte in MeCN at 23°C; 100 mV/s scan rate; GC disk electrode ($d = 1.6$ mm); all peaks were referenced versus ferrocene. ^bPotential of the forward peak. ^cPotential of the return peak.

^dThe peak-to-peak separation ΔE was calculated as $E_{\text{pf}} - E_{\text{pr}}$. ^e $E_{1/2}$ was estimated as $\frac{1}{2}(E_{\text{pf}} + E_{\text{pr}})$

For comparison, cyclic voltammograms of hydride complexes **3.26** and **3.29** show completely irreversible reduction waves at very negative potentials, −2.39 and −2.42 V, respectively, suggesting that the reduction products are likely unstable and very strong reductants are required for chemical reduction^{234, 235} (Figure 3.9, b and Table 3).



Scheme 3.15 Reduction of Ni^{II} -Me complex **3.30** to form **3.38**.

Attempted reduction of **3.26** and **3.29** by using 1 equivalent of a strong reductant, KC_8 , initially gives a mixture of paramagnetic products, as observed by EPR spectroscopy (See Figures 5.124-5.125 in the linked Appendix of Chapter 3). According to NMR analysis of the reaction mixtures, a mixture of diamagnetic products is also formed during the reduction of **3.26** and **3.29**; free ligand was also present among the reaction products after reduction of **3.26**. We were unable to identify the products of reduction of hydride complexes likely due to their low stability.

Interestingly, chemical reduction of the Ni^{II} -Me complex **3.30** with the very strong reductant KC_8 led to the formation of a new diamagnetic complex **3.38**, which was isolated in 33% yield and characterized by X-ray crystallography and NMR spectroscopy. According to the X-ray structure shown in Figure 3.10, **3.38** is a dimer, with a new C-C bond formed in the *para*-position of the pyridine rings, leading to overall pyridine ring reduction and dearomatization.

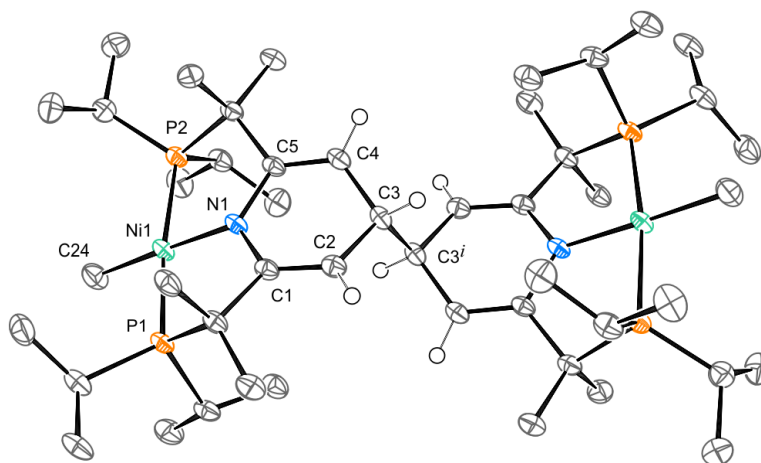


Figure 3.10 ORTEP diagram of complex **3.38** with the thermal ellipsoids set at 50% probability level. Hydrogen atoms except for those on the heterocycle are not shown. Selected interatomic distances (Å) and angles (deg.): Ni1–N1 1.9028(17), Ni1–C24 1.954(2), Ni1–P1 2.1510(6), Ni1–P2 2.1585(6), N1–C1 1.405(3), N1–C5 1.408(3), C1–C2 1.343(3), C2–C3 1.509(3), C3–C4 1.505(3), C4–C5 1.341(3), C3–C3ⁱ 1.570(4), ∠P1–Ni1–P2 171.19(2), ∠N1–Ni1–C24 177.29(9). Equivalent atoms are labeled with the superscript *i* (–*x*, 1–*y*, 1–*z*).

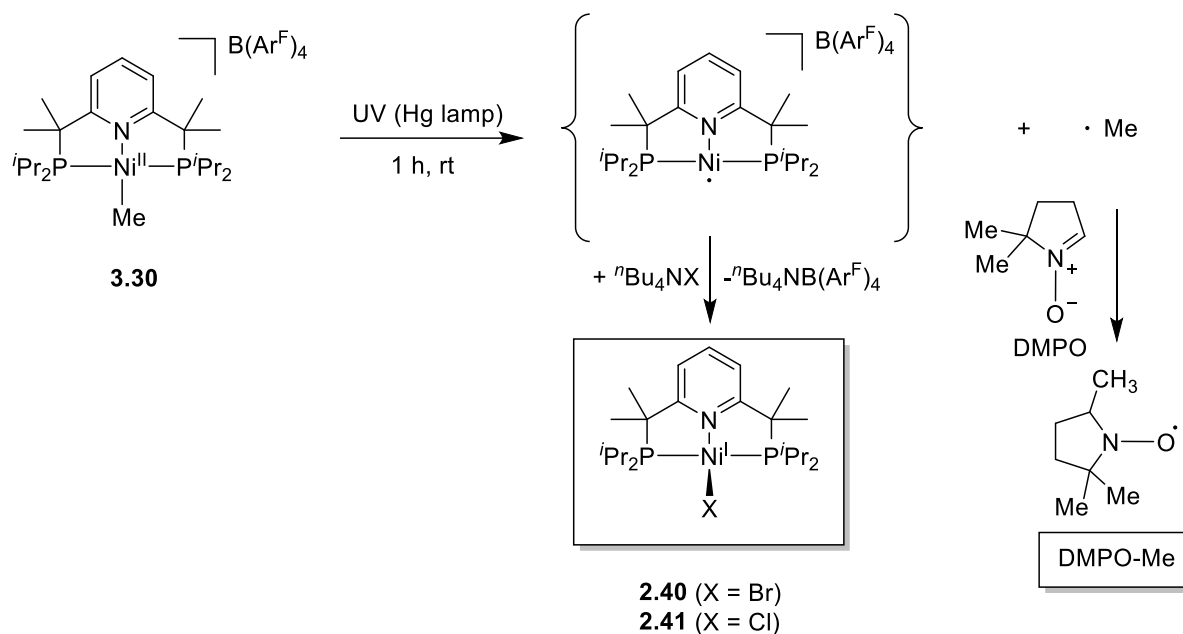
Similar to the dearomatized complex **3.34**, complex **3.38** shows bent heterocycle rings, and double bond character between the *ortho* and *meta* carbons. The geometry around the nickel center is also close to an ideal square planar geometry. The atom C3 deviates from the plane defined by atoms C1, C2, C4, C5, and N1 by 0.4235(19) Å. The C3–C3ⁱ bond length of 1.570(4) Å is longer than the C2–C3 (1.509(3) Å) and C3–C4 (1.505(3) Å) single bonds in the pyridine ring, which are longer than the olefinic C1–C2 (1.343(3) Å) and C4–C5 (1.341(3) Å) bonds. NMR analysis of complex **3.36** shows that the heterocyclic protons are also significantly upfield shifted from the parent complex and fall in the range of 4.5 to 3.6 ppm, consistent with pyridine ring dearomatization. This result shows that the reactivity of complex **3.30**, with its more electron-rich Ni–Me center, is predominantly ligand-based. In the previously reported Ni^{II} bromide and chloride complexes metal-based reduction was observed exclusively. The reasons behind ligand-based reactivity observed for Ni–Me complexes were analyzed through computational studies and are discussed below in more detail.

Attempts to reduce **3.33** did not furnish a dimeric complex, and only gave a mixture of paramagnetic species by EPR that we were not able to identify.

3.2.4 UV-Induced Homolysis of Nickel(II) Methyl Bond

An alternative way to access a transient Ni^{I} species from an organometallic Ni^{II} complexes would be a homolysis of a Ni–C bond.¹⁶⁰ We investigated the reactivity of Ni^{II} -Me complexes **3.30** and **3.32** under irradiation by mercury lamp at room temperature in an acetone solution in the presence or absence of a radical trap. Interestingly, initial trial experiments where we irradiated the solution of **3.30** without any additives produces a pink-colored solution already after 5 min.

To confirm whether Ni^{II} -Me bond homolysis occurs under these conditions, we performed the experiment in the presence of 5,5-dimethyl-1-pyrrolidine N-oxide (DMPO) as a radical trap, which could help to detect a transient Me radical. When we performed the irradiation for 1 hour at room temperature in the presence of an excess of DMPO, we observed a new signal of a DMPO-methyl adduct with $g = 2.007$, $A_{\text{N}} = 14.25$ G and $A_{\text{H}} = 21.10$ G (Figure 3.11, Scheme 3.16). The superhyperfine splitting parameters of the trapped radical are similar to those reported in the literature for a DMPO-Me radical adduct in acetone ($A_{\text{N}} = 14.2$ G, $A_{\text{H}} = 21.6$ G in acetone under gamma irradiation).²³⁶



Scheme 3.16 UV-induced reactivity of **3.30**.

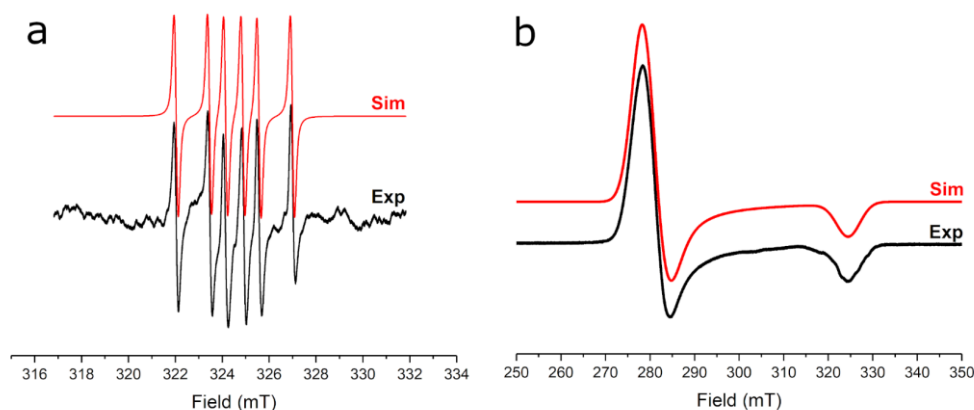


Figure 3.11 Experimental (black line) and simulated (red line) EPR spectra after UV irradiation of a) **3.30** after UV irradiation for 1 h at 298 K in the presence of excess DMPO in acetone- d_6 , b) **3.30** in the presence 1 equivalent of ${}^n\text{Bu}_4\text{NBr}$ after UV irradiation for 1 h at 95 K in frozen acetone- d_6 . Parameters for simulation: a) $g = 2.007$, $A_{\text{N}} = 14.25$ G, $A_{\text{H}} = 21.10$ G. b) $g_{\text{x}} = 2.328$, $g_{\text{y}} = 2.307$, $g_{\text{z}} = 1.998$ ($g_{\text{iso}} = 2.211$).

When the solution of **3.30** was irradiated in the absence of a radical trap, the low temperature EPR spectrum showed only weak signals with g values in the range from 2.17 to 2.04 which were tentatively simulated as a mixture of a nickel methyl species where the radical is most likely on the pyridine ring and a Ni^{I} cationic species resulting from the homolysis of the nickel methyl bond (See Figure 3.12). presence of 5,5-dimethyl-1-pyrroline N-oxide (DMPO) were obtained

from geometry-optimized structures using Gaussian, and the EPR parameters were obtained using ORCA on the complexes with the proper charges and spins. We also assign the former species as a ligand-based radical based on the isotropic g tensor value of 2.004 which corresponds to an organic radical, while the nature of the later metalloradical species is supported by an average g tensor value of 2.12 (g_x , g_y , and g_z of 2.02, 2.17 and 2.18, respectively), which is similar to the previously reported square-planar g_{iso} value for Ni^{I} halide species **2.42-2.43** ($g_{\text{iso}} \sim 2.12$) suggesting a possible square planar geometry (although the nature of the halide vs methyl ligands on the species could be the reason why the shape of the EPR spectra is different).

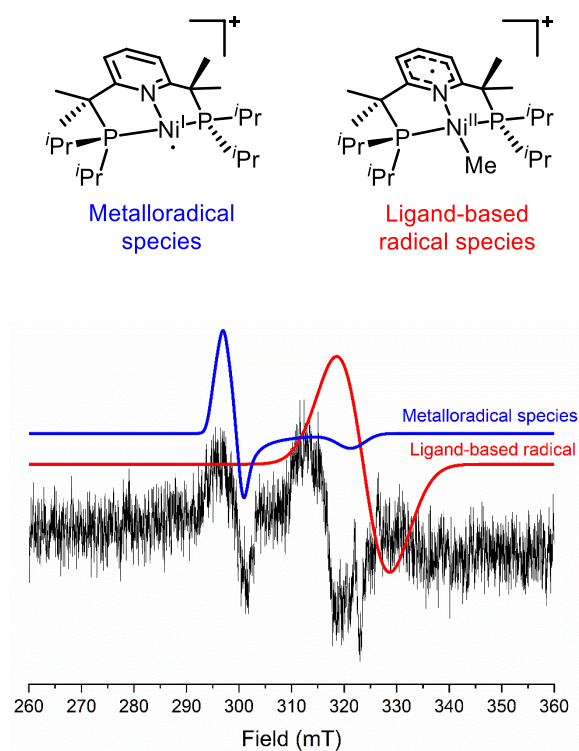


Figure 3.12 EPR spectra obtained at 93K in frozen acetone- d_6 from UV irradiation of a solution of **3.30** for 3.5 hours at rt. Possible metalloradical and ligand-based radical species are shown above.

However, the low intensity of the signal suggests that in the absence of stabilizing ligands, the resulting radical is likely to be unstable and to undergo further transformations. The nature of the cationic metalloradical species could be either a T-shaped three-coordinate Ni^{I} species similar to those reported by the Lee¹⁷⁶ or Gade¹⁷⁰ groups or solvent-stabilized tetracoordinate species.

Similarly, we have exposed complex **3.32** to UV irradiation for 3.5 hours at room temperature and we were able to observe some signal by EPR with *g*-values of 2.10, 2.03, and 1.97, but we were not able to assign it unambiguously (Figure 5.120 in the linked Appendix of Chapter 3)

In order to reliably detect the formation of possible Ni^I species, we performed the reaction in the presence of Br⁻ or Cl⁻ ions that can act as stabilizing ligands to form previously characterized stable Ni^I complexes **2.40** or **2.41** complexes, respectively (Scheme 3.16). To our satisfaction, irradiation of an acetone solution of **3.30** in the presence of 1 equiv. of ⁿBu₄NBr for 1h gave a pink-colored solution, whose EPR spectrum at 95 K shows a new rhombic signal with *g* values of 2.328, 2.307, and 1.998, close to the *g*-values of the previously characterized Ni^I bromide complex **2.40** with *g* = 2.316, 2.309, and 1.993 (See Figure 3.11 b).²²⁹ Similarly, a rhombic signal (*g* = 2.329, 2.307, and 1.998) was also observed in the presence of 1 equiv. of ⁿBu₄NCl, although the reaction was less clean (See Figure 5.114 in the linked Appendix of Chapter 3).

In direct contrast with the less bulky ⁱPr substituents, when ^tBu substituted complex **3.32** was irradiated in the presence of DMPO trap, we could not observe clean Ni–Me homolysis reactivity. No signals of DMPO-Me adduct were evident, with only a broad isotropic signal with a *g* value of 2.164 observed (See Figure 3.13 and Figure 5.121 in the linked Appendix of Chapter 3) which might be indicative of a metalloradical species with the methyl still bound on the complex rather than a homolysis product.

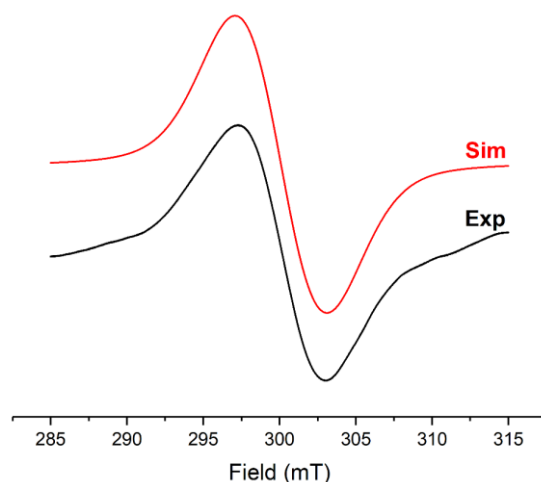


Figure 3.13 EPR spectra obtained at 298K in acetone- d_6 from UV irradiation of a solution of **3.30** for 1 hour with an excess of DMPO.

NMR analysis of **3.32** under irradiation for 1.5 h in acetone- d_6 show a significant amount of ligand decomposition, whereas irradiation of **3.30** for to 2 h in acetone- d_6 also shows only a very small amount of ligand decomposition. These experimental observations seem to suggest that **3.30** may undergo nickel methyl bond homolysis faster than decomposition of the complex, whereas **3.32** on the other hand decomposes faster under UV irradiation and that nickel methyl bond homolysis is less favorable.

3.2.5 Small Molecule Activation Reactivity

We hypothesized that introducing significant steric hindrance through the influence of four Me groups and t Bu or i Pr substituents at the phosphines might alter the reactivity of the nickel methyl and hydride complexes towards small molecule activation. However, the attempted reactions of complexes **3.26–3.33** with CO, CO₂, and ethylene failed to give significant amounts of any adducts or insertion products even up to 24 hours at 50 °C. Some minor degradation was observed upon prolonged heating of **3.27** under CO atmosphere for 8 h (see Figure 3.14 and Figure 3.15), however, no CO adducts could be detected by IR spectroscopy. The nature of the counter anion, B(Ar^F)₄ or BPh₄, did not affect the reactivity.

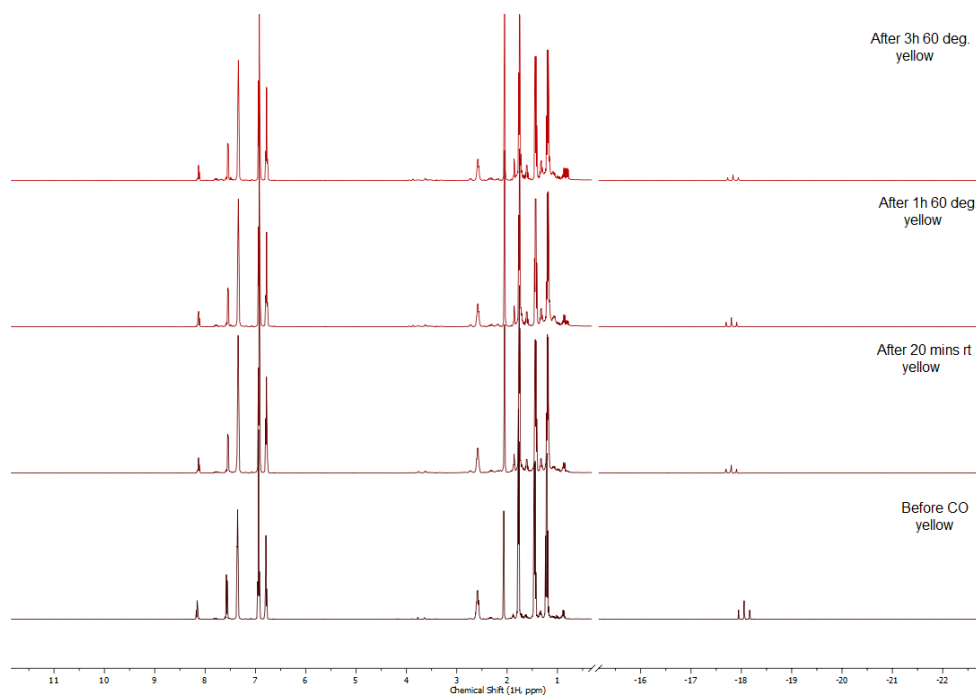


Figure 3.14 Stacked ^1H NMR spectra of the reaction of **3.27** with CO up to 3 hours at 60 °C (500 MHz, acetone- d_6).

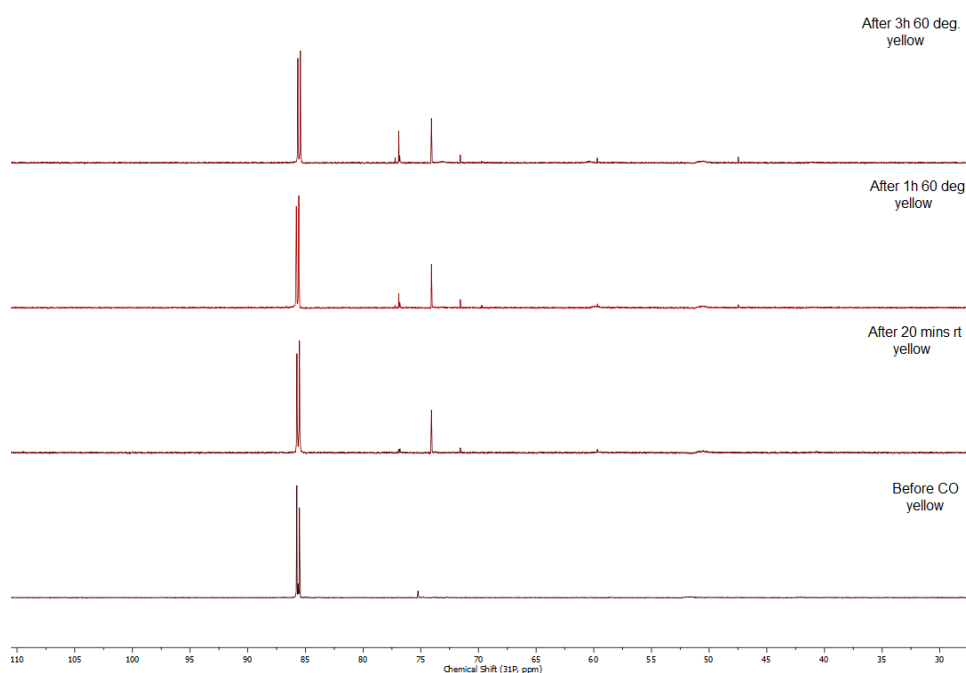


Figure 3.15 Stacked $^{31}\text{P}\{^1\text{H}\}$ NMR spectra of the reaction of **3.27** with CO up to 3 hours at 60 °C (202 MHz, acetone- d_6).

3.2.6 Oxygen reactivity

We then set out to study the reactivity of Ni hydride complexes **3.26-3.29** with O₂, to determine if any oxygen adducts can be detected. The less sterically hindered ⁱPr-substituted complex **3.26** readily reacts with O₂ in a deuterated acetonitrile solution, which leads to an immediate solution color change from light yellow to red then quickly to orange within a few minutes. The first species observed by ¹H NMR 2 minutes after reaction with O₂ appears to be paramagnetic; the disappearance of a characteristic Ni–H signal can also be observed. Upon prolonged reaction time, the paramagnetic species disappears to reveal only a mixture of unidentified diamagnetic complexes. (Figure 3.16 and Figure 3.17). ESI-MS analysis of the reaction mixture of **3.26** with O₂ suggest that some of the products formed are the oxidized ligands species, and could be assigned as the peak at around 60 ppm in Figure 3.17, as often appears in reactions that involve O₂ with other metals.

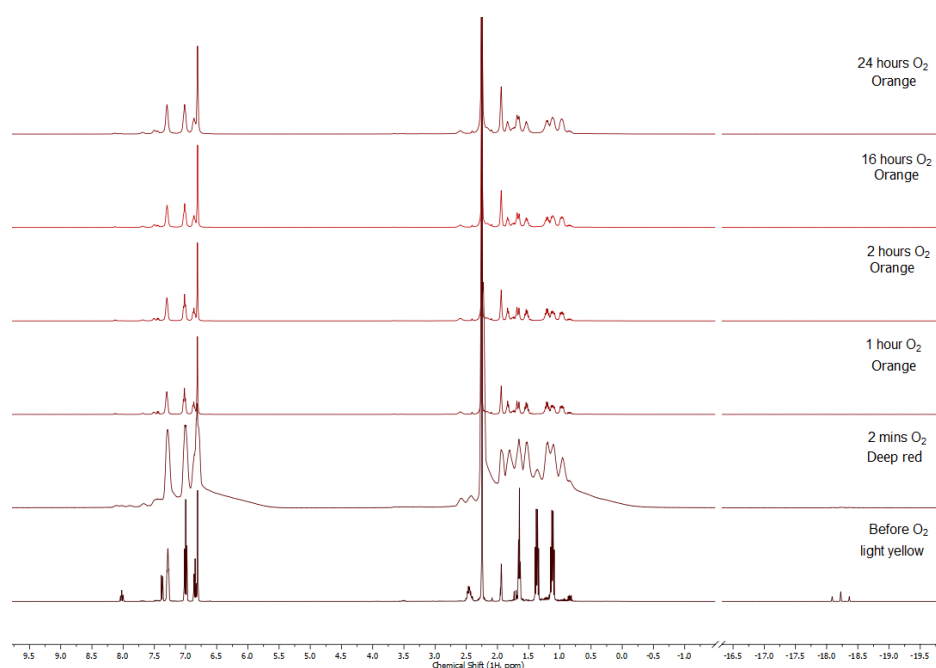


Figure 3.16 Stacked ¹H NMR spectra of the reaction of **3.27** with O₂ up to 24 hours (400 MHz, CD₃CN).

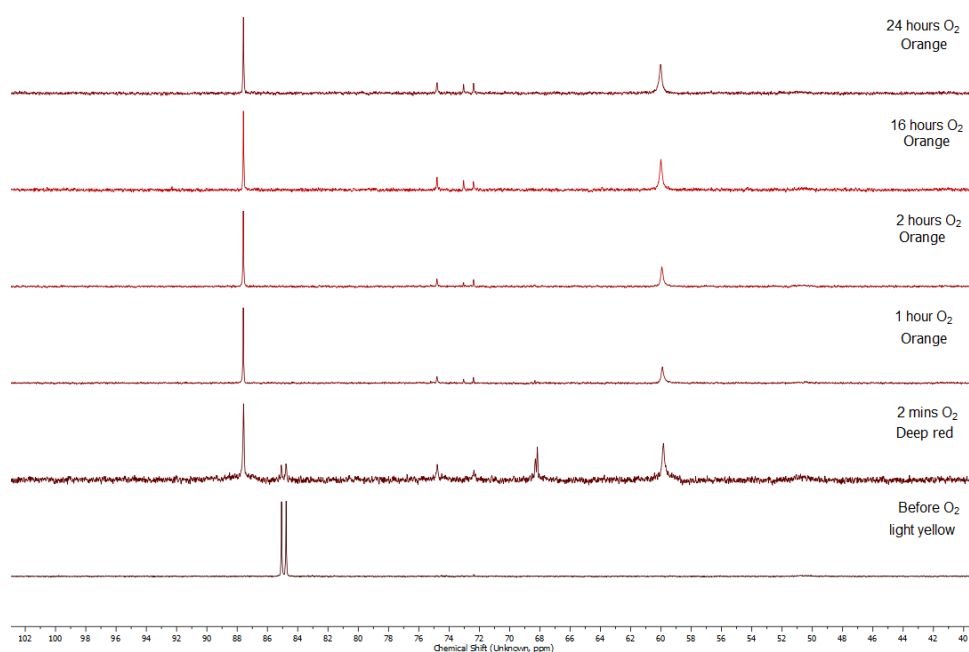


Figure 3.17 Stacked $^{31}\text{P}\{^1\text{H}\}$ NMR spectra of the reaction of **3.27** with O_2 up to 24 hours (162 MHz, CD_3CN).

The EPR spectrum recorded after reacting **3.26** with O_2 for 1 hour shows an axial signal with g_x and g_y values of 2.088 and 2.003, respectively (Figure 3.18). These g values that remain close to 2 are similar to the signals reported for known Ni superoxide complexes with NNN pincer ligands described by Gade et al.¹⁷² We also recorded the EPR spectrum of the reaction of **3.26** with O_2 in the presence of an excess of DMPO, and obtained the spectrum shown in Figure 5.118 of the linked Appendix of Chapter 3 with superhyperfine splitting constants ($A_N = 13.2$ G, $A_H = 8.11$ G, $g = 2.0025$), resembling those reported for characterized or proposed metal-superoxide adducts (for example, Co superoxide DMPO adduct, $A_N = 12.8$ G, $A_H = 7.68$ G, $g = 2.008$).²³⁷ Although we could not isolate or further characterize the product of the reaction with O_2 due to its low stability and further decomposition, we propose that the formation of a similar Ni superoxide complex could occur in this case.^{237, 238}

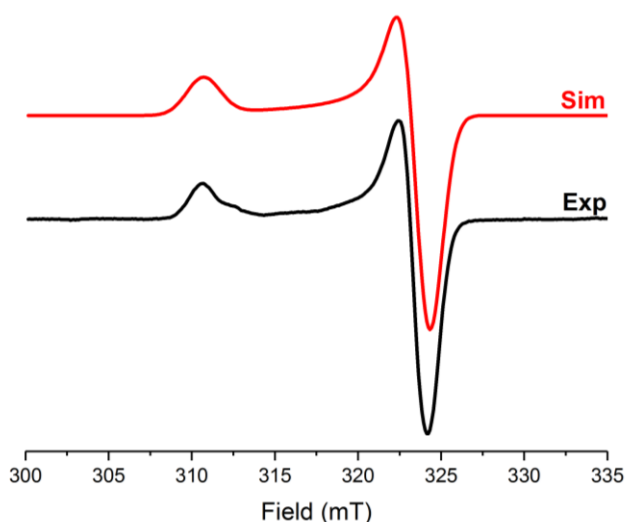


Figure 3.18 Experimental (black line) and simulated (red line) EPR spectra of the complex formed from the reaction of **3.26** with O₂ in frozen acetone at 84K. Parameters for simulation: $g_{\text{perp}} = 2.003$, $g_{\text{para}} = 2.088$

Interestingly, although Ni^{II} hydrides are usually considered to be highly reactive species, highly sterically hindered ^tBu-substituted Ni^{II} hydride **3.29** was stable under air or pure O₂ atmosphere for at least 24 hours according to ¹H and ³¹P{¹H} NMR studies (Figure 3.19 and Figure 3.20). The Ni^{II} methyl complexes **3.30** and **3.32** did not react with O₂ even after 22 h at rt (Figure 3.21 and Figure 3.22).

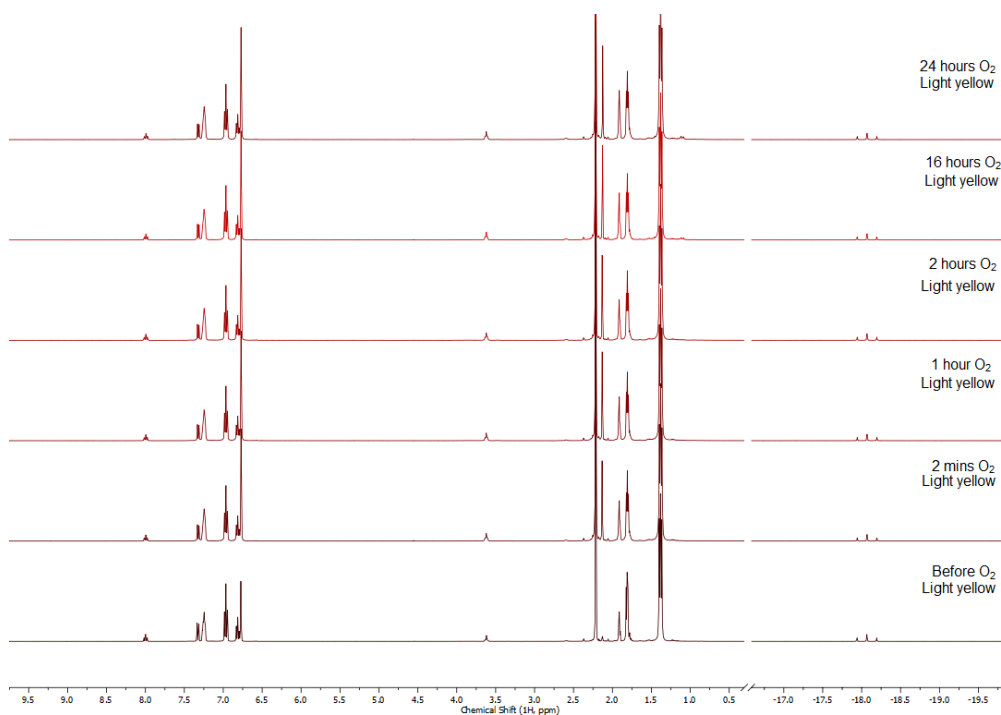


Figure 3.19 Stacked ^1H NMR spectra of the reaction of **3.29** with O_2 up to 24 hours (400 MHz, CD_3CN).

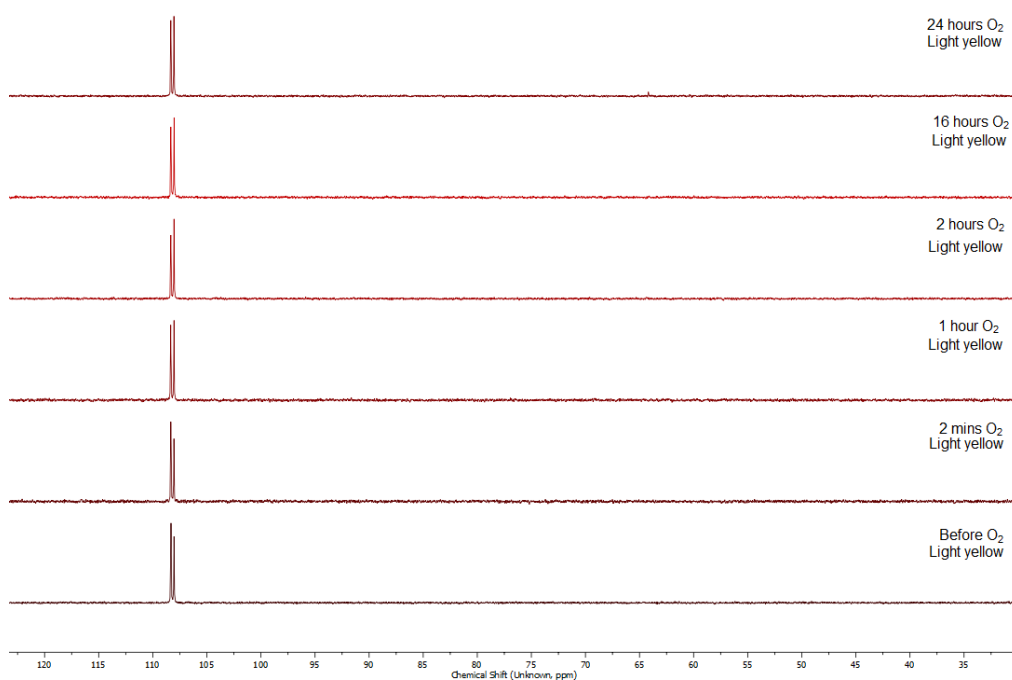


Figure 3.20 Stacked $^{31}\text{P}\{^1\text{H}\}$ NMR spectra of the reaction of **3.29** with O_2 up to 24 hours (162 MHz, CD_3CN).

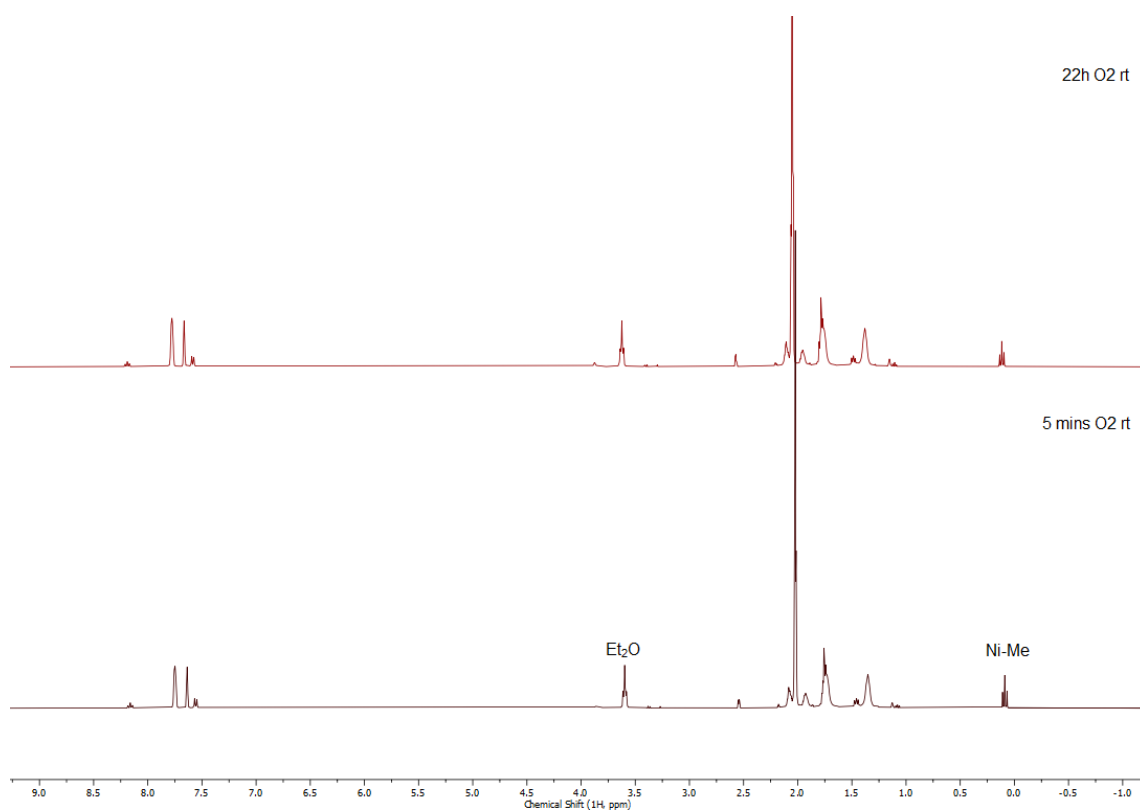


Figure 3.21 Stacked ^1H NMR spectra of the reaction of **3.32** with O_2 up to 22 hours at rt (400 MHz, acetone- d_6).

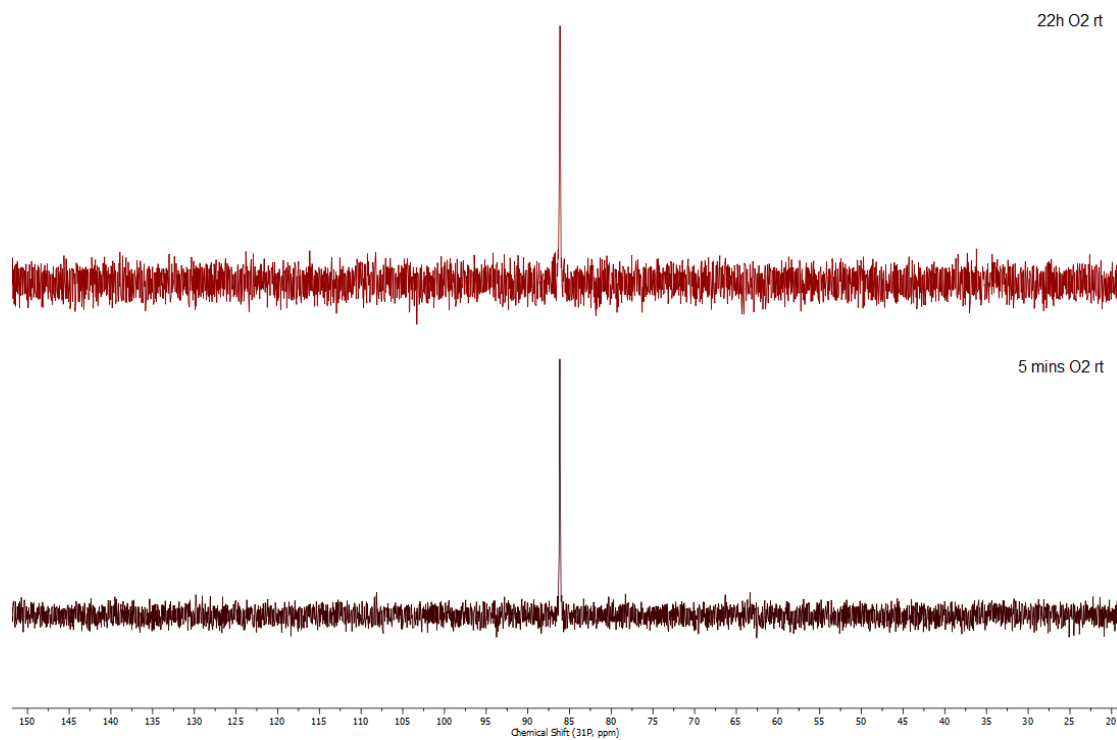


Figure 3.22 Stacked $^{31}\text{P}\{^1\text{H}\}$ NMR spectra of the reaction of **3.32** with O_2 up to 22 hours at rt (162 MHz, acetone- d_6).

These results demonstrate that controlling the steric bulk of pincer ligands leads to drastic differences in the stability and the reactivity towards small molecule activation. Imposing significant steric hindrance can lead to stabilization of normally highly reactive Ni–H and Ni–Me species in the presence of an O₂ atmosphere.

3.2.7 Computational Studies of the Reactivity of (Me₄PNP^R)Ni Complexes

3.2.7.1 Reduction of Nickel(II) Methyl Species

To shed light on the difference in reactivity of Ni^{II} halide, which leads to stable Ni^I complexes, and the reactivity of Ni^{II} methyl complexes that leads to dimerization through the *para* position of the pyridine ring, we performed frontier orbital analysis of the cationic species [(Me₄PNP^R)NiBr]⁺ (R = ⁱPr, [**iPrNiBr**]⁺; R = ^tBu, [**tBuNiBr**]⁺), [(Me₄PNP^R)NiMe]⁺ (R = ⁱPr, [**iPrNiMe**]⁺; R = ^tBu, [**tBuNiMe**]⁺) as well as tentative one-electron reduced neutral radical species [(Me₄PNP^R)NiMe][•] (R = ⁱPr, [**iPrNiMe**][•]; R = ^tBu, [**tBuNiMe**][•]) (see the optimized structure in Figure 3.23), analyzed their spin density distributions (Figure 3.24).

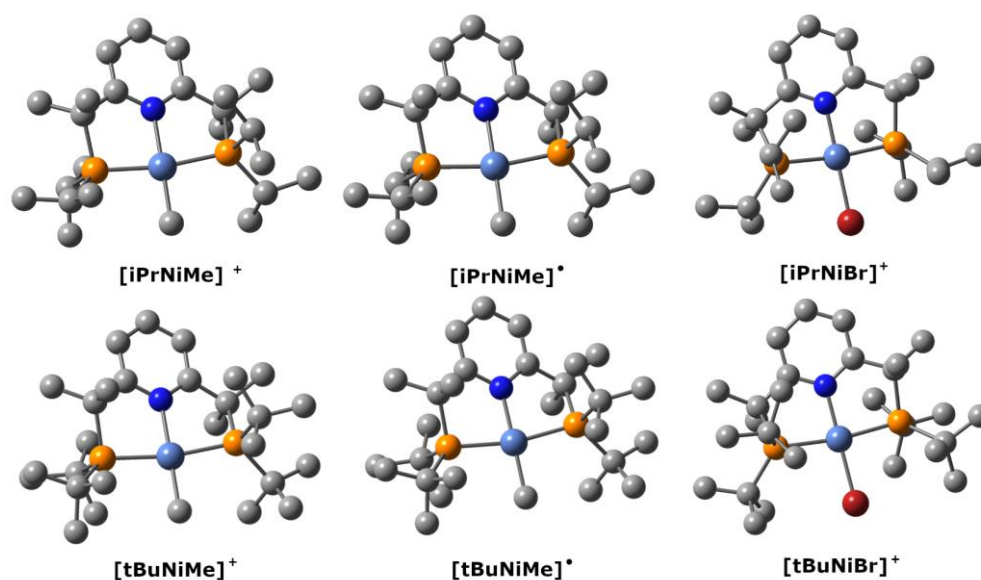


Figure 3.23 DFT-optimized structures of cationic Ni^{II}-Me [**iPrNiMe**]⁺ and [**tBuNiMe**]⁺; of cationic Ni^{II}-Br [**iPrNiBr**]⁺ and [**tBuNiBr**]⁺, and their one-electron-reduced products, the neutral species [**iPrNiMe**][•] and [**tBuNiMe**][•]. DFT optimized geometry. B3LYP, 6-311++G**/lanl2dz(Ni, Br).

Frontier orbital analysis shows that the LUMO of starting cationic complexes **[iPrNiMe]⁺** and **[tBuNiMe]⁺** (See Figure 3.27 and Figure 3.28) essentially has a pyridine-based character while the HOMO is metal based, with a mostly d_{z^2} character. The analysis of the one-electron reduced neutral species **[iPrNiMe][•]** and **[tBuNiMe][•]** shows that the SOMO is essentially the same as the LUMO of the cationic species, confirming that the starting material undergoes ligand-centered reduction. Figure 3.24 shows more clearly that the spin density is predominantly localized at the ligand, with the highest spin density at the *para*-carbon positions of the pyridine rings (0.492 and 0.47, respectively), while the spin density at the Ni centers was found to be close to zero (details of the atomic contribution of the spin density is shown in Figure 3.25 and Figure 3.26).

In Chapter 2, I showed that the spin density in neutral Ni^I halide (Me₄PNP^R)NiX complexes **2.40–2.43** (R = ⁱPr or ^tBu; X = Br or Cl) is largely localized at the metal center by DFT analysis, which is consistent with EPR studies that showed metal-based radical character with *g* tensor values around 2.12–2.24 depending on the nature of the species (see Figure 2.12 and Table 2.4).²²⁹ Therefore, if one-electron reduction of **[iPrNiMe]⁺** and **[tBuNiMe]⁺** leads to the initial formation of transient **[iPrNiMe][•]** and **[tBuNiMe][•]**, we can expect that the resulting ligand-based radical character of those complexes could lead to their dimerization by interaction with a second reduced species in solution and formation of a C–C bond. This dimerization was observed experimentally, where 2 equivalents of KC₈ were used to reduce the cationic Ni^{II} species **3.30**, forming the neutral Ni^{II} dimeric species **3.38** shown in Scheme 3.15. The localization of the spin density at the ligand as opposed to the metal could be due to the stronger σ -donor abilities of methyl vs. bromide, which would disfavor an electron-rich metalloradical species, forcing instead the radical to reside on the pyridine ring.

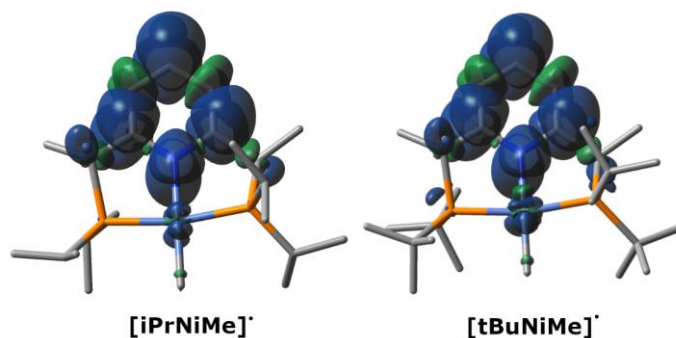


Figure 3.24 Spin density plots for complexes **[iPrNiMe][•]** and **[tBuNiMe][•]**. DFT optimized geometry, B3LYP, 6-311++G**/lanl2dz(Ni), isovalue = 0.0007. See Figures 3.20 and 3.21 for the atomic contribution to the spin densities.

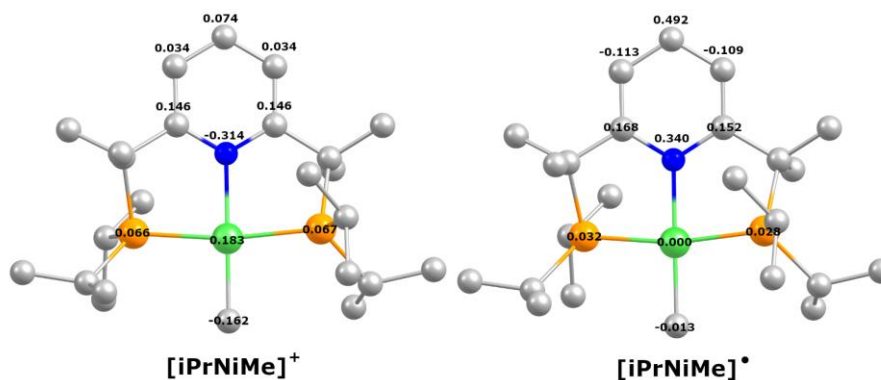


Figure 3.25 (left) Charge density (Truhlar's CM5 model) and (right) spin density (Mulliken) with the hydrogen summed for **[iPrNiMe]⁺** and **[iPrNiMe][•]**.

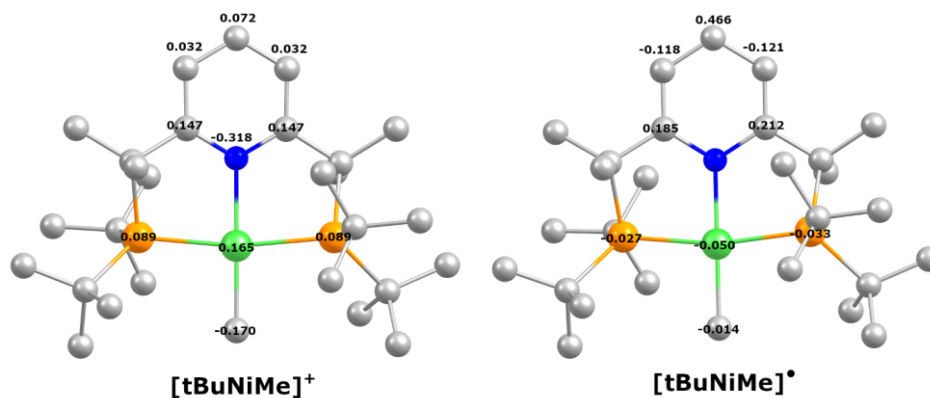


Figure 3.26 (left) Charge density (Truhlar's CM5 model) and (right) spin density (Mulliken) with the hydrogen summed for **[tBuNiMe]⁺** and **[tBuNiMe][•]**.

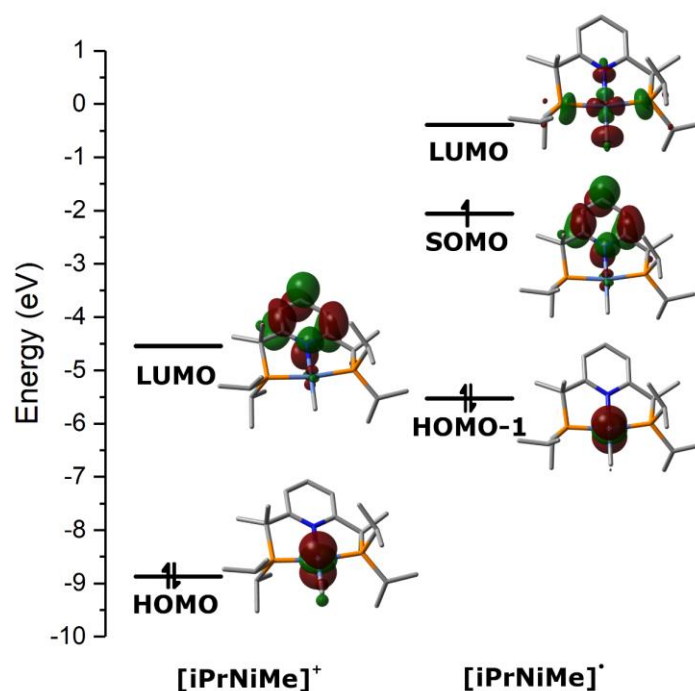


Figure 3.27 Molecular orbital diagram and HOMO-1, HOMO, SOMO, and LUMO representation of $[\text{iPrNiMe}]^+$ and $[\text{iPrNiMe}]^\bullet$. DFT optimized geometries, B3LYP, 6-311++G**/lanl2dz(Ni), alpha orbital representations, isovalue = 0.04.

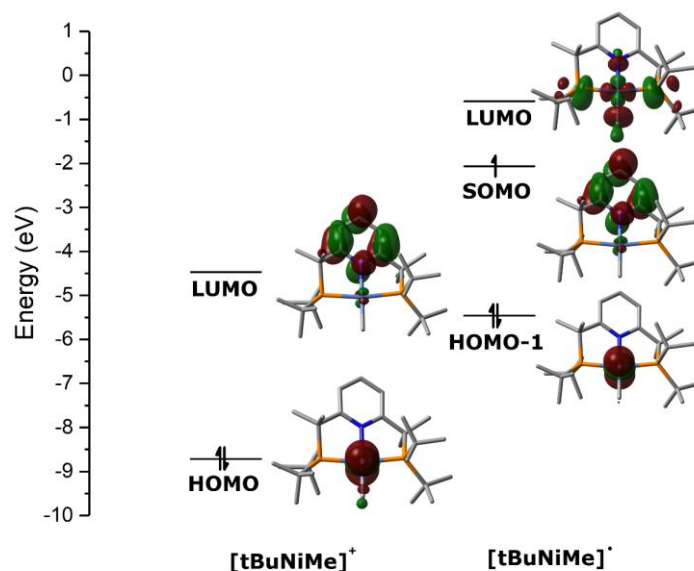


Figure 3.28 Molecular orbital diagram and HOMO, SOMO and LUMO representation of $[\text{tBuNiMe}]^+$ and $[\text{tBuNiMe}]^\bullet$. DFT optimized geometries, B3LYP, 6-311++G**/lanl2dz(Ni), alpha orbital representations, isovalue = 0.04.

3.2.7.2 Dearomatization of Nickel(II) Bromide Complexes with LiBEt₃H

The dearomatization of the pyridine ring in the *para* position by reaction with LiBEt₃H was previously investigated by the group of Jones in 2011.⁵³

Analysis of the molecular orbitals for cationic complexes [iPrNiBr]⁺ and [tBuNiBr]⁺ show that the LUMO of both complex is predominantly metal based, so at first glance, the dearomatization to form **iPrNiBrdearo** and **tBuNiBrdearo** should not be favored and reaction with LiBEt₃H should give the respective hydride species (Figure 3.29 and Figure 3.30). However, Truhlar's CM5 charge analysis of the bromo species show that the pyridine ring *para* position has a small, but significant positive charge (See Table 3.4, [iPrNiBr]⁺ 0.082; [tBuNiBr]⁺ 0.081), which means that nucleophilic attack on that carbon should be possible. Similar trend is observed for NBO charges on the corresponding atoms, with a charge of 0.063 for [iPrNiBr]⁺ and 0.126 for [tBuNiBr]⁺. Further analysis of the orbitals show that the LUMO+1 orbitals are very close in energy and could also be accessible to reactants, with the difference of energy between the LUMO and LUMO+1 of 0.100 eV and 0.225 eV for [iPrNiBr]⁺ and [tBuNiBr]⁺, respectively.

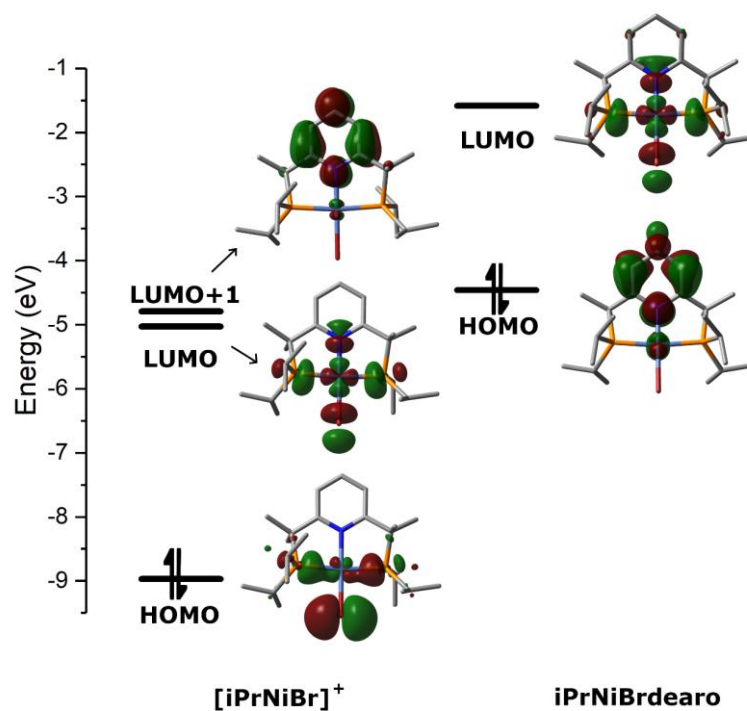


Figure 3.29 Molecular orbital diagram and of $[\text{iPrNiBr}]^+$ and iPrNiBrdearo . DFT optimized geometries, B3LYP, 6-311++G**/lanl2dz(Ni), alpha orbital representations, isovalue = 0.04.

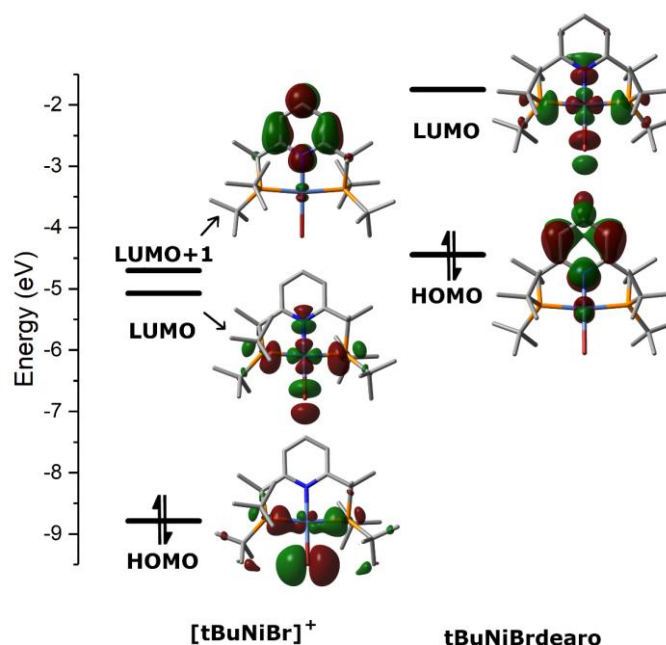
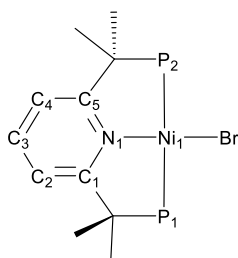


Figure 3.30 Molecular orbital diagram of $[\text{tBuNiBr}]^+$ and tBuNiBrdearo . DFT optimized geometries, B3LYP, 6-311++G**/lanl2dz(Ni), alpha orbital representations, isovalue = 0.04.

Table 3.4 Selected partial atomic charges with summed hydrogens (Truhlar's Charge model 5)^a for optimized complexes



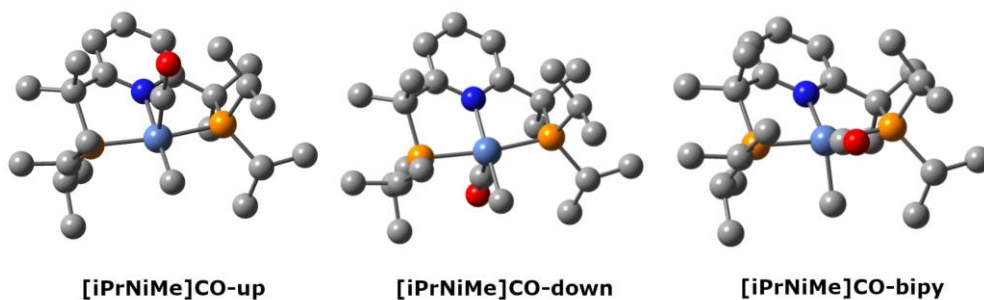
atom	[iPrNiBr] ⁺	[tBuNiBr] ⁺
Ni1	0.177	0.162
N1	-0.314	-0.319
P1	0.066	0.092
P2	0.066	0.092
C1	0.149	0.149
C2	0.040	0.038
C3	0.082	0.081
C4	0.040	0.038
C5	0.149	0.149
Br	-0.084	-0.155

^a Calculated using the Multiwfn program²³⁹

3.2.7.3 Absence of Reactivity of Nickel(II) Methyl Species with Small Molecules

In addition, to explain the lack of reactivity of the Ni–methyl complexes towards CO, CO₂, and ethylene, we tried to optimize the geometry of the tentative five-coordinate adduct of (Me₄PNP^R)Ni^{II}Me with CO as a model compound, using various initial geometries (square pyramidal or trigonal bipyramidal) and different orientations of CO relative to the complex coordination planes (See Figure 3.31 and Figure 3.32).

Initial geometries



Final geometries

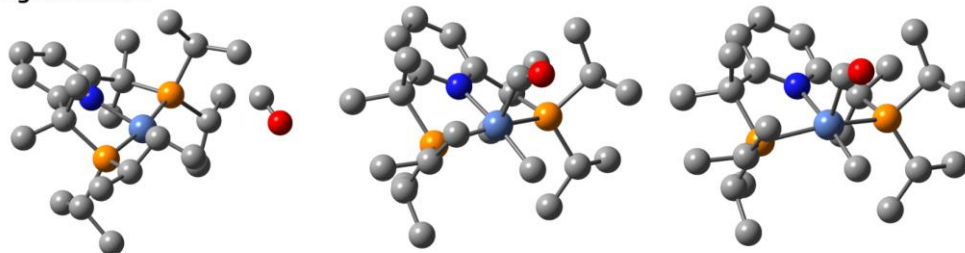
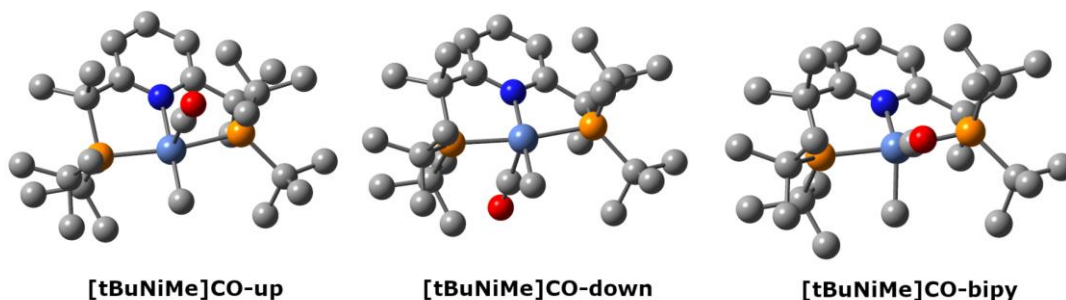


Figure 3.31 Geometries before and after optimization for [iPrNiMe]CO-up, [iPrNiMe]CO-down, and [iPrNiMe]CO-bipy. DFT optimized geometry. B3LYP, 6-311G**/lanl2dz(Ni), THF solvent continuum

Starting geometries



Final geometries

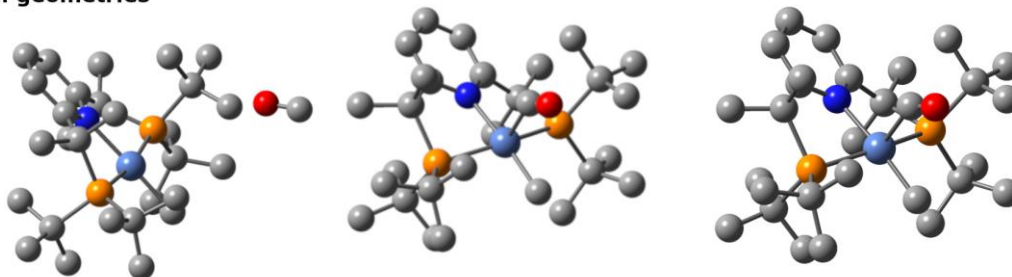


Figure 3.32 Geometries before and after optimization for [tBuNiMe]CO-up, [tBuNiMe]CO-down, and [tBuNiMe]CO-bipy. DFT optimized geometry. B3LYP, 6-311G**/lanl2dz(Ni), THF solvent continuum

In the case of the square pyramid starting geometry with the CO in the “up” fashion ([iPrNiMe]CO-up and [tBuNiMe]CO-up), no stable adducts with CO could be found, and CO

remained outside of coordination sphere of the metal after optimization (Ni–C distance exceeding 5 Å), which is an uphill process with ΔG of 5.8 kcal mol⁻¹ for *i*Pr and 6.3 kcal·mol⁻¹ for *t*Bu. In case of the same geometry with the CO in the “down” fashion ([*i*PrNiMe]CO-down and [*t*BuNiMe]CO-down) as well as the starting geometry where the CO is in a trigonal bipyramidal fashion ([*i*PrNiMe]CO-bipy or [*t*BuNiMe]CO-bipy), the geometry of tentative CO adducts showing Ni–C distances of 2.18-2.24 Å were optimized. However, in all cases binding of CO was found to be an uphill process with ΔG of 14.7 kcal mol⁻¹ or 18.6 kcal mol⁻¹, with the highest energy belonging to a *t*Bu complex (see Figure 3.33 and Figure 3.34).

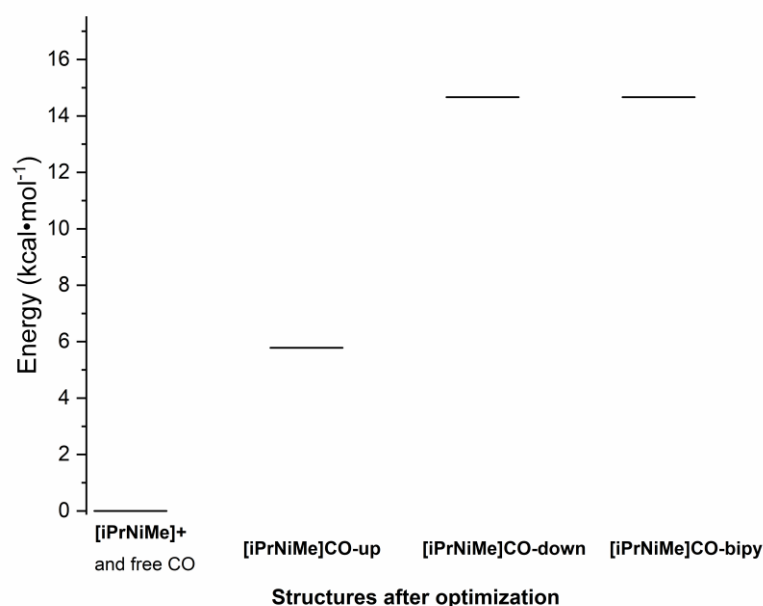


Figure 3.33 Energy diagram for the optimized structures [*i*PrNiMe]CO-up, [*i*PrNiMe]CO-down, [*i*PrNiMe]CO-bipy. DFT optimized geometry. B3LYP, 6-311G**/lanl2dz(Ni), THF solvent continuum

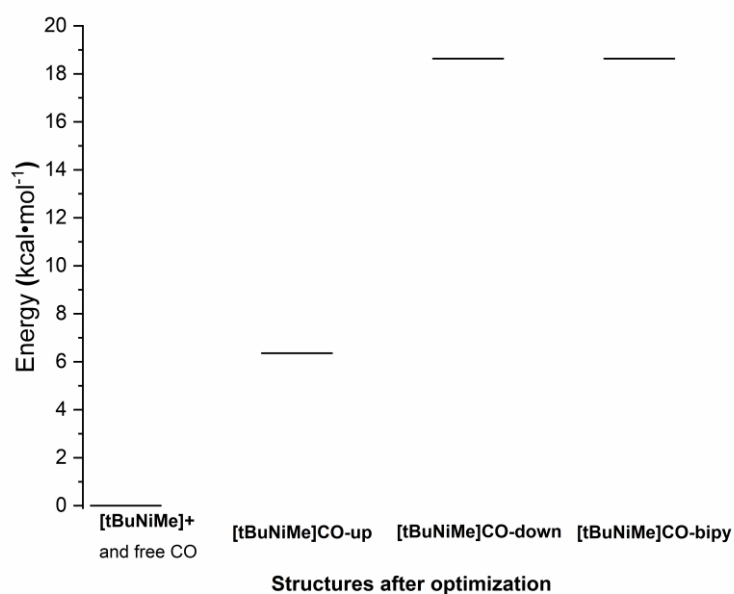


Figure 3.34 Energy diagram for the optimized structures [tBuNiMe]CO-up, [tBuNiMe]CO-down, [NiMe]CO-bipy. DFT optimized geometry. B3LYP, 6-311G**/lanl2dz(Ni), THF solvent continuum

3.3 Conclusion of Chapter 3

We showed that designing the PNP pincer ligand in which dearomatization through deprotonation of the phosphine arms is blocked by methylation leads to ligand reactivity at the *para*-carbon position with strong reductants. We reported two types of pyridine ring dearomatization, one via reduction in the *para* position with a hydride source, and another through dimerization with the formation of a new C–C bond. DFT studies confirmed that the proposed transient, one-electron reduced (Me₄PNP^R)Ni–Me species are expected to demonstrate ligand-based radical, rather than the metal-based radical character previously observed in (Me₄PNP^R)Ni^I–X (X = Br, Cl) complexes, explaining their *para*-carbon based reactivity.

In addition, we showed that steric hindrance affects the outcome of Ni–Me and Ni–H complexes' reactivity in small molecule activation. In the case of significantly sterically hindered Me₄PNP^{*t*Bu} ligand (**L2.6**), we were able to obtain an unexpectedly stable Ni hydride complex that did not

react with typical gaseous reagents and O₂ even after a prolonged reaction time. Reducing sterics by using the Me₄PNP^{*i*Pr} ligand (**L2.5**) led to the observation of a transient superoxide species.

3.4 Experimental Section

Solvents and reagents: All operations were performed using standard Schlenk or glovebox techniques under an N₂ atmosphere unless indicated otherwise. Unless otherwise indicated, all solvents and reagents were used as received. Non-deuterated solvents were taken from a solvent purification system (MBRAUN SPS). Acetone-*d*₆ was vacuum distilled over dried magnesium sulfate at low temperature. All other deuterated solvents were added to activated 3 Å molecular sieves. Methyl lithium 1M in diethyl ether and sodium tetraphenylborate were purchased from Kanto Chemicals. Sodium borohydride and lithium triethylborohydride were purchased from Tokyo Chemical Industry Co. Ltd. Copper(I) iodide was purchased from Nacalai Tesque Inc. Dimethylzinc 1M in heptane was purchased from Sigma. Potassium graphite was purchased from Strem Chemicals, Inc. Electrochemical grade tetrabutylammonium hexafluorophosphate (^{*n*}Bu₄NPF₆) from Fluka was used as the supporting electrolyte. Complexes [(Me₄PNP^R)Ni^{II}Br]Br (R = ^{*i*}Pr (**2.32**), ^{*t*}Bu (**2.34**)) and [(Me₄PNP^R)Ni^{II}Br]B(Ar^F)₄ (R = ^{*i*}Pr (**2.36**), ^{*t*}Bu (**2.38**)) were synthesized according to the procedures described in Chapter 2.

NMR, UV-vis, and electrochemical experiments were performed as described in Chapter 2

Liquid Chromatography coupled with High Resolution Mass Spectrometry (LC-ESI-HRMS) analyses: LC-ESI-HRMS measurements were done using a 1 mg/mL acetonitrile solution of the complexes, with the samples eluted through a 50 x 0.18 mm ODS column with 3.0 µm particle size. The gradient used for the liquid chromatography is 50% to 95% water (0.1% formic acid) to acetonitrile (0.1% formic acid) over 8 minutes. HRMS spectra were recorded on positive and/or negative mode for each sample. Mass-spectra of complexes **3.26** and **3.27** are not reported because they react instantly in the presence of oxygen either in the solvent or from air.

Electron Paramagnetic Resonance (EPR) spectroscopic analyses: X-band EPR spectra were recorded on an X-band JEOL JES-X330 instrument using liquid nitrogen-cooled cryostat in 5 mm diameter quartz tubes.

In a typical experiment *with the spin-trapping agent DMPO*: a 18 mM solution of **3.30** or **3.32** and a 180 mM solution of DMPO in acetone- d_6 was placed into a Young NMR tube under an N_2 and irradiated under UV light (mercury lamp) for 1 h before the solution was transferred into a sealed quartz capillary under an N_2 . Then, the capillary is transferred into a thin capillary EPR tube and inserted in the EPR cavity at room temperature.

In a typical experiment *without the spin-trapping agent*: a 4.5 mM solution of complex **3.30** or **3.32** in acetone- d_6 with or without 1 equiv of nBu_4NX ($X = Cl, Br$) was placed into 5 mm diameter quartz EPR tube and irradiated under UV light from a mercury lamp for 1h, then precooled in liquid nitrogen and quickly inserted into a pre-cooled EPR cavity.

In a typical experiment *involving a reduction using KC_8* : a 7.5 mM solution of the complexes was added to 1 equivalent of KC_8 in an EPR tube, mixed for 5 minutes until a color change is observed, and then precooled in liquid nitrogen and quickly inserted into a pre-cooled EPR cavity. The summary of experimental parameters is given in the linked Appendix of Chapter 3.

Simulation of the experimental spectrum were done using the Easyspin¹⁹⁸ package in Matlab R2016b¹⁹⁹ “Pepper” and “Garlic” functions were used for spectra simulation; g-values and superhyperfine splitting constants were optimized using least-square fitting procedure in EasySpin (esfit function, Levenberg/Marquardt algorithm). The hyperfine coupling constants (if any) and g tensor values are reported in the main text of the article.

X-ray diffraction studies: The X-ray diffraction experiments were done using the same instruments and parameters as described in Chapter 2. Below are details regarding to specific structures.

Complex **3.24** crystallize as a solvate with acetonitrile (1:1), complex **3.26** crystallizes as a solvate with a disordered toluene molecule (1:1). The unit cells of complexes **3.28** and **9** contain highly disordered solvent molecules, some of which were treated as a diffuse contribution to the overall scattering without specific atom positions by *PLATON/SQUEEZE*.²⁴⁰ Squeezed solvent info is not included in the formulae and related items such as molecular weights and calculated densities. Some trifluoromethyl groups of tetrakis[3,5-bis(trifluoromethyl)phenyl]borate are disordered for the crystals of **3.26**, **3.28**, **3.30**, and **3.32**. In the cases of **3.25** and **3.28**, the framework of tetraphenylborate and tetrakis[3,5-bis(trifluoromethyl)phenyl]borate anions, respectively, is found to be disordered. The isopropyl groups at the phosphorus atom are disordered for **3.26** and **7**. Crystals of **8** are substitutionally disordered with a hydride species. Severe disorder involve whole pincer ligand was present for complex **3.25**; this structure was refined based on data measured on a Cu source (jk329) and a Mo source (bjk002). The disorder was resolved using free variables and reasonable restraints on geometry and anisotropic displacement parameters.

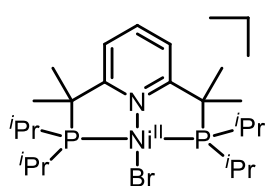
Detailed information about crystal structure determination can be accessed via supplementary cif files. The crystallographic data for the investigated compounds has been deposited in the Cambridge Crystallographic Data Centre as supplementary publication numbers CCDC 1943381-1943394. These data can be obtained free of charge via <https://www.ccdc.cam.ac.uk/structures/>.

Computational analyses: DFT calculations were performed using Gaussian 09 rev. E.01²¹¹ using unrestricted B3LYP^{212, 213} functional. For geometry optimization and for C, H, N, the 6-311++G** basis set was used while for Ni and Br atoms, the LANL2DZ electron-core potential basis was used. Geometry optimization was done starting from X-ray coordinates then artificially removing the counterion ($[\text{RNiL}]^+$ complexes, R = iPr, tBu; L = Br, Me), as well as artificially

including a radical ($[\text{R}^{\text{Ni}}\text{L}]^{\bullet}$ complexes, $\text{R} = \text{iPr}, \text{tBu}$; $\text{L} = \text{Br}, \text{Me}$) Vibrational frequencies calculations were used to confirm the absence of imaginary frequencies. For the determination of orbitals, full population analysis was done using the unrestricted open-shell formalism (UB3LYP) with single point calculations under the standard basis set used for geometry optimization. NPA analyses were also done on the final optimized geometries using the unrestricted open-shell formalism (UB3LYP) using the same basis set as geometry optimization. The xyz coordinates of geometry-optimized structures for the cationic and neutral complexes $[\text{iPrNiBr}]^+$, $[\text{tBuNiBr}]^+$ $[\text{iPrNiMe}]^+$, $[\text{iPrNiMe}]^{\bullet}$, $[\text{tBuNiMe}]^+$, and $[\text{tBuNiMe}]^{\bullet}$, for the homolysis product $[\text{iPrNi}]^{++}$, and for the CO adducts $[\text{iPrNiMe}]^+\text{CO-up}$, $[\text{iPrNiMe}]^+\text{CO-down}$, $[\text{iPrNiMe}]^+\text{CO-bipy}$, $[\text{tBuNiMe}]^+\text{CO-up}$, $[\text{tBuNiMe}]^+\text{CO-down}$, $[\text{tBuNiMe}]^+\text{CO-bipy}$ and the complex **3.25** in “up-up” and “up-down” conformation are copied from a .xyz file for convenient visualization and attached to the linked Appendix of Chapter 3.

The geometry optimization and calculation of the energy of possible CO adducts of the methyl complexes were performed using the unrestricted B3LYP functional, with 6-311G** basis set (no polarization) and the LANL2DZ electron-core potential basis for nickel in a THF solvent continuum. The CO atom was set at an arbitrary distance of 1.83 Å (Ni-C distance in $\text{Ni}(\text{CO})_4$) over ($[\text{5}]\text{CO-up}$ and $[\text{6}]\text{CO-up}$) or under ($[\text{5}]\text{CO-down}$ and $[\text{6}]\text{CO-down}$) the plane of the molecule as well as in a trigonal bipyramidal fashion ($[\text{5}]\text{CO-bipy}$ and $[\text{6}]\text{CO-bipy}$). The Gibbs free energy of the optimized geometries were compared to the sum of Gibbs free energy of the starting cationic complex without CO ($[\text{iPrNiMe}]^+$ or $[\text{tBuNiMe}]^+$), and the optimized free CO molecule, both optimized using the same parameters.

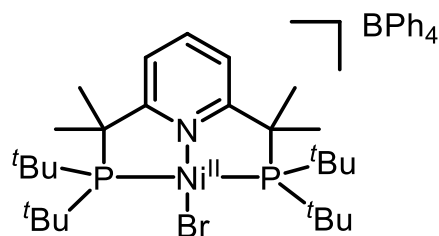
3.4.1 $[(\text{Me}_4\text{PNP}^{\text{iPr}})\text{Ni}^{\text{II}}\text{Br}]\text{BPh}_4$, **3.24**.



Sodium tetraphenylborate (NaBPh_4) (36.4 mg, 0.106 mmol, 1.08 equiv) was added to a solution of **2.32** (60.3 mg, 0.098 mmol) in THF and stirred at rt for 5 minutes. The solution was then evaporated and

washed with diethyl ether to remove the remaining salt. The insoluble complex was collected on a short celite plug and washed with acetone and then evaporated to give a light orange solid (58 mg, 0.068 mmol, 70%). Yellow crystals suitable for X-ray diffraction were grown from a concentrated acetonitrile solution at -30 °C under N₂. ¹H NMR (400 MHz, CDCl₃) δ 1.16–1.22 (m, 12H, PCH-CH₃), 1.51–1.55 (m overlap, 12H + 12 H, PCH-CH₃ + P-C(CH₃)₂C_{py}), 2.47–2.56 (m, 4H, P-CHCH₃), 6.57 (d, *J*_{HH} = 7.9 Hz, 2H, C_{py}-H_{meta}), 6.88 (t, *J*_{HH} = 7.3 Hz, 4H, BC_{Ar}-H_{para}), 7.02 (t, *J*_{HH} = 7.3 Hz, 8H, BC_{Ar}-H_{meta}), 7.16 (t, *J*_{HH} = 8.0 Hz, 1H, C_{py}-H_{para}), 7.42 (br m, 8H, BC_{Ar}-H_{ortho}). ¹³C{¹H} NMR (101 MHz, CDCl₃) δ 19.17 (PCH-CH₃), 19.73 (PCH-CH₃), 23.38 (vt, *J*_{PC} = 10.7 Hz, PCH-CH₃), 28.01 (P-C(CH₃)₂C_{py}), 49.99 (vt, *J*_{PC} = 8.2 Hz, P-C(CH₃)C_{py}), 120.52 (vt, *J*_{PC} = 4.4 Hz, C_{py,meta}), 121.88 (B-C_{Ar,para}), 125.67–125.74 (m, B-C_{Ar,meta}), 136.43 (B-C_{Ar,ortho}), 144.57 (C_{py,para}), 164.27 (dd, *J*_{BC} = 49.2 Hz, B-C_{Ar,ipso}), 172.38 (vt, *J*_{PC} = 7.1 Hz, C_{py,ortho}). ³¹P{¹H} NMR (162 MHz, CDCl₃) 73.74. ATR-IR (cm⁻¹): 3045 (w), 2973 (w), 2874 (w), 1571 (w), 1457 (m), 1388 (w), 1369 (w), 1287 (w), 1244 (w), 1152 (w), 1100 (w), 1032 (w), 932 (w), 884 (w), 844 (w), 811 (w), 732 (m), 701 (s), 653 (m). UV-vis (THF, [1·10⁻⁴ M]), λ_{max}, nm (ε, L mol⁻¹ cm⁻¹): 259 (21703), 276 (sh, 10429), 300 (6290), 345 (13442), 466 (1855). Anal. Calcd. For C₄₇H₆₃NP₂NiBrB: C, 66.15; H, 7.44; N, 1.64. Found: C, 65.92; H, 7.30; N, 2.27.

3.4.2 [(Me₄PNP^{Bu})Ni^{II}Br]BPh₄, 3.25.

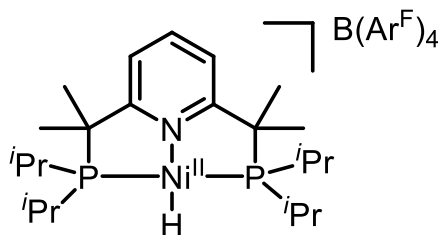


The same procedure to prepare **3.24** was used to prepare **3.25** starting from the previously reported **2.32** (50.0 mg, 0.075 mmol) and NaBPh₄ (26.8 mg, 0.078 mmol, 1.05 equiv) to afford a pink solid (59 mg, 0.065 mmol, 87%). Red

crystals suitable for X-ray diffraction were grown from a concentrated acetone solution at rt. ¹H NMR (400 MHz, CD₃CN) δ 1.42–1.45 (m, 18 H, Me of ^tBu), 1.56–1.87 (br m, 18H, Me of ^tBu),

1.90–1.96 (m overlapping with CD₃CN, 6H, P–C(CH₃)₂C_{py}), 2.05–2.07 (m, 6H, P–C(CH₃)₂C_{py}), 6.85 (t, $J_{\text{HH}} = 8.0$ Hz, 4H, BC_{Ar}–H_{para}), 7.00 (t, $J_{\text{HH}} = 7.3$ Hz, 8H, BC_{Ar}–H_{meta}), 7.28 (t, $J_{\text{HH}} = 6.2$ Hz, 8H, BC_{Ar}–H_{ortho}), 7.37 (d, $J_{\text{HH}} = 8.1$ Hz, 2H, C_{py}–H_{meta}), 8.05 (t, $J_{\text{HH}} = 8.0$ Hz, 1H, C_{py}–H_{para}). ¹³C{¹H} NMR (101 MHz, CD₃CN) δ 24.88 (P–C(CH₃)₂C_{py}), 32.15 (Me of ^tBu), 32.94 (br, Me of ^tBu), 36.05 (P–C(CH₃)₂C_{py}), 40.11 (C_{quat} of ^tBu), 41.55 (vt, $J_{\text{PC}} = 5.7$ Hz, C_{quat} of ^tBu), 53.12 (vt, $J_{\text{PC}} = 4.9$ Hz, P–C(CH₃)₂C_{py}), 121.44 (C_{py,meta}), 122.74 (B–C_{Ar,para}), 126.54–126.62 (m, B–C_{Ar,meta}), 136.99 (B–C_{Ar,ortho}), 144.35 (C_{py,para}), 164.74 (dd, $J_{\text{BC}} = 49.3$ Hz, B–C_{Ar,ipso}), 174.01 (C_{py,ortho}). ³¹P{¹H} NMR (162 MHz, CD₃CN) δ 87.15. ATR–IR (cm^{–1}): 3051 (w), 3036 (w), 2998 (w), 2973 (w), 2936 (w), 2875 (w), 1599 (w), 1579 (w), 1563 (w), 1458 (m), 1427 (m), 1388 (w), 1367 (w), 1267 (w), 1243 (w), 1181 (w), 1146 (w), 1129 (w), 1100 (w), 1065 (w), 1047 (w), 1032 (m), 932 (w), 885 (w), 848 (w), 811 (w), 757 (m), 129 (s), 701 (s), 673 (m). UV–vis (THF, [1·10^{–4} M]), λ_{max} , nm (ϵ , L mol^{–1} cm^{–1}): 260 (20652), 276 (sh, 10944), 363 (9239), 505 (2075). Anal. Calcd. For C₅₁H₇₁NP₂NiBrB: C, 67.35; H, 7.87; N, 1.54. Found: C, 66.72; H, 7.64; N, 1.56.

3.4.3 [(Me₄PNP^{*i*}Pr)Ni^{II}H]B(Ar^F)₄, 3.26.

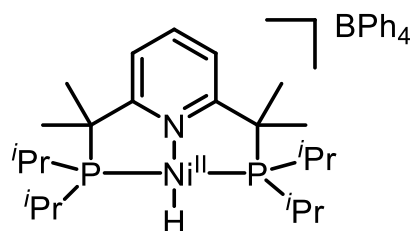


Sodium tetrakis[3,5-bis(trifluoromethyl)phenyl]borate (NaB(Ar^F)₄) (14.7 mg, 0.017 mmol) was added to a THF solution of **2.32** (10.0 mg, 0.017 mmol, 1 equiv) and stirred for 5 minutes. The mixture was then filtered over a short

celite plug and sodium tetrahydroborate (NaBH₄) (6.3 mg, 0.17 mmol) was added followed by vigorous stirring for 4 hours to give a light-yellow solution. The solution was evaporated, and diethyl ether was added to dissolve the complex without dissolving the salts. The solution was filtered on a short celite plug and the solvent was evaporated to obtain a pale-yellow powder (23 mg, 0.017 mmol, 100 %). Yellow crystals suitable for X-ray diffraction were obtained by slow crystallization of a concentrated toluene solution of **3.26** at –30 °C under N₂. ¹H NMR (400 MHz,

acetone- d_6) δ -18.05 (t, $J_{PH} = 54.8$ Hz, 1H, Ni-H), 1.17–1.22 (m, 12H, PCH-CH3), 1.40–1.46 (m, 12H, PCH-CH3), 1.77–1.79 (m, 12H, PCH-CH3), 2.54–2.62 (m, 4H, PCH-H-CH₃), 7.62 (d, $J_{HH} = 7.9$ Hz, 2H, C_{py}-Hmeta), 7.67 (br s, BC_{Ar}-Hpara), 7.77–7.79 (m, 8H, BC_{Ar}-Hortho), 8.23 (tt, $J_{HH} = 8.0, 1.3$ Hz, 1H, C_{py}-Hpara). $^{13}\text{C}\{^1\text{H}\}$ NMR (101 MHz, acetone- d_6) δ 20.68 (PCH-CH3), 21.11 (PCH-CH3), 24.20 (vt, $J_{PC} = 11.5$ Hz, PCH-CH₃), 26.15 27.89 (P-C(CH3)₂C_{py}), 51.27 (vt, $J_{PC} = 7.6$ Hz, P-C(CH₃)₂C_{py}), 118.37–118.53 (m, B-CAr,para), 120.52 (vt, $J_{PC} = 4.6$ Hz, Cpy,meta), 125.36 (q, $J_{CF} = 271.8$ Hz, BC_{Ar,meta}-CF3), 130.00 (qdd, $J_{CF} = 30.5$ Hz; $J_{CB} = 5.7$ Hz; $J_{CF} = 2.7$ Hz, B-CAr,metaCF₃), 135.52 (B-CAr,ortho), 143.16 (Cpy,para), 162.58 (dd, $J_{BC} = 49.9$ Hz, B-CAr,ipso), 172.28 (vt, $J_{PC} = 7.2$ Hz, Cpy,ortho). $^{31}\text{P}\{^1\text{H}\}$ NMR (162 MHz, acetone- d_6) δ 85.06 ^{19}F NMR (376 MHz, acetone- d_6): δ -63.14. ATR-IR (cm⁻¹): 2972 (w), 2940 (w), 1878 (w), 1925 (w), 1610 (w), 1564 (w), 1467 (w), 1389 (w), 1353 (s), 1270 (s), 1160 (s), 1118 (s), 1045 (m), 950 (w), 928 (w), 885 (m), 839 (m), 812 (w), 759 (w), 744 (w), 715 (m), 681 (m), 668 (s). UV-vis (THF, [1·10⁻⁴ M]), λ_{max} , nm (ϵ , L mol⁻¹ cm⁻¹): 238 (35148), 242 (sh, 32044), 263 (sh, 18636), 269 (19436), 295 (7079), 381 (1688), 418 (sh, 827). Anal. Calcd. For C₅₅H₅₆NP₂NiBF₂₄: C, 50.10; H, 4.28; N, 1.06. Found: C, 49.15; H, 3.98; N, 1.04.

3.4.4 [(Me₄PNP^{*i*Pr})Ni^{II}H]BPh₄, 3.27.

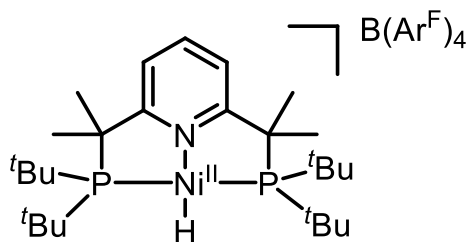


To a solution of **2.32** (100.0 mg, 0.163 mmol) in dry THF under an N₂ atmosphere was added NaBPh₄ (58.5 mg, 0.171 mmol, 1.05 equiv) and stirred for 5 minutes. The mixture was filtered over a short celite plug and to the solution is added

NaBH₄ (61.6 mg, 1.63 mmol, 10 equiv) and allowed to stir vigorously for 18 hours to give a dark solution. The solution is filtered on a short celite plug and the solvent is evaporated. Then, a minimum amount of acetonitrile or THF was added and the remaining salts were precipitated by adding pentane. The solids were filtered on a short celite pad and washed with a small amount

of THF or acetonitrile to dissolve most of the complex. The solvent was evaporated to obtain a pale-yellow powder (114 mg, 0.147 mmol, 91%). Yellow crystals suitable for X-ray diffraction were obtained by slow crystallization of a concentrated THF solution of **3.27** at -30 °C under N₂. ¹H NMR (400 MHz, CD₃CN) δ -18.23 (t, *J*_{PH} = 54.9 Hz, 1H, Ni-H), 1.09–1.15 (m, 12H, PCH-CH₃), 1.34–1.40 (m, 12H, PCH-CH₃), 1.64–1.66 (m, 12H, P-C(CH₃)₂C_{py}), 2.42–2.51 (m, 4H, PCH-CH₃), 6.84 (tt, *J*_{HH} = 7.3 Hz, *J*_{PH} = 1.6 Hz, 4H, BC_{Ar}-H_{para}), 6.99 (t, *J*_{HH} = 7.4 Hz, 8H, BC_{Ar}-H_{meta}), 7.25–7.30 (m, 8H, BC_{Ar}-H_{ortho}), 7.38 (t, *J*_{HH} = 8.0 Hz, 2H C_{py}-H_{meta}), 8.02 (tt, *J*_{HH} = 8.0 Hz, *J*_{PH} = 1.3 Hz, 1H, C_{py}-H_{para}). ¹³C{¹H} NMR (101 MHz, CD₃CN) δ .20.68 (PCH-CH₃), 21.12 (PCH-CH₃), 24.21 (vt, *J*_{PC} = 11.5 Hz, PCH-CH₃), 27.94 (P-C(CH₃)₂C_{py}), 51.21 (vt, *J*_{PC} = 7.6 Hz, P-C(CH₃)₂C_{py}), 120.39 (vt, *J*_{PC} = 3.8 Hz, C_{py,meta}), 122.76 (B-C_{Ar,para}), 126.58 (vdd, *J*_{BC} = 4.8 Hz, 2.4 Hz, B-C_{Ar,meta}), 136.73 (B-C_{Ar,ortho}), 142.90 (C_{py,para}), 164.79 (dd, *J*_{BC} = 98.4 Hz, 49.2 Hz, B-C_{Ar,ipso}), 172.22 (vt, *J*_{PC} = 7.2 Hz, C_{py,ortho}). ³¹P{¹H} NMR (162 MHz, CD₃CN) δ 84.91. ATR-IR (cm⁻¹): 3055 (w), 3029 (w), 2893 (w), 2971 (w), 2958 (w), 2931 (w), 2869 (w), 2290 (w), 1579 (w), 1563 (w), 1455 (w), 1427 (w), 1384 (w), 1367 (w), 1256 (w), 1240 (w), 1186 (w), 1151 (w), 1129 (w), 1116 (w), 1098 (w), 1068 (w), 1032 (w), 932 (w), 885 (w), 842 (w), 813 (w), 745 (m), 731 (m), 701 (s), 663 (m). UV-vis (THF, [1·10⁻⁴ M]), λ_{max}, nm (ε, L mol⁻¹ cm⁻¹): 260 (sh, 14681), 266 (sh, 12426), 275 (8605), 300 (4526), 340 (4702), 369 (sh, 3445). Anal. Calcd. For C₄₇H₆₄NP₂NiBrB: C, 72.89; H, 8.33; N, 1.81. Found: C, 72.04; H, 8.06; N, 2.24.

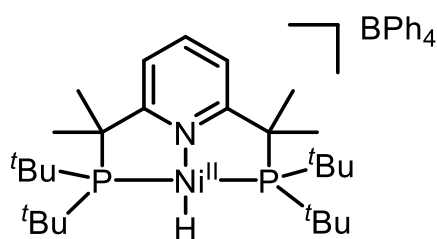
3.4.5 [(Me₄PNP^tBu)Ni^{II}H]B(Ar^F)₄, **3.28**.



The same procedure to prepare **3.26** was used to prepare **3.28** using **2.34** (10.0 mg, 0.015 mmol), NaB(Ar^F)₄ (13.2 mg, 0.015 mmol, 1.00 equiv) and NaBH₄ (5.6 mg, 0.15 mmol, 10 equiv). A pale-yellow solid was obtained (22

mg, 0.016 mmol, 100%). Yellow crystals suitable for X-ray diffraction were grown from a concentrated anhydrous THF solution of **3.28** at -30 °C under an N₂. ¹H NMR (400 MHz, acetone-d₆) δ -17.95 (t, *J*_{HP} = 50.4 Hz, 1H, Ni-H), 1.46–1.49 (m, 36H, Me of ^tBu), 1.95–1.97 (m, 12H, P-C(CH₃)C_{py}), 7.58 (d, *J*_{HH} = 8.1 Hz, 2H, C_{py}-H_{meta}), 7.67 (br s, 4H, BC_{Ar}-H_{para}), 7.76–7.80 (m, 8H, BC_{Ar}-H_{ortho}), 8.22 (t, *J*_{HH} = 8.1 Hz, 1H, C_{py}-H_{para}). ¹³C{¹H} NMR (101 MHz, acetone-d₆) δ 29.27–30.42 (overlap acetone-d₆ and P-C(CH₃)₂C_{py}), 31.65 (Me of ^tBu), 38.00 (vt, *J*_{PC} = 7.0 Hz, C_{quat} of ^tBu), 54.41 (vt, *J*_{PC} = 3.9 Hz, P-C(CH₃)₂C_{py}), 118.38–118.53 (m, B-C_{Ar,para}), 119.90 (vt, *J*_{PC} = 4.2 Hz, C_{py,meta}), 125.36 (q, *J*_{CF} = 271.9 Hz, BC_{Ar,meta}-CF₃), 130.00 (qdd, *J*_{CF} = 31.6 Hz; *J*_{CB} = 5.3 Hz; *J*_{CF} = 2.6 Hz, B-C_{Ar,meta}-CF₃), 135.52 (B-C_{Ar,ortho}), 143.31 (C_{py,para}), 162.58 (dd, *J*_{BC} = 49.9 Hz, B-C_{Ar,ipso}), 172.68 (vt, *J*_{PC} = 7.0 Hz, C_{py,ortho}). ³¹P{¹H} NMR (162 MHz, acetone-d₆) δ 108.22. ¹⁹F NMR (376 MHz, acetone-d₆) δ -63.12. ATR-IR (cm⁻¹): 3003 (w), 2965 (w), 2906 (w), 1919 (w), 1606 (w), 1564 (w), 1467 (w), 1392 (w), 1353 (m), 1270 (m), 1170 (m), 1125 (s), 1019 (w), 926 (w), 888 (m), 835 (w), 809 (w), 711 (m), 674 (m). UV-vis (THF, [1·10⁻⁴ M]), λ_{max}, nm (ε, L mol⁻¹ cm⁻¹): 274 (14904), 356 (6089), 477 (278). ESI-HRMS (*m/z*) calculated for [C₂₇H₅₂NNiP₂]⁺ = 510.2923, and for [C₃₂H₁₂BF₂₄]⁻ = 863.0649. Found for [C₂₇H₅₂NNiP₂]⁺ = 510.2912, and for [C₃₂H₁₂BF₂₄]⁻ = 863.0632. Anal. Calcd. For C₅₉H₆₄NP₂NiBF₂₄: C, 51.55; H, 4.69; N, 1.02. Found: C, 51.30; H, 4.81; N, 1.15.

3.4.6 [(Me₄PNP^tBu)Ni^{II}H]BPh₄, **3.29**.

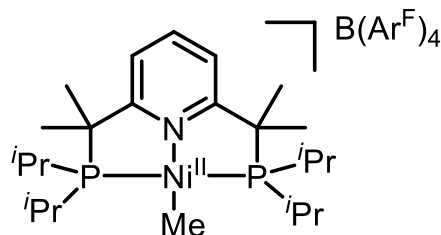


The same procedure to prepare **3.27** was used to prepare **3.29** using **2.34** (50.0 mg, 0.075 mmol), NaBPh₄ (26.8 mg, 0.078 mmol, 1.04 equiv), and NaBH₄ (28.2 mg, 0.75 mmol, 10 equiv) to afford a white solid (60 mg, 0.072 mmol, 97%).

Crystals suitable for X-ray diffraction were obtained by slow crystallization of a concentrated THF solution of **3.29** at -30 °C under N₂. ¹H NMR (400 MHz, CDCl₃) δ -18.13 (t, *J*_{HP} = 50.5

Hz, 1H, Ni-H), 1.36–1.40 (m, 36H, Me of ^tBu), 1.68–1.71 (m, 12H, C_{quat} of ^tBu), 6.79 (d, $J_{\text{HH}} = 8.0$ Hz, 2H, C_{py}-H_{meta}), 6.89 (t, $J_{\text{HH}} = 7.1$ Hz, 4H, BC_{Ar}-H_{para}), 7.03 (t, $J_{\text{HH}} = 7.3$ Hz, 8H, BC_{Ar}-H_{meta}), 7.39 (t, $J_{\text{HH}} = 8.1$ Hz, 1H (overlaps), C_{py}-H_{para}), 7.41–7.44 (m, 8H (overlaps), BC_{Ar}-H_{ortho}). ¹³C{¹H} NMR (101 MHz, CDCl₃) δ 29.98 (br, P-C(CH₃)₂C_{py}), 31.54 (Me of ^tBu), 37.48 (vt, $J_{\text{PC}} = 6.7$ Hz, C_{quat} of ^tBu), 53.48 (vt, $J_{\text{PC}} = 3.8$ Hz, P-C(CH₃)₂C_{py}), 118.69 (vt, $J_{\text{PC}} = 4.0$ Hz, C_{py,meta}), 121.78 (B-C_{Ar,para}), 125.61–125.69 (m, B-C_{Ar,meta}), 136.48 (B-C_{Ar,ortho}), 143.21 (C_{py,para}), 164.39 (dd, $J_{\text{BC}} = 49.4$ Hz, B-C_{Ar,ipso}), 171.08 (vt, $J_{\text{PC}} = 7.1$ Hz, C_{py,ortho}). ³¹P{¹H} NMR (162 MHz, CDCl₃) δ 107.78. ATR-IR (cm⁻¹): 3057 (w), 2995 (w), 2971 (w), 2901 (w), 1896 (w), 1579 (w), 1560 (w), 1478 (w), 1456 (W), 1427 (w), 1393 (w), 1366 (w), 1255 (w), 1176 (w), 1154 (w), 1128 (w), 1105 (w), 1069 (w), 1031 (w), 994 (w), 822 (w), 846 (w), 812 (w), 743 (s), 711 (s). UV-vis (THF, [1·10⁻⁴ M]), λ_{max}, nm (ε, L mol⁻¹ cm⁻¹): 260 (sh, 11568), 267 (sh, 9859), 275 (6506), 289 (4217), 341 (4154), 372 (sh, 2673). ESI-HRMS (m/z) calculated for [C₂₇H₅₂NNiP₂]⁺ = 510.2923, and for [C₂₄H₂₀B]⁻ = 319.1653. Found for [C₂₇H₅₂NNiP₂]⁺ = 510.2905, and for [C₂₄H₂₀B]⁻ = 319.1652. Despite multiple attempts, satisfactory elemental analysis could not be obtained. However, the sample was pure from other organometallic impurities according to ¹H, ¹³C and ³¹P NMR (See the linked Appendix of Chapter 3)

3.4.7 [(Me₄PNP^{*i*Pr})Ni^{II}Me]B(Ar^F)₄, 3.30.



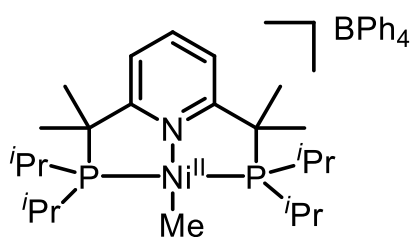
Method 1: Using MeLi. NaB(Ar^F)₄ (88.0 mg, 0.099 mmol) was added to a 20 mL vial containing a solution of **2.32** (60.0 mg, 0.099 mmol, 1.00 equiv) in THF (10 mL). After stirring for 5 minutes, MeLi (1.17 M in THF, 85 μL, 0.099 mmol, 1.00 equiv) was added to the solution, which was stirred at rt for 1 hour. The solution was then evaporated, washed with hexanes, filtered through a short celite pad and evaporated to afford a yellowish powder (106 mg, 0.079 mmol, 80%). Yellow crystals suitable for X-ray diffraction were obtained by slow crystallization in THF at -30°C.

Method 2: Using in situ prepared CuMe₂Li. NaB(Ar^F)₄ (66.0 mg, 0.075 mmol) was added to a 20 mL vial containing a solution of **2.32** (45.0 mg, 0.075 mmol, 1.00 equiv) in THF (10 mL) and stirred for 5 minutes. In another 5 mL vial a homogeneous solution of copper(I) iodide (14.1 mg, 0.075 mmol, 1.00 equiv) in diethyl ether (2 mL) was added to a cold solution of MeLi (1.17 M in THF, 127 uL, 0.15 mmol, 2.00 equiv). A yellow solid, lithium dimethylcuprate, precipitates instantly and the whole solution in the 5 mL vial was transferred quickly to the 20 mL vial, followed by a rapid color change to black. The solution was immediately filtered through a short celite pad, evaporated and washed with hexanes, filtered on celite and evaporated to afford a yellowish powder (92 mg, 0.069 mmol, 93%).

Method 3: Using ZnMe₂. NaB(Ar^F)₄ (72.1 mg, 0.0814 mmol) was added to a 20 mL vial containing a solution of **2.32** (50.0 mg, 0.0814 mmol, 1.00 equiv) in THF (10 mL). After stirring for 5 minutes, ZnMe₂ (1.0 M in hexanes, 163 uL, 0.163, mmol, 2.00 eq.) was added to the reaction, which was stirred at rt for 2 hours before gradually turning black. The solution filtered on through a short celite pad, evaporated, washed with diethyl ether, and dried under vacuum to afford a yellowish powder (85 mg, 0.064 mmol, 79%). ¹H NMR (400 MHz, acetone-d₆) δ -0.16 (t, *J*_{PH} = 8.5 Hz, 3 H, Ni-CH₃), 1.21–1.26 (m, 12H, PCH-CH₃), 1.43–1.49 (m, 12H, PCH-CH₃), 1.80–1.83 (m, 12H, P-C(CH₃)₂C_{py}), 2.59–2.68 (m, 4H, PCH-CH₃), 7.57 (d, *J*_{HH} = 7.3 Hz, 2H, C_{py}-H_{meta}), 7.66 (br s, 4H, BC_{Ar}-H_{para}), 7.77–7.79 (br m, 8H, BC_{Ar}-H_{ortho}), 8.18 (t, *J*_{HH} = 8.0 Hz, 1H, C_{py}-H_{para}). ¹³C{¹H} NMR (101 MHz, acetone-d₆) δ -16.33 (t, *J*_{PC} = 21.6 Hz, Ni-CH₃), 19.31 (PCH-CH₃), 19.91 (PCH-CH₃), 23.06 (vt, *J*_{PC} = 10.1 Hz, PCH-CH₃), 28.21 (P-C(CH₃)₂C_{py}), 50.55 (vt, *J*_{PC} = 8.1 Hz, P-C(CH₃)₂C_{py}), 118.37–118.53 (m, B-C_{Ar,para}), 120.39 (vt, *J*_{PC} = 4.2 Hz, C_{py,meta}), 125.36 (q, *J*_{CF} = 271.6 Hz, BC_{Ar,meta}-CF₃), 129.99 (qdd, *J*_{CF} = 31.7 Hz; *J*_{CB} = 5.0 Hz; *J*_{CF} = 2.4 Hz, B-C_{Ar,meta}-CF₃), 135.52 (B-C_{Ar,ortho}), 142.91 (C_{py,para}), 162.57 (dd, *J*_{BC} = 50.0 Hz, B-C_{Ar,ipso}), 171.95 (vt, *J*_{PC} = 6.9 Hz, C_{py,ortho}). ³¹P{¹H} NMR (162 MHz, acetone-d₆) δ 70.15.

^{19}F NMR (376 MHz, acetone- d_6) δ -63.14. ATR-IR (cm^{-1}): 2969 (w) 2879 (w), 1605 (w), 1567 (w), 1464 (w), 1391 (w), 1352 (m), 1271 (s), 1157 (m), 1118 (s), 1038 (w), 928 (w), 886 (m), 835 (w), 815 (w), 751 (m), 711 (m), 674 (m). UV-vis (THF, $[1 \cdot 10^{-4} \text{ M}]$), λ_{max} , nm (ϵ , $\text{L mol}^{-1} \text{ cm}^{-1}$): 274 (14904), 356 (6089). ESI-HRMS (m/z) calculated for $[\text{C}_{24}\text{H}_{46}\text{NNiP}_2]^+ = 468.2453$, and for $[\text{C}_{32}\text{H}_{12}\text{BF}_{24}]^- = 863.0643$. Found for $[\text{C}_{24}\text{H}_{46}\text{NNiP}_2]^+ = 468.2443$ and for $[\text{C}_{32}\text{H}_{12}\text{BF}_{24}]^- = 863.0661$. Despite multiple attempts, satisfactory elemental analysis could not be obtained due to traces of solvent. However, the sample was pure from organic/organometallic impurities according to ^1H , ^{13}C and ^{31}P NMR (See the linked Appendix of Chapter 3).

3.4.8 $[(\text{Me}_4\text{PNP}^{\text{iPr}})\text{Ni}^{\text{II}}\text{Me}]\text{BPh}_4$, **3.31**.

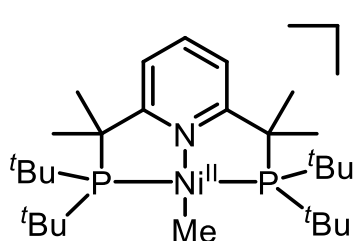


This complex was prepared following *Method 3* described for the preparation of **3.30** using **2.1** (50.0 mg, 0.0814 mmol), NaBPh_4 (27.8 mg, 0.0814 mmol, 1.00 equiv), and ZnMe_2 (1.0 M in hexanes, 163 μL , 0.163 mmol, 2.00 equiv). Washing was

done with hexanes then the solid was solubilized with a minimal amount of THF or acetonitrile and evaporated to afford an off-white powder (56 mg, 0.071 mmol, 87%). Pale yellow crystals suitable for X-ray diffraction were obtained by slow crystallization of a concentrated solution of **3.31** in THF at -30°C under a N_2 atmosphere. ^1H NMR (600 MHz, CD_3CN) δ -0.23 (t, $J_{\text{PH}} = 8.3$ Hz, 3H $\text{Ni}-\underline{\text{CH}_3}$), 1.13–1.16 (m, 12H, $\text{PCH}-\underline{\text{CH}_3}$), 1.38–1.41 (m, 12H, $\text{PCH}-\underline{\text{CH}_3}$), 1.68–1.70 (m, 12H, $\text{P}-\text{C}(\underline{\text{CH}_3})_2\text{C}_{\text{py}}$), 2.48–2.57 (m, 4H, $\text{PCH}-\underline{\text{CH}_3}$), 6.84 (t, $J_{\text{HH}} = 7.1$ Hz, 4H, $\text{BC}_{\text{Ar}}-\underline{\text{H}_{\text{para}}}$), 6.99 (t, $J_{\text{HH}} = 7.3$ Hz, 8H, $\text{BC}_{\text{Ar}}-\underline{\text{H}_{\text{meta}}}$), 7.27–7.28 (m, 8H, $\text{BC}_{\text{Ar}}-\underline{\text{H}_{\text{ortho}}}$), 7.33 (d, $J_{\text{HH}} = 8.1$ Hz, 8H, $\text{C}_{\text{py}}-\underline{\text{H}_{\text{meta}}}$), 7.98 (t, $J_{\text{HH}} = 8.0$ Hz, 1H, $\text{C}_{\text{py}}-\underline{\text{H}_{\text{para}}}$). $^{13}\text{C}\{^1\text{H}\}$ NMR (151 MHz, CD_3CN) δ -16.49 (t, $J_{\text{PC}} = 21.8$ Hz, $\text{Ni}-\underline{\text{CH}_3}$), 19.35 ($\text{PCH}-\underline{\text{CH}_3}$), 19.93 ($\text{PCH}-\underline{\text{CH}_3}$), 23.09 (vt, $J_{\text{PC}} = 10.1$ Hz, $\text{PCH}-\underline{\text{CH}_3}$), 28.27 (s, $\text{P}-\text{C}(\underline{\text{CH}_3})_2\text{C}_{\text{py}}$), 50.51 (vt, $J_{\text{PC}} = 8.0$ Hz, $\text{P}-\underline{\text{C}}(\text{CH}_3)_2\text{C}_{\text{py}}$), 120.27 (vt, $J_{\text{PC}} = 4.0$ Hz, $\underline{\text{C}_{\text{py,meta}}}$), 122.75 ($\text{B}-\underline{\text{C}_{\text{Ar,para}}}$), 126.5–126.6 (m, $\text{B}-\underline{\text{C}_{\text{Ar,meta}}}$), 136.73 ($\text{B}-\underline{\text{C}_{\text{Ar,ortho}}}$), 142.67 ($\underline{\text{C}_{\text{py,para}}}$), 164.79 (dd, $J_{\text{BC}} = 49.2$ Hz, $\text{B}-\underline{\text{C}_{\text{Ar,ipso}}}$), 171.88 (vt, $J_{\text{PC}} = 7.2$ Hz, $\underline{\text{C}_{\text{py,ortho}}}$).

$^{31}\text{P}\{^1\text{H}\}$ NMR (243 MHz, CD_3CN) δ 70.09. ATR-IR (cm^{-1}): 3042 (w), 2972 (w), 2878(w), 1709 (w), 1591 (w), 1570 (w), 1455 (w), 1389 (w), 1361 (w), 1266 (w), 1247 (w), 1153 (w), 1123(w), 1100 (w), 1072 (w), 1028 (w), 931 (w), 885 (w), 841 (w), 814 (w), 733 (m), 698 (s), 661 (m). UV-vis (THF, $[1 \cdot 10^{-4} \text{ M}]$), λ_{max} , nm (ϵ , $\text{L mol}^{-1} \text{ cm}^{-1}$): 267 (sh, 8014), 274 (sh, 5368), 291 (2999), 349 (3399), 383 (sh, 1861). ESI-HRMS (m/z) calculated for $[\text{C}_{24}\text{H}_{46}\text{NNiP}_2]^+ = 468.2453$, and for $[\text{C}_{24}\text{H}_{20}\text{B}]^- = 319.1653$. Found for $[\text{C}_{24}\text{H}_{46}\text{NNiP}_2]^+ = 468.2442$, and for $[\text{C}_{24}\text{H}_{20}\text{B}]^- = 319.1652$ Anal. Calcd. For $\text{C}_{48}\text{H}_{66}\text{NP}_2\text{NiB}$: C, 73.12; H, 8.44; N, 1.78. Found: C, 72.81; H, 8.12; N, 1.90.

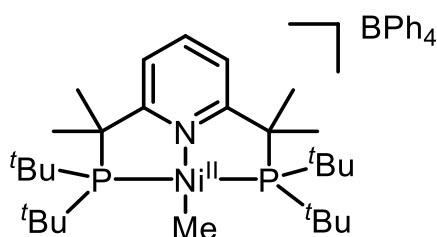
3.4.9 $[(\text{Me}_4\text{PNP}^t\text{Bu})\text{Ni}^{\text{II}}\text{Me}]\text{B}(\text{Ar}^{\text{F}})_4$, **3.32**.



This complex was prepared using the *Method 3* described for the preparation of **3.30** using **2.34** (50.0 mg, 0.0746 mmol), $\text{NaB}(\text{Ar}^{\text{F}})_4$ (66.1 mg, 0.0746 mmol, 1.00 equiv), and ZnMe_2 (1.0 M in hexanes, 149 μL , 0.149 mmol, 2.00 equiv), giving a yellowish powder (100 mg, 0.072 mmol, 97%). Orange crystals suitable for X-ray diffraction studies were obtained by vapor diffusion of diethyl ether into a concentrated benzene solution of **3.32** at rt. ^1H NMR (400 MHz, CD_3CN) δ 0.06 (t, $J_{\text{HP}} = 8.2$ Hz, 3H, Ni-CH₃), 1.24–1.35 (m, 18H, Me of ^tBu), 1.62–1.75 (m, 18H, Me of ^tBu), 1.81–1.88 (m, 6H, P-C(CH₃)₂C_{py}), 1.96–2.01 (m, 6H, P-C(CH₃)₂C_{py}), 7.34 (d, $J_{\text{HH}} = 8.1$ Hz, 2H, C_{py}-H_{meta}), 7.65–7.68 (m, 4H, BAr-H_{para}), 7.68–7.72 (m, 8H, BAr-H_{ortho}), 7.99 (t, $J_{\text{HH}} = 8.2$ Hz, 1H, C_{py}-H_{para}). $^{13}\text{C}\{^1\text{H}\}$ NMR (101 MHz, CD_3CN) δ -20.04 (weak signal, Ni-CH₃), 24.54 (P-C(CH₃)₂C_{py}), 31.97 (Me of ^tBu), 32.56 (br, Me of ^tBu), 36.07 (P-C(CH₃)₂C_{py}), 38.53 (C_{quat} of ^tBu), 39.26 (C_{quat} of ^tBu), 52.56 (vt, $J_{\text{PC}} = 4.7$ Hz, P-C(CH₃)₂C_{py}), 120.00 (C_{py,meta}), 125.42 (q, $J_{\text{CF}} = 272.5$ Hz, BAr_{meta}-CF₃), 129.90 (qdd, $J_{\text{CF}} = 31.6$ Hz; $J_{\text{CB}} = 5.9$ Hz; $J_{\text{CF}} = 2.9$ Hz, B-C_{Ar,meta}CF₃), 135.64 (B-C_{Ar,ortho}), 142.78 (C_{py,para}), 161.86–163.34 (m, B-C_{Ar,ipso}), 172.04 (C_{py,ortho}). $^{31}\text{P}\{^1\text{H}\}$ NMR

(162 MHz, CD₃CN) δ 86.05. ¹⁹F NMR (471 MHz, CDCl₃) δ -63.14. ATR-IR (cm⁻¹): 2972 (w), 2874 (w), 1605 (w), 1460 (w), 1392 (w), 1352 (m), 1271 (s), 1165 (m), 1124 (s), 1026 (m), 1014 (m), 927 (w), 887 (m), 834 (w), 807 (w), 40 (w), 709 (m), 674 (m). UV-vis (THF, [1·10⁻⁴ M]), λ_{max} , nm (ϵ , L mol⁻¹ cm⁻¹): 269 (sh, 13790), 279 (sh, 9966), 358 (3957), 455 (544). ESI-HRMS (m/z) calculated for [C₂₈H₅₄NNiP₂]⁺ = 524.3079, and for [C₃₂H₁₂BF₂₄]⁻ = 863.0643. Found for [C₂₈H₅₄NNiP₂]⁺ = 524.3072 and for [C₃₂H₁₂BF₂₄]⁻ = 863.0654. Despite multiple attempts, satisfactory elemental analysis could not be obtained due to traces of solvent. However, the sample was pure from organometallic impurities according to ¹H, ¹³C and ³¹P NMR (See the linked Appendix of Chapter 3).

3.4.10 [(Me₄PNP^tBu)Ni^{II}Me]BPh₄, **3.33**.

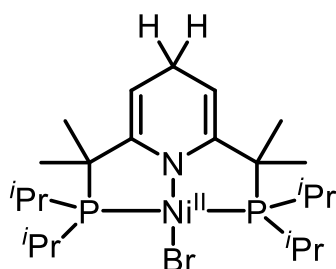


This complex was prepared following *method 3* described for the preparation of **3.30** using **2.34** (50.0 mg, 0.0746 mmol), NaBPh₄ (25.5 mg, 0.0746 mmol, 1.00 equiv), and ZnMe₂ (1.0 M in hexanes, 149 μ L, 0.149 mmol, 2.00 equiv).

Washing was done with hexanes, then the solid was solubilized with a minimal amount of THF or acetonitrile and evaporated to afford a light-yellow powder (51 mg, 0.062 mmol, 81%). Yellow crystals suitable for X-ray diffraction were obtained by slow crystallization of a concentrated solution of **3.33** in THF at -30 °C under a N₂ atmosphere. ¹H NMR (600 MHz, CD₃CN) δ 0.06 (t, J_{PH} = 8.3 Hz, 3H, Ni-CH₃), 1.23–1.38 (br s, 18H, Me of ^tBu), 1.62–1.74 (br s, 18H, Me of ^tBu), 1.79–1.88 (br s, 6H, P-C(CH₃)₂C_{py}), 1.95–2.00 (br s, 6H), 6.84 (t, J_{HH} = 7.6 Hz, 4H, BC_{Ar}-H_{para}), 6.99 (t, J_{HH} = 7.7 Hz, 8H, BC_{Ar}-H_{meta}), 7.23–7.31 (br m, 8H, BC_{Ar}-H_{ortho}), 7.34 (d, J_{HH} = 8.9 Hz, 2H, C_{py}-H_{meta}), 7.98 (t, J_{HH} = 8.1 Hz, 1H, C_{py}-H_{para}). ¹³C{¹H} NMR (151 MHz, CD₃CN) δ -20.06 (weak signal, Ni-CH₃), 24.58 (P-C(CH₃)C_{py}), 32.02 (Me of ^tBu), 32.57 (br, Me of ^tBu), 36.09 (P-C(CH₃)₂C_{py}), 38.54 (C_{quat} of ^tBu), 39.29 (C_{quat} of ^tBu), 52.59 (P-C(CH₃)₂C_{py}), 120.03 (C_{py,meta}), 122.76 (B-C_{Ar,para}), 126.57 (B-C_{Ar,meta}), 136.73 (B-C_{Ar,ortho}),

142.85 ($C_{py,para}$), 164.79 (q, $J_{BC} = 49.5$ Hz, B- $C_{Ar,ipso}$), 172.03 ($C_{py,ortho}$). $^{31}\text{P}\{^1\text{H}\}$ NMR (243 MHz, CD_3CN) δ 86.10. ATR-IR (cm^{-1}): 3032 (w), 2976 (w), 2897 (w), 2318 (w), 2288 (w), 1706 (w), 1573 (w), 1453 (w), 1361 (w), 1256 (w), 1167 (w), 1065 (w), 1026 (w), 925 (w), 841 (w), 809 (w), 734 (m), 701 (s). UV-vis (THF, $[1 \cdot 10^{-4}$ M]), λ_{max} , nm (ϵ , $\text{L mol}^{-1} \text{cm}^{-1}$): 274 (14904), 356 (6089). ESI-HRMS (m/z) calculated for $[\text{C}_{28}\text{H}_{54}\text{NNiP}_2]^+ = 524.3079$, and for $[\text{C}_{24}\text{H}_{20}\text{B}]^- = 319.1653$. Found for $[\text{C}_{28}\text{H}_{54}\text{NNiP}_2]^+ = 524.3043$ and for $[\text{C}_{24}\text{H}_{20}\text{B}]^- = 319.1323$. Despite multiple attempts, satisfactory elemental analysis could not be obtained due to traces of solvent that could not be fully removed under vacuum.

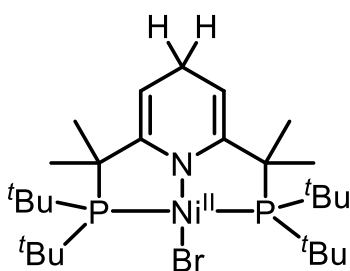
3.4.11 ($\text{Me}_4\text{PNP}^{i\text{Pr}}\cdot\text{H}$) $\text{Ni}^{\text{II}}\text{Br}$, **3.34**.



To a solution of **3.24** (50 mg, 0.058 mmol) in THF, LiBEt_3H (1.0 M in THF, 58 μL , 0.058 mmol, 1.00 equiv) was added and the solution instantly changed color to green. The solution was concentrated to 1 mL under reduced pressure, then diethyl ether was added and the solid was removed by filtration on a short celite plug. The diethyl ether solution was then evaporated under reduced pressure to obtain a green powder (27 mg, 0.050 mmol, 87%). Green crystals suitable for X-ray diffraction were grown from layering of diethyl ether on a concentrated benzene solution of **3.34** at rt under N_2 . ^1H NMR (400 MHz, C_6D_6) δ 1.28–1.31 (m, 12H, $\text{P}-\text{C}(\underline{\text{H}}_3)_2\text{C}_{py}$), 1.34–1.39 (m, 12H, $\text{PCH}-\underline{\text{H}}_3$), 1.55–1.60 (m, 12H, $\text{PCH}-\underline{\text{H}}_3$), 2.23–2.32 (m, 4H, $\text{PCH}-\underline{\text{H}}-\text{CH}_3$), 2.95 (m, 2H, $\text{C}_{hydroxy}-\underline{\text{H}}_{para}$), 4.23 (m, 2H, $\text{C}_{hydroxy}-\underline{\text{H}}_{meta}$). $^{13}\text{C}\{^1\text{H}\}$ NMR (101 MHz, C_6D_6) δ 18.45 ($\text{PCH}-\underline{\text{C}}\text{H}_3$), 20.25 ($\text{PCH}-\underline{\text{C}}\text{H}_3$), 23.68 (vt, $J_{PC} = 9.1$ Hz, $\text{P}\underline{\text{C}}\text{H}-\text{CH}_3$), 24.94 ($\underline{\text{C}}_{hydroxy,para}$), 26.11 ($\text{P}-\text{C}(\underline{\text{C}}\text{H}_3)_2\text{C}_{hydroxy,ortho}$), 43.78 (vt, $J_{PC} = 8.8$ Hz, $\text{P}-\underline{\text{C}}(\text{CH}_3)_2\text{C}_{hydroxy,ortho}$), 91.35 (vt, $J_{PC} = 6.6$ Hz, $\underline{\text{C}}_{hydroxy,meta}$), 160.99 (vt, $J_{PC} = 6.9$ Hz, $\underline{\text{C}}_{hydroxy,ortho}$). $^{31}\text{P}\{^1\text{H}\}$ NMR (162 MHz, C_6D_6) δ 62.48. ATR-IR (cm^{-1}): 2958 (w), 2919 (w), 2867 (w), 2838 (w), 2746 (w), 2163 (w), 1962 (w), 1646 (w), 1600 (w), 1459 (w), 1380 (w), 1333 (w), 1298 (w), 1240 (w), 1205 (w),

1160 (w), 1125 (w), 1095 (w), 1027 (m), 989 (w), 932 (w), 885 (w), 804 (w), 804 (w), 752 (w), 720 (w), 695 (m), 657 (s). UV-vis (CH_2Cl_2 , $[0.5 \cdot 10^{-4} \text{ M}]$), λ_{max} , nm (ϵ , $\text{L mol}^{-1} \text{ cm}^{-1}$): 233 (32419), 259 (sh, 16945), 286 (8256), 322 (13815), 352 (sh, 7213), 433 (2105), 656 (1001). ESI-HRMS (m/z) calculated for $[\text{C}_{23}\text{H}_{44}\text{NBrNiP}_2]^+ = 532.1402$. Found for $[\text{C}_{23}\text{H}_{44}\text{NBrNiP}_2]^+ = 532.1390$. Despite multiple attempts, satisfactory elemental analysis could not be obtained.

3.4.12 ($\text{Me}_4\text{PNP}^{\text{tBu}}\text{-H}$) $\text{Ni}^{\text{II}}\text{Br}$, **3.35**.

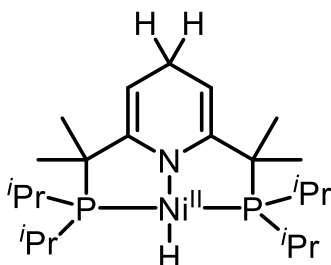


To a solution of **3.25** (16.0 mg, 0.0176 mmol) in THF, LiBEt_3H (1.0 M in THF, 14 μL , 0.014 mmol, 0.8 equiv) was added and the solution instantly changed color to green. The solution was concentrated to a volume of less than 1 mL, and 5 mL of diethyl ether was

added. The precipitate was filtered on a short celite pad, and the remaining diethyl ether solution was then evaporated under reduced pressure to afford a green powder (8 mg, 0.014 mmol, 77%). Green crystals suitable for X-ray diffraction were grown from the reaction of 1 equivalent of LiBEt_3H via layering of diethyl ether into a concentrated benzene solution of **3.35** at rt under N_2 . Crystals of **3.35** are disordered with a hydride species, which is not observed in **3.34**. ^1H NMR (400 MHz, C_6D_6) δ 1.32–1.37 (m, 6H, $\text{P-C}(\underline{\text{CH}_3})_2\text{C}_{\text{hydrophy}}$), 1.50–1.92 (m (overlap), 6H + 36H, $\text{P-C}(\underline{\text{CH}_3})_2\text{C}_{\text{py}} + \text{Me of } ^t\text{Bu}$), 2.73–2.88 (m, 2H, $\text{C}_{\text{hydrophy}}\text{-}\underline{\text{H}}_{\text{para}}$), 4.20–4.25 (m, 2H, $\text{C}_{\text{hydrophy}}\text{-}\underline{\text{H}}_{\text{meta}}$). $^{13}\text{C}\{^1\text{H}\}$ NMR (101 MHz, C_6D_6) δ 23.26 ($\text{P-C}(\underline{\text{CH}_3})_2\text{C}_{\text{hydrophy}}$), 24.53 ($\underline{\text{C}}_{\text{hydrophy,para}}$), 31.98 (br, Me of ^tBu), 33.88 ($\text{P-C}(\underline{\text{CH}_3})_2\text{C}_{\text{dehydrophy}}$), 39.14 ($\text{C}_{\text{quat of } ^t\text{Bu}}$), 39.72 ($\text{C}_{\text{quat of } ^t\text{Bu}}$), 47.77 ($\text{P-C}(\underline{\text{CH}_3})_2\text{C}_{\text{hydrophy}}$), 91.35 (vt, $J_{\text{PC}} = 6.3 \text{ Hz}$, $\underline{\text{C}}_{\text{hydrophy,meta}}$), 161.41 (vt, $J_{\text{PC}} = 6.4 \text{ Hz}$, $\underline{\text{C}}_{\text{hydrophy,ortho}}$). $^{31}\text{P}\{^1\text{H}\}$ NMR (162 MHz, C_6D_6) δ 71.18. ATR-IR (cm^{-1}): 2964 (m), 2893 (m), 2867 (s), 2732 (s), 2658 (m), 2511 (w), 2467 (w), 2318 (w), 2290 (w), 1191 (w), 1846 (w), 1642 (m), 1595 (w), 1457 (s), 1387 (m), 1365 (m), 1332 (m), 1298 (m), 1245 (w), 1169 (s), 1123 (m), 1024 (m), 933 (m), 895 (m), 809 (m), 718 (m), 687 (m). UV-vis (CH_2Cl_2 , $[1 \cdot 10^{-4} \text{ M}]$), λ_{max} , nm (ϵ , $\text{L mol}^{-1} \text{ cm}^{-1}$): 242 (28803), 282 (7740), 341 (14606), 466 (1125), 718 (254). ESI-HRMS (m/z) calculated

for $[\text{C}_{27}\text{H}_{53}\text{NBrNiP}_2]^+ = 590.2185$. Found for $[\text{C}_{23}\text{H}_{44}\text{NBrNiP}_2]^+ = 590.2172$. Despite multiple attempts, satisfactory elemental analysis could not be obtained.

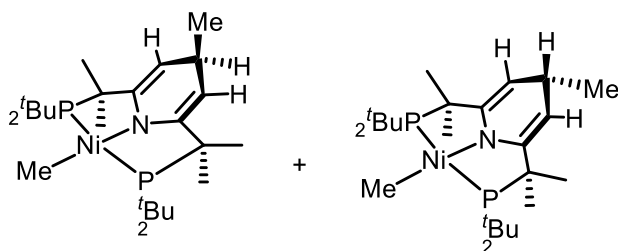
3.4.13 $(\text{Me}_4\text{PNP}^{i\text{Pr}}\cdot\text{H})\text{Ni}^{\text{II}}\text{H}$, **3.36**.



To a solution of **3.24** (30 mg, 0.049 mmol) in THF (10 mL) was added a 1M solution of LiEt_3H in THF (98 μL , 0.098 mmol, 2.00 equiv). The solution quickly turns green then dark brown upon addition. The solvent is evaporated, and the solid washed with diethyl

ether, the insoluble precipitate is filtered on a short celite pad, and the solvent evaporated to afford a brown solid. We did not report the yield because we could not isolate this complex cleanly, and some side products are still present. ^1H NMR (600 MHz, C_6D_6) δ -18.14 (t, $J_{\text{PH}} = 56.2$ Hz, 1H, Ni-H), 1.18–1.23 (m, 12H, PCH-CH₃), 1.30–1.33 (m 12H, PCH-CH₃), 1.41–1.43 (m, 12H, P-C(CH₃)₂ $\text{C}_{\text{hydropy}}$) 1.93–2.00 (m, 4H, PCH- CH_3), 3.48–3.50 (td, $J_{\text{HH}} = 3.4, 1.7$ Hz, 2H, $\text{C}_{\text{hydropy}}$ -H_{para}), 4.18–4.20 (m, 2H, $\text{C}_{\text{hydropy}}$ -H_{meta}). $^{13}\text{C}\{^1\text{H}\}$ NMR (151 MHz, C_6D_6) δ 20.28 (PCH-CH₃), 20.64 (PCH-CH₃), 24.05 (vt, $J_{\text{PC}} = 9.8$ Hz, PCH- CH_3), 26.28 (C_{hydropy,para}), 26.60 (P-C(CH₃)₂ $\text{C}_{\text{hydropy}}$), P-C(CH_3)₂ $\text{C}_{\text{hydropy}}$), 86.02 (vt, $J_{\text{PC}} = 5.6$ Hz, C_{hydropy,meta}), 161.14 (vt, $J_{\text{PC}} = 7.7$ Hz, C_{hydropy,ortho}). $^{31}\text{P}\{^1\text{H}\}$ NMR (162 MHz, C_6D_6) δ 81.10.

3.4.14 $[\text{Me}_4\text{PNP}^{t\text{Bu}}\cdot\text{Me}]\text{Ni}^{\text{II}}\text{Me}$, **3.37**.



Major isomer

3.37a

minor isomer

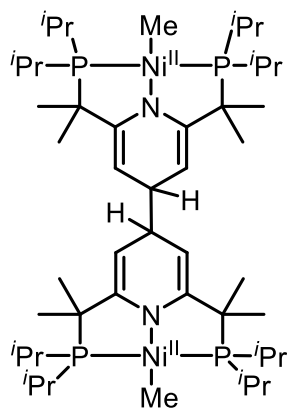
3.37b

2:1 in crystal
3:1 in NMR

To a solution of **3.25** (50 mg, 0.055 mmol) in THF (10 mL) at rt was added MeLi (3M solution in THF, 110 μL , 3 equiv). The solution was stirred for 15 minutes before the solution was concentrated to 1 mL under reduced pressure. To the solution was added 5 mL of pen-

tane, and the solid was removed by filtration on a short celite plug, then the solution was evaporated, giving a pink colored solid (35 mg, 74%, 0.041 mmol). Pink crystals suitable for X-ray crystallography studies were obtained by crystallization of a pentane solution of **3.37** at -30°C under a N₂ atmosphere. X-ray diffraction studies and NMR studies show that the product is a mixture of 2 isomers. With the methyl groups in the “up-up” fashion, the first isomer (major) has the methyl group on the dearomatized pyridine ring pointing away from the methyl groups, and the second (minor) is pointing in the same direction as the methyl on the arms. The ratio is about 3:1 by integration and about 2:1 in the solid state. Moreover, adding 5 equivalents of MeLi also gave the same conformers in a similar ratio. ¹H NMR (400 MHz, C₆D₆): δ -0.34 (t, *J*_{HP} = 7.9 Hz, overlap isomers 3H (major) + 1H (minor), Ni-CH₃), 1.14 (overlap isomers d, *J*_{HH} = 6.5 Hz, 3H (major) + 1H (minor), C_{dihydroxy}-CH₃), 1.40-1.49 (br m, overlap isomers 18H (major) + 6 H (minor) + THF, Me of *t*Bu), 1.50-1.55 (br m, overlap isomers 18H (major)¹ + 6H (minor)¹ + 2H (minor)², 1: Me of *t*Bu, 2: P-C(CH₃)₂C_{dihydroxy}), 1.55-1.60 (br m, 6H (major), P-C(CH₃)₂C_{dehydroxy}), 1.67-1.71 (br m, 2H (minor), P-C(CH₃)₂C_{dihydroxy}), 1.71-1.74 (br m, 6H (major), P-C(CH₃)₂C_{dihydroxy}), 3.22-3.28 (m, 1H (major), C_{dihydroxy}-H_{para}), 3.47-3.52 (br m, 0.3H (minor), C_{dihydroxy}-H_{para}), 4.01 (s, 0.6 H (minor), 4.29 (d, *J*_{HH} = 6.0 Hz, 2H (major), C_{dihydroxy}-H_{meta}). ¹³C{¹H} NMR (101 MHz, C₆D₆): δ -25.29 (overlap vt, *J*_{PC} = 25 Hz (major + minor), Ni-CH₃), 23.54 (br, P-C(CH₃)₂C_{dihydroxy}, minor), 23.65 (br, P-C(CH₃)₂C_{dihydroxy}, major), 25.24 (C_{dihydroxy}-CH₃, major), 25.64 (C_{dihydroxy}-CH₃, minor), 29.77 (C_{dihydroxy,para}, major), 29.92 (C_{dihydroxy,para}, minor), 31.66 (br, Me of *t*Bu, major), 31.96 (Me of *t*Bu, minor), 32.33 (br, Me of *t*Bu, major), 34.57 (Me of *t*Bu, minor), 34.91 (P-C(CH₃)₂C_{dihydroxy}, major), 37.18 (C_{quat} of *t*Bu, major), 39.15 (C_{quat} of *t*Bu, minor), 39.74 (C_{quat} of *t*Bu, major), 49.04 (P-C(CH₃)₂C_{py}, minor), 49.24 (P-C(CH₃)₂C_{py}, major), 91.86 (C_{dihydroxy,meta}, major), 92.73 (C_{dihydroxy,meta}, minor), 160.51 (C_{dihydroxy,ortho}, major). ³¹P{¹H} NMR (162 MHz, C₆D₆): δ 75.91 (major), 76.28 (minor).

3.4.15 [(Me₄PNP^{*i*Pr}_{dearom})Ni^{II}Me]₂, **3.38**.



To a solution of **3.30** (10.4 mg, 0.0078 mmol) in THF at rt, KC₈ (2.3 mg, 0.017 mmol, 2.2 equiv) was added and it was stirred for 1h. The solution was then filtered through a short celite plug and then evaporated to 1 mL and left to crystallize at -30 °C to obtain orange crystals (2.4 mg, 0.0026 mmol, 33%) that were suitable for X-ray diffraction. ¹H NMR (400 MHz, C₆D₆) δ -0.56 (t, *J*_{PH} = 8.2 Hz, 6H, Ni-CH₃), 1.11-1.17 (m, 24H, P-C(CH₃)₂C_{py}), 1.44-1.50 (m, 12H, PCH-CH₃), 1.50-1.53 (m, 12H, PCH-CH₃), 1.51-1.58 (m, 12H, PCH-CH₃), 1.56-1.59 (m, 12H, PCH-CH₃), 2.03-2.12 (m, 4H, PCH-CH₃), 2.16-2.25 (m, 4H, PCH-CH₃), 3.26-3.31 (m, 2H, C_{py}-H_{para}), 4.49-4.54 (m, 4H, C_{py}-H_{meta}). ¹³C{¹H} NMR (101 MHz, C₆D₆) δ -22.60 (vt, *J*_{PC} = 24.0 Hz, Ni-CH₃), 17.40 (P-C(CH₃)₂C_{py}), 19.42 (P-C(CH₃)₂C_{py}), 19.75 (PCH-CH₃), 20.90 (PCH-CH₃), 22.25 (vt, *J*_{PC} = 7.5 Hz, PCH-CH₃), 24.02 (vt, *J*_{PC} = 8.5 Hz, PCH-CH₃), 24.29 (PCH-CH₃), 29.88 (PCH-CH₃), 43.20 (C_{py,para}), 45.71 (vt, *J*_{PC} = 8.5 Hz, P-CH(CH₃)₂C_{py}), 90.12 (vt, *J*_{PC} = 5.8 Hz, C_{py,meta}), 159.27 (vt, *J*_{PC} = 7.6 Hz, C_{py,ortho}). ³¹P{¹H} NMR (162 MHz, C₆D₆) δ 64.43. Despite multiple attempts, satisfactory elemental analysis could not be obtained due to a starting material impurity that could not be completely removed after multiple recrystallizations.

Conclusions and Future Outlooks

This thesis provided a comprehensive study of the synthesis and reactivities of nickel complexes derived from a new class of tetramethyl-substituted Me₄PNP ligands. This new family of bulky, electron-rich tetramethylated PNP ligands allowed us to observe new types of metal- and ligand-based reactivity depending on the reaction conditions and on the nature of the ligand on the metal center.

In the case of simple halide complexes of Ni, the presence of the Me₄PNP ligand framework leads to predominantly metal-based reactivity in chemical and electrochemical reduction, which results in the formation of unusually stable Ni^I complexes. Interestingly, the steric hindrance of the ligand plays a crucial role in determining the geometry of these Ni^I complexes: while less hindered bis(isopropylphosphine)-substituted complexes adopted preferred seesaw geometry, more hindered bis(tert-butyl)phosphine-substituted analogues adopted square planar geometry due to steric clash between Me groups at the arms and bulky ^tBu groups. Overall, Me₄PNP family of ligand present new possibilities for stabilization of unusual oxidation states or geometries at the metal center and potentially allow for stabilization of usually reactive metalloradical species via steric protection.

However, the new bulky Me₄PNP ligands do not always play a role of the “truly innocent” spectator ligands. Depending on the electronic properties of the metal center, these ligands also lead to two unusual modes of pincer ligand dearomatization via reactivity in the *para* position. In the case of the reduction of Ni bromide complexes with a strong hydride source, hydride attack in the *para* position was observed leading to reduction of the pyridine ring. In another case, reduction of a nickel methyl complex in the presence of a strong one-electron reductant led to dimerization in the *para* position of the pyridine ring with the formation of a new carbon-carbon bond. Interestingly, both rare types of pincer ligand dearomatization in the *para* position eventually led

to the formation of new types of anionic mono- or binucleating pincer ligand with a central amide donor, which are also potentially interesting, highly electron-rich and bulky ligands.

The computational studies eventually revealed that the difference between metal- or ligand-based reactivities is controlled by the electronics at the metal center: less electron-rich nickel methyl and hydride complexes preferably reacted via reduction at the metal, while more-electron-rich complexes were reduced at the ligand. From the point of view of frontier orbital analysis, this was reflected in predominantly metal-localized and ligand-localized lowest occupied molecular orbitals, respectively.

The possibility of ligand-based reduction also points out that in order to create “truly-innocent” Me₄PNP ligand framework, protection of the *para* position of the pyridine ring is also required. Further studies of such complexes may lead to discovery of new types of stoichiometric or potentially catalytic reactivity in such highly reduced, sterically protected metal complexes.

4 Appendix of Chapter 2

The Appendix of Chapter 2 has been deposited online and can be found by accessing this permanent link here [Appendix of Chapter 2](#) or by following this address: <https://groups.oist.jp/sites/default/files/imce/u1542/Appendix%20of%20Chapter%202%202020-04-16%20Final.pdf>

5 Appendix of Chapter 3

The Appendix of Chapter 3 has been deposited online and can be found by accessing this permanent link here [Appendix of Chapter 3](#) or by following this address: <https://groups.oist.jp/sites/default/files/imce/u1542/Appendix%20of%20Chapter%203%202020-04-15%20Final.pdf>

Complete Reference List

- (1) Klosin, J.; Fontaine, P. P.; Figueroa, R., Development of Group IV Molecular Catalysts for High Temperature Ethylene- α -Olefin Copolymerization Reactions. *Acc. Chem. Res.* **2015**, 48, 2004-2016.
- (2) Nowlin, T. E.; Mink, R. I.; Kissin, Y. V., Supported Magnesium/Titanium-Based Ziegler Catalysts for Production of Polyethylene. In *Handbook of Transition Metal Polymerization Catalysts*, 2010; pp 131-155, ISBN: 9780470504437-9780470137987.
- (3) Roy, D.; Uozumi, Y., Recent Advances in Palladium-Catalyzed Cross-Coupling Reactions at ppm to ppb Molar Catalyst Loadings. *Advanced Synthesis & Catalysis* **2018**, 360, 602-625.
- (4) Moulton, C. J.; Shaw, B. L., Transition metal-carbon bonds. Part XLII. Complexes of nickel, palladium, platinum, rhodium and iridium with the tridentate ligand 2,6-bis[(di-*t*-butylphosphino)methyl]phenyl. *J. Chem. Soc., Dalton Trans.* **1976**, 1020-1024.
- (5) van Koten, G.; Timmer, K.; Noltes, J. G.; Spek, A. L., A novel type of Pt-C interaction and a model for the final stage in reductive elimination processes involving C-C coupling at Pt; synthesis and molecular geometry of [1,N,N'- ϵ -2,6-bis{(dimethylamino)methyl}-toluene]iodoplatinum(II) tetrafluoroborate. *J. Chem. Soc., Chem. Commun.* **1978**, 250-252.
- (6) van Koten, G.; Jastrzebski, J. T. B. H.; Noltes, J. G.; Spek, A. L.; Schoone, J. C., Triorganotin cations stabilized by intramolecular Sn-N coordination; synthesis and characterization of {C,N,N' -2,6-bis[(dimethylamino)methyl]phenyl}diorganotin bromides. *J. Organomet. Chem.* **1978**, 148, 233-245.
- (7) Castonguay, A.; Sui-Seng, C.; Zargarian, D.; Beauchamp, A. L., Syntheses and Reactivities of New PCsp₃P Pincer Complexes of Nickel. *Organometallics* **2006**, 25, 602-608.
- (8) Kennedy, A. R.; Cross, R. J.; Muir, K. W., Preparation and crystal structure of *trans*-[NiBr{C₆H₃-2,6-(CH₂PCy₂)₂}]. *Inorg. Chim. Acta* **1995**, 231, 195-200.
- (9) Huck, W. T. S.; Snellink-Rueel, B.; van Veggel, F. C. J. M.; Reinhoudt, D. N., New Building Blocks for the Noncovalent Assembly of *homo*- and *hetero*-Multinuclear Metallo dendrimers. *Organometallics* **1997**, 16, 4287-4291.
- (10) Kozhanov, K. A.; Bubnov, M. P.; Cherkasov, V. K.; Vavilina, N. N.; Efremova, L. Y.; Artyushin, O. I.; Odinets, I. L.; Abakumov, G. A., *o*-Semiquinonic PCP-pincer nickel complexes with alkyl substituents: versatile coordination sphere dynamics. *Dalton Trans.* **2008**, 2849-2853.
- (11) Kozhanov, K. A.; Bubnov, M. P.; Cherkasov, V. K.; Fukin, G. K.; Abakumov, G. A., An EPR study of the intramolecular dynamics in *o*-semiquinonic nickel complexes with a diphosphorous pincer ligand. *Chem. Commun.* **2003**, 2610-2611.
- (12) Cámpora, J.; Palma, P.; Del Río, D.; Alvarez, E., CO Insertion Reactions into the M-OH Bonds of Monomeric Nickel and Palladium Hydroxides. Reversible Decarbonylation of a Hydroxycarbonyl Palladium Complex. *Organometallics* **2004**, 23, 1652-1655.
- (13) Cámpora, J.; Palma, P.; del Río, D.; Mar Conejo, M.; Alvarez, E., Synthesis and Reactivity of a Mononuclear Parent Amido Nickel Complex. Structures of Ni[C₆H₃-2,6-(CH₂PiPr₂)₂](NH₂) and Ni[C₆H₃-2,6-(CH₂PiPr₂)₂](OMe). *Organometallics* **2004**, 23, 5653-5655.

- (14) Castonguay, A.; Beauchamp, A. L.; Zargarian, D., Preparation and Reactivities of PCP-Type Pincer Complexes of Nickel. Impact of Different Ligand Skeletons and Phosphine Substituents. *Organometallics* **2008**, *27*, 5723-5732.
- (15) Boro, B. J.; Duesler, E. N.; Goldberg, K. I.; Kemp, R. A., Synthesis, Characterization, and Reactivity of Nickel Hydride Complexes Containing 2,6-C₆H₃(CH₂PR₂)₂ (R = tBu, cHex, and iPr) Pincer Ligands. *Inorg. Chem.* **2009**, *48*, 5081-5087.
- (16) Groux, L. F.; Belanger-Gariepy, F.; Zargarian, D., Phosphino-indenyl complexes of nickel(II). *Can. J. Chem.* **2005**, *83*, 634-639.
- (17) Schmeier, T. J.; Hazari, N.; Incarvito, C. D.; Raskatov, J. A., Exploring the reactions of CO₂ with PCP supported nickel complexes. *Chem. Commun.* **2011**, *47*, 1824-1826.
- (18) Levina, V. A.; Rossin, A.; Belkova, N. V.; Chierotti, M. R.; Epstein, L. M.; Filippov, O. A.; Gobetto, R.; Gonsalvi, L.; Lledos, A.; Shubina, E. S.; Zanolini, F.; Peruzzini, M., Acid-Base Interaction between Transition-Metal Hydrides: Dihydrogen Bonding and Dihydrogen Evolution. *Angew. Chem., Int. Ed.* **2011**, *50*, 1367-1370.
- (19) van der Boom, M. E.; Liou, S.-Y.; Shimon, L. J. W.; Ben-David, Y.; Milstein, D., Nickel promoted C-H, C-C and C-O bond activation in solution. *Inorg. Chim. Acta* **2004**, *357*, 4015-4023.
- (20) Castonguay, A.; Beauchamp, A. L.; Zargarian, D., New Derivatives of PCP-Type Pincer Complexes of Nickel. *Inorg. Chem.* **2009**, *48*, 3177-3184.
- (21) Gomez-Benitez, V.; Baldovino-Pantaleon, O.; Herrera-Alvarez, C.; Toscano, R. A.; Morales-Morales, D., High yield thiolation of iodobenzene catalyzed by the phosphinite nickel PCP pincer complex: [NiCl{C₆H₃-2,6-(OPPh₂)₂}]. *Tetrahedron Lett.* **2006**, *47*, 5059-5062.
- (22) Vabre, B.; Lindeperg, F.; Zargarian, D., Direct, one-pot synthesis of POCOP-type pincer complexes from metallic nickel. *Green Chem.* **2013**, *15*, 3188-3194.
- (23) Vabre, B.; Petiot, P.; Declercq, R.; Zargarian, D., Fluoro and Trifluoromethyl Derivatives of POCOP-Type Pincer Complexes of Nickel: Preparation and Reactivities in SN₂ Fluorination and Direct Benzylation of Unactivated Arenes. *Organometallics* **2014**, *33*, 5173-5184.
- (24) Lapointe, S.; Vabre, B.; Zargarian, D., POCOP-Type Pincer Complexes of Nickel: Synthesis, Characterization, and Ligand Exchange Reactivities of New Cationic Acetonitrile Adducts. *Organometallics* **2015**, *34*, 3520-3531.
- (25) Lapointe, S.; Zargarian, D., On the mechanism of Ni(II)-promoted Michael-type hydroamination of acrylonitrile and its substituted derivatives. *Dalton Trans.* **2016**, *45*, 15800-15810.
- (26) Estudiante-Negrete, F.; Hernandez-Ortega, S.; Morales-Morales, D., Ni(II)-POCOP pincer compound [NiCl{C₁₀H₅-2,10-(OPPh₂)₂}] an efficient and robust nickel catalyst for the Suzuki-Miyaura coupling reactions. *Inorg. Chim. Acta* **2012**, *387*, 58-63.
- (27) Chakraborty, S.; Krause, J. A.; Guan, H., Hydrosilylation of Aldehydes and Ketones Catalyzed by Nickel PCP-Pincer Hydride Complexes. *Organometallics* **2009**, *28*, 582-586.
- (28) Zhang, J.; Medley, C. M.; Krause, J. A.; Guan, H., Mechanistic Insights into C-S Cross-Coupling Reactions Catalyzed by Nickel Bis(phosphinite) Pincer Complexes. *Organometallics* **2010**, *29*, 6393-6401.
- (29) Chakraborty, S.; Patel, Y. J.; Krause, J. A.; Guan, H., Catalytic properties of nickel bis(phosphinite) pincer complexes in the reduction of CO₂ to methanol derivatives. *Polyhedron* **2012**, *32*, 30-34.
- (30) Pandarus, V.; Zargarian, D., New Pincer-Type Diphosphinito (POCOP) Complexes of Nickel. *Organometallics* **2007**, *26*, 4321-4334.

- (31) Hao, J.; Vabre, B.; Mougang-Soume, B.; Zargarian, D., Small Molecule Activation by $\text{POC}_{\text{sp}^3}\text{OP}$ -Nickel Complexes. *Chem. - Eur. J.* **2014**, *20*, 12544-12552.
- (32) Hao, J.; Mougang-Soume, B.; Vabre, B.; Zargarian, D., On the Stability of a $\text{POC}_{\text{sp}^3}\text{OP}$ -Type Pincer Ligand in Nickel(II) Complexes. *Angew. Chem., Int. Ed.* **2014**, *53*, 3218-3222.
- (33) Pandarus, V.; Castonguay, A.; Zargarian, D., Ni(II) complexes featuring non-metallated pincer-type ligands. *Dalton Trans.* **2008**, 4756-4761.
- (34) Spasyuk, D. M.; Zargarian, D.; van der Est, A., New POCN-Type Pincer Complexes of Nickel(II) and Nickel(III). *Organometallics* **2009**, *28*, 6531-6540.
- (35) Spasyuk, D. M.; Zargarian, D., Monomeric and dimeric nickel complexes derived from a pincer ligand featuring a secondary amine donor moiety. *Inorg. Chem.* **2010**, *49*, 6203-6213.
- (36) Zhang, B.-S.; Wang, W.; Shao, D.-D.; Hao, X.-Q.; Gong, J.-F.; Song, M.-P., Unsymmetrical Chiral PCN Pincer Palladium(II) and Nickel(II) Complexes of (Imidazoliny)aryl Phosphinite Ligands: Synthesis via Ligand C-H Activation, Crystal Structures, and Catalytic Studies. *Organometallics* **2010**, *29*, 2579-2587.
- (37) Spasyuk, D. M.; Gorelsky, S. I.; van der Est, A.; Zargarian, D., Characterization of Divalent and Trivalent Species Generated in the Chemical and Electrochemical Oxidation of a Dimeric Pincer Complex of Nickel. *Inorg. Chem.* **2011**, *50*, 2661-2674.
- (38) Yang, M.-J.; Liu, Y.-J.; Gong, J.-F.; Song, M.-P., Unsymmetrical Chiral PCN Pincer Palladium(II) and Nickel(II) Complexes with Aryl-Based Aminophosphine-Imidazoline Ligands: Synthesis via Aryl C-H Activation and Asymmetric Addition of Diarylphosphines to Enones. *Organometallics* **2011**, *30*, 3793-3803.
- (39) Sanford, J.; Dent, C.; Masuda, J. D.; Xia, A., Synthesis, characterization and application of pincer-type nickel iminophosphinite complexes. *Polyhedron* **2011**, *30*, 1091-1094.
- (40) Fan, L.; Foxman, B. M.; Ozerov, O. V., N-H Cleavage as a Route to Palladium Complexes of a New PNP Pincer Ligand. *Organometallics* **2004**, *23*, 326-328.
- (41) Ozerov, O. V.; Guo, C.; Fan, L.; Foxman, B. M., Oxidative Addition of N-C and N-H Bonds to Zerovalent Nickel, Palladium, and Platinum. *Organometallics* **2004**, *23*, 5573-5580.
- (42) Liang, L.-C.; Chien, P.-S.; Huang, Y.-L., Intermolecular Arene C-H Activation by Nickel(II). *J. Am. Chem. Soc.* **2006**, *128*, 15562-15563.
- (43) Liang, L.-C.; Chien, P.-S.; Lin, J.-M.; Huang, M.-H.; Huang, Y.-L.; Liao, J.-H., Amido Pincer Complexes of Nickel(II): Synthesis, Structure, and Reactivity. *Organometallics* **2006**, *25*, 1399-1411.
- (44) Adhikari, D.; Huffman, J. C.; Mindiola, D. J., Structural elucidation of a nickel boryl complex. A recyclable borylation Ni(II) reagent of bromobenzene. *Chem. Commun.* **2007**, 4489-4491.
- (45) Adhikari, D.; Pink, M.; Mindiola, D. J., Mild protocol for the synthesis of stable nickel complexes having primary and secondary silyl ligands. *Organometallics* **2009**, *28*, 2072-2077.
- (46) Fryzuk, M. D.; Montgomery, C. D., Amides of the platinum group metals. *Coord. Chem. Rev.* **1989**, *95*, 1-40.
- (47) Ingleson, M. J.; Fullmer, B. C.; Buschhorn, D. T.; Fan, H.; Pink, M.; Huffman, J. C.; Caulton, K. G., Influence of the d-Electron Count on CO Binding by Three-Coordinate $[(\text{tBu}_2\text{PCH}_2\text{SiMe}_2)_2\text{N}]\text{Fe}$, -Co, and -Ni. *Inorg. Chem.* **2008**, *47*, 407-409.
- (48) Fryzuk, M. D.; MacNeil, P. A., Hybrid multidentate ligands. Tridentate amidophosphine complexes of nickel(II) and palladium(II). *J. Am. Chem. Soc.* **1981**, *103*, 3592-3.

- (49) Tondreau, A. M.; Boncella, J. M., The synthesis of PNP-supported low-spin nitro manganese(I) carbonyl complexes. *Polyhedron* **2016**, *116*, 96-104.
- (50) Abdul Goni, M.; Rosenberg, E.; Meregude, S.; Abbott, G., A methods study of immobilization of PONOP pincer transition metal complexes on silica polyamine composites (SPC). *J. Organomet. Chem.* **2016**, *807*, 1-10.
- (51) Castro-Rodrigo, R.; Chakraborty, S.; Munjanja, L.; Brennessel, W. W.; Jones, W. D., Synthesis, Characterization, and Reactivities of Molybdenum and Tungsten PONOP Pincer Complexes. *Organometallics* **2016**, *35*, 3124-3131.
- (52) DeRieux, W.-S. W.; Wong, A.; Schrodi, Y., Synthesis and characterization of iron complexes based on bis-phosphinite PONOP and bis-phosphite PONOP pincer ligands. *J. Organomet. Chem.* **2014**, *772-773*, 60-67.
- (53) Kundu, S.; Brennessel, W. W.; Jones, W. D., Synthesis and Reactivity of New Ni, Pd, and Pt 2,6-Bis(di-*tert*-butylphosphinito)pyridine Pincer Complexes. *Inorg. Chem.* **2011**, *50*, 9443-9453.
- (54) Kundu, S.; Brennessel, W. W.; Jones, W. D., Making M-CN bonds from M-Cl in (PONOP)M and (dippe)Ni systems (M = Ni, Pd, and Pt) using *t*-BuNC. *Inorg. Chim. Acta* **2011**, *379*, 109-114.
- (55) Salem, H.; Shimon, L. J. W.; Diskin-Posner, Y.; Leitun, G.; Ben-David, Y.; Milstein, D., Formation of Stable trans-Dihydride Ruthenium(II) and 16-Electron Ruthenium(0) Complexes Based on Phosphinite PONOP Pincer Ligands. Reactivity toward Water and Electrophiles. *Organometallics* **2009**, *28*, 4791-4806.
- (56) Barloy, L.; Malaise, G.; Ramdeehul, S.; Newton, C.; Osborn, J. A.; Kyritsakas, N., Synthesis and Structural Studies of Binuclear Platinum(II) Complexes with a Novel Phosphorus-Nitrogen-Phosphorus Ligand. *Inorg. Chem.* **2003**, *42*, 2902-2907.
- (57) Vechorkin, O.; Proust, V.; Hu, X., Functional Group Tolerant Kumada-Corriu-Tamao Coupling of Nonactivated Alkyl Halides with Aryl and Heteroaryl Nucleophiles: Catalysis by a Nickel Pincer Complex Permits the Coupling of Functionalized Grignard Reagents. *J. Am. Chem. Soc.* **2009**, *131*, 9756-9766.
- (58) Madhira, V. N.; Ren, P.; Vechorkin, O.; Hu, X.; Vicic, D. A., Synthesis and electronic properties of a pentafluoroethyl-derivatized nickel pincer complex. *Dalton Trans.* **2012**, *41*, 7915-7919.
- (59) Breitenfeld, J.; Scopelliti, R.; Hu, X., Synthesis, Reactivity, and Catalytic Application of a Nickel Pincer Hydride Complex. *Organometallics* **2012**, *31*, 2128-2136.
- (60) Haenel, M. W.; Oevers, S.; Angermund, K.; Kaska, W. C.; Fan, H. J.; Hall, M. B., *Angew. Chem., Int. Ed.* **2001**, *40*, 3596.
- (61) Ohff, M.; Ohff, A.; van, d. B. M. E.; Milstein, D., Highly Active Pd(II) PCP-type Catalysts for the Heck Reaction. *J. Am. Chem. Soc.* **1997**, *119*, 11687-11688.
- (62) Dani, P.; Karlen, T.; Gossage, R. A.; Gladiali, S.; Van, K. G., Hydrogen-transfer catalysis with pincer-aryl ruthenium(II) complexes. *Angew. Chem., Int. Ed.* **2000**, *39*, 743-745.
- (63) Yu, R. P.; Darmon, J. M.; Milsmann, C.; Margulieux, G. W.; Stieber, S. C. E.; DeBeer, S.; Chirik, P. J., Catalytic Hydrogenation Activity and Electronic Structure Determination of Bis(arylimidazol-2-ylidene)pyridine Cobalt Alkyl and Hydride Complexes. *J. Am. Chem. Soc.* **2013**, *135*, 13168-13184.
- (64) Gorgas, N.; Stoeger, B.; Veiros, L. F.; Pittenauer, E.; Allmaier, G.; Kirchner, K., Efficient Hydrogenation of Ketones and Aldehydes Catalyzed by Well-Defined Iron(II) PNP Pincer Complexes: Evidence for an Insertion Mechanism. *Organometallics* **2014**, *33*, 6905-6914.

- (65) Vabre, B.; Spasyuk, D. M.; Zargarian, D., Impact of backbone substituents on POCOP-Ni pincer complexes: a structural, spectroscopic, and electrochemical study. *Organometallics* **2012**, *31*, 8561-8570.
- (66) Benito-Garagorri, D.; Becker, E.; Wiedermann, J.; Lackner, W.; Pollak, M.; Mereiter, K.; Kisala, J.; Kirchner, K., Achiral and Chiral Transition Metal Complexes with Modularly Designed Tridentate PNP Pincer-Type Ligands Based on N-Heterocyclic Diamines. *Organometallics* **2006**, *25*, 1900-1913.
- (67) Cloutier, J.-P.; Vabre, B.; Mounang-Soumé, B.; Zargarian, D., Synthesis and Reactivities of New NCN-Type Pincer Complexes of Nickel. *Organometallics* **2015**, *34*, 133-145.
- (68) Fryzuk, M. D.; Carter, A.; Westerhaus, A., Synthesis and stereochemistry of reactive mono(amido phosphine) derivatives of zirconium(IV) and hafnium(IV). X-ray crystal structures of fac-HfCl₃[N(SiMe₂CH₂PMe₂)₂] and mer-ZrCl₃[N(SiMe₂CH₂P(CHMe₂)₂)₂]. *Inorg. Chem.* **1985**, *24*, 642-648.
- (69) Kozlov, V. A.; Aleksanyan, D. V.; Nelyubina, Y. V.; Lyssenko, K. A.; Petrovskii, P. V.; Vasil'ev, A. A.; Odinets, I. L., Hybrid Thiophosphoryl-Benzothiazole Palladium SCN-Pincer Complexes: Synthesis and Effect of Structure Modifications on Catalytic Performance in the Suzuki Cross-Coupling. *Organometallics* **2011**, *30*, 2920-2932.
- (70) Albrecht, M.; van Koten, G., Platinum group organometallics based on "pincer" complexes: sensors, switches, and catalysts. *Angew. Chem., Int. Ed.* **2001**, *40*, 3750-3781.
- (71) Anastas, P. T.; Warner, J. C., *Green chemistry : theory and practice*. Oxford University Press: Oxford [England]; New York, 1998; ISBN: 0198502346-9780198502340; 0198506988-9780198506980.
- (72) Shih, W.-C.; Ozerov, O. V., One-Pot Synthesis of 1,3-Bis(phosphinomethyl)arene PCP/PPN Pincer Ligands and Their Nickel Complexes. *Organometallics* **2015**, *34*, 4591-4597.
- (73) Hartwig, J. F., *Organotransition metal chemistry : from bonding to catalysis*. 2010; ISBN: 9781891389535-89138953X.
- (74) Xiao, S.; Trogler, W. C.; Ellis, D. E.; Berkovitch-Yellin, Z., Nature of the frontier orbitals in phosphine, trimethylphosphine, and trifluorophosphine. *J. Am. Chem. Soc.* **1983**, *105*, 7033-7037.
- (75) Marynick, D. S., π -Accepting abilities of phosphines in transition-metal complexes. *J. Am. Chem. Soc.* **1984**, *106*, 4064-4065.
- (76) Tossell, J. A.; Moore, J. H.; Giordan, J. C., Energies of π -acceptor orbitals in silane, phosphine, hydrogen sulfide, and hydrogen chloride and their permethylated derivatives. *Inorg. Chem.* **1985**, *24*, 1100-1103.
- (77) Giordan, J. C.; Moore, J. H.; Tossell, J. A., Anion states of organometallic molecules and their ligands. *Acc. Chem. Res.* **1986**, *19*, 281-286.
- (78) Spessard, G. O.; Miessler, G. L., *Organometallic chemistry*. Prentice-Hall: Upper Saddle River, N.J., 1997; ISBN: 0136401783-9780136401780.
- (79) Leyssens, T.; Peeters, D.; Orpen, A. G.; Harvey, J. N., How Important Is Metal-Ligand Back-Bonding toward YX₃ Ligands (Y = N, P, C, Si)? An NBO Analysis. *Organometallics* **2007**, *26*, 2637-2645.
- (80) Tolman, C. A., Steric effects of phosphorus ligands in organometallic chemistry and homogeneous catalysis. *Chem. Rev.* **1977**, *77*, 313-348.
- (81) Pal, S., Pyridine: A Useful Ligand in Transition Metal Complexes. In *Pyridine*, 2018; ISBN: 9781789234220-9781789234237.

- (82) Eicher, T.; Hauptmann, S.; Speicher, A., *The chemistry of heterocycles : structure, reactions, syntheses and applications*. 2012; ISBN: 9783527328680-3527328688.
- (83) Immirzi, A.; Musco, A., A method to measure the size of phosphorus ligands in coordination complexes. *Inorg. Chim. Acta* **1977**, *25*, L41-L42.
- (84) Brown, T. L.; Lee, K. J., Ligand steric properties. *Coord. Chem. Rev.* **1993**, *128*, 89-116.
- (85) White, D.; Taverner, B. C.; Leach, P. G. L.; Coville, N. J., Quantification of substituent and ligand size by the use of solid angles. *J. Comput. Chem.* **1993**, *14*, 1042-1049.
- (86) Niksch, T.; Görls, H.; Weigand, W., The Extension of the Solid-Angle Concept to Bidentate Ligands. *European Journal of Inorganic Chemistry* **2010**, *2010*, 95-105.
- (87) Billbrey, J. A.; Kazez, A. H.; Locklin, J.; Allen, W. D., Exact Ligand Solid Angles. *J. Chem. Theory Comput.* **2013**, *9*, 5734-5744.
- (88) Vabre, B.; Lambert, M. L.; Petit, A.; Ess, D. H.; Zargarian, D., Nickelation of PCP- and POCOP-Type Pincer Ligands: Kinetics and Mechanism. *Organometallics* **2012**, *31*, 6041-6053.
- (89) Gagliardo, M.; Chase, P. A.; Brouwer, S.; Van Klink, G. P. M.; Van Koten, G., Electronic Effects in PCP-Pincer Ru(II)-Based Hydrogen Transfer Catalysis. *Organometallics* **2007**, *26*, 2219-2227.
- (90) Peris, E.; Crabtree, R. H., Key factors in pincer ligand design. *Chemical Society Reviews* **2018**, *47*, 1959-1968.
- (91) Ye, X.; Plessow, P. N.; Brinks, M. K.; Schelwies, M.; Schaub, T.; Rominger, F.; Paciello, R.; Limbach, M.; Hofmann, P., Alcohol Amination with Ammonia Catalyzed by an Acridine-Based Ruthenium Pincer Complex: A Mechanistic Study. *J. Am. Chem. Soc.* **2014**, *136*, 5923-5929.
- (92) Rohmann, K.; Kothe, J.; Haenel, M. W.; Englert, U.; Hölscher, M.; Leitner, W., Hydrogenation of CO₂ to Formic Acid with a Highly Active Ruthenium Acridophos Complex in DMSO and DMSO/Water. *Angew. Chem. Int. Ed.* **2016**, *55*, 8966-8969.
- (93) Gunanathan, C.; Milstein, D., Selective synthesis of primary amines directly from alcohols and ammonia. *Angew. Chem., Int. Ed.* **2008**, *47*, 8661-8664.
- (94) Goldberg, J. M.; Wong, G. W.; Brastow, K. E.; Kaminsky, W.; Goldberg, K. I.; Heinekey, D. M., The Importance of Steric Factors in Iridium Pincer Complexes. *Organometallics* **2015**, *34*, 753-762.
- (95) Smit, T. M.; Tomov, A. K.; Gibson, V. C.; White, A. J. P.; Williams, D. J., Dramatic Effect of Heteroatom Backbone Substituents on the Ethylene Polymerization Behavior of Bis(imino)pyridine Iron Catalysts. *Inorg. Chem.* **2004**, *43*, 6511-6512.
- (96) Mukherjee, A.; Milstein, D., Homogeneous Catalysis by Cobalt and Manganese Pincer Complexes. *ACS Catalysis* **2018**, *8*, 11435-11469.
- (97) Elangovan, S.; Garbe, M.; Jiao, H.; Spannenberg, A.; Junge, K.; Beller, M., Hydrogenation of Esters to Alcohols Catalyzed by Defined Manganese Pincer Complexes. *Angew. Chem., Int. Ed.* **2016**, *55*, 15364-15368.
- (98) Zell, T.; Milstein, D., Hydrogenation and Dehydrogenation Iron Pincer Catalysts Capable of Metal-Ligand Cooperation by Aromatization/Deaomatization. *Acc. Chem. Res.* **2015**, *48*, 1979-1994.
- (99) Junge, K.; Schröder, K.; Beller, M., Homogeneous catalysis using iron complexes: recent developments in selective reductions. *Chem. Commun.* **2011**, *47*, 4849-4859.
- (100) Junge, K.; Papa, V.; Beller, M., Cobalt-Pincer Complexes in Catalysis. *Chem. Eur. J.* **2019**, *25*, 122-143.
- (101) Zargarian, D.; Castonguay, A.; Spasyuk, D. M., ECE-type pincer complexes of nickel. *Top. Organomet. Chem.* **2013**, *40*, 131-174, ISBN: 9783642310805-9783642310812.

- (102) Gunanathan, C.; Milstein, D., Applications of Acceptorless Dehydrogenation and Related Transformations in Chemical Synthesis. *Science* **2013**, *341*, 1229712.
- (103) Gunanathan, C.; Milstein, D., Bond Activation and Catalysis by Ruthenium Pincer Complexes. *Chem. Rev. (Washington, DC, U. S.)* **2014**, *114*, 12024-12087.
- (104) Szabó, K. J., Pincer Complexes as Catalysts in Organic Chemistry. In *Organometallic Pincer Chemistry*, van Koten, G.; Milstein, D., Eds. Springer Berlin Heidelberg: Berlin, Heidelberg, 2013; pp 203-241, ISBN: 9783642310812.
- (105) Selander, N.; Szabó, K. J., Catalysis by Palladium Pincer Complexes. *Chem. Rev.* **2011**, *111*, 2048-2076.
- (106) Chelucci, G.; Baldino, S.; Baratta, W., Recent Advances in Osmium-Catalyzed Hydrogenation and Dehydrogenation Reactions. *Acc. Chem. Res.* **2015**, *48*, 363-379.
- (107) Choi, J.; MacArthur, A. H. R.; Brookhart, M.; Goldman, A. S., Dehydrogenation and Related Reactions Catalyzed by Iridium Pincer Complexes. *Chem. Rev. (Washington, DC, U. S.)* **2011**, *111*, 1761-1779.
- (108) Albrecht, M.; Morales-Morales, D., Pincer-Type Iridium Complexes for Organic Transformations. In *Iridium Complexes in Organic Synthesis*, 2008; pp 299-323, ISBN: 9783527623075-9783527319961.
- (109) Serrano-Becerra, J. M.; Morales-Morales, D., Applications in catalysis and organic transformations mediated by platinum group PCP and PNP aromatic-based pincer complexes. Recent advances. *Curr. Org. Synth.* **2009**, *6*, 169-192.
- (110) Shi, R.; Zhang, Z.; Hu, X., Nickamine and Analogous Nickel Pincer Catalysts for Cross-Coupling of Alkyl Halides and Hydrosilylation of Alkenes. *Acc. Chem. Res.* **2019**, *52*, 1471-1483.
- (111) Vechorkin, O.; Barmaz, D.; Proust, V.; Hu, X., Ni-Catalyzed Sonogashira Coupling of Nonactivated Alkyl Halides: Orthogonal Functionalization of Alkyl Iodides, Bromides, and Chlorides. *J. Am. Chem. Soc.* **2009**, *131*, 12078-12079.
- (112) Wang, Z.; Li, X.; Xie, S.; Zheng, T.; Sun, H., Transfer hydrogenation of ketones catalyzed by nickel complexes bearing an NHC [CNN] pincer ligand. *Appl. Organomet. Chem.* **2019**, *33*, e4932.
- (113) Connelly, S. J.; Zimmerman, A. C.; Kaminsky, W.; Heinekey, D. M., Synthesis, Structure, and Reactivity of a Nickel Dihydrogen Complex. *Chem. Eur. J.* **2012**, *18*, 15932-15934.
- (114) Schneck, F.; Ahrens, J.; Finger, M.; Stückl, A. C.; Würtele, C.; Schwarzer, D.; Schneider, S., The elusive abnormal CO₂ insertion enabled by metal-ligand cooperative photochemical selectivity inversion. *Nature Communications* **2018**, *9*, 1161.
- (115) Andérez-Fernández, M.; Vogt, L. K.; Fischer, S.; Zhou, W.; Jiao, H.; Garbe, M.; Elangovan, S.; Junge, K.; Junge, H.; Ludwig, R.; Beller, M., A Stable Manganese Pincer Catalyst for the Selective Dehydrogenation of Methanol. *Angew. Chem. Int. Ed.* **2017**, *56*, 559-562.
- (116) Bruneau-Voisine, A.; Wang, D.; Roisnel, T.; Darcel, C.; Sortais, J.-B., Hydrogenation of ketones with a manganese PN₃P pincer pre-catalyst. *Catal. Commun.* **2017**, *92*, 1-4.
- (117) Perez, M.; Elangovan, S.; Spannenberg, A.; Junge, K.; Beller, M., Molecularly Defined Manganese Pincer Complexes for Selective Transfer Hydrogenation of Ketones. *ChemSusChem* **2017**, *10*, 83-86.
- (118) Zhang, L.; Tang, Y.; Han, Z.; Ding, K., Lutidine-Based Chiral Pincer Manganese Catalysts for Enantioselective Hydrogenation of Ketones. *Angew. Chem. Int. Ed.* **2019**, *58*, 4973-4977.

- (119) Glatz, M.; Stöger, B.; Himmelbauer, D.; Veiros, L. F.; Kirchner, K., Chemoselective Hydrogenation of Aldehydes under Mild, Base-Free Conditions: Manganese Outperforms Rhenium. *ACS Catalysis* **2018**, *8*, 4009-4016.
- (120) Machan, C. W.; Stanton, C. J.; Vandezande, J. E.; Majetich, G. F.; Schaefer, H. F.; Kubiak, C. P.; Agarwal, J., Electrocatalytic Reduction of Carbon Dioxide by $\text{Mn}(\text{CN})(2,2' \text{-bipyridine})(\text{CO})_3$: CN Coordination Alters Mechanism. *Inorg. Chem.* **2015**, *54*, 8849-8856.
- (121) Riplinger, C.; Carter, E. A., Influence of Weak Brønsted Acids on Electrocatalytic CO_2 Reduction by Manganese and Rhenium Bipyridine Catalysts. *ACS Catalysis* **2015**, *5*, 900-908.
- (122) Smieja, J. M.; Sampson, M. D.; Grice, K. A.; Benson, E. E.; Froehlich, J. D.; Kubiak, C. P., Manganese as a Substitute for Rhenium in CO_2 Reduction Catalysts: The Importance of Acids. *Inorg. Chem.* **2013**, *52*, 2484-2491.
- (123) Zeng, Q.; Tory, J.; Hartl, F., Electrocatalytic Reduction of Carbon Dioxide with a Manganese(I) Tricarbonyl Complex Containing a Nonaromatic α -Diimine Ligand. *Organometallics* **2014**, *33*, 5002-5008.
- (124) Bauer, J. O.; Chakraborty, S.; Milstein, D., Manganese-Catalyzed Direct Deoxygenation of Primary Alcohols. *Acs Catalysis* **2017**, *7*, 4462-4466.
- (125) Das, U. K.; Ben-David, Y.; Diskin-Posner, Y.; Milstein, D., N-Substituted Hydrazones by Manganese-Catalyzed Coupling of Alcohols with Hydrazine: Borrowing Hydrogen and Acceptorless Dehydrogenation in One System. *Angew. Chem. Int. Ed.* **2018**, *57*, 2179-2182.
- (126) Chakraborty, S.; Gellrich, U.; Diskin - Posner, Y.; Leitun, G.; Avram, L.; Milstein, D., Manganese - Catalyzed N - Formylation of Amines by Methanol Liberating H_2 : A Catalytic and Mechanistic Study. *Angew. Chem. Int. Ed.* **2017**, *56*, 4229-4233.
- (127) Chakraborty, S.; Das, U. K.; Ben-David, Y.; Milstein, D., Manganese Catalyzed α -Olefination of Nitriles by Primary Alcohols. *J. Am. Chem. Soc.* **2017**, *139*, 11710-11713.
- (128) Srimani, D.; Diskin-Posner, Y.; Ben-David, Y.; Milstein, D., Iron Pincer Complex Catalyzed, Environmentally Benign, E-Selective Semi-Hydrogenation of Alkynes. *Angew. Chem., Int. Ed.* **2013**, *52*, 14131-14134.
- (129) Langer, R.; Leitun, G.; Ben-David, Y.; Milstein, D., Efficient Hydrogenation of Ketones Catalyzed by an Iron Pincer Complex. *Angew. Chem., Int. Ed.* **2011**, *50*, 2120-2124, S2120/1-S2120/11.
- (130) Zell, T.; Butschke, B.; Ben-David, Y.; Milstein, D., Efficient Hydrogen Liberation from Formic Acid Catalyzed by a Well-Defined Iron Pincer Complex under Mild Conditions. *Chem. Eur. J.* **2013**, *19*, 8068-8072.
- (131) Sharma, A.; Hartwig, J. F., Metal-catalysed azidation of tertiary C-H bonds suitable for late-stage functionalization. *Nature* **2015**, *517*, 600-604.
- (132) Pony Yu, R.; Hesk, D.; Rivera, N.; Pelczer, I.; Chirik, P. J., Iron-catalysed tritiation of pharmaceuticals. *Nature* **2016**, *529*, 195-199.
- (133) Sharninghausen, L. S.; Mercado, B. Q.; Crabtree, R. H.; Hazari, N., Selective conversion of glycerol to lactic acid with iron pincer precatalysts. *Chem. Commun.* **2015**, *51*, 16201-16204.
- (134) Zhang, G.; Scott, B. L.; Hanson, S. K., Mild and Homogeneous Cobalt-Catalyzed Hydrogenation of C-C, C-O, and C-N Bonds. *Angew. Chem.* **2012**, *124*, 12268-12272.

- (135) Obligacion, J. V.; Chirik, P. J., Bis(imino)pyridine Cobalt-Catalyzed Alkene Isomerization–Hydroboration: A Strategy for Remote Hydrofunctionalization with Terminal Selectivity. *J. Am. Chem. Soc.* **2013**, *135*, 19107-19110.
- (136) Daw, P.; Chakraborty, S.; Garg, J. A.; Ben-David, Y.; Milstein, D., Direct Synthesis of Pyrroles by Dehydrogenative Coupling of Diols and Amines Catalyzed by Cobalt Pincer Complexes. *Angew. Chem.* **2016**, *128*, 14585-14589.
- (137) van der Vlugt, J. I.; Pidko, E. A.; Vogt, D.; Lutz, M.; Spek, A. L., CuI Complexes with a Noninnocent PNP Ligand: Selective Dearomatization and Electrophilic Addition Reactivity. *Inorg. Chem.* **2009**, *48*, 7513-7515.
- (138) Vogt, M.; Nerush, A.; Iron, M. A.; Leitus, G.; Diskin-Posner, Y.; Shimon, L. J. W.; Ben-David, Y.; Milstein, D., Activation of Nitriles by Metal Ligand Cooperation. Reversible Formation of Ketimido- and Enamido-Rhenium PNP Pincer Complexes and Relevance to Catalytic Design. *J. Am. Chem. Soc.* **2013**, *135*, 17004-17018.
- (139) Vogt, M.; Rivada-Wheelaghan, O.; Iron, M. A.; Leitus, G.; Diskin-Posner, Y.; Shimon, L. J. W.; Ben-David, Y.; Milstein, D., Anionic Nickel(II) Complexes with Doubly Deprotonated PNP Pincer-Type Ligands and Their Reactivity toward CO₂. *Organometallics* **2013**, *32*, 300-308.
- (140) Milstein, D.; Gunanathan, C. Preparation of ruthenium complexes with quinolinyl or acridinyl based pincer ligands for use as catalysts in the process for preparing amines from alcohols and ammonia. WO2010018570A1, 2010.
- (141) Gunanathan, C.; Shimon, L. J. W.; Milstein, D., Direct Conversion of Alcohols to Acetals and H₂ Catalyzed by an Acridine-Based Ruthenium Pincer Complex. *J. Am. Chem. Soc.* **2009**, *131*, 3146-3147.
- (142) Daw, P.; Kumar, A.; Oren, D.; Espinosa-Jalapa, N. A.; Srimani, D.; Diskin-Posner, Y.; Leitus, G.; Shimon, L. J. W.; Carmieli, R.; Ben-David, Y.; Milstein, D., Redox Noninnocent Nature of Acridine-Based Pincer Complexes of 3d Metals and C–C Bond Formation. *Organometallics* **2020**, *39*, 279-285.
- (143) Gao, Y.; Yip, J. H. K., Selective Hypochlorous Acid Detection by Electronic Tuning of Platinum–4,5-bis(diphenylphosphino)acridine–Thiolate Complexes. *Inorg. Chem.* **2019**, *58*, 9290-9302.
- (144) Daw, P.; Kumar, A.; Espinosa-Jalapa, N. A.; Ben-David, Y.; Milstein, D., Direct Synthesis of Amides by Acceptorless Dehydrogenative Coupling of Benzyl Alcohols and Ammonia Catalyzed by a Manganese Pincer Complex: Unexpected Crucial Role of Base. *J. Am. Chem. Soc.* **2019**, *141*, 12202-12206.
- (145) Daw, P.; Kumar, A.; Espinosa-Jalapa, N. A.; Diskin-Posner, Y.; Ben-David, Y.; Milstein, D., Synthesis of Pyrazines and Quinoxalines via Acceptorless Dehydrogenative Coupling Routes Catalyzed by Manganese Pincer Complexes. *ACS Catalysis* **2018**, *8*, 7734-7741.
- (146) Gellrich, U.; Khusnutdinova, J. R.; Leitus, G. M.; Milstein, D., Mechanistic Investigations of the Catalytic Formation of Lactams from Amines and Water with Liberation of H₂. *J. Am. Chem. Soc.* **2015**, *137*, 4851-4859.
- (147) Xie, Y.; Ben-David, Y.; Shimon, L. J. W.; Milstein, D., Highly Efficient Process for Production of Biofuel from Ethanol Catalyzed by Ruthenium Pincer Complexes. *J. Am. Chem. Soc.* **2016**, *138*, 9077-9080.
- (148) Lippert, C. A.; Arnstein, S. A.; Sherrill, C. D.; Soper, J. D., Redox-Active Ligands Facilitate Bimetallic O₂ Homolysis at Five-Coordinate Oxorhenium(V) Centers. *J. Am. Chem. Soc.* **2010**, *132*, 3879-3892.
- (149) Wang, K.; Stiefel, E. I., Toward Separation and Purification of Olefins Using Dithiolene Complexes: An Electrochemical Approach. *Science* **2001**, *291*, 106-109.

- (150) van Leest, N. P.; Tepaske, M. A.; Oudsen, J.-P. H.; Venderbosch, B.; Rietdijk, N. R.; Siegler, M. A.; Tromp, M.; van der Vlugt, J. I.; de Bruin, B., Ligand Redox Noninnocence in $[\text{Co}^{\text{III}}(\text{TAML})]^{0/-}$ Complexes Affects Nitrene Formation. *J. Am. Chem. Soc.* **2020**, *142*, 552-563.
- (151) Bart, S. C.; Chłopek, K.; Bill, E.; Bouwkamp, M. W.; Lobkovsky, E.; Neese, F.; Wieghardt, K.; Chirik, P. J., Electronic Structure of Bis(imino)pyridine Iron Dichloride, Monochloride, and Neutral Ligand Complexes: A Combined Structural, Spectroscopic, and Computational Study. *J. Am. Chem. Soc.* **2006**, *128*, 13901-13912.
- (152) Bouwkamp, M. W.; Bowman, A. C.; Lobkovsky, E.; Chirik, P. J., Iron-Catalyzed $[2\pi + 2\pi]$ Cycloaddition of α,ω -Dienes: The Importance of Redox-Active Supporting Ligands. *J. Am. Chem. Soc.* **2006**, *128*, 13340-13341.
- (153) Sylvester, K. T.; Chirik, P. J., Iron-Catalyzed, Hydrogen-Mediated Reductive Cyclization of 1,6-Enynes and Diynes: Evidence for Bis(imino)pyridine Ligand Participation. *J. Am. Chem. Soc.* **2009**, *131*, 8772-8774.
- (154) Talukdar, K.; Issa, A.; Jurss, J. W., Synthesis of a Redox-Active NNP-Type Pincer Ligand and Its Application to Electrocatalytic CO_2 Reduction With First-Row Transition Metal Complexes. *Frontiers in Chemistry* **2019**, *7*.
- (155) Gusev, D. G., Revised Mechanisms of the Catalytic Alcohol Dehydrogenation and Ester Reduction with the Milstein PNN Complex of Ruthenium. *Organometallics* **2020**, *39*, 258-270.
- (156) Sinha, V.; Govindarajan, N.; de Bruin, B.; Meijer, E. J., How Solvent Affects C–H Activation and Hydrogen Production Pathways in Homogeneous Ru-Catalyzed Methanol Dehydrogenation Reactions. *ACS Catalysis* **2018**, *8*, 6908-6913.
- (157) Miyake, Y.; Nakajima, K.; Higuchi, Y.; Nishibayashi, Y., Synthesis and Redox Properties of PNP Pincer Complexes Based on N-Methyl-4,4'-bipyridinium. *European Journal of Inorganic Chemistry* **2014**, *2014*, 4273-4280.
- (158) Frew, J. J. R.; Damian, K.; Van Rensburg, H.; Slawin, A. M. Z.; Tooze, R. P.; Clarke, M. L., Palladium(II) Complexes of New Bulky Bidentate Phosphanes: Active and Highly Regioselective Catalysts for the Hydroxycarbonylation of Styrene. *Chem. Eur. J.* **2009**, *15*, 10504-10513.
- (159) Naghipour, A.; Sabounchei, S. J.; Morales-Morales, D.; Hernández-Ortega, S.; Jensen, C. M., Synthesis of a new class of unsymmetrical PCP' pincer ligands and their palladium (II) complexes: X-ray structure determination of $\text{PdCl}\{\text{C}_6\text{H}_3\text{-2-CH}_2\text{PPh}_2\text{-6-CH}_2\text{PtBu}_2\}$. *J. Organomet. Chem.* **2004**, *689*, 2494-2502.
- (160) Jones, G. D.; Martin, J. L.; McFarland, C.; Allen, O. R.; Hall, R. E.; Haley, A. D.; Brandon, R. J.; Kanovalova, T.; Desrochers, P. J.; Pulay, P.; Vicic, D. A., Ligand Redox Effects in the Synthesis, Electronic Structure, and Reactivity of an Alkyl-Alkyl Cross-Coupling Catalyst. *J. Am. Chem. Soc.* **2006**, *128*, 13175-13183.
- (161) Schultz, J. W.; Fuchigami, K.; Zheng, B.; Rath, N. P.; Mirica, L. M., Isolated Organometallic Nickel(III) and Nickel(IV) Complexes Relevant to Carbon–Carbon Bond Formation Reactions. *J. Am. Chem. Soc.* **2016**, *138*, 12928-12934.
- (162) Breitenfeld, J.; Ruiz, J.; Wodrich, M. D.; Hu, X., Bimetallic Oxidative Addition Involving Radical Intermediates in Nickel-Catalyzed Alkyl–Alkyl Kumada Coupling Reactions. *J. Am. Chem. Soc.* **2013**, *135*, 12004-12012.
- (163) Proutiere, F.; Aufiero, M.; Schoenebeck, F., Reactivity and Stability of Dinuclear Pd(I) Complexes: Studies on the Active Catalytic Species, Insights into Precatalyst Activation and Deactivation, and Application in Highly Selective Cross-Coupling Reactions. *J. Am. Chem. Soc.* **2012**, *134*, 606-612.

- (164) Pandey, D. K.; Ankade, S. B.; Ali, A.; Vinod, C. P.; Punji, B., Nickel-catalyzed C–H alkylation of indoles with unactivated alkyl chlorides: evidence of a Ni(I)/Ni(III) pathway. *Chem. Sci.* **2019**, *10*, 9493-9500.
- (165) Lin, C.-Y.; Power, P. P., Complexes of Ni(I): a “rare” oxidation state of growing importance. *Chemical Society Reviews* **2017**, *46*, 5347-5399.
- (166) Chakraborty, U.; Urban, F.; Mühldorf, B.; Rebreyend, C.; de Bruin, B.; van Velzen, N.; Harder, S.; Wolf, R., Accessing the CpArNi(I) Synthon: Reactions with N-Heterocyclic Carbenes, TEMPO, Sulfur, and Selenium. *Organometallics* **2016**, *35*, 1624-1631.
- (167) Pelties, S.; Herrmann, D.; de Bruin, B.; Hartl, F. e.; Wolf, R., Selective P4 activation by an organometallic nickel(I) radical: formation of a dinuclear nickel(II) tetraphosphide and related di- and trichalcogenides. *Chem. Commun.* **2014**, *50*, 7014-7016.
- (168) Pribanic, B.; Trincado, M.; Eiler, F.; Vogt, M.; Comas-Vives, A.; Grützmacher, H., Hydrogenolysis of Polysilanes Catalyzed by Low-Valent Nickel Complexes. *Angew Chem Int Ed Engl* **2020** <https://doi.org/10.1002/ange.201907525>.
- (169) Vogt, M.; de Bruin, B.; Berke, H.; Trincado, M.; Grützmacher, H., Amino olefin nickel(I) and nickel(0) complexes as dehydrogenation catalysts for amine boranes. *Chem. Sci.* **2011**, *2*, 723-727.
- (170) Rettenmeier, C. A.; Wadepohl, H.; Gade, L. H., Electronic structure and reactivity of nickel(I) pincer complexes: their aerobic transformation to peroxo species and site selective C–H oxygenation. *Chem. Sci.* **2016**, *7*, 3533-3542.
- (171) Rettenmeier, C. A.; Wenz, J.; Wadepohl, H.; Gade, L. H., Activation of Aryl Halides by Nickel(I) Pincer Complexes: Reaction Pathways of Stoichiometric and Catalytic Dehalogenations. *Inorg. Chem.* **2016**, *55*, 8214-8224.
- (172) Rettenmeier, C. A.; Wadepohl, H.; Gade, L. H., Structural Characterization of a Hydroperoxo Nickel Complex and Its Autoxidation: Mechanism of Interconversion between Peroxo, Superoxo, and Hydroperoxo Species. *Angew. Chem. Int. Ed.* **2015**, *54*, 4880-4884.
- (173) Rettenmeier, C.; Wadepohl, H.; Gade, L. H., Stereoselective Hydrodehalogenation via a Radical-Based Mechanism Involving T-Shaped Chiral Nickel(I) Pincer Complexes. *Chem. - Eur. J.* **2014**, *20*, 9657-9665.
- (174) Sahoo, D.; Yoo, C.; Lee, Y., Direct CO₂ Addition to a Ni(0)–CO Species Allows the Selective Generation of a Nickel(II) Carboxylate with Expulsion of CO. *J. Am. Chem. Soc.* **2018**, *140*, 2179-2185.
- (175) Yoo, C.; Kim, Y.-E.; Lee, Y., Selective Transformation of CO₂ to CO at a Single Nickel Center. *Acc. Chem. Res.* **2018**, *51*, 1144-1152.
- (176) Yoo, C.; Lee, Y., A T-Shaped Nickel(I) Metalloradical Species. *Angew Chem Int Ed Engl* **2017**, *56*, 9502-9506.
- (177) Yoo, C.; Oh, S.; Kim, J.; Lee, Y., Transmethylation of a four-coordinate nickel(I) monocarbonyl species with methyl iodide. *Chem. Sci.* **2014**, *5*, 3853-3858.
- (178) Adhikari, D.; Mossin, S.; Basuli, F.; Dible, B. R.; Chipara, M.; Fan, H.; Huffman, J. C.; Meyer, K.; Mindiola, D. J., A Dinuclear Ni(I) System Having a Diradical Ni₂N₂ Diamond Core Resting State: Synthetic, Structural, Spectroscopic Elucidation, and Reductive Bond Splitting Reactions. *Inorg. Chem.* **2008**, *47*, 10479-10490.
- (179) Kreye, M.; Freytag, M.; Jones, P. G.; Williard, P. G.; Bernskoetter, W. H.; Walter, M. D., Homolytic H₂ cleavage by a mercury-bridged Ni(I) pincer complex [{(PNP)Ni}₂{μ-Hg}]. *Chem. Commun.* **2015**, *51*, 2946-2949.
- (180) Wenz, J.; Rettenmeier, C. A.; Wadepohl, H.; Gade, L. H., Catalytic C–F bond activation of geminal difluorocyclopropanes by nickel(i) complexes via a radical mechanism. *Chem. Commun.* **2016**, *52*, 202-205.

- (181) Grueger, N.; Wadeppohl, H.; Gade, L. H., A readily accessible PNP pincer ligand with a pyrrole backbone and its Ni^{II} chemistry. *Dalton Trans.* **2012**, 41, 14028-14030.
- (182) Dudnik, A. S.; Fu, G. C., Nickel-Catalyzed Coupling Reactions of Alkyl Electrophiles, Including Unactivated Tertiary Halides, To Generate Carbon–Boron Bonds. *J. Am. Chem. Soc.* **2012**, 134, 10693-10697.
- (183) Zimmermann, P.; Limberg, C., Activation of Small Molecules at Nickel(I) Moieties. *J. Am. Chem. Soc.* **2017**, 139, 4233-4242.
- (184) Yoo, C.; Ajitha, M. J.; Jung, Y.; Lee, Y., Mechanistic Study on C–C Bond Formation of a Nickel(I) Monocarbonyl Species with Alkyl Iodides: Experimental and Computational Investigations. *Organometallics* **2015**, 34, 4305-4311.
- (185) Wongnate, T.; Ragsdale, S. W., The Reaction Mechanism of Methyl-Coenzyme M Reductase: HOW AN ENZYME ENFORCES STRICT BINDING ORDER. *J. Biol. Chem.* **2015**, 290, 9322-9334.
- (186) Seravalli, J.; Ragsdale, S. W., Pulse-Chase Studies of the Synthesis of Acetyl-CoA by Carbon Monoxide Dehydrogenase/Acetyl-CoA Synthase: Evidence for a random mechanism of methyl and carbonyl addition. *J. Biol. Chem.* **2008**, 283, 8384-8394.
- (187) Rosiak, D.; Okuniewski, A.; Chojnacki, J., Novel complexes possessing Hg–(Cl, Br, I)···OC halogen bonding and unusual Hg₂S₂(Br/I)₄ kernel. The usefulness of τ_4' structural parameter. *Polyhedron* **2018**, 146, 35-41.
- (188) Hill, E. A.; Zhao, N.; Filatov, A. S.; Anderson, J. S., Nickel(II)-methyl complexes adopting unusual seesaw geometries. *Chem. Commun.* **2020**.
- (189) Grove, D. M.; Van Koten, G.; Mul, P.; Zoet, R.; Van der Linden, J. G. M.; Legters, J.; Schmitz, J. E. J.; Murrall, N. W.; Welch, A. J., Syntheses and characterization of unique organometallic nickel(III) aryl species. ESR and electrochemical studies and the x-ray molecular study of square-pyramidal [Ni{C₆H₃(CH₂NMe₂)₂-o,o'}I₂]. *Inorg. Chem.* **1988**, 27, 2466-2473.
- (190) Martinez, G. E.; Ocampo, C.; Park, Y. J.; Fout, A. R., Accessing Pincer Bis(carbene) Ni(IV) Complexes from Ni(II) via Halogen and Halogen Surrogates. *J. Am. Chem. Soc.* **2016**, 138, 4290-4293.
- (191) van de Kuil, L. A.; Grove, D. M.; Gossage, R. A.; Zwikker, J. W.; Jenneskens, L. W.; Drenth, W.; van Koten, G., Mechanistic Aspects of the Kharasch Addition Reaction Catalyzed by Organonickel(II) Complexes Containing the Monoanionic Terdentate Aryldiamine Ligand System [C₆H₂(CH₂NMe₂)₂-2,6-R-4]. *Organometallics* **1997**, 16, 4985-4994.
- (192) Holmes, A. J.; Rayner, P. J.; Cowley, M. J.; Green, G. G. R.; Whitwood, A. C.; Duckett, S. B., The reaction of an iridium PNP complex with parahydrogen facilitates polarisation transfer without chemical change. *Dalton Trans.* **2015**, 44, 1077-1083.
- (193) Miyake, Y.; Nakajima, K.; Higuchi, Y.; Nishibayashi, Y., Synthesis and Redox Properties of PNP Pincer Complexes Based on N-Methyl-4,4'-bipyridinium. *Eur. J. Inorg. Chem.* **2014**, 2014, 4273-4280.
- (194) Yang, L.; Powell, D. R.; Houser, R. P., Structural variation in copper(I) complexes with pyridylmethanamide ligands: structural analysis with a new four-coordinate geometry index, τ_4 . *Dalton Trans.* **2007**, 955-964.
- (195) Okuniewski, A.; Rosiak, D.; Chojnacki, J.; Becker, B., Coordination polymers and molecular structures among complexes of mercury(II) halides with selected 1-benzoylthioureas. *Polyhedron* **2015**, 90, 47-57.
- (196) Blackaby, W. J. M.; Sabater, S.; Poulten, R. C.; Page, M. J.; Folli, A.; Krewald, V.; Mahon, M. F.; Murphy, D. M.; Richards, E.; Whittlesey, M. K., Mono- and dinuclear

- Ni(i) products formed upon bromide abstraction from the Ni(I) ring-expanded NHC complex [Ni(6-Mes)(PPh₃)Br]. *Dalton Trans.* **2018**, 47, 769-782.
- (197) Neese, F., The ORCA program system. *Wiley Interdisciplinary Reviews: Computational Molecular Science* **2012**, 2, 73-78.
- (198) Stoll, S.; Schweiger, A., EasySpin, a comprehensive software package for spectral simulation and analysis in EPR. *J. Magn. Res.* **2006**, 178, 42-55.
- (199) MathWorks, I., *MATLAB : the language of technical computing : computation, visualization, programming : installation guide for UNIX version 5*. Natwick : Math Works Inc., 1996.1996.
- (200) Leonid, S. *Chemissian*, v. 4.53; 2005-2017.
- (201) Guzei, I. A.; Wendt, M., An improved method for the computation of ligand steric effects based on solid angles. *Dalton Trans.* **2006**, 3991-3999.
- (202) Bondi, A., van der Waals Volumes and Radii. *J. Phys. Chem.* **1964**, 68, 441-451.
- (203) McQuarrie, D. A.; Simon, J. D., *Physical chemistry : a molecular approach*. p xxiii, 1360 pages, 0935702997 (acid-free paper).
- (204) De Buysser, K.; Herman, G. G.; Bruneel, E.; Hoste, S.; Van Driessche, I., Determination of the number of unpaired electrons in metal-complexes. A comparison between the Evans' method and susceptometer results. *Chem. Phys.* **2005**, 315, 286-292.
- (205) Carlin, R. L., *Magnetochemistry*. Springer-Verlag Berlin Heidelberg 1986; p XI, 328, ISBN: 0387158162 (U.S.).
- (206) Sheldrick, G., SHELXT - Integrated space-group and crystal-structure determination. *Acta Crystallogr., Sect. A: Found. Adv.* **2015**, 71, 3-8.
- (207) Sheldrick, G., Crystal structure refinement with SHELXL. *Acta Crystallogr., Sect. C: Struct. Chem.* **2015**, 71, 3-8.
- (208) Dolomanov, O. V.; Bourhis, L. J.; Gildea, R. J.; Howard, J. A. K.; Puschmann, H., OLEX2: a complete structure solution, refinement and analysis program. *J. Appl. Crystallogr.* **2009**, 42, 339-341.
- (209) Farrugia, L., WinGX and ORTEP for Windows: an update. *J. Appl. Crystallogr.* **2012**, 45, 849-854.
- (210) Parsons, S.; Flack, H. D.; Wagner, T., Use of intensity quotients and differences in absolute structure refinement. *Acta Crystallogr., Sect. B* **2013**, 69, 249-259.
- (211) M. J. Frisch, G. W. T., H. B. Schlegel, G. E. Scuseria, M. A. Robb, J. R. Cheeseman, G. Scalmani, V. Barone, B. Mennucci, G. A. Petersson, H. Nakatsuji, M. Caricato, X. Li, H. P. Hratchian, A. F. Izmaylov, J. Bloino, G. Zheng, J. L. Sonnenberg, M. Hada, M. Ehara, K. Toyota, R. Fukuda, J. Hasegawa, M. Ishida, T. Nakajima, Y. Honda, O. Kitao, H. Nakai, T. Vreven, J. A. Montgomery, Jr., J. E. Peralta, F. Ogliaro, M. Bearpark, J. J. Heyd, E. Brothers, K. N. Kudin, V. N. Staroverov, T. Keith, R. Kobayashi, J. Normand, K. Raghavachari, A. Rendell, J. C. Burant, S. S. Iyengar, J. Tomasi, M. Cossi, N. Rega, J. M. Millam, M. Klene, J. E. Knox, J. B. Cross, V. Bakken, C. Adamo, J. Jaramillo, R. Gomperts, R. E. Stratmann, O. Yazyev, A. J. Austin, R. Cammi, C. Pomelli, J. W. Ochterski, R. L. Martin, K. Morokuma, V. G. Zakrzewski, G. A. Voth, P. Salvador, J. J. Dannenberg, S. Dapprich, A. D. Daniels, O. Farkas, J. B. Foresman, J. V. Ortiz, J. Cioslowski, and D. J. Fox *Gaussian, Inc.*, E.01: Wallingford CT, 2013.
- (212) Lee, C. T.; Yang, W. T.; Parr, R. G., Development of the Colle-Salvetti Correlation-Energy Formula into a Functional of the Electron-Density. *Phys. Rev. B* **1988**, 37, 785-789.

- (213) Becke, A. D., Density - functional thermochemistry. III. The role of exact exchange. *J. Chem. Phys.* **1993**, *98*, 5648-5652.
- (214) *Mathematica*, Wolfram Research, Inc.: Champaign, IL, 2010.
- (215) Holmes, A. J.; Rayner, P. J.; Cowley, M. J.; Green, G. G. R.; Whitwood, A. C.; Duckett, S. B., The reaction of an iridium PNP complex with parahydrogen facilitates polarisation transfer without chemical change. *Dalton Trans.* **2015**, *44*, 1077-1083.
- (216) Enthaler, S.; Brück, A.; Kammer, A.; Junge, H.; Irran, E.; Gülak, S., Exploring the Reactivity of Nickel Pincer Complexes in the Decomposition of Formic Acid to CO₂/H₂ and the Hydrogenation of NaHCO₃ to HCOONa. *ChemCatChem* **2015**, *7*, 65-69.
- (217) Adhikary, A.; Krause, J. A.; Guan, H., Configurational Stability and Stereochemistry of P-Stereogenic Nickel POCOP-Pincer Complexes. *Organometallics* **2015**, *34*, 3603-3610.
- (218) Oren, D.; Diskin-Posner, Y.; Avram, L.; Feller, M.; Milstein, D., Metal-Ligand Cooperation as Key in Formation of Dearomatized Ni(II)-H Pincer Complexes and in Their Reactivity toward CO and CO₂. *Organometallics* **2018**, *37*, 2217-2221.
- (219) Li, H.; Goncalves, T. P.; Zhao, Q.; Gong, D.; Lai, Z.; Wang, Z.; Zheng, J.; Huang, K.-W., Diverse catalytic reactivity of a dearomatized PN₃P*-nickel hydride pincer complex towards CO₂ reduction. *Chem. Commun.* **2018**, *54*, 11395-11398.
- (220) Chakraborty, S.; Bhattacharya, P.; Dai, H.; Guan, H., Nickel and Iron Pincer Complexes as Catalysts for the Reduction of Carbonyl Compounds. *Acc. Chem. Res.* **2015**, *48*, 1995-2003.
- (221) Vasudevan, K. V.; Scott, B. L.; Hanson, S. K., Alkene Hydrogenation Catalyzed by Nickel Hydride Complexes of an Aliphatic PNP Pincer Ligand. *Eur. J. Inorg. Chem.* **2012**, *2012*, 4898-4906, S4898/1-S4898/9.
- (222) Wilson, G. L. O.; Abraha, M.; Krause, J. A.; Guan, H., Reactions of phenylacetylene with nickel POCOP-pincer hydride complexes resulting in different outcomes from their palladium analogues. *Dalton Trans.* **2015**, *44*, 12128-12136.
- (223) Mousa, A. H.; Bendix, J.; Wendt, O. F., Synthesis, characterization, and reactivity of PCN pincer nickel complexes. *Organometallics* **2018**, *37*, 2581-2593.
- (224) Wellala, N. P. N.; Dong, H. T.; Krause, J. A.; Guan, H., Janus POCOP Pincer Complexes of Nickel. *Organometallics* **2018**, *37*, 4031-4039.
- (225) van, d. V. J. I.; Lutz, M.; Pidko, E. A.; Vogt, D.; Spek, A. L., Cationic and neutral Ni(II) complexes containing a non-innocent PNP ligand: formation of alkyl and thiolate species. *Dalton Trans* **2009**, 1016-23.
- (226) Curado, N.; Maya, C.; Lopez-Serrano, J.; Rodriguez, A., Boryl-assisted hydrogenolysis of a nickel-methyl bond. *Chem. Commun.* **2014**, *50*, 15718-15721.
- (227) Jonasson, K. J.; Wendt, O. F., Synthesis and Characterization of a Family of POCOP Pincer Complexes with Nickel: Reactivity Towards CO₂ and Phenylacetylene. *Chem. Eur. J.* **2014**, *20*, 11894-11902.
- (228) Martínez-Prieto, L. M.; Melero, C.; del Río, D.; Palma, P.; Cámpora, J.; Álvarez, E., Synthesis and Reactivity of Nickel and Palladium Fluoride Complexes with PCP Pincer Ligands. NMR-Based Assessment of Electron-Donating Properties of Fluoride and Other Monoanionic Ligands. *Organometallics* **2012**, *31*, 1425-1438.
- (229) Lapointe, S.; Khaskin, E.; Fayzullin, R. R.; Khusnutdinova, J. R., Stable Nickel(I) Complexes with Electron-Rich, Sterically-Hindered, Innocent PNP Pincer Ligands. *Organometallics* **2019**, *38*, 1581-1594.
- (230) Gwak, J.; Ahn, S.; Baik, M.-H.; Lee, Y., One metal is enough: a nickel complex reduces nitrate anions to nitrogen gas. *Chem. Sci.* **2019**, *10*, 4767-4774.

-
- (231) Ohtsu, H.; Tanaka, K., An Organic Hydride Transfer Reaction of a Ruthenium NAD Model Complex Leading to Carbon Dioxide Reduction. *Angew. Chem. Int. Ed.* **2012**, *51*, 9792-9795.
- (232) Fukushima, T.; Ghosh, D.; Kobayashi, K.; Ohtsu, H.; Kitagawa, S.; Tanaka, K., Four-Electron Reduction of a New Ruthenium Dicarbonyl Complex Having Two NAD Model Ligands through Decarboxylation in Water. *Inorg. Chem.* **2016**, *55*, 11613-11616.
- (233) Ohtsu, H.; Fujii, S.; Tsuge, K.; Tanaka, K., Novel synthesis of a four-electron-reduced ruthenium(II) NADH-type complex under water-gas-shift reaction conditions. *Dalton Trans.* **2016**, *45*, 16130-16133.
- (234) Connelly, N. G.; Geiger, W. E., Chemical Redox Agents for Organometallic Chemistry. *Chem. Rev.* **1996**, *96*, 877-910.
- (235) Zanello, P., *Inorganic electrochemistry : theory, practice and applications*. Royal Society of Chemistry: Cambridge, 2003; ISBN: 0854046615-9780854046614.
- (236) Yarkov SP, B. V., Zubarev VE, Spin trap in study of acetone radiolysis using nitrones. *Khim Vys Energ* **1980**, *14*, 115-120.
- (237) Hamilton, D. E.; Drago, R. S.; Telser, J., Spin trapping of a cobalt-dioxygen complex. *J. Am. Chem. Soc.* **1984**, *106*, 5353-5355.
- (238) Khusnutdinova, J. R.; Rath, N. P.; Mirica, L. M., The Aerobic Oxidation of a Pd(II) Dimethyl Complex Leads to Selective Ethane Elimination from a Pd(III) Intermediate. *J. Am. Chem. Soc.* **2012**, *134*, 2414-2422.
- (239) Lu, T.; Chen, F., Multiwfn: A multifunctional wavefunction analyzer. *J. Comput. Chem.* **2012**, *33*, 580-592.
- (240) Spek, A., PLATON SQUEEZE: a tool for the calculation of the disordered solvent contribution to the calculated structure factors. *Acta Crystallogr., Sect. C: Struct. Chem.* **2015**, *71*, 9-18.